Photoluminescence of ZnO Grown by Eclipse Pulsed Laser Deposition

A thesis submitted in partial fulfillment
of the requirements for the Degree
of
Doctor of Philosophy in Physics
in the
University of Canterbury

by

Rueben Mendelsberg

University of Canterbury
2009

Abstract

ZnO thin films and nanostructures were grown by eclipse pulsed laser deposition (EPLD) for the first time. On bare sapphire held at 600 °C, a complex nanostructured surface was formed when ablating a metallic Zn target in an oxygen ambient. Nanorods grown by a vapor-solid mechanism clumped together in well separated, micron-sized regions. Nanoscale pyramids with 6 fold symmetry formed between the nanorod clumps by vapor-liquid-solid growth. Strong photoluminescence (PL) was observed from the EPLD grown samples, an order of magnitude stronger than PLD grown nanorods formed under similar growth conditions. Low temperature PL was dominated by the I_7 exciton, which still has an unknown origin. Excitation intensity dependence of I_7 was drastically different than the rest of the nearby excitonic features, behavior which has not been previously reported for bound excitons in ZnO. I_7 also showed large, seemingly random variations in intensity across the surface of each sample compared to the other nearby recombinations, suggesting a structural connection.

Introduction of a buffer layer had a profound effect on the morphology and PL from EPLD grown ZnO from a metallic Zn target. Pt has a high melting temperature, which helped suppress the vapor-liquid-solid nanostructure growth resulting in thin-film formation. For standard PLD, the ZnO film showed large grains separated by cracks on the surface. Due to the reduced growth rate in the EPLD geometry, the ZnO layer had a high density of nanoscale pores, reminiscent of the porous Pt buffer layer. Strong PL emission, which was dominated by I_7, was observed from the ZnO/Pt/Al_2O_3 which showed unusual blue/violet emission when the EPLD geometry was used for growth. Thin ZnO buffer layers deposited at reduced temperature also had a profound effect on EPLD grown ZnO, resulting in a random array of nanorods with alignment which was dependent on the growth temperature of the buffer layer. Buffer layers offer another dimension in the control over epitaxial structures and show large potential for EPLD growth of ZnO.

Pb was the dominant impurity in the Zn targets used for EPLD growth, hinting at a Pb-related origin for the I_7 peak. To explore this idea, hydrothermally grown bulk ZnO was ion-implanted with Pb and then annealed in oxygen at 600 °C to repair damage to the crystal. PL emission intensity was substantially reduced in the Pb-implanted ZnO but the line widths were preserved. No evidence of an I_7 feature was seen for Pb concentrations of up to 0.10%, three orders of magnitude higher than the expected level in the EPLD grown ZnO. However, this does not rule out a Pb-related complex as the origin of I_7 since Pb has complicated interations with the impurities and native defects in ZnO. Instead of I_7, other sharp excitonic features were observed near the band edge. A bound exciton with a localization energy of 12.4 ± 0.2 meV was observed in the Pb-implanted samples and was attributed to neutral interstitial Pb donors. Pb-implantation produced a clear PL signature which is unique enough to unambiguously detect

its presence in ZnO.

EPLD also proved successful at depositing oxides of the noble metals. Ir, Pt, Pd, and Ru targets were ablated in oxygen and argon ambients and films were collected on room temperature substrates. Growth in argon resulted in pure metal films while oxidized layers were obtained in oxygen. This was clearly evident by the semiconductor-like transmission spectra observed for the oxidized samples. The high fluence used for these growths promoted the oxidation of these resilient metals while the shadow mask blocked most of the molten particulates generated by the high fluence. EPLD is an excellent way to produce oxides from metallic targets, a technique which should be explored in more detail for many material systems.

Acknowledgements

It is impossible to complete a PhD thesis without help from several other people. First and foremost I would like to thank all of the technicians in the physics and chemistry workshop. Without their expertise, the chances of having complex working experiments are slim. Many thanks to Russel Gillard for his help with my amateur designs for various components, which were expertly crafted by Nick Oliver. Russel Gillard also stepped in as the liquid He guy when we really needed it, allowing me to take important low temperature measurements. Bob Flygenring was the first liquid He guy I worked with and he's stepped into those shoes once again after retirement. This provided liquid He at a crucial time late in my studies. Thanks for keeping things nice and cold, my thesis and several others are only possible because of the effort of these guys.

Wayne Smith, head of the physics mechanical deserves many thanks since he is involved with most of the equipment I had my hands on. Creative solutions to pretty much any problem come from his direction and he's truly an asset to the department. Stephen Hemmingsen is another technician who, like Wayne, has his hands in pretty much everything. He's helped with liquid He and N production on many occasions and his design skills are excellent to say the least. I certainly can't forget to thank everybody in the electrical workshop as well. Geoff Graham, Graeme MacDonald, and Ross Ritchie keep things running smoothly in the optics lab. Without their help, my experiments would have taken at least 10 times longer and likely driven me crazy.

The nanofabrication lab in the electrical and computer engineering department is full of state of the art equipment and amateur scientists. Gary Turner and Helen Devereux somehow manage to keep everybody safe and all the equipment running. They both helped me tremendously and continue to help the dozens of students coming through that lab every year. My guess is that hundreds of successful research projects would not have been possible without them and the other key players maintaining the nanolab. Thanks a billion.

The technicians may keep the experiments running but much responsibility is placed on senior students when it comes to training the new students. Fortunately for me, I had the help of one (now Dr.) Chito Kendrick from electrical engineering. Chito taught me pretty much everything I know about working with vacuum chambers. He put up with my relentless questions with a smile. His work ethic is second to none and he was a real pleasure to work with. He also managed to put up with me on several fishing trips. The fact that I knew some good spots must have helped and somehow he managed to catch the biggest fish of the day, except once or twice.

Chito was certainly not the only senior student to help me in the vacuum lab. Ian Farrell was another key factor in my success, always willing to lend a hand. He does a great job keeping the PLD lab running smoothly. Furthermore, he

is comfortable in a clean room environment and has good protocols, something which I have picked up on. If Ian was in the lab the day before, you know it was gonna be 100% clean and tidy when you arrived. The same can not always be said about me, so I better thank Ian for cleaning up several of my messes too.

Compared to vacuum labs, optics labs are a horse of a different color. Paul Miller helped me understand these strange colored horses and introduced me to the wonderful world of photoluminescence. Paul and I had many interesting debates over various aspects of PL and ZnO in general. I doubt I would understand half as much about light emission without these debates, which forced me to verbalize my thoughts and solidify my arguments.

Having climbed the ranks from project student to PhD candidate, I too became the senior student who guided new students. The first two project students I had underneath my wing were Craig Polley and Michael Kerler and deserve my thanks. First of all, these were the best project students I worked with as a senior student, which made things much easier for me. More importantly, this thesis is the hybridization of ideas from both of their research projects with my own work. They helped me to find an interesting niche which was unexplored in the heavily researched field of ZnO.

The rest of the solid state research group also deserves acknowledgement. Scott Choi, Young-Wook Song, Masaed Almotari, and all the project students who came through have contributed to my scientific knowledge in one way or another. In particular I need to thank Martin Henseler, who had the unfortunate luck to have me as an office mate. Him and I had many conversations and debates about ZnO, data processing, and nearly anything else you could think of. Somehow, he managed to put up with me for several years and in doing so, I learned many useful tidbits of physics with only minimal distractions. I only hope that Martin gained as much from our discussions as I did.

I also must thank my project supervisors. Professor Roger Reeves gave me the opportunity to undertake a PhD thesis and gave me the freedom I needed to develop my ideas. He trusted me with many tasks, which taught me a lot more then what is recorded in this thesis. I got to attend several conferences and Roger even sent me to a tropical island for one. I really appreciate all you've done for me and the rest of the group. My secondary supervisor, Associate Professor Steve Durbin also deserves much thanks from me. He is always pushing forward and provides excellent ideas and creative solutions. He pushed me to apply for the IBM Visiting Scholars Programme and I was one of two students selected. Those three months in San Jose were a real learning experience and I wouldn't have even applied if it wasn't for Steve. I really owe you for that one! Roger, Steve, and Associate Professor Simon Brown, the third project supervisor, all deserve many thanks and are valuable assets to the university.

Of course I now have to thank all my friends and family. I've met many great people while I've been in New Zealand and they've all made it a comfortable place for me to study. My family on the north island was my inspiration for

coming to New Zealand in the first place. My Nanna and Koro, along with the rest of the whanau have made New Zealand truly feel like home. My family back in Denver has also been supportive, never questioning my motives and always looking forward to my visits. My brother Aaron and sisters Tovah and Sarah have been there for me always and were a constant source of support and motivation. Many thanks to little Leona, my first niece who was brought into this world the same day I finished typing this thesis. Many thanks to my mum as well, always there for me when I needed some advice or guidance. Last, and certainly most importantly, I have to thank my Dad. He was my main support line, providing the financial and emotional support I needed to move across the world by myself when I was 18. Theres no way I could have done it without ya Pa, this thesis is for you!

Contents

List of Figures

List of Tables

Chapter 1

Introduction

Lets just say I was testing the bounds of reality. I was curious to see what would happen. Thats all it was: curiosity.

-Jim Morrison

Along with necessity and the occasional fortunate accident, curiosity is what has pushed the bounds of art, music, and all areas of science. In particular, curiosity is the life-blood of the modern day physicist. Of course making lots of money by developing some sort of device is good motivation, but it is not what drives real progress in physics. It is the intrinsic human need to understand the universe which powers the discoveries. For thousands of years this need has changed the face of the world and mankind. Today, with all this information right at our fingertips, curiosity can be extensively indulged and it is the main motivation for this PhD thesis in physics.

It is the curiosity about light and the very small that fueled this project. Nanostructured materials for optoelectronic devices are gaining much interest internationally. Among other things in this thesis, the morphology and light emitting properties of nanostructured ZnO produced by a method called eclipse pulsed laser deposition (EPLD) were studied. The work encompassed by this thesis, some of which has already been published,[1–3] represents the first time ZnO and noble metal oxides have been grown by EPLD. The various structures which were produced showed novel morphologies and light emitting behavior. The goal of this thesis was not to make a usable device, but to understand more about EPLD growth of oxides and the fundamental light emission processes in ZnO and its nanostructures.

Why ZnO? Well, ZnO is a wide band gap semiconductor which has many

useful properties. At room temperature the band-gap of ZnO is 3.3 eV [4] meaning its transparent to visible light but absorbs UV radiation. ZnO has been used for years in sun screens and lotions because of its efficient UV absorption. In fact, ZnO-microparticle-based sunscreens are currently considered to be the most effective. [5] The wide band gap of ZnO also means it is a candidate material for blue and UV LED's and lasers. However, stable *p*-type ZnO of device quality has not yet been realized. Once this hurdle is overcome, ZnO based lasers may be powerful and versatile enough to outperform the inefficient Ar^+ laser which is so crucial to modern spectroscopy.

Why not GaN? Sure, gallium nitride is a popular wide band gap semiconductor but ZnO has two key advantages. The first is the recent commercial availability of high quality bulk ZnO. Cermet Inc., Atlanta, GA have succeeded in providing high quality melt-grown ZnO using a highly pressurized system. [6] High quality ZnO can be also be grown by the hydrothermal method and is available from Tokyo Denpa Co., Ltd., Tokyo, Japan. [7] A third competitor in the business is Eagle Picher Industries Inc., Miami, OK who produce ZnO wafers by a vapor transport method using H_2 as a carrier gas. [8] These three growth methods have highly contrasting growth rates and varying impurity concentrations. This results in samples with different optical and electrical properties coming out of the three companies. Since its availability around 1998, bulk ZnO produced by these three methods has been the subject of many thorough investigations. [8–21] High quality bulk ZnO has many potential uses in devices and is already being used for excellent GaN epitaxy due to the small lattice mismatch of about 2%. [22,23] It may one day prove useful for homoepitaxial growth of *p*-type ZnO.

The second, perhaps more important key advantage that ZnO has over GaN is an exciton binding energy which is nearly 3 times larger in ZnO. When a semiconductor absorbs a photon an electron-hole pair is created. In sufficiently pure samples, the motion of the electron and hole is correlated by the Coulomb interaction and they orbit each other. This bound state of the electron-hole pair is called an exciton which is bound with an energy which is characteristic of the material. The exciton binding energy is the amount of energy required to dissociate the exciton into an uncorrelated free electron and free hole. ZnO has an exciton binding energy of 60 meV [24] while that of GaN is only about 24 meV. [25] Optical absorption and emission is greatly enhanced by the formation and radiative recombination of excitons. Excitonic-based devices have many advantages over classic devices such as increased switching speed and efficiency. [26] They may

even become an integral part of a viable quantum computing scheme.[27] Since ZnO has such a high exciton binding energy, these excitonic devices will theoretically be able to preform at temperatures exceeding 600 K. GaN based excitonic devices would fail well before that. The role of excitons in the photoluminescence spectrum and electronic band structure of ZnO are covered in detail in chapter 3.

A wide band gap and large exciton binding energy are not the only attractive properties of ZnO. At room temperature and atmospheric pressure the thermodynamically stable phase of ZnO is the wurtzite crystal structure. Wurtzite belongs to the $C_{6\nu}^4$ space group and is characterized by two unique lattice constants a and c where $c/a = \sqrt{8/3} = 1.6330$ in the ideal case.[4] One oxygen atom is surrounded by four Zn atoms (and vice versa) in tetrahedral coordination which is indicative of sp^3 type bonding.[18] Wurtzite ZnO consists of interleaved hexagonal-close-packed Zn and O sublattices displaced from one another by $3c/8$ along the c-axis. The result is a lack of inversion symmetry meaning the ZnO lattice is not centrosymmetric. This leads to a spontaneous electrical polarization along the c-axis giving ZnO ferroelectric and piezoelectric properties. Piezoelectric ZnO-based surface acoustic wave devices for chemical sensing[28] and communications[29] have already been demonstrated. More recently a group out of the Georgia Institute of Technology has created nanogenerators based off of ZnO nanowires.[30] The piezoelectric nature of ZnO creates a current when the nanowires are bent. The idea is to have self powered nanosystems which get their energy from vibrations. These nanogenerators have already been integrated into fibers with the goal of having clothing which can generate electricity for personal electronics simply from walking. The non-centrosymmetric nature of wurtzite ZnO also means that the c-plane cuts have Zn and O polar faces. The difference between the properties of the two faces has been investigated but there is still much to be understood.[19,31]

Along with radiation hardness[32–34] and nonlinear optical properties,[35,36] the ability to make ZnO ferromagnetic has gained much attention from research groups around the world. Doping with traditional magnetic ions such as Co[37,38] or Er[39] has resulted in room temperature ferromagnetic ZnO films[37,39] and nanostructures[38]. Dilute magnetic semiconductors (DMS) are the key to spintronic devices[40] and the next generation of exotic devices exploiting the magneto-optic effect in DMS materials[41]. Couple the ferromagnetism together with ferroelectricity and a new class of materials called multiferroics emerges.[42] Cr-doped ZnO exhibiting multiferroic behavior at room temperature has recently been

reported.[43] Add the strong interaction that ZnO has with UV radiation and some novel, multifunctional devices will be possible.

Investigation into ZnO has been going on for centuries. Zinc was first smelted in Zawar, India in the 13th century.[44] A white ZnO powder was produced as a byproduct which was then used in a remedy for sore eyes. The zinc smelting technique was then taken to China in the 16th or 17th century where it was used to produce brasses with high zinc contents. Europeans imported zinc from China shortly afterwords and it was listed as an element on the periodic table by Antoine Lavoisier in 1789.[45] The first use of the semiconducting nature of ZnO was for radio signal rectifiers in build-your-own radio sets in the 1920's.[18] Since then, investigation into the nature of ZnO has skyrocketed, growing exponentially in the last two decades. Figure 1.1 shows the number of publications about ZnO, GaN, and nano-related research in each year as found by the Web of Science. The ZnO data was gathered with the search string `ZnO OR ¨zinc oxide¨` in the 'topic' field and a similar one was used for GaN. Searching for the publications about nano-related materials was more complicated and so the search string was `nanostructure* OR nanocyrstal* OR nanoparticle* OR nanocolloid* OR nanowire* OR nanotech*`. This was to disclude research about nanosecond spectroscopy and biological results such as nanophytoplankton if using something simple such as `nano*`.

About 1% of the 34,242 ZnO studies shown in figure 1.1 were published before 1960. During this time investigation into the fundamental properties of ZnO was being undertaken. The first electron diffraction study on ZnO was published in 1935 by a group out of Purdue University.[46] Optical and electical properties were studied next with the first temperature dependent Hall experiment on ZnO published in 1954.[47] Fluorescence of ZnO also gained new interest in 1954 after some initial experiments by some German groups in the 1930's.[48] In 1968 a commercially available ZnO varistor was produced by Panasonic along with General Electric, Westinghouse, and Asae.[†] These varistors provided pulse voltage suppresion for TV recievers and surge protection during lightning stikes. They allowed for a broader range of semiconducting electronic devices to be used in industrial applications and at home. In 1987 the National Science Foundation helped the number of internet hosts increase by a factor of ten.[‡] The rapid exhanges of information that were made possible boosted many areas of research,

[†]See http://www.panasonic.net/history/corporate/products/inp1968.html
[‡]See http://www.davesite.com/webstation/net-history3.shtml

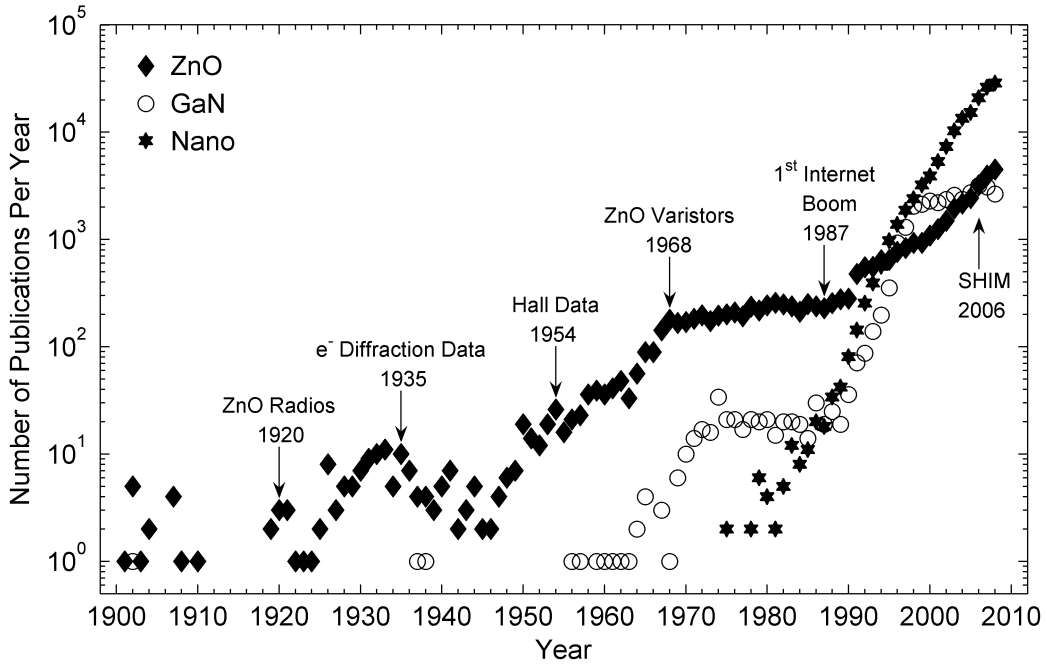

Figure 1.1: Publications about ZnO, GaN, and nano-related research as databased by the Web of Science.

contributing to the rapid rise in ZnO, GaN, and nano-related research seen in the late 80's and early 90's.

Imaging technology for the nanoscale has been and always will be a crucial foundation for materials science. Today the most popular choice for high magnification imaging is the scanning electron microscope (SEM) which has had a rich history in development. A precursor to the SEM was the scanning transmission electron microscope (STEM). It turns out that the first ever STEM image was taken of a ZnO crystal at a magnification of 8000 times.[49] Since then over 50,000 SEM's have been sold around the world. The sharp increase in GaN research shown in figure 1.1 in 1965 may be a result of the commercial availability of SEM's at the time. Another boost in materials science, particularly nanotechnology, will certainly be seen in the near future due to the development of the scanning helium ion microscope (SHIM).[50] It is the first revolution in electron microscopy in decades and may one day provide resolution as good as a modern day transmission electron microscope without the sample preparation. Quantitative stoichiometric contrast with submicron resolution as already been achieved by looking at the backscattered ions in Rutherford Backscattering Imaging mode. The SHIM will most certainly play a role in the near future of ZnO as ZnO is known to show

the richest variety of nanostructured forms out of any material studied so far. Eventually, ionoluminescence experiments performed in a SHIM will revolutionize the study of nanostructured light emitting materials like ZnO.

In 2008 over 4,500 articles were published about ZnO with about half of them related to nanostructured material. Only one of those publications[1] was about EPLD grown ZnO and this work and more is discussed in great detail throughout this thesis. Standard and eclipse pulsed laser deposition are discussed first followed by the photoluminescence (PL) spectrum of bulk ZnO. PL spectroscopy is a powerful diagnostic tool for wide direct gap semiconductors like ZnO and is used extensively throughout this work. Chapter 4 shows the EPLD growth and characterization of ZnO nanostructures onto *c*-axis sapphire (Al_2O_3). Following on from this, the effect of thin buffer layers on the morphology and PL spectrum of EPLD grown ZnO is presented in chapter 5. The main impurity in the targets used to grow these samples was Pb and the effects of Pb-implantation into bulk ZnO are discussed in 6.

The final chapter of results shows the extension of the EPLD technique to noble-metal oxides. Ir, Pt, Pd, and Ru metallic targets were used for EPLD growth of the corresponding oxides. Fully oxidized material was not achieved but nevertheless, the material did provide very high quality Schottky contacts to bulk ZnO. This thesis represents the first time ZnO and noble metal oxides have been grown by EPLD. Further investigation of ZnO is a must for the material science community and EPLD is a way to produce some novel morphologies which may prove useful for the next generation of exotic magneto-opto-electronic devices.

Chapter 2

Eclipse Pulsed Laser Deposition

2.1 Standard pulsed laser deposition

It was Thomas Maiman who first demonstrated stimulated optical emission, creating the world's first laser from a ruby crystal (Cr^{3+}:Al_2O_3) on 16th May, 1960.[51] At the time it was considered to be a solution without a problem. Since then the laser has found its way into aspects of daily life which Maiman and his group would have never dreamed of. From entertainment, to data storage, to cosmetic surgery, to geology, to military applications, to positioning systems, to eye correction, to communication, to saving and even taking lives, no other tool in the history of mankind has shown more widespread use and versatility save perhaps the wheel or mastery of the open flame. Scientists are arguably the biggest benefactor of laser technology, enabling advances in nearly every niche and corner of the physical sciences. Lasers may be the key to fusion technology which could easily solve the global energy crisis. A slightly more modest approach is taken to the laser by material scientists. Apart from the many uses for sample characterization, many research groups around the world have adopted the laser to deposit materials in thin film and nanostructured form. This idea is known as pulsed laser deposition (PLD) which has been applied to perhaps the widest variety of materials out of any growth technique.

It only took 5 years after the invention of the laser for the first PLD experiment to be published. In 1965 Smith and Turner out of Rochester, New York deposited optically smooth thin films of Sb_2S_3, As_2S_3, fuchsine ($C_20H_19N_3 \cdot HCl$), Se, Ni-dimethylglyoxime ($Ni(C_4H_7N_2O_2)_2$), ZnTe, Te, MoO_3, $PbCl_2$ (using carbon), PbTe, and Ge using the first harmonic of a ruby laser.[52] The materials were deposited by focusing the laser at 45° incidence onto powders, or in some cases single crystals, which were placed in a vacuum bell. Unheated glass, BaF_2, mica,

or As_2S_3 substrates were placed 20 to 50 mm away from the target to collect the ejected material in a thin film. The ejected material is first evaporated and then partially ionized into an expanding plume of plasma, a process which is known as laser ablation.[53,54]

Without Q-switching, the ruby laser which Smith and Turner used output 3 J in 1 ms.[52] The resulting power density at the focus was about 10^6 W/cm^2. The energy density per pulse, or fluence, was 10^3 J/cm^2 and is the standard unit for laser intensity for PLD. Despite this incredibly high fluence by today's standard, InSb and ZnO powders could not be evaporated and no films were produced. At the time, not much interest was gained by Smith and Turner's work as other technologies being developed concurrently, such as molecular beam epitaxy (MBE), showed more promise at the time. The biggest hurdle for PLD to overcome was the inadequacies of the ruby laser. A higher power laser with a shorter pulse width is desirable for congruent and stoichiometric ablation of multicomponent targets.[53] Thus, the development of the PLD technique had to wait several years for laser technology to evolve.

International interest in PLD was finally sparked in 1987 after collaborators from Bell Labs and Rutgers University deposited superconducting $YaBa_2Cu_3O_{1-x}$ (YBCO) films with a T_c around 85 K.[55] It was the development of the UV excimer laser which made this work possible. Excimer lasers using KrF as a gain medium lase at 248 nm (4.96 eV) and are capable of delivering 1 J in $25 - 30$ ns. This gives power densities of about 10^7 W/cm^2 while keeping the fluence around $1 - 10$ J/cm^2. The high energy UV photons produced by excimers are more easily absorbed by some materials than the 694.3 nm light from a ruby laser. A much wider range of materials can be efficiently ablated with excimers or the harmonics of Nd^{3+}:YAG lasers (355 nm or 266 nm) including perovskites and wide-band-gap semiconductors like GaN and ZnO.

These high energy, short pulse-width excimer lasers provide the pulse profiles necessary to congruently ablate target materials with up to 6 components. Congruent ablation means stoichiometric conservation between the target and deposit. This is especially attractive to groups working on superconductors and ferroelectrics due to the highly complex stoichiometry and structure of these materials. However, if oxygen or nitrogen is a constituent of the target then ablation usually takes place in a background O_2 or N_2 atmosphere.[1,56–66] This is to compensate for O and N loss during laser ablation and is required to achieve the correct stoichiometry for many materials containing these species. Some groups

will even use activated O or N plasma sources to enhance reactions within the plume and on the substrate surface.[56]

The short pulse-width excimer also minimizes residual target heating which helps to reduce particulate ejection during laser ablation.[53] These particulates are micron sized pieces of the target material, some of which are molten when they are ejected. They will seriously disrupt the crystal growth during PLD and are the main drawback of the PLD technique. Smooth, particulate-free layers are required for most (opto)electronic devices which may have been the main reason why PLD did not gain interest in its early days. Despite this particulate problem, smooth PLD grown films of many materials have been obtained and show quality comparable to or better than those produced by other conventional techniques.

For the work of this thesis, a fairly standard high vacuum (HV) PLD chamber was used and is shown in figure 2.1. The laser was a Lambda Physik COMPex 262349 excimer running on KrF which lases at 248 nm (4.96 eV). A circular aperture with a diameter of 6 mm was used to select the most uniform part of the excimer's intensity profile. The result was a more uniform energy density at the target and a more symmetric plume with less particulates. Exact determination of the effective laser fluence is quite difficult. To truly measure the fluence arriving at the target requires good knowledge of the laser spot size, beam energy, and its intensity profile. Measuring spot sizes from ablation experiments will only give the spot size of the portions of the laser beam which are above the ablation threshold. Different groups will have different optical arrangements which will result in a broad range of intensity profiles on the target. Reported fluences may represent average fluence across the target, peak fluence, or in some cases may be meaningless. Unless a universal standard is agreed upon, reproducing laser conditions is really only possible using the same laser and optical arrangement. All in all, the uncertainty in the fluences reported in this thesis may be as much as 25%, perhaps more so when an unapertured spot is used.

A 750 mm focal length fused-quartz lens with an antireflective coating was used to focus the beam though a quartz window and onto the target. The target was set closer to the lens then the focal length and the typical spot size on the target for ZnO growth was estimated to be 1.5 mm^2. During PLD growth the targets were rotated at 0.9 Hz by a variable speed stepper motor. This was to spread out the laser damage on the target which will help to reduce particulate generation. 0.9 Hz was chosen since the laser pulse-repetition rate was 10 Hz and the laser needs to hit different spots on the target with every revolution.

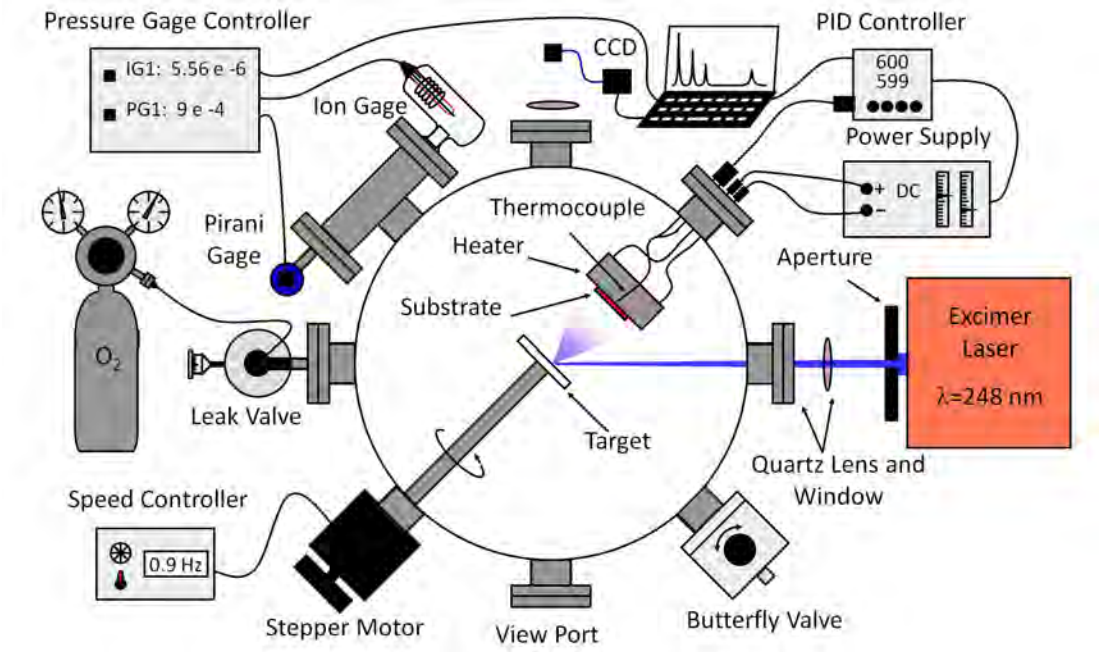

Figure 2.1: Top view of the HV chamber used for PLD growth of all the samples discussed in this thesis.

To catch the ablated material in a high-quality film or nanostructured form, a substrate was placed 53 mm from the target. Substrates were attached to a MeiVac SU200-HH two inch resistive heater block using silver paste. Good thermal contact was achieved by this method allowing for substrate temperatures as high as 800 °C. Typical substrate temperature for ZnO growth was 600 °C. An Omega KQIN-116U-12 K-type thermocouple was placed within the heating block just a few mm away from the substrate. Temperature of the heater was controlled by an Omron E5CK temperature controller with PID control. DC power for the heater was supplied by a Hewlett Packard 6274B power supply. A laptop computer was interfaced with the Omron controller via a Matlab graphical user interface created by the author of this thesis. This Matlab GUI was able to program the Omron controller and monitor the temperature in real time, logging the data into a file.

Pressure was also monitored by Matlab by interfacing with the SRS-IGC100 ion gauge controller via an RS232 connection. An SRS PG105-UHV convection enhanced Pirani gauge was used to measure the pressure in the high pressure regime; from atmosphere down to 10^{-3} Torr. For lower pressures a Dunyway I-100-K iridium coated ion-gauge was used. Both gauges were operated by the SRS

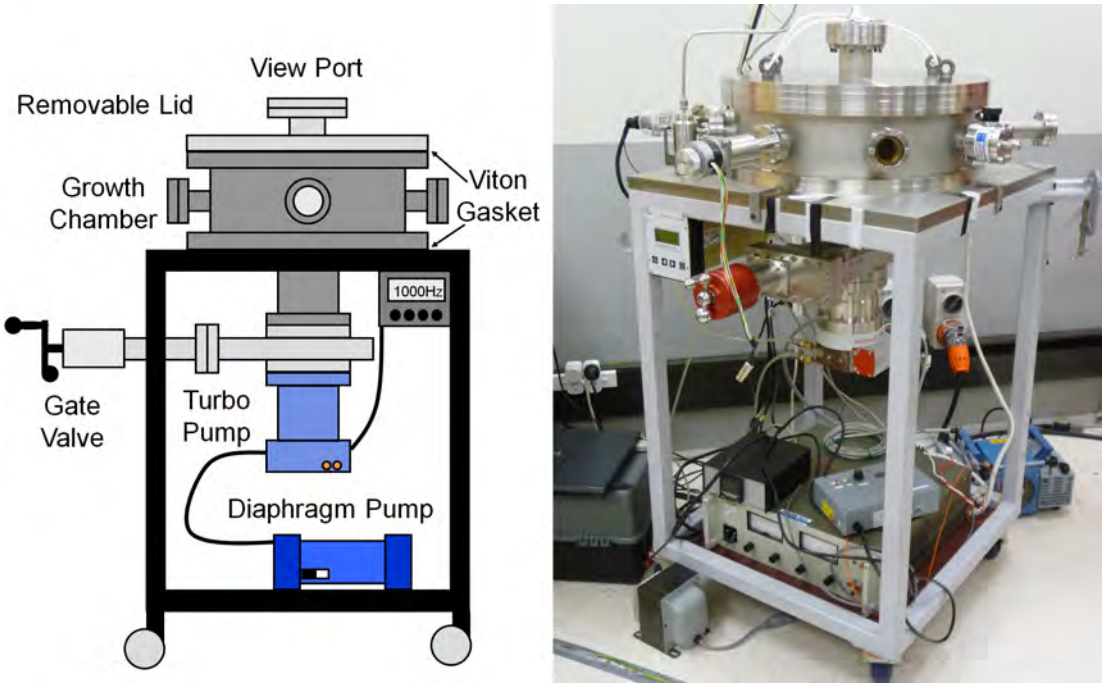

Figure 2.2: Side view and photograph of the HV chamber.

gauge controller which communicated the measurements to the laptop computer. A base pressure of about 5×10^{-6} Torr was achieved in the chamber using a Pfeiffer TMU 262 turbomolecular drag pump backed by a Pfeiffer MVP 055-3 diaphragm pump. The arrangement is shown in figure 2.2 which shows a side view schematic and photograph of the chamber. Once evacuated, high purity O_2 gas (99.999%) was let into the chamber though the leak valve before growth began. A maximum O_2 pressure of about 250 mTorr was reached once the turbomolecular pump was partially shielded by the gate valve to avoid overloading it. Access to the chamber was via the removeable 1 inch thick stainless steel lid which was placed on top of the chamber. The main seals were large viton gaskets which were held closed by atmospheric pressure. To bring the chamber to atmospheric pressure so it could be opened, air was let in through the butterfly valve in a slow, controlled fashion.

There were three view ports which gave optical access to various parts of the chamber. One was located on top of the chamber and allowed for visual inspection of the laser induced plume. A second view port was located on the side of the chamber which faced the substrate. This view port was used to ensure the substrates were still attached to the heater during growth. The thermal contact of the substrate to the heater could also be observed though this view

port. If good contact was made then the substrates glowed the same uniform reddish color as the heater block. A third view port faced the target. It was used to ensure the laser was lined up properly if there was any ambiguity once the chamber was closed and evacuated. Also, the optical emission spectrum of the plume could be analyzed using an OceanOptics USB2000 CCD spectrometer. This was done through the top view port or the view port facing the target. The light was collected and focused into the collimator of an optic fiber using a 50 mm quartz lens. An optical emission (OE) spectra from a plume induced from a ceramic ZnO target (99.999%) in 10^{-4} Torr O_2 at fluences of 2, 3, 4, 5, and 6 J/cm^2 is shown in figure 2.3(a).

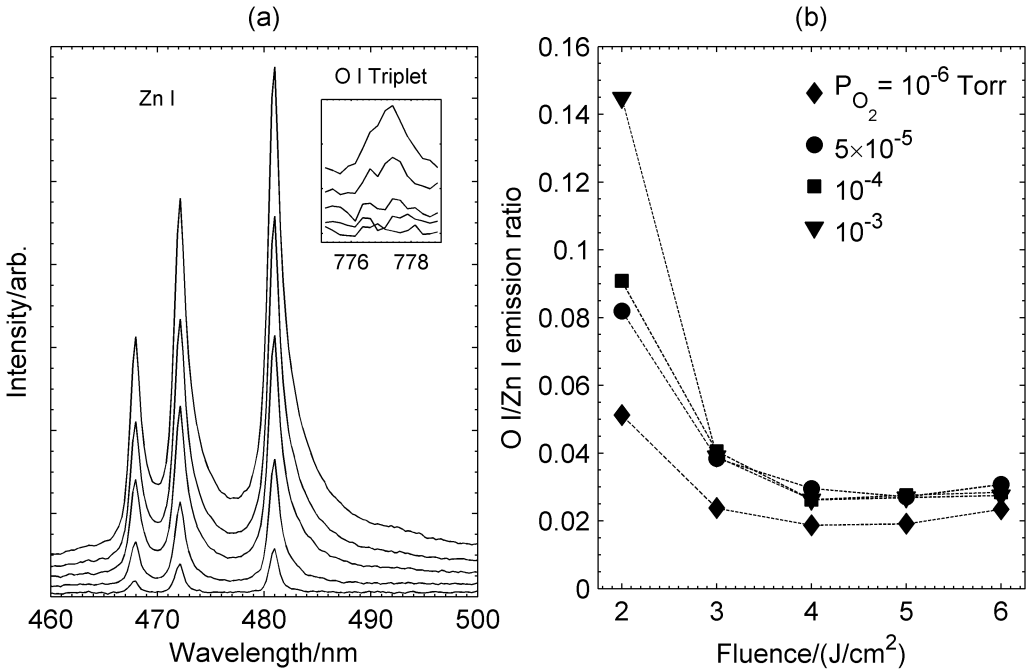

Figure 2.3: (a) Optical emission spectra in the Zn I triplet region from a ZnO plume in 10^{-4} Torr O_2 induced by a KrF excimer from a ceramic ZnO target at fluences of 2, 3, 4, 5, and 6 J/cm^2. The spectra are offset vertically for clarity with fluence increasing with increasing baseline. (b) Emission intensity ratio of the O I triplet at 777.4 nm to the Zn I peak at 481.0 nm

.

Emission from neutral zinc (Zn I) dominated the OE spectra with the three strongest Zn I lines appearing at 467.9, 472.2, and 481.0 nm.[67] Only one small feature could be attributed to neutral oxygen (O I) which was an unresolved triplet around 777.4 nm as shown in the inset. No features due to singly ionized zinc (Zn II) or oxygen (O II) could be seen in any of the spectra so plasma temperatures could not be extracted by use of the Saha equation.[53] Figure 2.3(b)

shows the intensity ratio of the O I peak to the strongest Zn I peak as a function of fluence for several oxygen ambient pressures. However, no solid conclusions can be drawn from this data given the noise level in the spectra taken at the lowest few fluences. OE spectroscopy is a powerful tool for *in-situ* PLD diagnostics but a much more sophisticated optical set up, such as that found in reference 67, is required for truly meaningful experiments on ZnO plumes.

Target preparation is an important part of PLD. A properly prepared, dense target is essential for growth of high quality films with low particulate densities. This has been shown for PLD of TiO_2 from a ceramic TiO_2 target.[59] For ZnO growth, a dense ceramic ZnO target is the most popular choice for PLD.[56,61,62,64,65,68–70] These targets can be obtained from the Kurt J. Lesker Company. However, high purity ZnO targets (99.999%) are relatively expensive and have been studied extensively. For the work of this thesis metallic Zn target were used for the majority of the growths. PLD of oxides from mettalic targets is not new,[56–58,71,72] but has not seen nearly as much attention as growth from ceramics or single crystals. Aside from being cheaper, the mettalic targets also simplify the ablation process since they are composed of one element. Incongruent ablation is not a problem for metallic targets. Metal targets will also efficiently absort IR lasers meaning the first harmonic of a Nd^{3+}:YAG can be used for ablation. Less fluence is typically needed for growth from metallic targets as compared to the ceramic counterparts. This is of particular interest for industrial purposes where energy conservation is important.

To obtain oxides from metallic targets, growth takes place in a relatively high oxygen ambient pressure in the 100 mTorr range.[1,71,72] Typical plume temperatures during PLD are around 50,000 K meaning that oxidation occurs within the plume,[53] and continues on the substrate if it is at an elevated temperature. Oxidation on the surface is particularly effective for ZnO since Zn has a low melting point (420 °C). Use of an RF oxygen plasma source enhances oxidation during PLD of oxides and can lead to an improvement in film quality.[56,58]

An interesting extension of the PLD technique which improves ionization within the plume and may increase oxidation is called aurora PLD.[73] In this modification the ablation takes place in the presence of a magnetic field. Increased ionization has been confirmed from optical emission spectroscopy when a magnetic field is present.[70,73,74] Use of the aurora technique for ZnO grown at room temperature lead to a 4 fold increase in photoluminescence intensity and a 2 fold decrease in carrier concentration.[70] Conventional PLD has its limits and

novel extensions to this technique can prove to be quite effective at improving film characteristics. One such extension is known as eclipse PLD and is the main technique used in this thesis.

2.2 Eclipse PLD

Solar and lunar eclipses have fascinated people for millennia. In 2000 BC Chinese authors spoke of flames eating the sun and dragons eating the moon.[†] Christopher Colombus used a Greek almanac to predict a lunar eclipse while stranded in Jamaica in the 16^{th} century. After his men mistreated the locals, their food supply was cut off. Columbus told the locals the almighty was angry and would remove the moon from the sky if the supply was not restored. Dinner was served. In a PLD experiment, the large particulates can be blocked by putting an obstacle in the direct path from the plume origin to the substrate, eclipsing the plume. An ambient background gas is introduced into the chamber which allows the small clusters, atoms, and ions to diffuse around the eclipsing object and collect on the substrate. Eclipse pulsed laser deposition (EPLD) is a simple modification of the PLD technique which can be implemented in most deposition chambers. Figures 2.4(a)-(d) show the implementation of the EPLD technique used in this thesis. The substrates were placed directly behind the shadow mask and are not in the field of view in figures 2.4(a)-(b).

The EPLD technique was first pioneered for growth of YBCO superconducting thin films in Japan in 1994.[60] The superconducting properties of YBCO are highly dependent on the surface smoothness and Kinoshita et al.[60] were able to use EPLD to prepare smooth superconducting YBCO films with T_c as high as 93 K. The particulate blocking achieved by the shadow mask is shown clearly in figure 2.4 for an Ir target ablated in 100 mTorr O_2. The Ir target was not easily ablated with the 248 nm laser so a high fluence around 15 J/cm^2 was needed. This high fluence likely caused subsurface explosions which lead to molten particulate ejection.[53,75,76] The sparks seen during the Ir ablation shown in figure 2.4(a) were also present during Pt ablation. Figure 2.4(d) shows an SEM image of a Pt particulate that has landed on the substrate. This particulate was clearly molten as it left the target since the shock wave from the impact with the substrate was flash frozen into the particulate. These particulates are effectively blocked by the substrate but can bounce off each other and the side walls of the chamber.

[†]See http://eclipse.gsfc.nasa.gov

Close inspection of figure 2.4(a) shows a particulate bouncing off of the bottom of the chamber and making it into the region behind the shadow mask, likely landing on the substrate. These violent subsurface explosions were not seen for Pd ablation shown in figure 2.4(b) where only the green plasma was seen with no orange sparks. Similarly, ablation of Zn metallic target produced a blue/violet plume with no sparking.

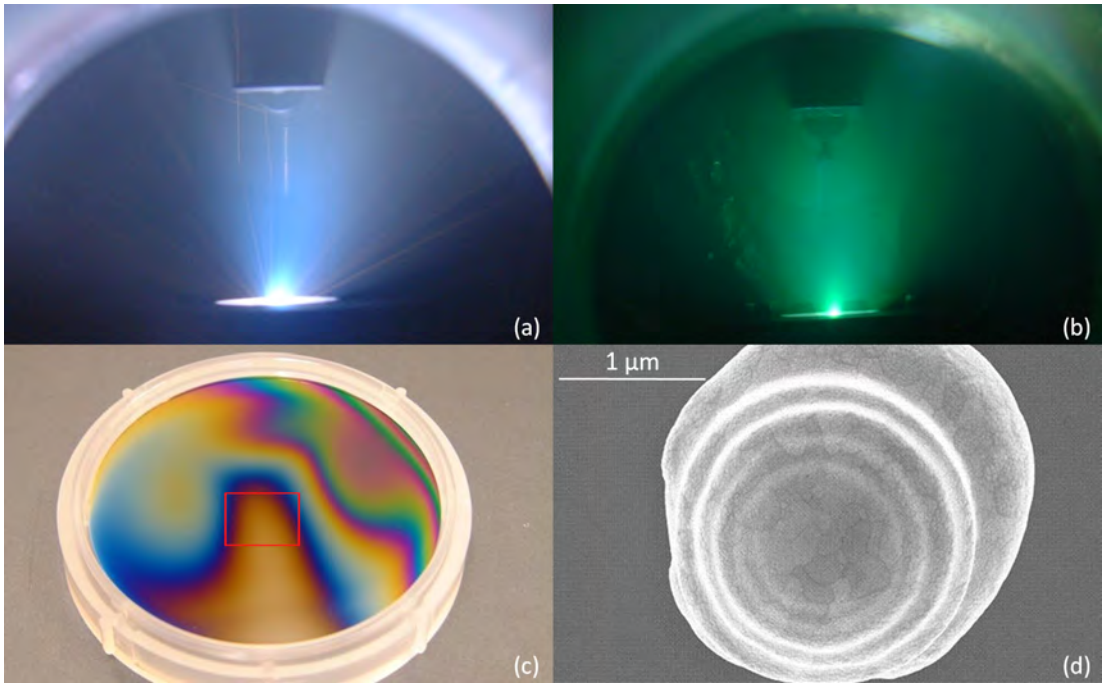

Figure 2.4: (a) Iridium plume in 100 mTorr O_2 with square shadow mask. (b) Palladium plume in 50 mTorr O_2 with square shadow mask. (c) Ir_xO sample grown on 2 inch Si⟨100⟩ wafer at room temperature. Red box shows the approximate mask position. (d) SEM image of a Pt particulate collected on a sapphire substrate.

Like all modifications and growth techniques, EPLD has its pro's and con's. The main downside of EPLD growth, especially from a industrial viewpoint, is the drastic reduction in the growth rate. Deposition rates are typically cut by factors of 5 when a shadow mask is introduced into the system.[60,77,78] However, low deposition rates are not always bad as they tend to lead to higher quality films. Uniformity of PLD produced films is also a problem. Usually the thickness will vary as $cos^{p+3}\theta$ where θ is the polar angle of ejection measured from the target-surface normal and p is an exponent describing the forward peaked nature of the laser induced plume.[53] For EPLD grown samples the thickness distribution drastically changes and usually shows a thin spot in the middle.[66,78] The effect of the shadow mask on the thickness can be seen in figure 2.4(c) which shows an Ir_xO

film deposited onto a 2 inch Si⟨100⟩ wafer by EPLD using a square shadow mask. Behind the mask and the post which holds it the thickness was relatively uniform compared to the regions outside the mask, as indicated by the interference fringes. The interference pattern shown on the sample in figure 2.4 was not symmetrical about the plume origin, which was lined up with the center of the shadow mask to within 1 mm. This was due to the plume turning effect which will steer the plume toward the laser as the etch pitch evolves during PLD.[53]

Since the first published experiments, EPLD has been applied to many materials including TiN[77], $SrTiO_3$[73], NiO[73], $SrRuO_2$[63], $PbZr_{0.48}Ti_{0.52}O_3$[79], and others. In this thesis the EPLD technique has been extended to ZnO and noble-metal oxides. The properties and morphologies of the oxides produced for this thesis were intriguing and unique to EPLD growth. In the case of the noble metal oxides, Schottky diodes with remarkable characteristics were produced by EPLD growth onto bulk ZnO as discussed in section 7.4. This technique has some advantages over standard PLD and can be modified even further to try and compensate for the disadvantages introduced by the shadow mask. A change in geometry or the introduction of a strong water-cooled rare earth magnet as a shadow mask in the eclipse-aurora hybrid PLD technique[73] can help to compensate for the low deposition rate, thin spot in the middle, and can even enhance crystal quality. Despite use of a simpler approach to EPLD, the materials produced for this thesis were of high optical quality and even created working devices. Of the several thousand publications about PLD, less than 30 were published about EPLD. Hopefully the work of this thesis and that done by all the other groups working on EPLD will progress the technique and encourage more interest into its use and investigation.

Chapter 3

Photoluminescence Spectroscopy of ZnO

3.1 Luminescence and ZnO Band Structure

Light emission from solids is a phenomenon which has intrigued man for centuries. Thomas Edison was familiar with the concept and used blackbody radiation to light the globe and line his pockets. The incandescent light bulb may have changed the lives of those of us living in cities, but its time is quickly coming to an end. Demand for high efficiency alternatives has been driven by a looming energy crisis. The United States passed the Clean Energy Act of 2007 which bans the use of inefficient light bulbs by 2014. Australia passed more stringent legislation requiring that light bulbs produce at least 15 lm/W by the end of 2009. Fluorescent lighting has become the current standard for energy efficient lighting but it will soon be overtaken by solid state alternatives. Semiconducting light emitting diodes (LED) have already begun to replace incandescent bulbs in many applications where the required power output is relatively small. After a few more advances, white LED's will produce a high-power, eye-friendly spectrum and become the standard for high efficiency lighting in nearly every application. ZnO may be the key to this technology but first we must understand more about the light emission processes in its bulk and nanostructured forms.

Luminescence in wide bandgap semiconductors is an observable manifestation of the electronic band structure of the material. The electron orbitals of the constituent atoms and their crystal structure is what gives an ordered solid its quasi-discreet band structure. A simplified schematic of the conduction bands and 3 valence bands of pure wurtzite ZnO near the Brillouin zone center where $k = 0$ (Γ-point) is shown in figure 3.1(a). It is the crystal field and spin-orbit coupling which splits the valence band into three sub-bands at the Γ-point.[4,16,17,20,24] These sub-bands are labeled A, B, and C in order of increasing depth below

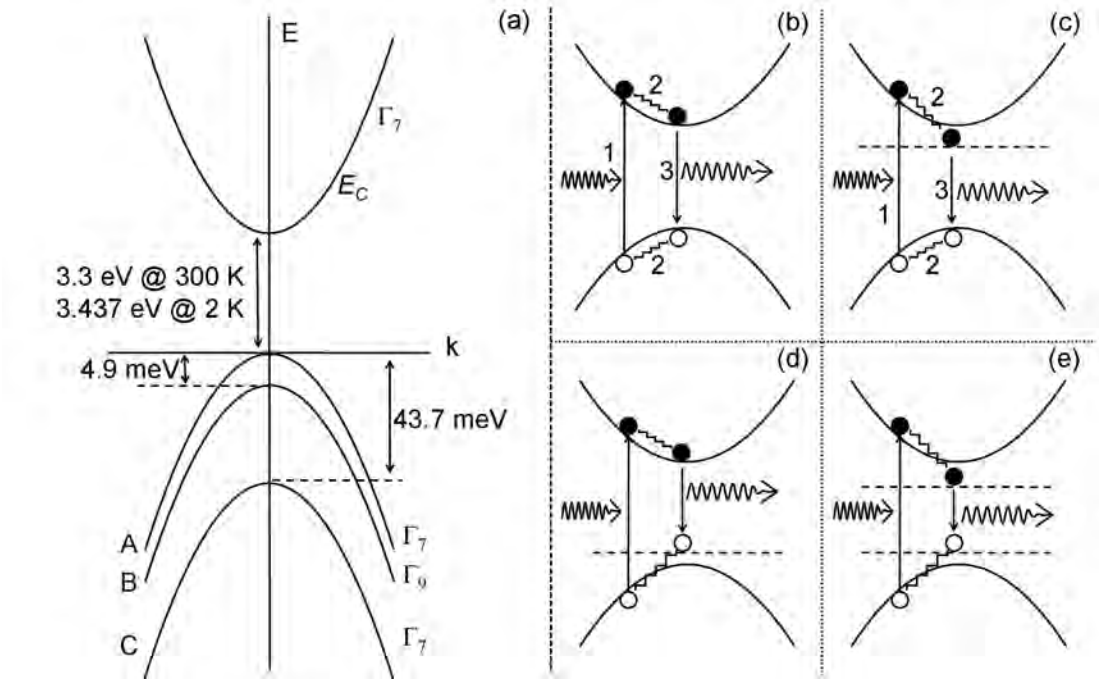

Figure 3.1: (a) The conduction band and three valence bands of wurtzite ZnO along with bandgaps, band splittings, and band symmetries. (b) Optical absorption, relaxation, and emission of a photon due to a band-to-band transition. (c) Recombination of a neutral donor with a free hole, hD^0. (d) Recombination of a neutral acceptor with a free electron, eA^0. (e) Donor-acceptor pair recombination

the conduction band according to standard convention. Group theory can be used to describe the symmetry of the electron's wavefunctions within each of the bands[80,81] and the symmetry assignments are shown in figure 3.1. In ZnO the A and C valence bands along with the conduction band have Γ_7 symmetry while the B valence band has Γ_9 symmetry.[9] Most other semiconductors with the wurtzite structure have the A and B valence band symmetries swapped ($A-\Gamma_9$ and $B-\Gamma_7$).[81] This reversal of valence band symmetry was the subject of controversy with some magneto-optical experiments suggesting the traditional 9-7-7 wurtzite valence band ordering.[21,82] However, in a detailed theoretical study it was shown that this data could be explained with a 7-9-7 valence band ordering by assuming a negative Landé g-factor for holes in the A valence band.[20]

Like GaN, ZnO is a direct-gap semiconductor which efficiently emits radiation at or near the bandgap energy. In direct-gap semiconductors the minima of the conduction band lines up with the maxima of the valence band at the Γ-point. Hence, photoexcited electrons and holes can recombine without the need for a third particle (phonon) to conserve momentum. In the simplest form, optical

emission usually takes place in three steps as seen in figure 3.1(b). An above gap photon gets absorbed creating an electron-hole pair. The photoexcited electron and hole are out of thermal equilibrium with their surroundings and will quickly and nonradiatively relax to the conduction band minima and valence band maxima respectively. At the Γ-point the electron-hole pair is still out of equilibrium and will radiatively recombine, emitting a photon at the bandgap energy if they are close enough for their wavefunctions to significantly overlap. This process is known as a band-to-band transition and is one of many which lead to light emission in semiconductors. If the electron-hole pair was excited by a photon the light emission is called photoluminescence (PL). Bombardment from an electron beam leads to cathodoluminescece which can be preformed in an SEM and provides luminescence maps with very high spatial resolution.[16] Thermally excited electron hole pairs give thermoluminescence and ion-beam induced luminescence is called ionoluminescence. There are many ways for semiconductors to emit light but for this thesis PL spectroscopy was the main diagnostic tool used to characterize the ZnO samples.

PL spectroscopy is a direct probe of a semiconductor's electronic band structure. It can be used to qualitatively address a materials purity and structural quality by studying the PL features intrinsic to the material, such as the band-to-band transition and free excitonic features described in section 3.2. Furthermore, the presence of impurities or structural defects in a semiconductor will alter the band structure, introducing mid-gap states which can be detected by PL. Figure 3.1(c) shows an emission process where an electron relaxes down into an unoccupied donor level before recombining. In this free-to-bound transition a free hole recombines with a neutral donor, hD^0. The energy of the photon emitted in an hD^0 transition is given by[83]

$$h\nu = E_{\mathrm{g}}(T) - E_{\mathrm{D}} + 1/2k_{\mathrm{B}}T \tag{3.1}$$

where E_{g} is the bandgap, E_{D} is the energy binding the donor electron to the donor atom or defect (known throughout this thesis as the donor binding energy), k_{B} is Boltzmann's constant, and T is the temperature. A free-to-bound recombination can also occur for free electrons and neutral acceptors, eA^0, as depicted in figure 3.1(d). This process produces a photon with an energy given by equation 3.1 where E_{D} is replaced by E_{A} which is the acceptor binding energy (that which binds the hole to the acceptor atom). Identifying a free-to-bound transition in the spectra means that the impurity binding energy, E_{D} or E_{A}, can be determined.

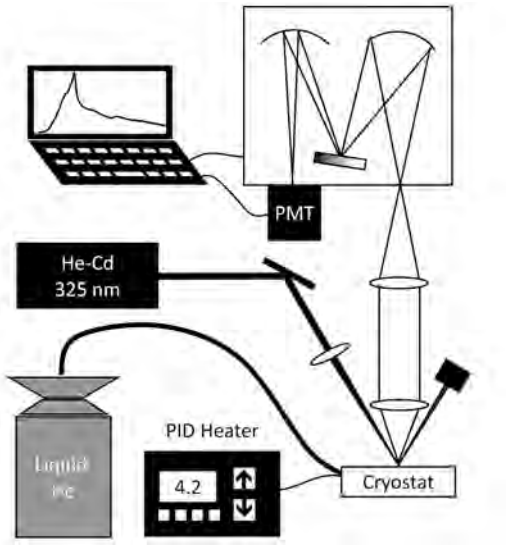

Figure 3.2: Photoluminescence set up using the 325.0 nm (3.815 eV) line from a 25 mW He-Cd laser for above-gap excitation.

This information can be use to identify the chemical or structural nature of the donor/acceptor in the sample. If both donors and acceptors are present in the sample, which is usually the case with real semiconductors, then donor-acceptor pair (DAP) recombination is sometimes seen in the spectra. This occurs when an electron on a neutral donor and the hole from a neutral acceptor radiatively recombine as depicted in figure 3.1(e). It is believed that DAP transitions are seen in the PL spectrum of ZnO[16,21] and this type of transition is discussed in section 3.6.

It is the non destructive nature and easy parameter control of the laser excitation which makes PL spectroscopy such a powerful technique for materials characterization. The experimental set up used for the PL spectroscopy measurements is shown in figure 3.2. A 25 mW He-Cd laser operating at 325.0 nm (3.815 eV) provided above bandgap excitation of the samples. The angle of incidence of the laser was between 40° and 60° from the normal. Light emitted in the direction normal to the sample surface was collected and collimated by a 100 mm quartz lens with high UV transmission. A quartz lens was used to focus the collimated beam into a 1 m Spex1700 Spectrometer. The focusing lens was f-matched to the spectrometer to maximize collection efficiency. Dispersion of the PL signal was done with either a 1200 or 2400 lines/mm UV-blazed diffraction grating and detected with a water-cooled photomultiplier tube (PMT) operating in photon counting mode. A stepper motor attached to the grating sinebar lead screw gave

a minimum spectral step size of 0.001 nm although 0.01 nm was usually sufficient for the sharpest bulk ZnO PL spectrum. Spectrometer slit widths were in the area of 25-50 μm for the bulk samples at low temperature. Depending on the grating, this gave a spectral bandwidth between 0.14 and 0.55 Å. For the UV spectrum in the near band edge (NBE) region of ZnO, this works out to be about 0.13 to 0.50 meV.

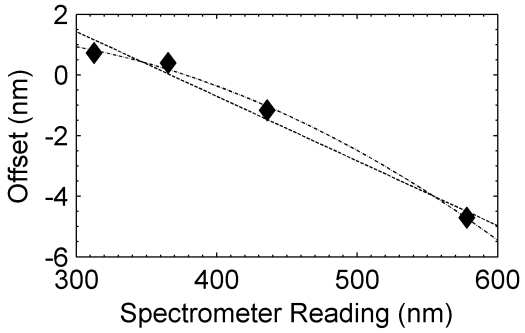

Figure 3.3: Spectrometer offset with linear and quadratic fit. The quadratic fit was subtracted from the measured wavelengths before converting to energy.

Wavelength calibration of the spectrometer was done in software after the data was gathered. Four known transitions of a Hg lamp covering the visible and UV spectrum were scanned with the spectrometer. The lamp was placed on the optic rail holding the lenses as far from the f-matched focusing lens as possible. Figure 3.3 shows a typical spectrometer calibration curve along with a straight line and quadratic fit. The quadratic fit was subtracted from the raw measured wavelengths read off the spectrometer. This provided a wavelength dependent correction which was accurate to 0.05 nm or better across the UV-visible range (300-630 nm). A new calibration curve was taken for each PL experiment at the end of the day or after any manual changes in the spectrometer calibration. Over time scales of weeks and months, the only parameter of the calibration polynomial which changed significantly was the constant offset. This was due to occasional resynchronization of the spectrometer hardware with the controlling software.

PL emission efficiency is maximum at low temperature and many features show up when the samples are cold that would not be seen at room temperature. To accommodate this, the samples were placed inside of a liquid-helium-cooled Oxford cryostat capable of reaching temperatures as low as 3.5 K. Silver paste was used to attach the samples to one end of a copper cold finger which had the liquid He pumped over the other end. A thermocouple and resistive heater

wire were wrapped around the cold finger for temperature monitoring and control using an Oxford PID (proportional-integral-differential) controller. This enabled temperature dependent PL measurements from 3.5 to 300 K which are discussed in detail in section 3.7.

The PL equipment described here was optimized for high spectral resolution of strong UV signals which are characteristic of ZnO. This set up was also effective for PL experiments on GaN. Many complex modifications of the PL technique have been developed to extract a wealth of information which is unattainable by low temperature PL spectra alone. Temperature and excitation intensity dependent PL techniques are a simple extension which can help to identify the nature of a peak in the low temperature PL spectrum. These techniques were used extensively throughout this thesis. However, magnetic field dependence of the PL spectrum is perhaps the most valuable PL extension, providing unambiguous peak assignments from the peak splittings (or lack thereof).[4,16,17,20] Band symmetries can be deduced from the polarization dependence of the PL spectrum provided the correct assumptions are made.[20] Time resolved PL provides information about the dynamics of the light emission processes which are sensitive to crystal quality and impurity concentrations.[21] In this thesis, the time, polarization, and magnetic field dependences were not investigated. This fact notwithstanding, the low temperature, temperature dependent, and excitation intensity dependent PL spectra discussed throughout this thesis show that high quality ZnO can be produced by EPLD.

3.2 Free Excitons

Band-to-band, free-to-bound, and DAP recombinations are not even half of the story when it comes to PL from wide bandgap semiconductors like ZnO. In sufficiently pure semiconductors with good crystallinity, the Coulomb interaction between the photoexcited electron and hole correlates their motion and binds them together. The correlated motion can be thought of as an orbit of the electron and hole around the mutual center of mass. This bound state of the electron-hole pair is a quasi-particle called an exciton which is the fundamental quantum of excitation in a semiconductor. The energy of an exciton in a given material is given by[81]

$$E_{\mathrm{ex}}(n_{\mathrm{B}}, \mathbf{K}) = E_{\mathrm{g}} - \mathrm{Ry}^* \frac{1}{n_{\mathrm{B}}^2} + \frac{\hbar^2 \mathbf{K}^2}{2M} \tag{3.2}$$

where E_g is the bandgap, $n_B = 1, 2, 3, \ldots$ is the principal quantum number, $\mathbf{K} = \mathbf{k}_e + \mathbf{k}_h$ is the wave vector of the exciton and $M = m_e + m_h$ is the excitonic mass given by the sum of the effective masses of the electron, m_e, and the hole, m_h. Ry^* is the excitonic Rydberg and is given by

$$Ry^* = (13.6\,\text{eV})\frac{\mu}{m_0}\frac{1}{\epsilon^2} \tag{3.3}$$

where $\mu = \frac{m_e m_h}{m_e + m_h} m_0$ is the reduced mass of the exciton, ϵ is the dielectric constant of the medium, and m_0 is the free electron mass. $Ry^* \frac{1}{n_B^2}$ is the energy which binds the electron and hole together, i.e. its the exciton binding energy, $E_B(n_B)$. From here on out it is assumed that the exciton is in the ground state ($n_B = 1$) unless otherwise indicated. The last term in equation 3.2 represents the kinetic energy of the exciton as it moves though the lattice. In practice, the exciton will quickly thermalize with the lattice and lose its kinetic energy before recombining (going to the Γ-point in the Brillouin Zone). Thus, the energy of the emitted photon is $h\nu = E_g - E_B$. Exciton binding energies in semiconductors are typically in the 5-30 meV range. As mentioned in the introduction, ZnO has an exciton binding energy of 60 meV which is the highest for any direct-gap semiconductor besides the Cu-halides, i.e. CuCl ($E_g = 3.399\,\text{eV}$, $E_B = 130\,\text{meV}$)[84] and CuBr ($E_g = 3.9\,\text{eV}$, $E_B = 108\,\text{meV}$)[85].

Equation 3.2 shows that the exciton is analogous to the hydrogen atom.[†] Excitons have a hydrogenic series of excited states which converges to E_g as $n_B \to \infty$. Excitons can be assigned a Bohr radius which is given by[81]

$$a_B^{ex} = a_B \epsilon \frac{m_0}{\mu} \tag{3.4}$$

where a_B is the Bohr radius of a hydrogen atom. In ZnO the excitonic radius is $a_B^{ex} \approx 2\,\text{nm}$.[4,16] Thus, in ZnO (and coincidentally for all semiconductors) the wavefunction of the exciton extends over several lattice constants so the effective mass approximation is valid. This approximation was used to derive equations 3.2 to 3.4. Excitons which extend over several unit cells are known as Wannier excitons which were first described in 1937.[86] On the other hand, in insulating ionic crystals with a low ϵ the Coulomb interaction is strong and a_B^{ex} is less than a lattice spacing and the exciton is localized within a single unit cell. In this case the effective mass approximation is not valid and a different approach must be

[†]Actually the positronium system, the bound state of an electron and positron, is a closer analogy to an exciton since the e^- and e^+ have identical masses.

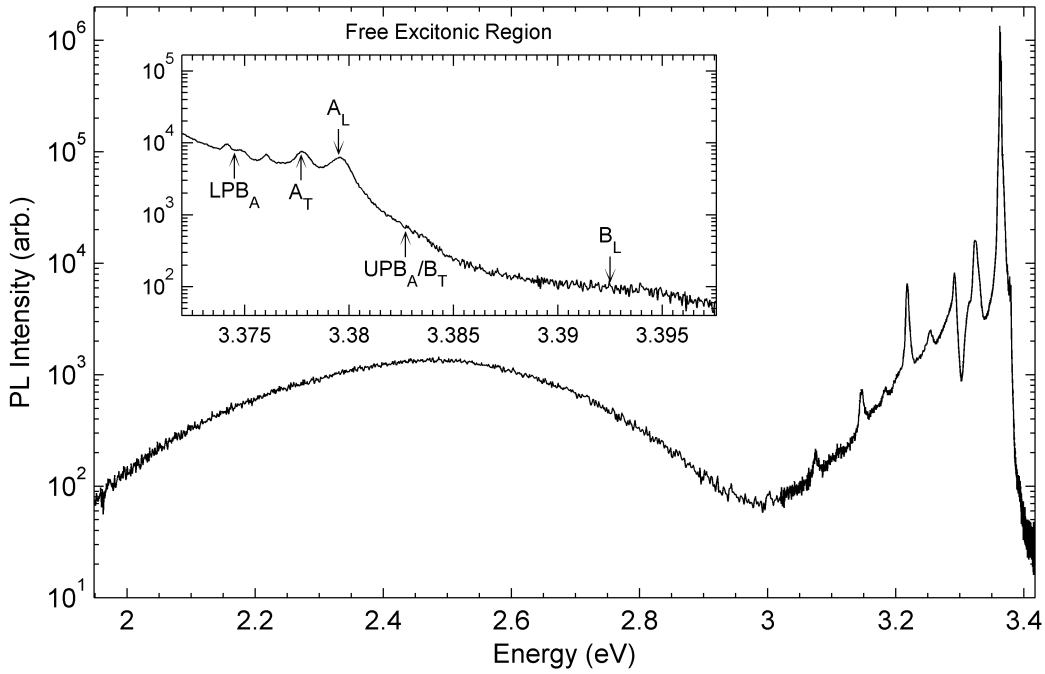

Figure 3.4: PL spectrum from the Zn face of *c*-axis undoped bulk ZnO grown by the hydrothermal method (Tokyo Denpa). The free excitonic region is shown in the inset.

taken. This type of exciton is known as a Frenkel exciton and was first described in 1931.[87,88] Wannier excitons are the main mechanism for emission in the high quality ZnO produced today and the excitonic spectrum of ZnO has been studied in great detail.[4,10–12,16–18,20,21,24,82] However, even after over 60 years of research into ZnO there are still mysteries to be uncovered about the behavior of its excitons.

Figure 3.4 shows the low temperature (4 K) PL spectrum from the Zn polar face of a hydrothermally grown bulk ZnO wafer with *c*-axis orientation. The PL was dominated by UV emission with several sharp features. Most of these features were excitonic in nature and will be discussed in subsequent sections. A broad green luminescence was also seen which is commonly observed in ZnO and other wide-gap semiconductors.[14,21,25,81,89] This green luminescence is from one of many possible deep defect levels in ZnO and is not excitonic.[14,16] The inset of figure 3.4 shows the region of the spectrum where the *free* excitonic features appear. In high quality ZnO, excitonic transitions are so efficient that band-to-band transitions are effectively quenched at low enough temperatures.

In the experimental geometry shown in figure 3.2, excitons from the *A* valence band in c-axis ZnO are strongly allowed due to the symmetry of their

wavefunctions and the selection rules for the wurtzite crystal structure . The overall symmetry of an excitonic wavefunction is given by the direct product of the symmetries of the electron and hole wavefunctions which, for the A-exciton is[20,81]

$$\Gamma_7 \otimes \Gamma_7 = \Gamma_1 \oplus \Gamma_2 \oplus \Gamma_5 \tag{3.5}$$

meaning the A-exciton should split into 3 distinct PL peaks having Γ_1, Γ_2, and Γ_5 symmetries. However, the Γ_2 exciton is forbidden without an external magnetic field due to the selection rules for wurtzite ZnO.[20,82] Thus two peaks corresponding to the A-exciton are observed in the PL spectrum of ZnO and are labeled A_{T} and A_{L} in the inset of figure 3.4. A_{T} has Γ_5 symmetry and has transverse character, it is the so called transverse A exciton. The Γ_1 exciton is longitudinal in nature. The terms transverse and longitudinal refer to the orientation of the polarization wave associated with the exciton as it travels through the lattice. This is shown diagrammatically in figure 3.5. For the transverse exciton, the

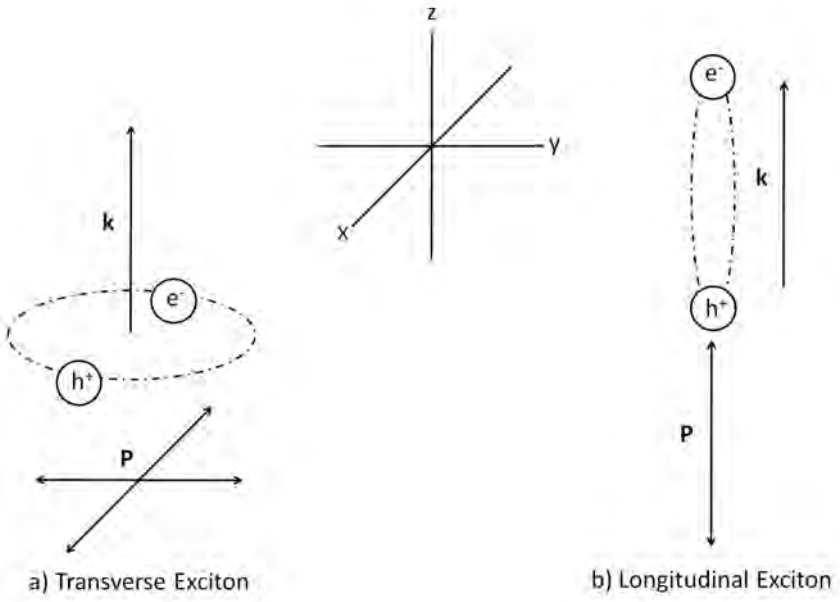

Figure 3.5: Schematic model of (a) transverse and (b) longitudinal excitons. The wave vector and components of the polarization wave associated with the exciton are labeled **k** and **P** respectively.

electron-hole pair can be thought of as orbiting in the xy-plane while traveling in the z direction with wave vector **k**. The polarization wave, **P**, will usually follow the electron-hole motion and will also be restricted to the xy-plane, hence we have purely $\mathbf{P} \perp \mathbf{k}$. On the other hand, a longitudinal exciton can be visualized

as an electron hole pair orbiting with highly elliptical motion in the yz-plane while traveling in the z-direction. In this case $\mathbf{k}$ is parallel to $\mathbf{P}$ which has a negligible x-component. The energy of these two configurations is slightly different with the longitudinal excitons having a slightly higher energy.[24,81,90] The longitudinal-transverse exciton energy splitting is a direct result of the electron-hole exchange interaction[90] and is proportional to the oscillator strength of the exciton[81]. Mixed-mode excitons in ZnO have also been observed which have both a longitudinal and a transverse character.[91]

Emission possibly arising from excitons with holes in the B-valence band is also seen in the inset of figure 3.4. For B-excitons we have an overall symmetry of[20,81]

$$\Gamma_9 \otimes \Gamma_7 = \Gamma_6 \oplus \Gamma_5 \tag{3.6}$$

meaning that B-excitons will also split into a non-degenerate transverse and longitudinal mode. For this particular piece of bulk ZnO, only a weak peak was seen in the region corresponding to B_{T} (3.384 eV[24]) No emission was seen or expected from B_{L} (Γ_6) as it is forbidden at $\mathbf{k} = 0$.[20] The occasional appearance of B_{L} in a PL spectrum is due to the fact that photons have a finite momentum and recombination usually occurs just outside the Γ-point in the Brillouin zone.[92] C excitons are not seen in this experimental geometry and are usually only seen when the collected light has $\mathbf{E} \parallel \mathbf{c}$, independent of its band symmetry ordering.[93] Also absent in this PL spectrum are emissions from any of the excited states of the A or B-excitons which immediately discludes the possibility of extracting the exciton binding energies from this data.

These free excitons are able to propagate through the crystal in the directions allowed by their symmetrical relationship with the underlying lattice. Excitons are relatively short lived with lifetimes in the 100-1000 ps range for bulk ZnO crystals.[4,21,94] In this time they can typically diffuse as far as 100-200 nm[91,95] With laser penetration depths of 40-50 nm they can easily propagate to the surface before recombination occurs. Of course many excitons will recombine much faster than their decay lifetimes, which releases a photon of energy $E_{\mathrm{g}} - E_{\mathrm{B}}$ within the crystal. This photon will propagate within the lattice and will likely be quickly reabsorbed into an exciton since it is at resonance with the exciton energy. The newly created exciton then travels a short distance and becomes a photon. The photon becomes an exciton again and so on and so forth. This coupling between the exciton and photon can be described by another quasi-particle called a polariton.

There are several types of polaritons but they are all mixtures of a photon with a dipole-carrying excitation (described by a polarization wave) of a dense medium. Phonons are an example of such a dipole-carrying excitation since they are vibrations of the ionic lattice. Thus, phonon-polaritons will form when infrared light passes though a solid.[96] Surface-plasmon-polaritons form when the surface plasmons interact with light at or near the plasmon resonances.[97] Surface magnons, or magnetic spin waves, carry a magnetic dipole and will form magnon-polaritons with incident radiation at frequencies near the magnon resonance in ferromagnetic materials.[98] In fact, a polarization wave will accompany light traveling in a dense medium for frequencies as high as the x-ray region. In other words, light propagating though semiconductors, insulators, metals, liquids and even sufficiently dense gases propagates as a polariton of some kind.[81]

In polar semiconductors like ZnO, the transverse excitons will couple strongly with the photon field produced from their recombinations. This strong coupling has a marked effect on the dispersion relation for the exciton-polaritons. According to the quantum mechanical non-crossing principle, when the dispersion relations of two interacting levels (photon and exciton) cross as a function of $\mathbf{k}$, the two levels will repel each other at the crossing point.[81] This results in the exciton-polariton dispersion curve splitting into two branches called the upper and lower polariton branches, the splitting being proportional to the coupling strength and dependent on the angle. Emission from polaritons from regions of the upper and lower branches with high lifetimes are likely the cause of the peaks labeled UPB_A and LPB_A in the inset of figure 3.4. The LPB_A peak is actually hidden underneath three sharper peaks but is revealed by increasing the sample temperature or subjecting the sample to simultaneous below-gap excitation as presented later. Polaritonic effects have been studied in detail in many systems[21,24,81,92,96–99] and may result in some very novel devices such as room temperature ZnO lasers with zero lasing threshold[99].

The picture of the free excitonic PL features used throughout this thesis is based on those reported by Meyer et al.[16] However, it must be noted that in the polariton picture, the concept of excitons breaks down. Thus, A_T is actually referring to an exciton-like polariton on the flat part of the lower polariton branch as described by Reynolds et al.[92] However, Klingshirn[100] points out that the A_L state shown in figure 3.5(b) (spin triplet with Γ_1 symmetry) should be energetically lower than A_T state (spin singlet with Γ_5 symmetry), in contrast to the assignments by Meyer et al.[16] The term 'longitudinal exciton' is used in several

other reports[4,21,90,92,101], but is actually referring to a mixed mode exciton which is not allowed for $\mathbf{k} \perp c$. Thus, Klingshirn[100] assigns the A_{T} and A_{L} features to polaritons on the upper and lower polariton branches respectively (UPB_A and LPB_A). Coincidentally, UPB_A is at the same energy as the 'longitudinal exciton' at $k = 0$. The small feature at 3.383 eV would then be emission from LPB_B. Such assignments do not change the identification of the feature labeled LPB_A in figure 3.4, which is recombination from a photon-like polariton near the bottleneck region of the lower polariton branch.[92] Such conflicts in the literature are a natural part of scientific research and in the end they contribute a great deal toward real progress.

3.3 Bound Excitons

In real semiconductors there are a multitude of imperfections in the crystal structure. Native defects such as vacancies, interstitials and dislocations along with substitutional or interstitial impurities are usually all present in some concentration. These imperfections are what make semiconductors useful in the first place, providing the donors and acceptors necessary for functional devices. Free electrons and holes can scatter off or bind to these defects and impurities which can help or inhibit device performance. Through careful study of the growth of such materials, the concentration of the various imperfections can be controlled. A careful balance is required to achieve material with the desired qualities for a given application.

Excitons will also bind to imperfections in the lattice, losing some of their energy in the process. They become localized around the imperfections and are trapped until they recombine. Radiative recombination of localized excitons produce photons which are red-shifted from those produced by free exciton recombination. This energy difference is called the localization energy, E_{Loc}, and is dependent on the nature of the imperfection. If the thermal energy of the environment is more than E_{Loc} for a given impurity, excitons cannot bind to it or they are quickly delocalized though phonon interactions. Many such imperfections may be present in a single sample, each having a unique and characteristic localization energy. The result is a complicated excitonic luminescence spectrum with many features which allows PL to qualitatively detect defects and impurities. In fact, about 75% of the integrated PL intensity over the UV to visible range shown in figure 3.4 is from bound excitonic recombination.

ZnO is intrinsically n-type with the dominant imperfections being donor impurities. As such, neutral donors are present in appreciable concentrations at low temperatures. Excitons can bind to these neutral donors forming a complex called a neutral donor bound exciton, D^0X. For typical neutral donors in ZnO the exciton localization energies are in the range of 10-30 meV.[16] The D^0X recombination region of the PL spectrum of bulk ZnO is shown in figure 3.6. Many narrow peaks are seen in this region which usually dominates the PL spectrum of ZnO at low temperatures. In this case the three dominating features are the I_4, I_5, and I_{6a} excitons. These are A-excitons bound to neutral donors and they were identified in this spectrum by their localization energy, i.e. the spacing between the I_x peak and A_T. Excitons from the B valence band can also bind to these neutral donors. The peaks labeled I_4^B, I_5^B, and I_{6a}^B are the B-excitons bound to the same donors which give rise to the dominant D^0X emissions from the A valence band. These peaks are separated from their A-exciton counterparts by 4.5 ± 0.3 meV which is in agreement with reported value of 4.9 meV for the A-B valence band splitting.[16]

The I_x notation for these excitonic features has been used historically in many excitonic material systems. The numbering convention used here is that which was adopted by Meyer et al.[16] in a detailed study identifying the origin of some of these peaks. In that study I_4 was assigned to neutral hydrogen and I_{6a} to neutral aluminum donors. Many other features were identified but the origin of I_5 was not deduced and is unknown at present. The appearance of a hydrogen related peak in this hydrothermal wafer is not surprising as KOH and LiOH were used as mineralizers for the ZnO growth.[102] Ohashi et al.[102] report Al impurities in the hydrothermally grown ZnO from Tokyo Denpa, originating from impurities in the ZnO source.

Ionized donors can also trap excitons and ionized donor bound emission , D^+X, is present in the spectrum of figure 3.6. Emission from I_0 and a few other sharp peaks in the vicinity were determined to be D^+X recombinations by magneto-PL experiments.[103] E_{Loc} of D^+X complexes are only around a few meV and these peaks die out very quickly as the temperature of the system is raised. It was shown that I_0 is the complementary D^+X transition of I_{6a}, referred to as I_{6a}^+ from here on out. In the spectra shown in figure 3.6, the measured localization of the I_{6a}^+ exciton agrees well with the reported values for I_0.[16,103]. The sharp peaks in between the I_{6a}^+ and A_T peaks can be attributed to the D^+X counterparts of the I_4 and I_5 excitons. Strong evidence for this is found from the temperature

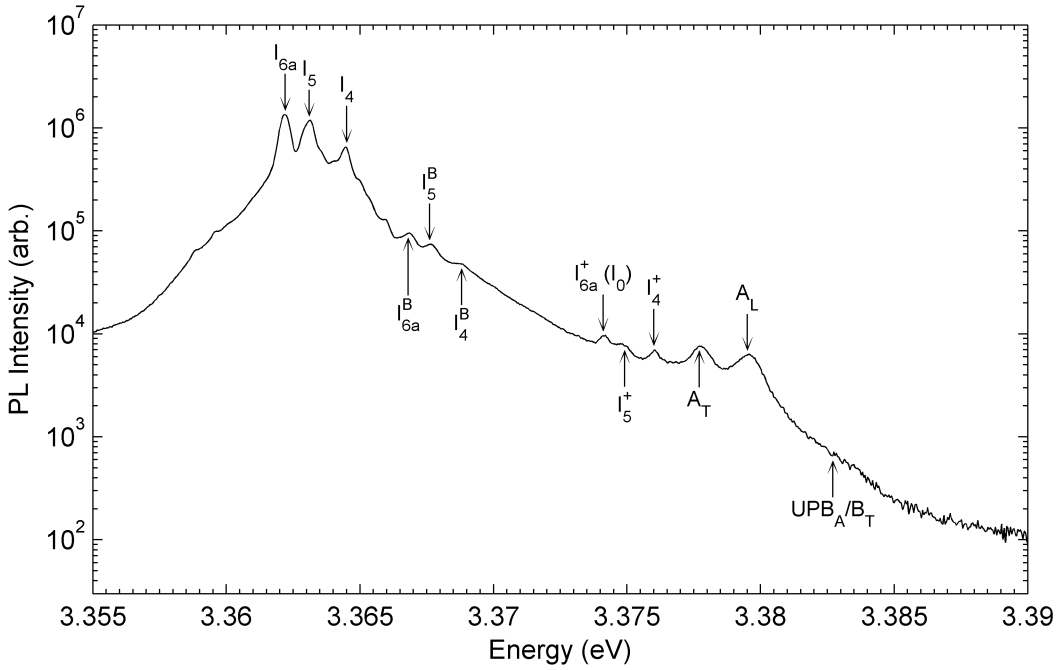

Figure 3.6: Donor bound exciton region of the PL spectrum from the Zn face of c-axis undoped bulk ZnO grown by the hydrothermal method (Tokyo Denpa).

dependence, presented shortly, and in chapter 6 where these peaks disappeared along with the I_4 and I_5 excitons after annealing.

The appearance of ionized donors at such low temperatures suggests the presence of residual acceptors in the sample which are partially compensating the donor concentration. Neutral acceptors can also bind excitons, forming A^0X complexes, but this emission was absent in the PL shown in figure 3.6. A^0X peaks should appear at lower energies than the D^0X peaks since they are expected to have a higher E_{Loc}.[4,16,21] Ionized acceptors can also bind excitons provided the electron to hole mass ratio is in the right range.[103] There have been relatively few reports about acceptor bound excitons in ZnO. They have been reported in deliberately acceptor doped ZnO, even being identified as the dominant emission at low temperature.[104,105] However, all the reports about acceptor bound excitons in ZnO, just like reports about p-type ZnO in general, are relatively tentative and have not yet gained international attention.

Extended structural defects such as dislocation loops, stacking faults, and surface traps will also bind excitons. Typically, these kinds of traps have a higher localization energy than impurity defects. A commonly seen structurally bound exciton in ZnO recombines around 3.335 eV.[11,16] Alves et al.[11] performed spatially

resolved cathodoluminescence (CL) on the 3.335 eV emission band which showed a spotty pattern indicative of extended structural defect emission. It seemed to correlate relatively well with cracks on the surface. For the sample with the PL shown in figure 3.6, this emission was not seen implying a smooth surface with minimal cracking. This is to be expected for the Tokyo Denpa hydrothermally grown bulk ZnO crystals.[7]

Bound exciton emission tends to dominate the PL spectrum from all excitonic, light-emitting material systems. Line widths for these transitions are always sharp (especially for D^0X and A^0X emission) since the excitons are localized. Thus, they avoid thermal broadening effects connected with a Boltzmann kinetic energy distribution which governs free exciton line widths.[106] The total concentration of all imperfection related binding centers along with their capture cross sections are usually too high compared to the diffusion length of the free exciton for free excitonic emission to dominate. However, recently a Japanese-French collaboration has successfully produced ZnO showing PL emission dominated by free A-excitons indicating a very low residual donor concentration.[107] These samples were homoepitaxially grown on Tokyo Denpa ZnO substrates by liquid phase epitaxy. A low residual donor concentration is required before stable and reliable p-type ZnO can be grown and this work by Robin et al.[107] may be the first step.

3.4 Two Electron Satellites

Neutral donors in a semiconductor can be thought of as an electron bound to the effective positive charge of the impurity nucleus which is shielded by the core and valence electrons. In the effective mass approximation, the donor electron will have hydrogenic wavefunctions and a series of excited states which can be approximated by

$$E_{e^-}(n_{\mathrm{B}}) = E_{\mathrm{D}}\frac{1}{n_{\mathrm{B}}^2} \tag{3.7}$$

where n_{B} is the principal quantum number and E_{D} is donor binding energy, i.e. the energy binding the electron in its ground state to the donor. Usually when a D^0X complex recombines the donor electron is unperturbed and remains in the ground state. Sometimes however, the donor electron is kicked up into the $n_{\mathrm{B}} = 2$ excited state as the donor bound exciton recombines, taking the necessary energy from the exciton. The resulting photon is redshifted from the primary recombination line by the amount ΔE_{TES} which is the energy difference

between the $n_B = 1$ and $n_B = 2$ states of the donor electron. This type of secondary recombination is unique to D^0X complexes and is known as a two-electron satellite (TES) transition.

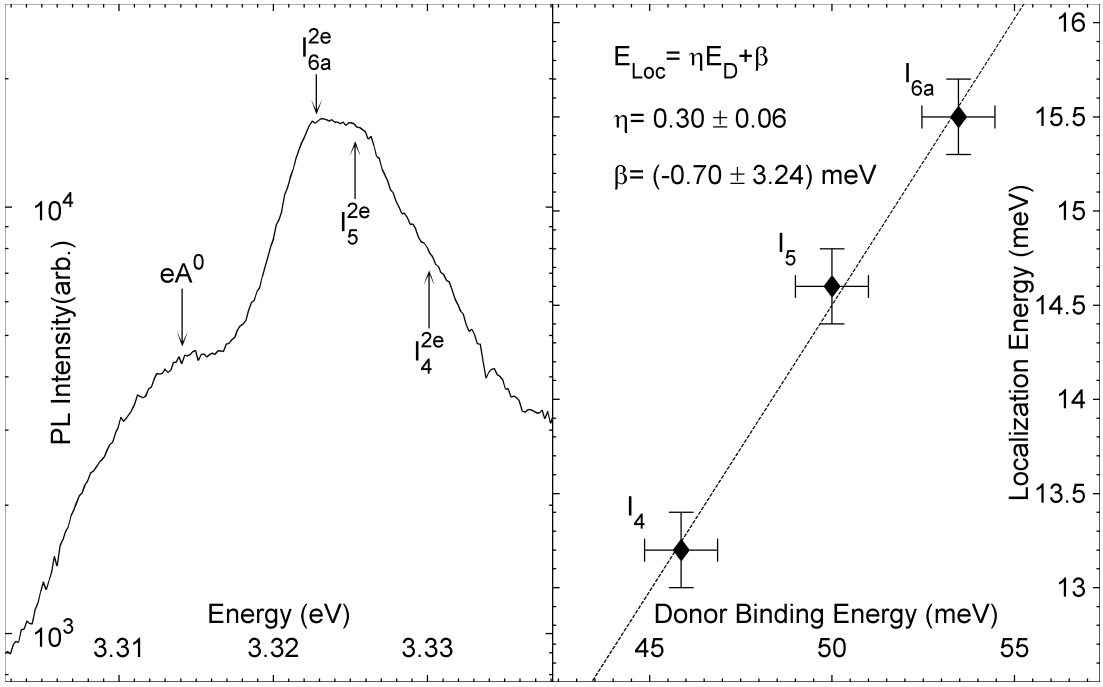

Figure 3.7: (a) TES emission from hydrothermally grown bulk ZnO. (b) Haynes plot showing linear behavior with the expected slope of 0.3

Figure 3.7(a) shows the TES region of the Tokyo Denpa bulk ZnO wafer discussed throughout this chapter. Positions of the TES transitions for the I_4, I_5, and I_{6a} bound excitons are indicated in the figure. The positions were measured by eye with an uncertainty of ± 1 meV. Also seen is an eA^0 transition at 3.314 eV which has been convincingly assigned to acceptor-like basal plane stacking faults having an acceptor binding energy of 130 ± 3 meV.[83] Examination of equation 3.7 shows that $E_D = \frac{4}{3}\Delta E_{TES}$. Peak positions, localization energies, TES separations, and calculated donor binding energies are shown in table 3.1. Uncertainties on absolute peak positions for the sharp peaks are ± 1 meV which is due mainly to the spectrometer calibration. Uncertainties on energy differences between two sharp peaks is ± 0.2 meV or better which covers two steps of the spectrometer in the UV region. The values for all the quantities in table 3.1 are in good agreement with those published by Meyer et al.[16] and others[21,24] with a spread in the literature values of about 1 meV.

In 1960 J.R. Haynes provided concrete evidence of donor and acceptor bound

Table 3.1: PL peak positions and localization energies along with TES position, separations, and calculated donor binding energies for the Zn face of bulk ZnO.

Peak	E_{PL}[a](eV)	E_{Loc}[b](meV)	E_{TES}[c](eV)	ΔE_{TES}[c](meV)	E_{D}[c](meV)
UPB_A/B_{T}	3.383	–	–	–	–
LPB_A	3.375	–	–	–	–
A_{L}	3.380	–	–	–	–
A_{T}	3.378	–	–	–	–
I_0	3.375	2.8	–	–	–
I_1	3.374	3.5	–	–	–
I_4	3.365	13.2	3.330	34.4	46
I_5	3.363	14.6	3.325	37.5	50
I_{6a}	3.362	15.5	3.323	40.1	53

[a] ± 1 meV on absolute peak positions due to calibration fluctuations
[b] ± 0.2 meV on differences in peak positions for two sharp peaks
[c] ± 1 meV calculation and/or eyeball error

excitons in Si.[106] His experiments revealed a linear relationship between E_{Loc} and E_{D} for a given D^0X (A^0X) of the donor (acceptor) which binds it. From this, Haynes reasoned that a D^0X complex is a hole which is bound to a positive donor ion by an electron-pair bond, analogous to the covalent bond. This rule of thumb is now called Haynes rule with constants of proportionality typically in the 0.1 range. Figure 3.7(b) shows a Haynes plot along with the straight line fit $E_{Loc} = \eta E_{\mathrm{D}} + \beta$ where $\eta = 0.30 \pm 0.09$ and $\beta = -0.58 \pm 4.37$ meV. The uncertainties on these constants takes into account the uncertainties of E_{D} and E_{Loc} shown in figure 3.7 as described for linear fits in appendix A. The η and β values deduced from this experiment are in good agreement with the accepted values for ZnO.[4,16,21] Appearance of TES transitions confirms the D^0X nature of the dominant PL at low temperature and allows for a simple measure of donor binding energies in excitonic semiconductors.

3.5 Phonon Assisted Luminescence

Lattice vibrations quantized by phonons can interact with electrons, holes, and excitons. This coupling leads to the so called phonon replicas commonly seen in the PL and absorption spectra of many materials. The exciton-phonon interaction is similar to the electron-phonon interaction which has three basic origins. At low temperature, Frölich coupling with the longitudinal optical (LO) phonons is

the largest contributor to the exciton-phonon coupling in polar materials with a large ionic character like ZnO and GaN.[108] This type of coupling is due to the Coulomb interaction between the exciton and the longitudinal electric field created by the LO-phonons. Excitons and phonons can also interact through the deformation potential set up by the acoustic and optical phonons. The deformation potential is set up by the periodic deformation of the atomic arrangement caused by the phonons.[81] The third way excitons and phonons can interact is though piezoelectric fields. These are generated by acoustic phonons in certain directions of noncentrosymmetric crystals. If the total exciton-phonon coupling is strong enough, the exciton can bind with one or several phonons becoming a quasiparticle known as an exciton-polaron.[109] Formation of exciton-polarons is enhanced when the total binding energy of the exciton complex is comparable to the LO-phonon energy.[110] This is true for the I_{6a} complex which has a total binding energy of 76 meV compared to the LO-phonon energy of 72 meV.

The concept of exciton-polarons is similar to the polaron, which is the quasiparticle describing electron propagation though the lattice.[111] A free electron (hole) in a lattice will locally polarize the surroundings, attracting the cations (anions) and repelling the anions (cations). The resulting distortion of the lattice can be described by a superposition of preferentially LO-phonons.[81] The polaron is the electron plus the cloud of LO-phonons that accompanies it as it travels. Polarons have a different effective mass and dispersion relation than a free electron in the crystal. Excitons can couple to the phonons in the same way as electrons do. For luminescence this manifests as the appearance of Stokes and anti-Stokes LO-phonon replicas from excitonic related emission peaks.[110,112]

Figure 3.8 shows the Stokes LO-replicas from the I_{6a} peak and the TES transitions. They are constantly spaced 72 meV apart which is equal to the LO-phonon energy in ZnO.[4] No replicas are seen from the A_T peak due to its low intensity compared to I_{6a}. On the high energy side of I_{6a}^{1LO}, a dip is seen in the spectrum which is due to quantum mechanical Fano interference.[110] When a discreet state exists within a continuum, quantum mechanical interference takes place which can reduce PL emission intensities from the discreet level.[113] In this case the discreet level is the I_{6a}^{1LO} exciton-polaron and the continuum is the thermal phonon bath. Fano interference is seen in high quality crystals and the dip has a marked effect on the intensity of the I_{6a}^{1LO} peak, bringing it below the I_{6a}^{2LO} intensity. This phenomenon caused some authors to incorrectly assign the I_{6a}^{2LO} peak to a donor-acceptor-pair transition (see section 3.6).[16,21]

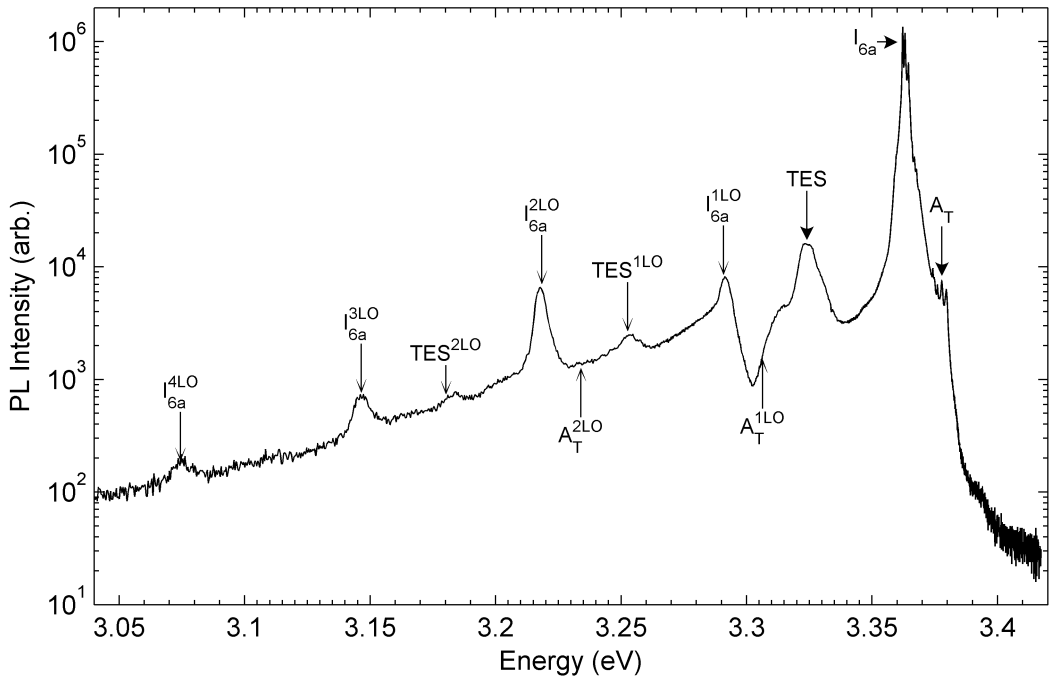

Figure 3.8: PL emission from bulk ZnO in the LO-phonon replica region. Positions of LO-replicas of A_{T} are shown for reference but do not appear in the spectrum. Positions of the thin headed arrows were calculated from the measured position of the thick headed ones.

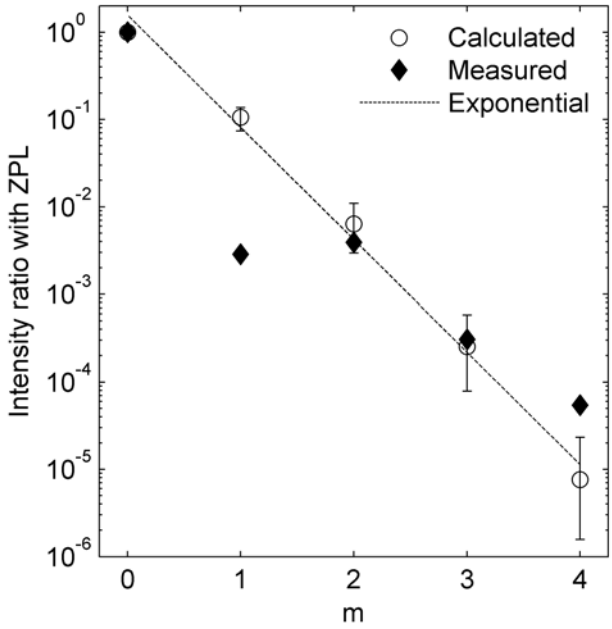

Figure 3.9: Measured and calculated intensity ratios of the m^{th} LO-phonon replicas to the zero phonon line for a Huang-Rhys factor of $S = 0.12 \pm 0.04$. The straight line fit is a simple exponential fit to the data calculated with equation 3.8.

A quantitative estimate of the Fano interference effect can be made by using the Franck-Condon approximation which gives[114]

$$I_m = \frac{e^{-S}S^m}{m!} \quad m = 0, 1, 2, 3 \ldots \tag{3.8}$$

where I_m is the intensity of the m^{th} replica, and S is the Huang-Rhys factor. A value of $S = 0.12 \pm 0.04$ was obtained by weighted least squares fitting using the intensity ratios of the 2^{nd}, 3^{rd}, and 4^{th} phonon replicas to the zero phonon line. The calculated and measured phonon intensity ratios are shown in figure 3.9. Decent agreement is seen between the measured and calculated intensities except for the $1LO$-replica. This data point was not used for the fit due to the Fano resonance effect. From the figure it can be seen that Fano resonance has cut the intensity of this peak down by a factor of nearly 20. The straight line in the figure shows a simple exponential fit to the calculated ratios, which is a good approximation of equation 3.8. The fitted decay constant was -2.9 ± 0.1 which has no easily recognizable relationship to S. Trial and error shows that the exponential approximation is only valid for S values less then about 2. S is proportional to the strength of the exciton-phonon coupling and the relatively low value here may be surprising since the Frölich coupling in ZnO is strong. However, there are no reports of S-values for the I_{6a} peak in ZnO.

In this sample no anti-Stokes peaks were present on the high energy side of the principal recombination line a.k.a. the zero phonon line. At low temperature the thermal population of LO-phonons is too low for significant anti-Stokes processes. However, the strong exciton-phonon coupling in ZnO allows anti-Stokes phonon replicas at low temperature due to interactions of excitons with phonons created by the Stokes LO-phonon replicas.[112] The Stokes and anti-Stokes lines may not be symmetric about the zero phonon line implying different coupling states for the Stokes and anti-Stokes exciton-polarons.[110] Exciton-phonon interactions are intrinsic to the material and must be understood as they will effect device performance no matter how good the material quality is.

3.6 Donor Acceptor Pair Recombination

Both donors and acceptors are present in real semiconductors. They may be substitutional or interstitial impurities or native defects such as vacancies and anti-sites. In unintentionally doped ZnO the residual donor concentration is much

higher than the acceptor concentration leading to naturally n-type material. This is one of the main difficulties in producing stable p-type ZnO. The presence of both donors and acceptors leads to a compensation effect in real semiconductors which provides a polycentric radiative recombination channel known as a donor-acceptor-pair (DAP) transition.

At a given temperature a certain percentage of the donors will be thermally ionized which can be approximated using simple Boltzmann statistics by

$$\frac{N_{\mathrm{D}}^{\mathrm{th}+}}{N_{\mathrm{D}}} \approx \exp\left(-E_{\mathrm{D}}/k_{\mathrm{B}}T\right) \tag{3.9}$$

where N_{D} is the total concentration of donors, k_{B} is Boltzmann's constant and T is the temperature. The same approximation can be used for acceptors. For E_{D} or E_{A} values which are typically greater than 30 meV, equation 3.9 shows essentially all the donors and acceptors will be neutral at liquid He temperatures. However, donors and acceptors can also be ionized by compensating each other. When neutral donors and neutral acceptors are sufficiently close together, the wavefunctions of the donor electron and the acceptor hole will overlap and the electron will jump to the acceptor. This leaves behind an ionized donor and an ionized acceptor. Unlike thermally ionized impurities, this compensated DAP does not contribute to the conductivity since the donor electron and acceptor hole from a pair are localized to that pair.

When photoexcited free electrons and free holes are created in a partially compensated semiconductor, they can lose some of their energy by binding to the ionized donors and acceptors respectively. Even after losing this energy the electron and hole, which have neutralized the compensated donors and acceptors, are still out of thermal equilibrium. If these photoexcited carriers are bound to the respective centers of the same DAP, radiative recombination can occur which gives a photon of energy[81]

$$\hbar\omega_{\mathrm{DAP}} = E_{\mathrm{g}} - E_{\mathrm{D}} - E_{\mathrm{A}} + \frac{e^2}{\epsilon R} \tag{3.10}$$

where e is the charge on the electron and R is the distance between the donor and acceptor in the pair. After the recombination an ionized donor and ionized acceptor are left behind. The last term in equation 3.10 is the Coulomb attraction between these ionized impurities which lowers their energy. The lost energy is carried away by the blue-shifted photon. If the donors and acceptors are substitu-

tionally incorporated into the lattice, their separation will be in discreet intervals. This can lead to the appearance of several sharp DAP peaks corresponding to separations which are integer multiples of the lattice constants.[115]

No clear evidence of a DAP transition was seen in the PL from the bulk ZnO sample studied in this chapter. DAP transitions are usually identified by their dependence on temperature and excitation power. These dependences are discussed in detail in the next two sections which show clearly that the I_{6a}^{2LO} peak is not a DAP transition. Time resolved PL is the third experiment required to unambiguously identify a DAP transition. The closer DAP's will recombine first meaning DAP transitions will red-shift with increasing time after a short laser pulse. DAP recombination is usually seen in naturally n-type materials which have been intentionally doped with acceptors. Their appearance in a PL spectrum may allow a quantitative estimate of acceptor binding energies or impurity concentrations.[116]

3.7 Temperature Dependence

A single PL spectrum is usually not sufficient to confidently identify the origin of the observed emission peaks. Peak emission energies can change from sample to sample and day to day due to strain, surface modification, or small systematic errors in the experiment. Localization energies of bound excitons can be used to identify the peaks but this requires a resolvable and unambiguously identified free excitonic peak. One of the best ways to extend the PL technique and provide confident peak assignments is to analyze the evolution of the PL spectrum as the temperature of the system is raised. In the previous sections the peak assignments were ultimately based off of the temperature dependence as presented below.

Figure 3.10 shows the temperature evolution of the PL emission from the free and bound excitons in bulk ZnO. The spectra have been offset vertically for clarity by multiplying the intensities. Baseline for each spectra can be taken as the value at 3.385 eV. Typical excitonic behavior can be seen for all the peaks, they decayed in intensity and red-shifted as the temperature was increased. At low temperatures the spectrum was dominated by D^0X transitions which died away quickly compared to the free excitonic peaks. Bound exciton emission will die away first as the bound-excitons are thermally dissociated from the binding centers and become free excitons. This results in an initial increase in the free

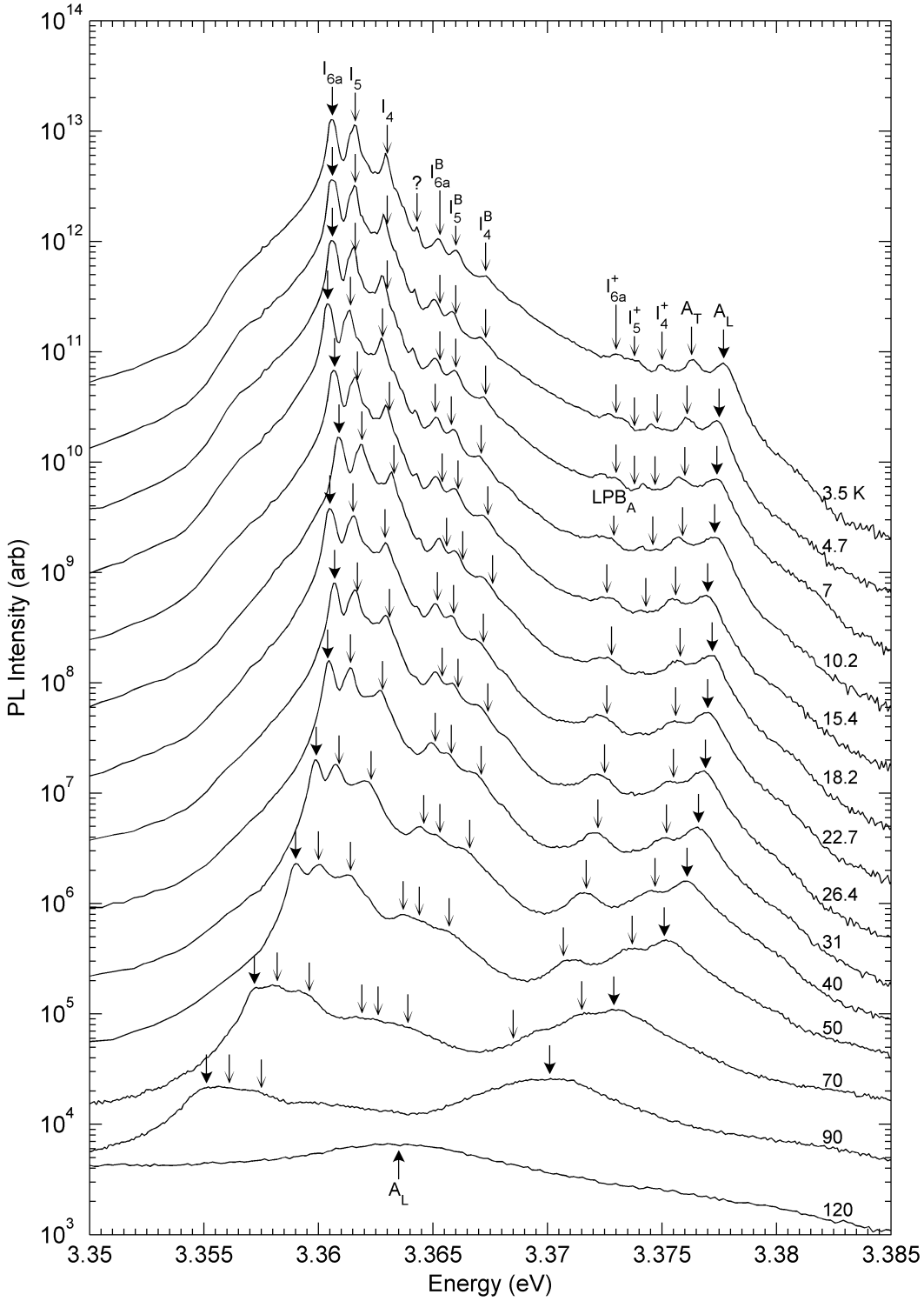

Figure 3.10: Temperature Dependent PL of the excitons in bulk ZnO (offset vertically). Markers indicating position of A_{T} and LPB_A were a constant distance from the A_{L} peak. All the other markers were calculated by assuming a constant separation to $I_{6\mathrm{a}}$.

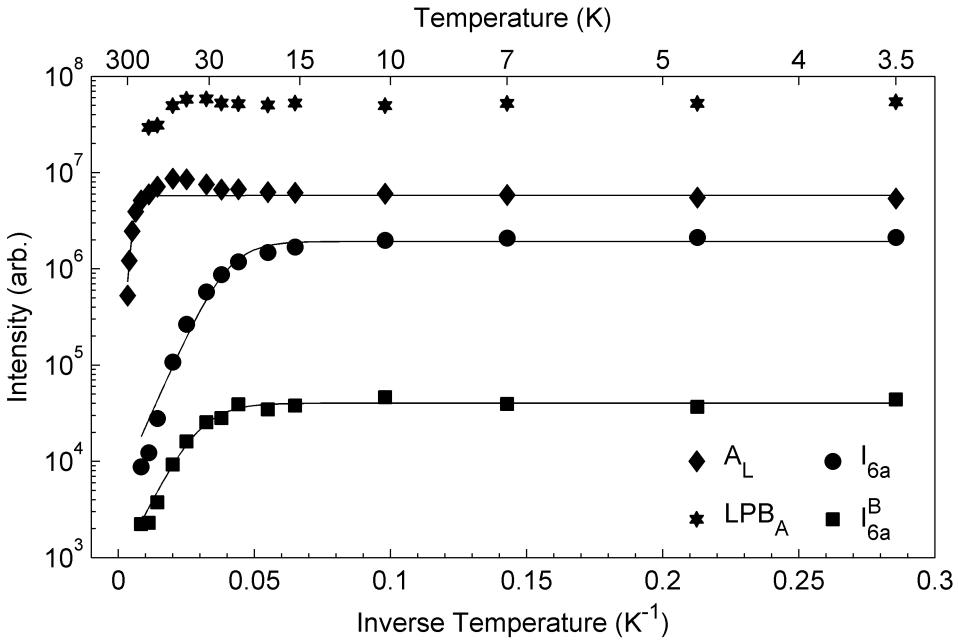

Figure 3.11: Arrhenius plot of the PL peak intensity for the free excitons and the I_{6a} and I^{B}_{6a} donor bound excitons.

excitonic emission as temperature gets raised from 3.5-50 K as seen in the Arrhenius plot of absolute peak intensities shown in figure 3.11. Peak intensities were simply read off the spectra at the emission maxima of each feature. The LPB_A peak also increases with temperature up to about 40 K, confirming that it is not a shallow bound exciton. By 90 K the free excitonic emission dominated the spectrum due to the large excitonic binding energy. They do not get thermally dissociated until well above room temperature and free excitonic emission has been observed up to 700 K ($kT \approx 60$ meV).[117] These facts are what confidently identify the free excitonic and polariton peaks in the ZnO PL spectrum.

The solid lines shown in figure 3.11 are the least squares fits of a model which assumes one nonradiative recombination channel with Arrhenius-type thermally activated behavior. Diagrammatically this is shown in figure 3.12. The E_1 state is the radiative recombination in question while the E_2 state is a higher energy level which may or may not be optically active. As the temperature increases the E_2 state becomes populated by electrons in the one particle picture or excitons in the two particle picture. This comes at the expense of the E_1 population which quenches the radiative E_1 recombination. Using Boltzmann statistics it can be shown that the luminescence intensity of the E_1 transition follows the

temperature as

$$I(T) = \frac{I(0)}{1 + A\exp\left(\frac{-E_a}{k_B T}\right)} \tag{3.11}$$

where $I(0)$ is the intensity at 0 K, A is a constant relating to the degeneracy of the E_1 and E_2 levels, and $E_a = E_2 - E_1$ is the activation energy of the nonradiative recombination channel. For bound excitons the activation energy corresponds to the localization energy of the exciton and the E_2 state is the free exciton. For free excitonic peaks the activation energy corresponds to the binding energy and the E_2 state is an uncorrelated free electron and free hole. For two nonradiative decay paths equation 3.11 can be written as[118]

$$I(T) = \frac{I(0)}{1 + A\exp\left(\frac{-E_a}{k_B T}\right) + B\exp\left(\frac{-E_b}{k_B T}\right)} \tag{3.12}$$

where E_b is the activation energy of the second decay path and B is a constant. For this thesis the convention $E_b > E_a$ will be used. In real samples with some degree of disorder, the second decay path can be used to represent the average effect of n nonradiative channels which is more accurately described by

$$I(T) = \frac{I(0)}{1 + A_1\exp\left(\frac{-E_1}{k_B T}\right) + A_2\exp\left(\frac{-E_2}{k_B T}\right) + \ldots + A_n\exp\left(\frac{-E_n}{k_B T}\right)}. \tag{3.13}$$

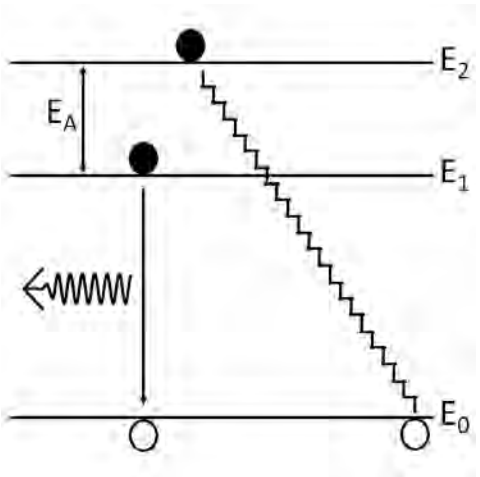

Figure 3.12: Diagram of thermally activated luminescence quenching. E_1 is the optically active transition. As temperature increases the system will be excited to a higher energy state E_2 which may or may not be optically active. According to Boltzmann statistics, the result is a smaller and smaller population in the E_1 state as temperature rises, quenching the luminescence.

Table 3.2: Fitted parameters for the intensity decay with temperature described with one nonradiative recombination channel (equation 3.11).

Parameter	A_{L}	$I_{6\mathrm{a}}$	$I_{6\mathrm{a}}^{\mathrm{B}}$
$I(0)$ (arb.)	$(1.2 \pm 0.3) \times 10^3$	$(9.68 \pm 0.01) \times 10^5$	$(8.1 \pm 0.3) \times 10^4$
A (arb.)	140 ± 80	363 ± 2	50 ± 30
E_{a} (meV)	80 ± 10	12.7 ± 0.1	12 ± 2

For this bulk ZnO sample the data shown in figure 3.11 was well fit with a single nonradiative recombination channel (equation 3.11). Table 3.2 shows the fitted parameters along with the uncertainties given by the 95% confidence intervals as calculated by the IGOR curve fitting package. It must be noted here that equation 3.11 describes the integrated intensity of the emission and the data which is shown in figure 3.11 and used for the fits are the absolute peak intensities. This leads to an underestimate in the fitted activation energies as the peaks broaden with temperature (see page 47). The activation energies of the $I_{6\mathrm{a}}$ and $I_{6\mathrm{a}}^{\mathrm{B}}$ peaks were 12.8 ± 0.1 meV and 12 ± 2 meV. These activation energies are equal to each other and comparable to the localization energies. Such agreement gives confidence to the assignment of these excitons to B-excitons bound to the dominant donors. Furthermore, if the $I_{\mathrm{x}}^{\mathrm{B}}$ peaks were A-excitons bound to different donors they should decay quicker than the dominating peaks since they would have a smaller localization energy. The peak marked with a question mark in figure 3.10 was an A-exciton bound to an unknown donor and it died away quicker than the $I_{\mathrm{x}}^{\mathrm{B}}$ peaks. This again would not be the case if the $I_{\mathrm{x}}^{\mathrm{B}}$ peaks were bound A-excitons.

An activation energy of 80 ± 10 meV was fitted to the 6 highest temperature data points of the free excitonic peak (A_{L}). Only the high temperature data was used for the fit to ensure that the initial increase in intensity did not effect the result. The initial increase was caused by thermal dissociation of D^0X peaks into free excitons. The fitted activation energy for A_{L} was close to the 60 meV exciton binding energy for ZnO. The overestimate came from the contribution of the 1LO-replica as it moved closer in energy to the zero phonon line as temperature increased. A decreasing spacing between the 1LO-replica and the zero phonon line observed in this sample is typical and well accounted for by theory as will be discussed shortly.

Excitonic peak positions generally follow the temperature dependence of the bandgap energy, which decreases as temperature increases. An empirical model

commonly used for the temperature dependence of the bandgap is the Varshni equation[119]

$$E_{\mathrm{g}}(T) = E_{\mathrm{g}}(0) - \frac{\nu T^2}{\mu + T} \tag{3.14}$$

where ν and μ are material dependent constants. Problems arise for this model when the experimental temperature is less than the Debye temperature.[120] This is usually the case for PL experiments which are typically carried out from 1-300 K, leading to a large spread in reported ν and μ values. A more successful semi-empirical model has been developed which is based on the accepted interpretation that the decreasing bandgap is caused by thermal expansion of the lattice and the electron-phonon interaction. Using an Einstein approximation for the average energy of the lattice vibration, Manoogian and Leclerc proposed[121]

$$E_{\mathrm{g}}(T) = E_{\mathrm{g}}(0) - UT^s - V\theta\left[\coth\left(\frac{\theta}{2T}\right) - 1\right] \tag{3.15}$$

where θ is the effective phonon temperature and U, s, and V are material dependent constants. The second term in equation 3.15 is the effect of the lattice dilation and the third term is the contribution from the electron-phonon interaction.

Typically, the electron-phonon interaction causes the majority of the bandgap shrinkage with the lattice dilation contributing only 2 to 20% of the shift depending on the semiconductor.[120,122] By ignoring the lattice dialation, it can be shown that equation 3.15 simplifies to the Varshni equation in the $T \ll \theta$ limit and that the $\nu = \frac{3}{8}\theta_{\mathrm{D}}$ where θ_{D} is the Debye temperature.[120] A more useful 3 parameter equation than the Varshni equation in the $U = 0$ limit, first proposed by Viña et al.[123], is given by

$$E_{\mathrm{g}}(T) = E_{\mathrm{g}}(0) - \frac{\alpha\theta}{\exp(\theta/T) - 1} \tag{3.16}$$

where α is proportional to the electron-phonon interaction and θ is the effective phonon temperature. Comparison of equation 3.16 to one proposed by Pässler[122] shows that Viña's model considers only the short wavelength phonons. The Manoogian equation (3.15) can be reduced to equation 3.16 by setting $U = 0$, $V = \alpha/2$, and using the relation $2[\exp(x)-1]^{-1} = \coth(x/2)-1$. This simple 3 parameter model has been successfully applied to several material systems.[12,122,124]

Figure 3.13 shows the position of the A_{L} and $I_{6\mathrm{a}}$ peaks with the dotted lines showing the weighted least squares fit of equation 3.16. The uncertainties shown in the figure were used for the weighting, with more emphasis placed on those

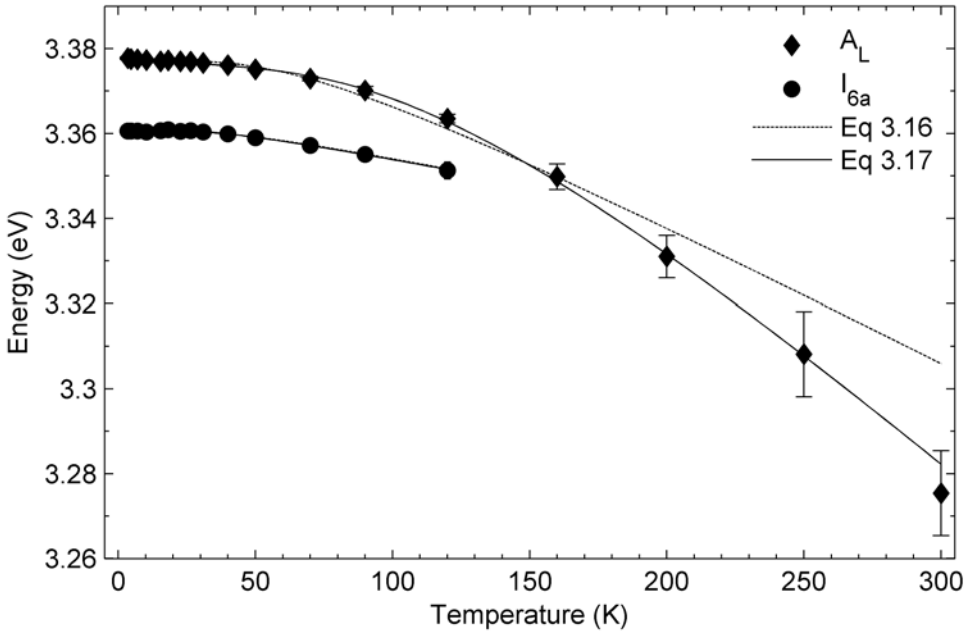

Figure 3.13: Emission energy as a function of temperature for bulk ZnO. The dotted lines are the least squares fit of equation 3.16 and the solid lines are the best fit to equation 3.17.

points with smaller uncertainties. The low temperature region where the emission from the D^0X peaks are still resolvable is shown more closely in figure 3.14. As can be seen in the two figures, this model has nearly the right shape but has some trouble fitting the data over the entire temperature range. The solid lines in the figures are the least squares fit of a slightly modified form of the Manoogian equation (3.15) given by

$$E_{\mathrm{g}}(T) = E_{\mathrm{g}}(0) - UT - \frac{\alpha\theta}{\exp(\theta/T) - 1} \tag{3.17}$$

which sets $s = 1$ in equation 3.15 and rewrites the second term into the more intuitive Bose-Einstein form of equation 3.16. In this model the lattice dilation is not ignored and its effect on the bandgap is assumed to be linear with temperature. The addition of the contribution from the lattice dilation has significantly improved the fit for the free excitonic peak over the entire temperature range. This may come as a surprise since the molar volume of bulk ZnO changes by only 0.17% from 4.2 to 296 K.[125]

Table 3.3 shows the fitted constants for the two models along with the 95%

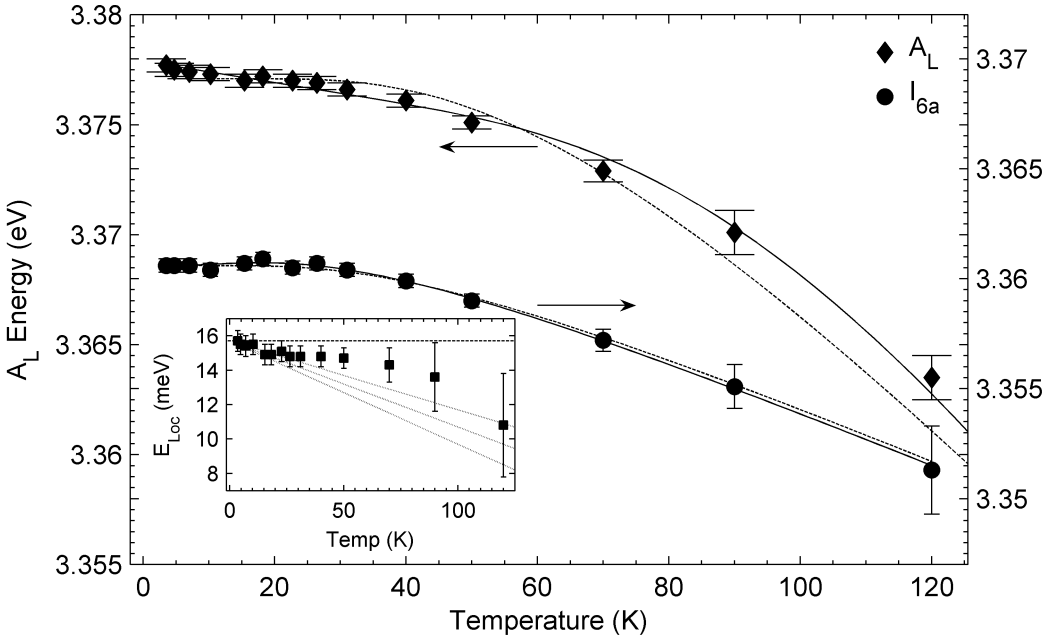

Figure 3.14: Emission energy as a function of temperature for bulk ZnO in the low temperature region. The dotted lines are the least squares fit of equation 3.16 and the solid lines are equation 3.17. The localization energy of I_{6a} is shown in the inset. The dotted lines in the inset have a negative slope of $U = (5 \pm 1)\,\mathrm{meV/K}$.

confidence bounds. Also shown is the reduced χ^2 parameter which is given by[126]

$$\chi^2_{\mathrm{R}} = \frac{1}{N-P} * \sum \left(\frac{y_i - y_i^F}{e_i} \right)^2 \tag{3.18}$$

where N is the number of data points, P is the number of parameters in the fit, y_i is the i^{th} data point, y_i^F is the calculated data, and e_i is the uncertainty in the data. χ^2_{R} can be used to compare similar fits when the number of parameters is not constant, such as the case for equations 3.16 and 3.17. A five fold reduction of the χ^2_{R} parameter is seen for the 4 parameter Manoogian equation compared to that for equation 3.16 for the A_{L} peak. This shows that over the temperature range from 1-300 K the lattice dilation cannot be ignored. The value obtained for the free excitonic peaks, which all follow the A_{L} dependence, agreed well with reported values for Eagle-Picher vapor grown bulk ZnO.[127] In the study by Hamby et al.[127], a calculated value of $U = 5.5 \times 10^{-5}\,\mathrm{eV}$ was obtained using reported values for bulk modulus, bandgap pressure coefficient, and the mean thermal expansion coefficient. For the bound excitons, which all follow the I_{6a} dependence, there was minimal reduction in the χ^2_{R} value when adding the U

Table 3.3: Fitted constants of the emission energies of the A_L and I_{6a} peaks .

Model	Parameter	A_L	I_{6a}
Bose-Einstein (3.16)	$E(0)$ (eV)	3.3771 ± 0.0002	3.3606 ± 0.0001
	α (eV/K)	$(3.3 \pm 0.6) \times 10^{-4}$	$(1.3 \pm 0.1) \times 10^{-4}$
	θ (K)	190 ± 30	130 ± 10
	χ^2_R	2.5	0.27
Manoogian (3.17)	$E(0)$ (eV)	3.3779 ± 0.0003	3.3605 ± 0.0006
	U (eV/K)	$(5 \pm 1) \times 10^{-5}$	$(-2 \pm 5) \times 10^{-6}$
	α (eV/K)	$(5 \pm 2) \times 10^{-4}$	$(1.4 \pm 0.5) \times 10^{-4}$
	θ (K)	370 ± 80	100 ± 80
	χ^2_R	0.5	0.18

parameter. It was determined to be essentially zero as seen in table 3.3. At 120 K, which was the highest temperature the I_{6a} peak was still resolvable, the contribution from the lattice dilation to the shift in the A_L peak was 6 ± 1 meV representing about 40% of the total redshift. This was roughly the same as the difference in localization energies of I_{6a} at 3.5 and 120 K. The dotted lines in the inset of figure 3.13 were drawn with slopes of $U = (5 \pm 1)$ meV/K, which was that found for the free excitonic peaks. This is evidence that bound excitons are not effected by the lattice dialation as much as free excitons. Bound excitons have hydrogenic-like wavefunctions which are localized while free excitons have Bloch-like wavefunctions extending over the lattice. Since these free excitons 'feel' the whole lattice at once, it is not unreasonable that their energy will depend more on the lattice dialation than bound excitons.

For both the A_L and I_{6a} peaks the α parameter calculated by each of the fits agreed within the uncertainties shown. Comparing the values shows the free excitons in this sample were coupled roughly 3 times stronger to the LO-phonons then the bound excitons were. Effective phonon temperatures, θ, calculated with equation 3.16 were roughly the same for the free and bound excitonic peaks. A large difference was seen between the θ values for the two fits for the free excitons while the bound excitons had agreeing values. The reason is likely due to the temperature range which the data spans. A value close to the $\theta = 190 \pm 30$ K value for A_L computed with equation 3.16 is obtained when only the data for $T < 120$ K is used to fit the Manoogian equation (3.17) to A_L. For an accurate measurement of θ with smaller uncertainties, data from temperatures above θ is probably required.

Another effect of temperature is to broaden the PL emission lines. For excitonic peaks this broadening is given by[128]

$$\Gamma(T) = \Gamma_0 + \gamma_{\mathrm{ph}} T + \frac{\Gamma_{\mathrm{LO}}}{\exp\left(\frac{\theta_{\mathrm{LO}}}{T}\right) - 1} \tag{3.19}$$

where Γ_0 is the inhomogeneous line width, γ_{ph} is the acoustic phonon coupling strength, and θ_{LO} is the LO-phonon temperature. For bulk ZnO the features are too close together in the 3.5-300 K temperature range for accurate analysis of the temperature dependence of the line shape. Deconvolution of the PL from bulk ZnO into its components using multi-peak fitting is also prevented by the close proximity of the many features. However, line shape analysis of the excitonic features can be carried out by means other than PL spectroscopy.[108]

Behavior of the phonon replicas with respect to temperature is different from the excitonic zero phonon lines. This region of the spectrum is shown in figure 3.15. For radiative recombination involving phonons, conservation of momentum can be fulfilled for excitons with $\mathbf{k} \neq 0$. According to Permogorov's theory,[129] the line shape of the m^{th} LO-phonon replica is given by

$$I_{\mathrm{m}}(E_{\mathrm{K}}) \propto E_{\mathrm{K}}^{\frac{1}{2}} \exp\left(\frac{E_{\mathrm{K}}}{k_{\mathrm{B}} T}\right) W_m(E_{\mathrm{K}}) \tag{3.20}$$

where $I_{\mathrm{m}}(E_{\mathrm{K}})$ is the emission intensity of the mth LO-replica of an exciton with kinetic energy E_{K}. $W_m(E_{\mathrm{K}})$ is the probability of exciton recombination via the mth LO-replica channel. It can be expressed as a power law given by $W_m(E_{\mathrm{K}}) \propto E_{\mathrm{K}}^L$ where L is 1 if the probability depends on E_{K} and 0 if not. This leads to a peak emission energy which described by[69]

$$E_{\mathrm{mLO}} = E_0 - m E_{\mathrm{LO}} + \left(L + \frac{1}{2}\right) k_{\mathrm{B}} T \tag{3.21}$$

where E_0 is the peak energy of the zero phonon line and E_{LO} is the LO-phonon energy. Theoretically[81,129] and experimentally[4,21,69,130] it has been shown that $L = 1$ for 1LO-replicas and $L = 0$ for 2LO-replicas. Inspection of the equation 3.20 using these L values shows that LO-replica peaks will broaden linearly with temperature, and that the integrated intensity ratio of the 1 and 2LO-replicas is also linearly dependent on the temperature.[81,129] The arrows in figure 3.15 indicating the LO-replica positions show the calculated positions using equation 3.21. Good agreement between calculated and observed peak energies are ob-

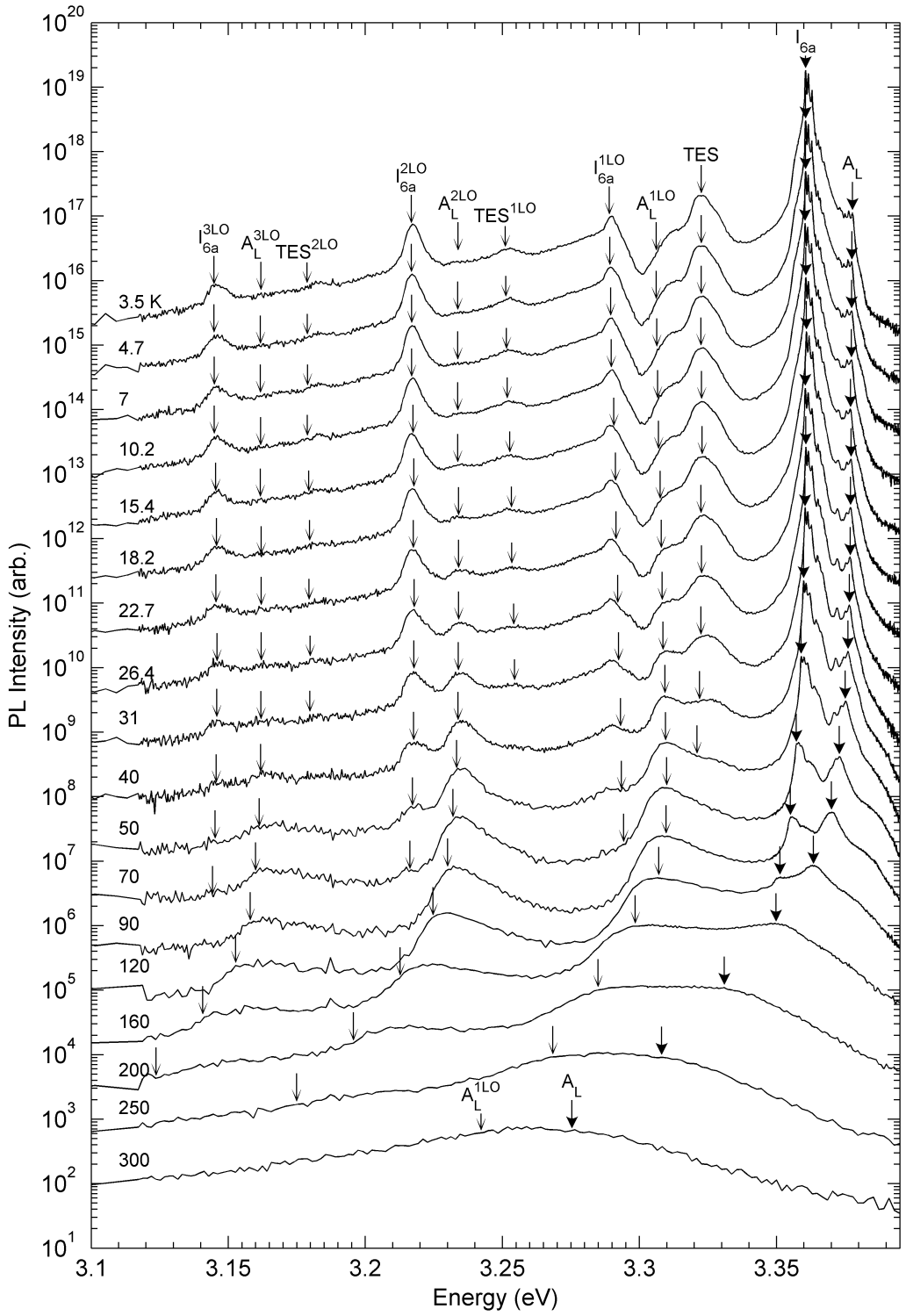

Figure 3.15: Temperature Dependent PL of the UV/violet region in hydrothermally grown bulk ZnO (offset vertically for clarity). Thin-headed arrows show calculated positions calculated from the measured peaks indicated with thick arrows.

tained with $L = 1$, 0, and 0 for $m = 1$, 2, and 3 respectively. This behavior with temperature can be used to identify LO-replica peaks and is further proof that the I_{6a}^{2LO} peak is not a DAP recombination. The TES transitions are also shown in figure 3.15 and they followed the temperature dependence of the D^0X peaks as expected. Arrows indicting the TES transitions were simply kept at a constant spacing from I_{6a} at each temperature. The LO-replicas from the TES transitions were also seen at the positions calculated using equation 3.21. Phonon replicas are intrinsic to the material and get stronger as the quality improves. They may help or hinder devices and either way understanding exciton-phonon interactions is an important step in developing optoelectronic technology.

Temperature dependence of the deep level emission is shown in figure 3.16. Intensity did not noticeably decay until the temperature reached 50 K. An Arrhenius plot is shown in the inset which gave an activation energy of 17 ± 1 meV. This is much smaller than the expected activation energies of 100 meV or greater for deep level defects. A redshift with increasing temperature was observed for the deep level emission which is consistent with free to bound peaks as they should follow the temperature dependence of the bandgap. However, accurate analysis of the deep level is not possible with the data shown in figure 3.16 due to the low signal level. The slit widths of the spectrometer for this temperature dependent PL experiment were 20 μm in order to resolve the excitonic features and avoid saturating the PMT. As a result the signal from the deep level emission was very low. There are many origins for the deep level emissions in ZnO[4,14,16,81], too many to be able to identify those which cause the emission shown in figure 3.16. Complementary experiments providing independent defect identification and/or manipulation would be necessary for meaningful analysis of the visible emission from wide-gap semiconductors.

The ratio of the UV to visible intensity is high in bulk ZnO samples. UV:visible ratios are sometimes used as a measure for the overall crystal quality of bulk, thin-films, and nanostructures of wide-gap semiconductors. However much care must be taken when comparing UV to visible intensity ratios between samples, especially when comparing to published values. Different experimental set-ups will have different optical responses across the entire spectrum. Some authors will correct their data but the fine details of the process are never discussed. The actual optical response of a typical PL system depends on the response of the detectors, the wavelength dependent efficiency of the diffraction grating, and the placement of the collection optics. Lens placement will significantly

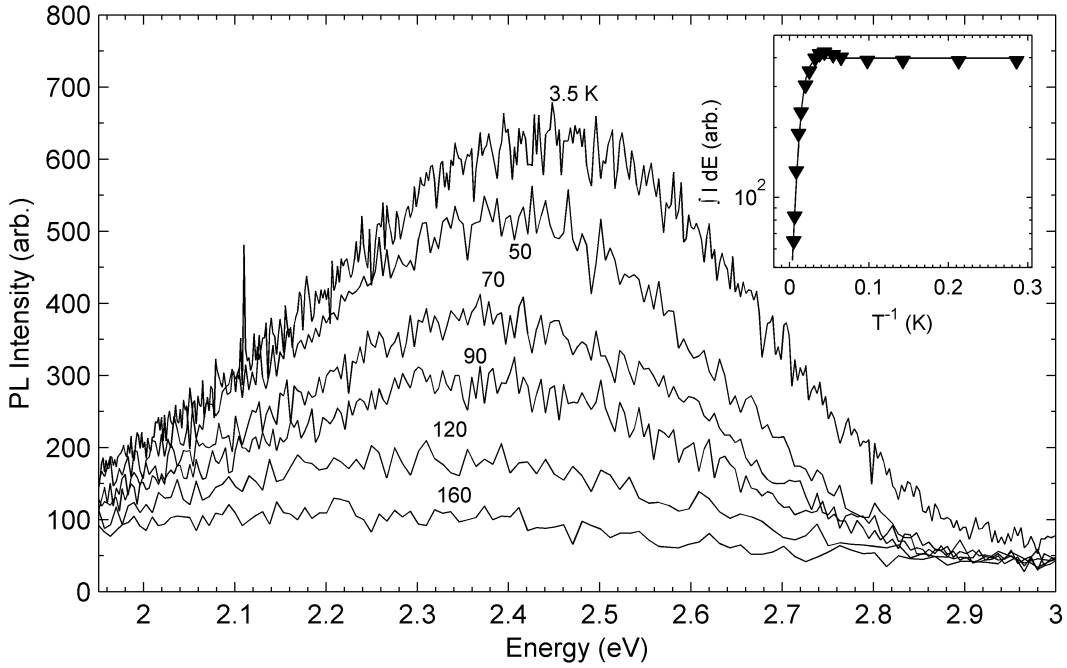

Figure 3.16: PL emission from the deep level as a function of temperature (shown above each spectra). An Arrhenius fit is shown in the inset.

effect the response due to the wavelength dependent focal length of the lenses. The set up shown in figure 3.2 was used for several different experiments, like most university graduate research labs. Lenses were removed and had to be repositioned for each experiment, meaning the optical response of the system was not consistent from day to day. For an accurate measure of the optical response of a system, a blackbody radiator with a known temperature must be placed at the sample location with the collection lenses in the experimental position. Unfortunately this was not practical and all the spectra presented in this thesis are uncorrected for the system's response. Thus, the UV to visible intensity ratios are not comparable from day to day for the set up shown in figure 3.2.

Comparison of intensity values or ratios is only possible for a group samples which have been placed in the cryostat in the same experimental run with the same lens placements. In this way, information about the relative crystal qualities of the sample group can be extracted but the actual values or ratios are meaningless. System response was not a problem for the band edge region since the system was optimized for UV emission and is essentially flat over short wavelength ranges. It does however significantly effect the shape of the deep level emission which spans more than 200 nm in a range where the system response is

not flat. This makes peak fitting of this region unreliable and further complicates the analysis of the deep levels.

Temperature dependent PL is one of the most useful extensions to the PL technique. It is also one of the easiest to implement in the lab. The main concern is to ensure the sample has enough time at a given temperature for thermal equilibrium to be reached. Emission intensity of a peak which is sensitive to temperature allows for an accurate determination of when thermal equilibrium has been reached. Decay and shift of the features can allow for confident identification of their origin. While this may not give information regarding the exact chemical or structural origin, temperature dependent PL can be used to identify the type of emission, i.e. separating the free excitons from D^0X and D^+X transitions or distinguishing between DAP recombination and LO-replicas. Simply relying on peak positions or spacings allows for tentative identification of PL features at best. Temperature dependent PL was used throughout this thesis and proved to be perhaps the most valuable extension to the standard low temperature PL experiment.

3.8 Excitation Intensity Dependence

Perhaps the easiest parameter to vary in a PL experiment is the laser intensity. By simply placing a filter with a known transmission curve in front of the laser, excitation intensity can be precisely varied over several orders of magnitude. Figure 3.10 shows the PL as a function of excitation intensity for the Zn face of hydrothermally grown ZnO. The spot size was roughly 0.3 mm^2 with the resulting unattenuated excitation intensity at the sample of about 7 $\mathrm{W/cm}^2$. Using a set of neutral density filters the laser power was attenuated over two and a half orders of magnitude down to 0.02 $\mathrm{W/cm}^2$. For this experiment the laser spot was in the exact same position of the same sample as the temperature dependent PL experiment discussed in the previous section. A temperature of 3.5 K was maintained throughout the experiment.

Using a set of coupled rate equations it can be shown the the PL emission intensity generally follows a power law $I \propto L^{\zeta}$ where L is the laser emission intensity.[131] The exponent ζ is related to the origin of the transition. For band to band transitions $\zeta = 2$ as the recombination probability of a free electron and hole is proportional to the product of the electron and hole concentrations.[117,131,132]

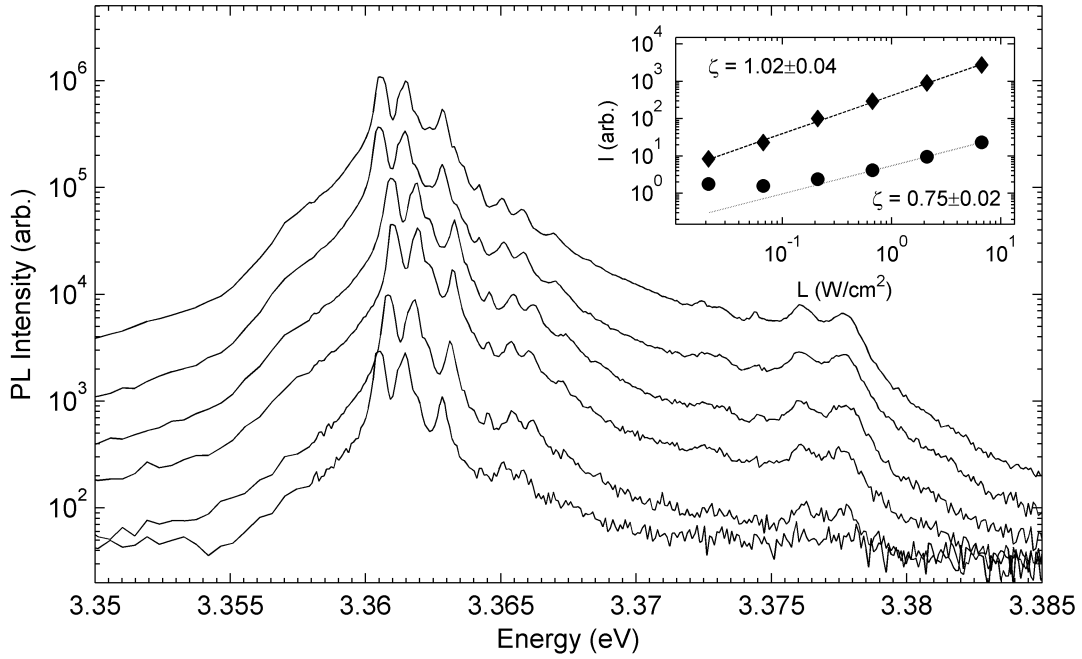

Figure 3.17: Power dependent PL of the excitonic region at 3.5 K. The integrated intensity of the D^0X peaks (diamonds) and the deep level emission (circles) is shown in the inset.

Excitonic features have $1 \leq \zeta \leq 2$ and for free to bound and DAP recombination $\zeta = 1$. The inset in figure 3.17 shows a log-log plot of the integrated emission intensity versus the excitation intensity for the UV and deep level emission in bulk ZnO. The relative intensity of all the excitonic features stayed roughly constant as laser intensity was varied. This means the measured ζ value applies to all the peaks in this region and deconvolution would not have given meaningful results. An exponent of $\zeta = 1.02 \pm 0.04$ was obtained when fitting a straight line to all 6 UV data points. Unfortunately this does not really say much about the origin of the emission. Exponents as high as 1.7 have been observed for donor and acceptor bound excitons in CdTe[131] and there is a large range of reported ζ values for the UV features in ZnO. ζ values ranging from 1.3 to about 1.8 have been observed and are dependent on the morphology and growth conditions.[117,133–135] A value of $\zeta = 0.75 \pm 0.02$ was observed for the deep level emission which is consistent with (defect-related) free to bound or DAP recombination. Only the 3 highest excitation intensities were used for the fit of the deep levels where the signal was still above the noise.

Figure 3.18 shows the power dependence of the blue/UV range covering the LO-phonon replica region. The absolute intensity of the I_{6a}^{2LO} peak is shown in

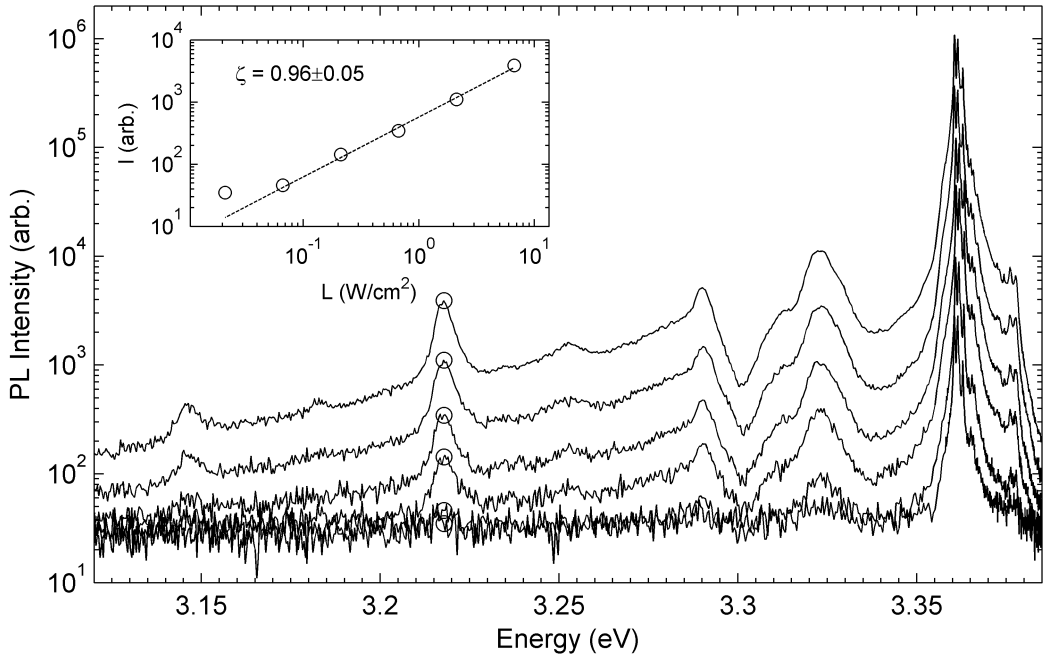

Figure 3.18: Power dependent PL of the phonon replica region. The absolute intensity of the I_{6a}^{2LO} peak is shown in the inset.

the inset. A value of $\zeta = 0.96 \pm 0.05$ was obtained for this peak which was higher than the 0.6-0.8 expected for DAP transitions.[115,131] This is further confirmation that this peak at about 3.2 eV is not a DAP recombination. Absolute intensity values were used here to reduce the error from integrating the baseline emission under the peak. No error is expected to be introduced in the extracted ζ value as the full width at half maximum (FWHM) stays constant with excitation intensity. Furthermore, DAP recombination is expected to blue shift with increasing excitation according to the relation[136]

$$L = D\frac{(h\nu_m - h\nu_\infty)^3}{h\nu_B + h\nu_\infty - 2h\nu_m}\exp\left(-\frac{2(h\nu_B - h\nu_\infty)}{h\nu_m - h\nu_\infty}\right) \tag{3.22}$$

where $h\nu_m$ is the maximum peak emission energy, $h\nu_\infty$ is the peak emission from an infinitely spaced pair ($h\nu_\infty = E_g - E_D - E_A$). $h\nu_B$ is a the emission energy from a pair with a separation equal to twice the Bohr radius of the shallow impurity, and D is a constant of proportionality. Blueshifting is a direct result of the decrease in the distance between the donor and acceptor of a pair with increasing excitation intensity. No blueshifting was seen for any peak with increasing excitation intensity in this bulk ZnO sample. Also, no redshifting or broadening was observed in any part of the spectrum meaning laser heating effects

were negligible at these low excitation intensities.

In the low excitation regime studied here, there was no significant interaction between the excitons or between excitons and photoexcited carriers. As laser intensity is increased, the exciton density also increases which can lead to optically pumped stimulated emission by several polariton scattering processes.[132] This has been observed in ZnO bulk, thin films and nanostructures in the kW/cm^2 to MW/cm^2 excitation intensity range.[35,132,133,137] At high enough excitation intensity, exciton density is so high their wavefunctions overlap. Emission under these conditions is is due to electron-hole plasma formation which is a collective state of all the optically excited carriers.[81] Stimulated emission can also be observed from electron-hole plasmas when the optical excitation is sufficiently high to invert the plasma.[132]

Unfortunately, for this bulk ZnO sample the power dependence did not reveal new information. When a value of $\zeta = 1$ is extracted from the data, there is nothing concrete that can be said about the origin of the emission peak. One of the reasons for the observed linear dependence may be the relatively low excitation intensities used for this experiment. The power law relation is usually only valid over about 2 orders of magnitude.[131] Spanning more than this results in a varying ζ value which gives curved log-log plots of emission versus excitation intensity. Actual laser intensities at the sample, along with the uncertainty, are not always reported. Intensities covered in various studies may be spanning different orders of magnitude leading to the large spread in reported ζ values. In summary, excitation intensity is another easily varied parameter which can reveal important aspects about the PL spectrum from a semiconductor. However, it must be coupled with other PL techniques before any solid conclusions about excitonic origins or dynamics can be made.

3.9 Simultaneous Above- and Below-Gap Excitation

Precise control over free carrier concentrations make semiconducting materials useful for electronic and optoelectronic devices. Imperfections, such as impurities or structural defects, are the source of the free carriers in semiconductors. More imperfections lead to higher carrier concentrations along with degraded structural quality. Mid-gap donor and acceptor states are also introduced by these imperfections, altering the materials electronic structure. As such, free carrier

concentration and PL are intimately linked. Mid-gap states can be optically active and these centers bind the excitons, producing complex PL spectra with many sharp features. PL emission intensity is dependent on the structural quality and purity of the crystal so the intensity will usually decay with increasing carrier concentration. bandgap energy can also be dependent on the free carrier concentration, producing an observable Moss-Burstein blueshift when the Fermi level gets pushed into the conduction band.[138] Redshifting can be induced by high carrier concentrations due to many-body effects which renormalize the bandgap.[132,139] Emission energies of the various types of processes comprising PL emission in semiconductors are all sensitive to these changes in the bandgap. Dependence of the PL emission peaks on the free carrier concentration can prove quite useful for understanding more about their origins.

Free carriers also have a profound effect on the excitonic relaxation and emission processes. In semiconductors, the Coulomb interaction between the electron and the hole gets screened by the presence of free carriers, reducing its strength.[139] Exciton binding energy gets reduced because of this screening and the result is a blueshift in the free excitonic emission. Exciton localization energies also get reduced because of this screening and bound excitonic emission energies will blueshift even further. Reynolds et al.[140] showed that the bandgap renormalization is the dominant effect in bulk ZnO by observing a redshift in the excitonic features with increasing carrier concentration. No such effect was observed for the bulk-like GaN in that study. Another result by Reynolds, published on the same data a year later,[92] showed that screening of the excitons from the binding centers resulted in an increase in free exciton and polariton emission intensities and a decrease in the D^0X transition. This was attributed to a lower probability for exciton capture by a trapping defect, giving the free excitons more time to radiatively recombine.

Free carrier concentrations in the studies by Reynolds[92,140] were controlled by an Ar^+ ion laser providing below-gap excitation (BGE) at 514.5 nm (2.407 eV). For BGE, electrons get excited across the bandgap by a two step process involving two photons. A mid-gap defect state is necessary for this process to occur, providing a stepping stone across the gap. At minimum, the BGE energy needs to be half of the bandgap and will be more efficient for higher energies. Because two-photon absorption involves an intermediate state, the photoexcited electron-hole pair will have a small probability of forming an exciton. Thus, BGE will not contribute to the excitonic PL emission, allowing for a truly separate pump

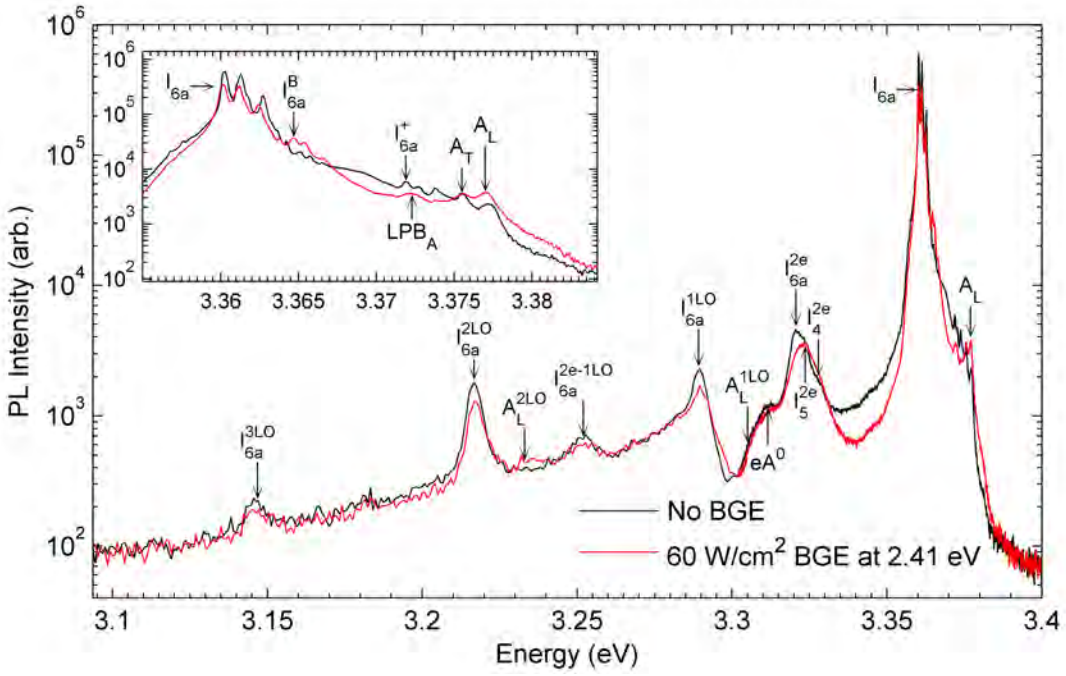

Figure 3.19: Low temperature PL emission from bulk ZnO simultaneously excited with 3 W/cm^2 of 3.815 eV photons and 60 W/cm^2 of 2.408 eV photons.

and probe beam. BGE provides a highly reliable source of free carriers for a semiconductor without modifying its physical or electronic structure or raising its temperature significantly. In fact, BGE is the only way to carry out controlled experiments which probe the dependence of the low temperature PL emission, for a single sample location, on the free carrier concentration.

Figure 3.19 shows the PL emission from a spot on the hydrothermally grown bulk ZnO with and without BGE. For this experiment, the above-gap excitation was provided by the 325 nm He-Cd laser line at an intensity of about 3 W/cm^2. BGE was done with the 514.5 nm (2.407 eV) line of an Ar^+ laser, focused to a slightly larger spot at an intensity of 60 W/cm^2. Angle of incidence for both lasers was comparable, both around 35-45° from the normal. For a significant effect, a much higher intensity than than used by Reynolds et al.[92,140] was needed for this sample. As mentioned earlier, BGE forms free carriers via a mid gap defect state. In the 7 years since the Reynolds publications, significant improvement has been made in the quality of the commercially available ZnO crystals. Background carrier concentrations have dropped significantly which has been accompanied by an increase in the PL efficiencies and a decrease in the line widths. This is easily seen by noting D^0X emission in the sample studied by Reynolds et al.[92,140] was

much broader than the bulk spectra presented throughout this chapter. Thus, higher BGE intensities were need to produce sufficient free carrier concentrations due to the smaller concentration of mid-gap states in these more recently grown samples. No PL emission was detected from the ZnO under BGE without the above-gap excitation as well. The data around 3.1 and 3.4 eV shows that there was no background introduced by the Ar^+ laser in this region of the spectrum.

Simultaneous BGE at $60\,W/cm^2$ resulted in a striking effect on the NBE emission as shown in the inset of figure 3.19. The I_4, I_5, and I_{6a} intensities were quenched by about 45% while the A_L emission increased by about 60%. Emission from the A_T peak was essentially uneffected by the laser. This is in contrast to Reynolds et al.[92] who observed an increase in both the *A*-excitonic peaks. Furthermore, a much smaller redshifting was observed in the sample studies here and was just barely measurable. Differences in the overall crystal quality may be the reason for such discrepancies and effects which were washed out in older samples can now observed in more recently grown bulk ZnO. Differences in the intrinsic behavior of the two samples could also be the cause as vapor transport was used to grow the bulk in the Reynolds studies. LPB_A emission from the recent Tokyo Denpa material can be clearly seen with BGE since the D^+X peaks were efficiently quenched by the laser. The shallow donors binding the $D^{0,+}X$ transitions did not get photoionized by the below-gap photons and any ionized donors will have been photoneutralized by the carriers excited by the below-gap photons. Reynolds et al.[92] used an increase in the LPB_A peak intensity with BGE to identify it as a polariton mode. In this sample LPB_A intensity may have increased but the background from the ionized donors hides this. These ionized donors were not present in the studies by Reynolds et al.[92,140] since the dominant donors in hydrothermal and vapor transport material are different.

Unexpected behavior was observed from the *B*-excitons bound to the neutral donors. An increase in intensity by nearly 80% was observed for the *B*-bound excitons compared to the 45% decrease of the *A*-bound excitons. This shows that the two sets of emission peaks are indeed from fundamentally different origins. No mention of the *B*-excitons was made by Reynold et al.[92,140] and effects from the holes generated by BGE were not accounted for due to their small lifetime. However, the difference in the behavior of the bound *A*- and *B*-excitons indicates the screening process does depend on the hole as they determine the flavor of the exciton. Exactly why the bound *B*-excitons show an increase in emission with increasing free carrier concentration is unknown at this time. Emission

from the B_{T} region also increases but this is overlapped by emission from UPB_A. An increase in free B-excitons could account for the large increase in the I_x^{B} emissions if screening effects on the A and B-excitons are significantly different. More investigation is needed on this phenomena which will require some intutitive experimentation for solid answers.

At lower emission energies the dependence of the features generally followed the behavior of their principal recombination counterparts. Emission intensities of the LO-replicas of the $I_{6\mathrm{a}}$ peak were quenched by the same factor as $I_{6\mathrm{a}}$ was, further strengthening their connection and adding more evidence that the $I_{6\mathrm{a}}^{2LO}$ peak is not a DAP recombination. Under BGE the A_{L}^{2LO} peak was observed but the A_{L}^{1LO} peak was unresolvable, presumably due to the nearby Fano resonance of $I_{6\mathrm{a}}$. Some strange behavior was observed for the TES transitions, which did not quench uniformly and may be suggesting the presence of a background defect related peak. The eA^0 transition due to stacking faults, at energies just below the TES emissions, did not quench with BGE. This would be expected for eA^0 transitions where the limiting factor is a low acceptor concentration. In this case increasing the free electron concentration will not effect the emission intensity. Such a peak may be lying underneath the TES emissions. In the worst case, this behavior shows the supposed TES peaks are from a different origin and perhaps the Haynes plots with $\eta \approx 0.3$, which so many groups have come to rely on, are incorrect. An in-depth theoretical treatment of TES transitions and how they interact with free carriers would prove useful for this study and may uncover some interesting phenomena. The dramatic quenching of the background seen on the high energy side of the TES transitions could also reveal fundamental information about the impurities and defects with very low concentrations.

Like the temperature and intensity excitation dependencies, the effects of free carriers induced by BGE can be used to separate and identify features in the PL spectrum of light emitting semiconductors. The work presented throughout this chapter has been focused on bulk ZnO, which has been extensively studied for years. However, with each passing year, the material properties change and the scientific community must keep up with the times. This work fills a much needed hole in the literature about the properties of the high-quality materials being prepared today. There simply has not been a report showing the PL dependence of temperature, excitation intensity, and free carrier concentration on the modern hydrothermally grown ZnO. All the information gathered in this chapter proved invaluable for the analysis presented in the next three, particularly for chapter 6

which shows the PL behavior of this same wafer after ion-implantation of Pb. Detailed PL experiments can provide valuable information to crystal growers and provide interesting platforms for investigating the fundamental physics of light-matter interactions.

Chapter 4

EPLD Growth of Nanostructured ZnO on *c*-axis Sapphire

4.1 Shadow Mask Placement and Oxygen Pressure

Pulsed laser deposition is a growth technique with a long list of process parameters. Laser fluence F, spot size on the target A_S, wavelength λ, pulse width τ_L, and pulse repetition rate R_L will all effect the plume characteristics. Background gas partial pressures, gas flow rates, and target-to-substrate distance d_{TS} are also important in PLD and have an impact on stoichiometry and growth rates. While the highly energetic nature of PLD allows for deposition onto substrates at room temperature, significant improvement in material quality can be achieved by heating the substrates before, during, and even after the growth. Ball park estimates for the appropriate parameter ranges can be obtained for a given material but optimization of the growth conditions requires controlled experiments. For oxide growth, usually the O_2 pressure or substrate temperature is varied while the other deposition parameters are held constant.[1,56,59,61,62] To truly optimize the growth conditions for a given application, several such controlled experiments covering a wide parameter space are necessary.

Eclipse PLD adds even more parameters to the mix. Shadow mask size, shape, and position will have a considerable impact on the deposition. This section discusses the combined effect of shadow mask position and oxygen pressure on the EPLD growth of ZnO from a metallic Zn target. These parameters were chosen since they have the most influence on the diffusion of material around the mask. A series of ten ZnO samples were produced with one reference sample grown by standard PLD and nine by EPLD. A $(16 \times 16)\,\mathrm{mm}^2$ square shadow mask made from stainless steel was placed at three positions relative to the substrate.

Target-to-substrate separation, d_{TS}, was 53 mm with the shadow masks placed at 17, 25, and 33 mm corresponding to $\frac{1}{3}d_{\mathrm{TS}}$, $\frac{1}{2}d_{\mathrm{TS}}$, and $\frac{2}{3}d_{\mathrm{TS}}$. At each mask position three samples were grown at O_2 partial pressures of 100, 150, and 200 mTorr. The reference PLD sample was grown at 100 mTorr. High-quality nanostructures with a novel morphology were produced which showed interesting and potentially useful optical properties. Some of these results has already been published[1,2] but more detail is included here.

4.1.1 Growth and Morphology

ZnO is typically grown on *c*-axis sapphire as it has hexagonal structure and is readily available. It was used for growth of all the (E)PLD grown samples discussed in this thesis. There is roughly an 18% in-plane lattice mismatch between the sapphire and ZnO *c*-planes which usually leads to a high density of dislocations in the deposited ZnO.[4] Before growth the substrates were ultrasonically cleaned in a three step process. They were first sonicated for 10 minutes in trichloroehylene followed by 10 minutes in acetone and then 10 minutes in methanol. Dry N_2 gas was used to quickly dry the substrates after the methanol step.

The substrates were then mounted onto the heater block using silver paste. First, the substrates were heated to 300 °C at 5 °C/min in air to set the silver paste. The chamber was then evacuated to 5×10^{-6} Torr base pressure while the substrate temperature was ramped up at 20 °C/min. Before growth, the substrates were held at 700 °C for 1 h to outgas and thermally clean the surface. Temperature was then ramped down to 600 °C for the growths. Once the growth temperature was reached the oxygen partial pressure was raised to the growth value. Unfortunately, the HV chamber was not equipped with a gas flow controller. Assuming the pressure gauge and turbopump operate consistently, flow rates could be approximately reproduced by having a set current in the turbopump current for a given pressure. This required a balance of the O_2 flow, controlled by the leak vale, and the pumping efficiency which was controlled by the gate valve between the pump and chamber. After deposition the samples were held at the growth temperature for roughly 10 minutes before ramping the temperature down at 20 °C/min.

Laser fluence for all growths was 4 J/cm^2 with a spot size on the target of about 1.5 mm^2. A single 99.995% Zn metallic target from the Kurt J. Lesker Corporation was used for all growths. No target resurfacing was attempted since impurities

can be incorporated into the deposited samples from the target resurfacing step.[62] Normally a fresh target face is used for PLD as the particulate generation is minimum. However, as the growth proceeds the fresh target surface changes drastically. The last laser pulse sees a much more deteriorated surface than the first pulse, adversely affecting the stability of the plume conditions.

As a sputter target gets hit with more and more laser pulses, the surface will roughen and cone shaped features pointing in the direction of the incoming laser beam will appear.[53] Once these cones are formed successive laser pulses can break the tips off and send them toward the substrate. They are then reshaped into cones which are broken off again etc etc. After a while the surface will show essentially the same cone morphology to every laser pulse. Despite the high particulate generation, a well used surface will actually give a more consistent plume from laser pulse to laser pulse. The EPLD technique provides a way to effectively reduce the particulate incorporation into the samples so the consistency of a plume from a well used target can be taken advantage of.

Figure 4.1 shows SEM images of the reference sample grown without a shadow mask. A random array of nanorods was formed on the sapphire surface with good alignment perpendicular to the substrate. It can be seen in the top down images that the nanorods had an irregular hexagonal cross-section. This indicates growth was along the *c*-axis as expected for ZnO growth onto *c*-axis sapphire.[4,141,142] Cross-sectional SEM images are shown in figure 4.1(g) and (h) and were taken by cleaving the sample in air along an in-plane sapphire lattice direction. Rod lengths of 900 nm were attained after a 2 h growth using 72,000 laser pulses at $R_{\mathrm{L}} = 10\,\mathrm{Hz}$. This gave a growth rate of 0.125 Å/pulse (7.5 nm/min). Diameter of the rods at the base were 200 nm and tapered down to about 50 nm at the tips. The resulting density of rods was about 65 rods/$\mu\mathrm{m}^2$ which was uniform across the sample. Some rods have grown at random angles out of the substrate and collided with their neighbors during growth. From the SEM cross-sections it can be seen that the length of these rods was roughly the same as the non-tilted rods. Different crystal directions grow at different rates,[143] which implies that the tilted rods have also grown along their *c*-axis.

Despite the lack of a shadow mask, the surface of the reference PLD sample was relatively unparticulated over areas larger than 500 $\mu\mathrm{m}^2$. Nanorods grew off of the jagged, micron-sized particulates as seen in figure 4.1(d). The jagged nature of these particulates suggests they originate from large solid target fragments from a rough, well used surface. This sample was the first one grown with the

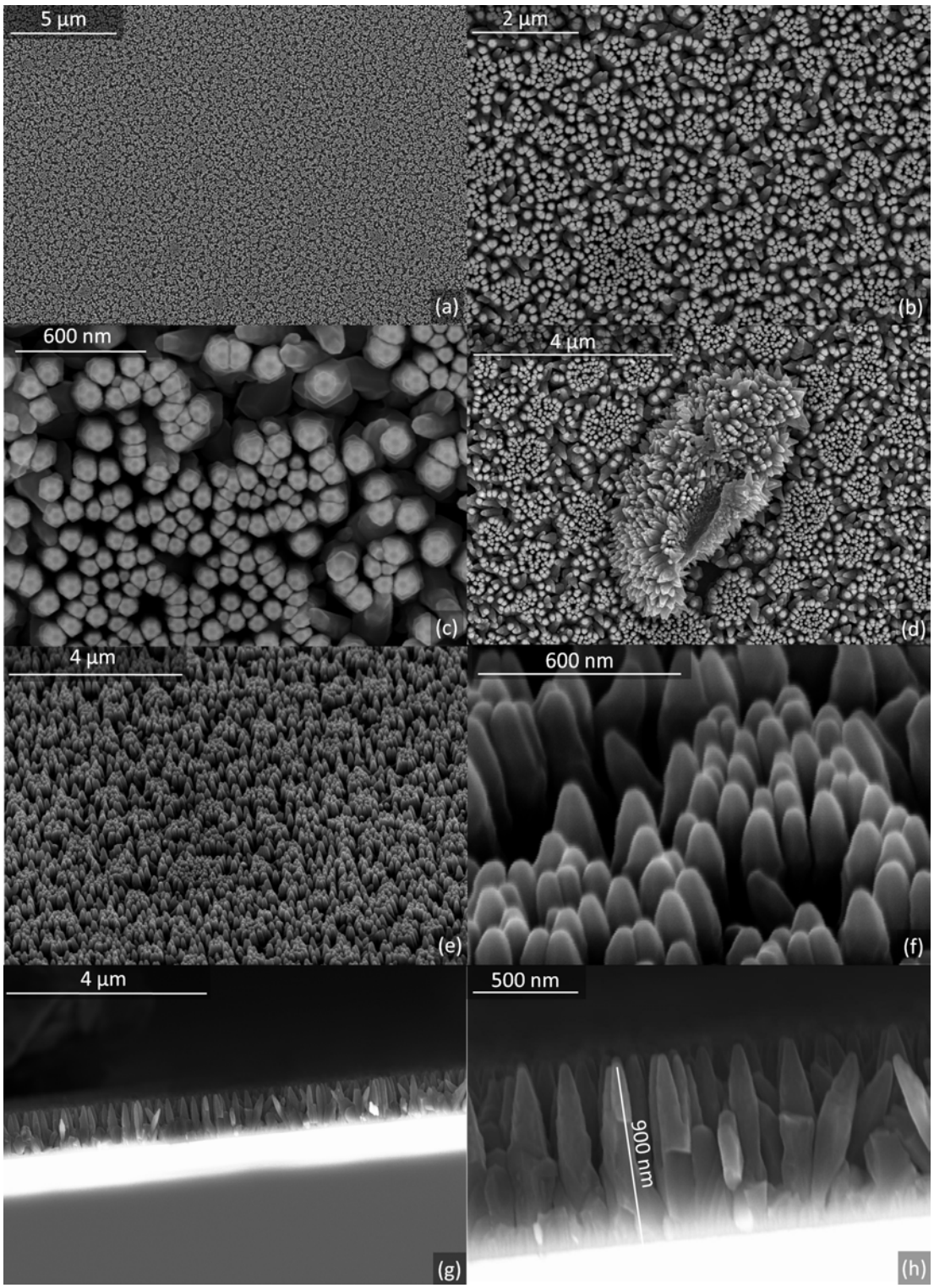

Figure 4.1: SEM images of ZnO nanorods grown by standard PLD. Top down images are shown in (a)-(c) with a particulate shown in (d). Tilt images at 45° are shown in (e) and (f) with cross-sectional images shown in (g) and (h)

new Zn target, showing significant target deterioration occurred during the first growth.

Figures 4.2, 4.3, and 4.4 show the morphology of the 9 EPLD grown samples as a function of O_2 pressure and shadow mask position. Nanostructured surfaces with a complex morphology were observed for all the samples. The structures clumped together into micron sized regions where irregularly shaped nanorods were formed. Cross-sectional SEM of one of these clumps in figure 4.4(a) shows that the rods grew to about 200 nm tall and did not taper significantly. A vapor-solid (VS) growth mechanism can account for this and leads to the observed lack of a capping particle.[65] Many of the rods in these micro-clumps grew at an angle and did not point straight out of the substrate. These angled rods appear to be growing along crystallographic directions of the substrate since they were preferentially pointing in 3 directions separated by 120°. This effect was most pronounced in the sample grown with the mask placed at 17 mm, as best seen in figure 4.4(b).

In between the micro-clumps the samples were covered with structures showing characteristics of a vapor-liquid-solid (VLS) growth mechanism. Figure 4.4(c) shows a tilted SEM image of a 6-sided pyramid with a base width of about 200 nm. A similar structure was seen in the top down image in figure 4.4(d). These structures were formed by growth starting from a liquid Zn droplet on the surface of the substrate. Since the substrate temperature of 600 °C was higher than the melting point of Zn (420 °C), nanometer sized liquid Zn droplets will have formed on the surface.[65] These droplets fed the nanohexamid growth by solidifying at the base while absorbing the vapors from the plume. Since these droplets were Zn, they were easily incorporated into the nanohexamid as it grew. Due to the low growth rate per pulse, the material of the droplet crystallized faster than new adatoms were being absorbed. This reduced the radius of the liquid drop as growth continued, leading to the pronounced tapering and pyramidal shape. On top of the nanohexamids were obvious capping particles with diameters around 50 nm. These remnants of the Zn droplets crystallized after the last laser pulse and are intrinsic characteristics of VLS growth.

Appearance of both VS and VLS grown structures suggests a complex growth mechanism for EPLD of ZnO onto sapphire. VS structures will form off of solid ZnO nanocrystallites formed in the initial growth stages.[144] This was facilitated by the low growth rate which gave the adatoms time and space enough to diffuse around the hot substrate and crystallize into micron sized regions. Nanorods

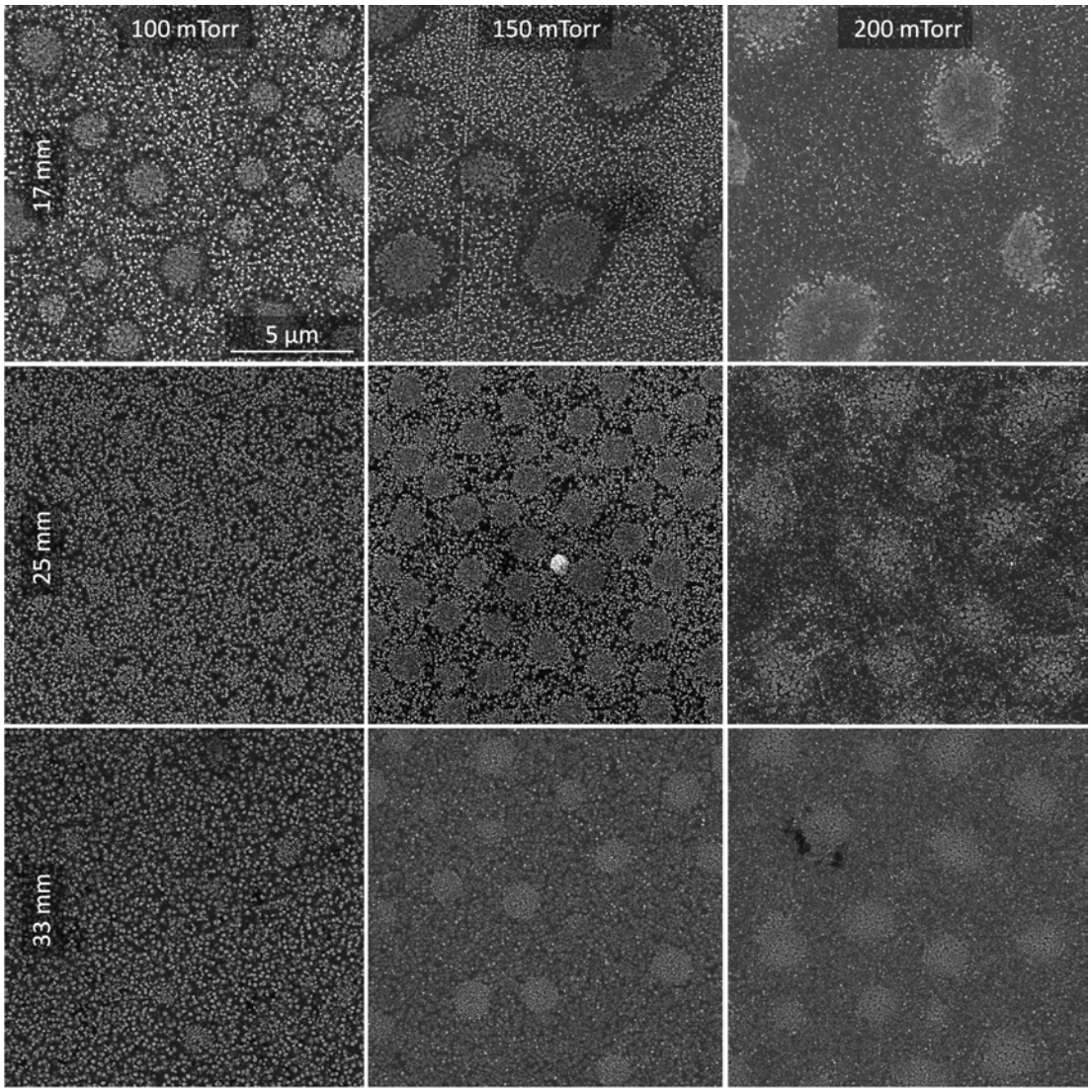

Figure 4.2: SEM images of ZnO nanostructures grown by EPLD. Oxygen partial pressure is shown along the top and shadow mask distance from target is shown along the right.

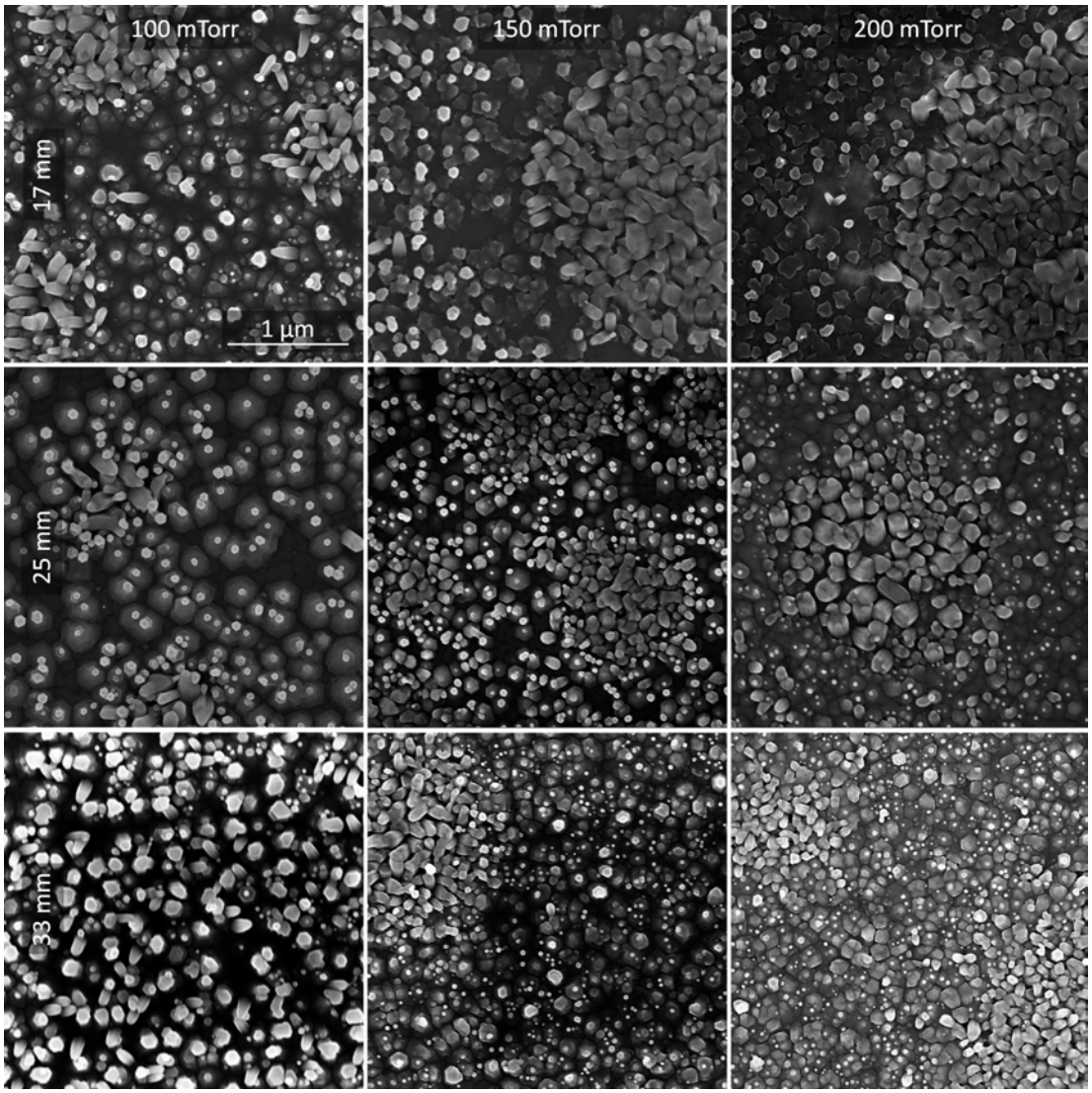

Figure 4.3: High magnification SEM images of ZnO nanostructures grown by EPLD. Oxygen partial pressure is shown along the top and shadow mask distance from target is shown along the right.

then formed on top of these solid crystallites by a VS mechanism. However, PLD using a Zn metallic target is expected to give Zn rich growth conditions under most circumstances. The extra Zn in the initial stages can gather into nanometer sized molten drops which do not immediately oxidize. These drops do not move around on the surface due to surface tension. Instead, VLS growth will proceed from the molten Zn drop resulting in the observed nanohexamid formation in between the VS grown micro-clumps. In the standard PLD case, the growth was heavily Zn rich so the substrate was covered in molten Zn droplets with minimal ZnO crystal nucleation. Nanorods then grew solely by a VLS process. Since the growth rate is much higher for PLD than for EPLD, new material was incorporated into the droplet nearly as fast as it crystallized. This led to the micron sized rods with gradual tapering. No obvious capping particles were observed on the standard PLD grown nanorods but sometimes this requires use of a TEM with high resolution.[65]

By carefully inspecting the surfaces in the top down SEM images, it can be seen that increasing the oxygen pressure for a given shadow mask position gave a higher growth rate. At 100 mTorr the structures in between the micro-clumps were well separated from each other. As O_2 pressure was increased to 150 mTorr the density of the structures increased and the bases began to connect. By 200 mTorr the regions between the clumps showed a highly structured yet continuous surface. The micro-clumps also appeared to have gained more material as O_2 pressure was increased. This observed increase in growth rate was due to enhanced diffusion of material around the shadow mask by the higher background gas pressure. Effect of shadow mask placement on growth rates can also be seen in figures 4.2 and 4.3. Adatoms will have the easiest time getting around the shadow mask when it is placed half way between the target and substrate. Samples grown with the mask at half way had the highest growth rate. This was seen by noting that these samples had the highest density of micro-clumps and connected nanohexamids at a given oxygen O_2 pressure.

Particulate elimination was the main reason for the introduction of a shadow mask for growth by PLD. In this experiment the particulate density was relatively low to begin with and few particulates were seen in the shadowed regions of the samples. However, collisions between the large particulates can lead to particulate deposition in the shadowed region. Figures 4.4(e)-(g) show SEM images of particulates located at the edge of the samples, which were still inside the shadowed region but close to the edge. These particulates originated from solid fragments

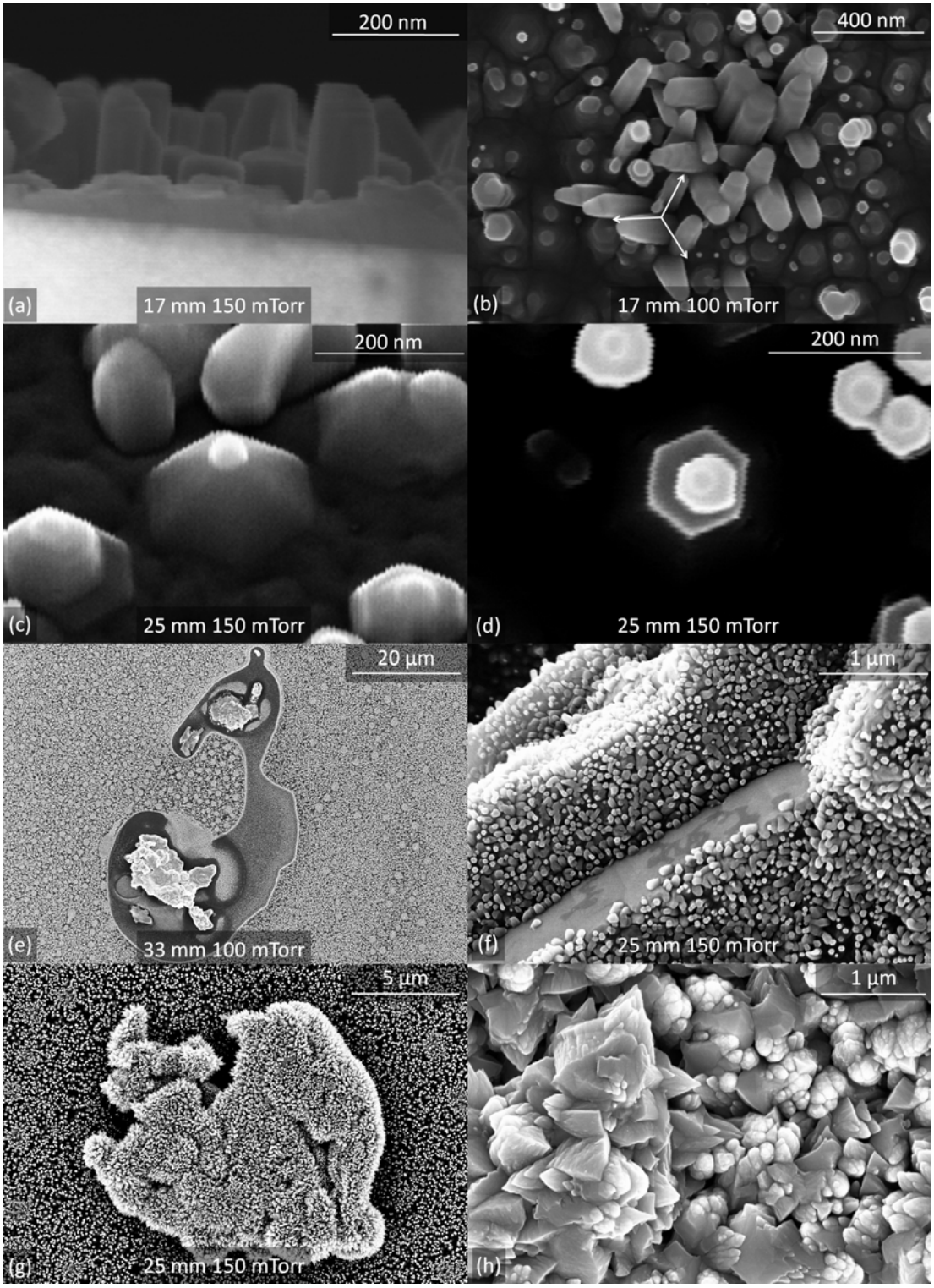

Figure 4.4: Various SEM images of ZnO nanostructures grown by EPLD: (a) cross-section of a micro-clump of nanorods, (b) micro-clump of angled nanorods, (c) titled SEM image of a ZnO nanohexamid, (d) top down image of a nanohexamid, (e) particulate alien, (f) nanorods grown on a large Zn particulate, (g) Zn particulate coated in nanorods, and (h) growth on the shadow mask from the side facing the target.

of the target which were dislodged by the laser and carried to the substrate with the expanding plume. Nanorod formation could clearly be seen on the surface of the large jagged particulates. Figure 4.4(f) shows a large Zn particulate which was covered in short nanorods except for one crystal face which looked perfectly clean. Apparently the laser cleaved a nearly perfect crystal face in the particulate which the adatoms could not stick to.

EPLD of oxides using metallic targets is a cost effective way to produce unusual morphologies for small scale applications. These complex nanostructured surfaces have a high surface area which is an advantage for chemical sensing applications. Innovative ideas can also increase the value of the technique. Figure 4.4(h) shows the material which was collected on the side of the shadow mask facing the plume. A highly textured surface was seen which was the result of an extremely high growth rate and particulate incorporation. Finding a use for this material would decrease wasted resources and extend the application of this technique. The side of the mask facing the substrate also gets a deposit but at a significantly reduced rate. Using substrates as shadow masks is a way to add value to the EPLD technique in a simple and economical way.

4.1.2 Temperature Dependent PL

All ten samples in this series showed PL spectra characteristic of heteroepitaxial ZnO. Figure 4.5 shows the low temperature PL (3.6 K) from the PLD grown sample along with the three EPLD grown samples deposited at an O_2 pressure of 150 mTorr. The inset shows the near band edge region of the sample grown with the mask at 33 mm. Peak assignments in the figure were based on positions and the temperature and power dependence of the emission. Figure 4.6 shows the temperature dependence of the reference sample grown by standard PLD. A free excitonic peak with an energy of 3.378 eV at 15 K dominated the spectrum at high temperatures. It is labeled as the transverse A-exciton (A_T) for reasons discussed further along but was likely the superposition of the A_T and A_L peaks. Arrhenius fitting using equation 3.13 was not possible for this data as background laser scatter was inconsistent and became an issue as temperature was raised.

On the other hand, fitting of the position of the A_T emission using the modified Manoogian equation (equation 3.17) was successful and is shown in figure 4.7. Data points from 3.6 and 300 K were added to the fit from other experimental runs. The parameters fitted using equation 3.17 are shown in the figure along

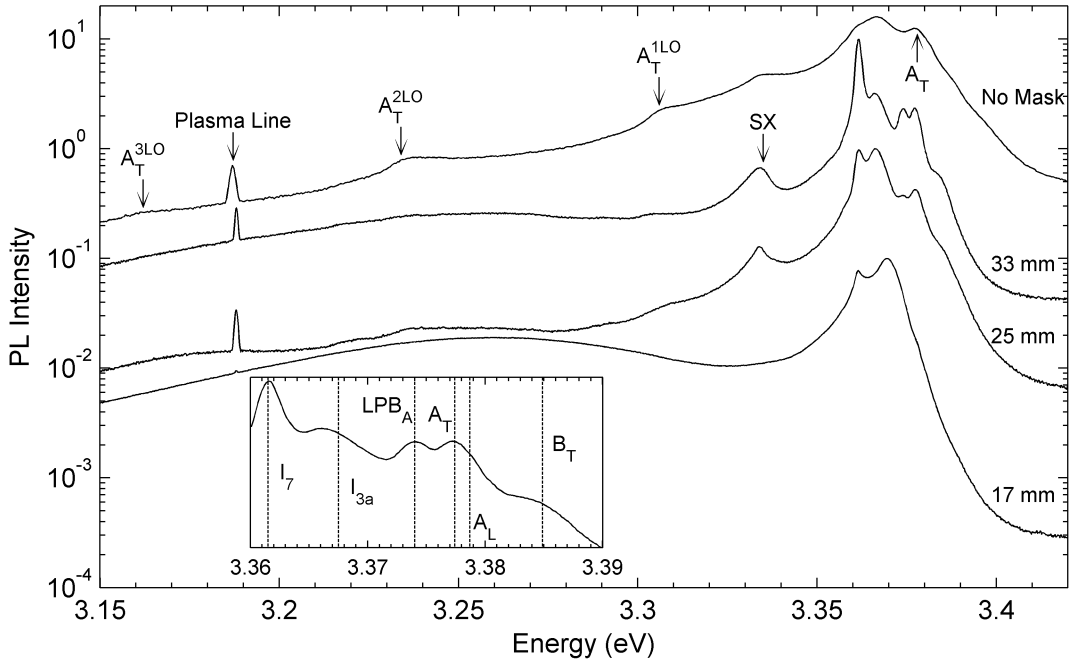

Figure 4.5: PL spectra taken at 3.6 K from the reference sample grown by standard PLD and the three EPLD samples grown at 150 mTorr (offset vertically for clarity). Inset shows the NBE region of the [150 mTorr, 33 mm] sample.

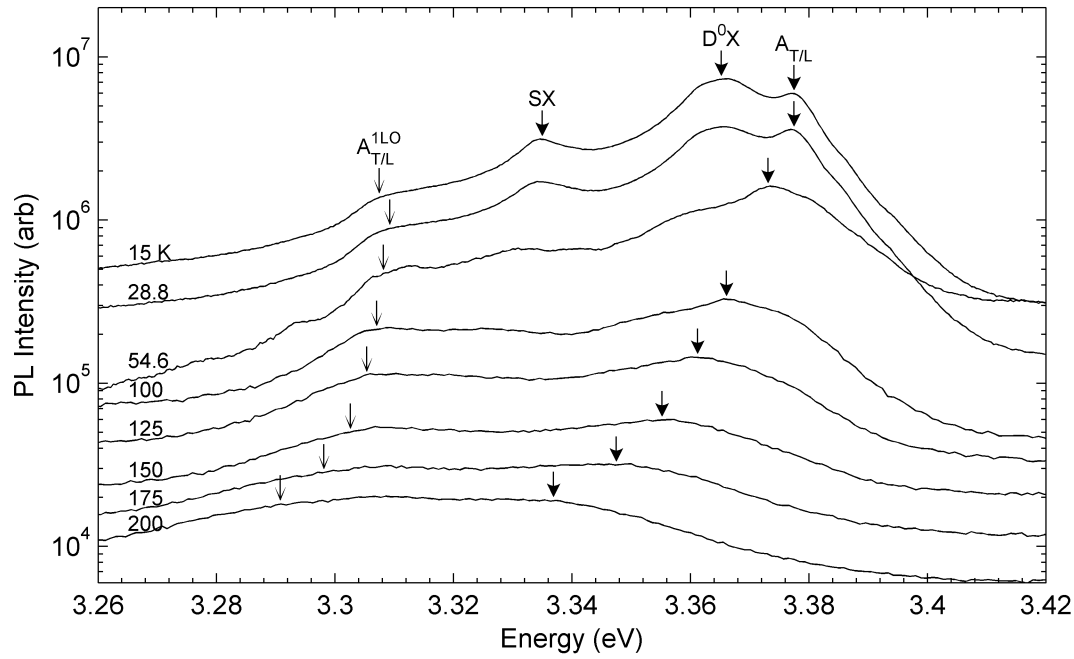

Figure 4.6: Temperature dependent PL from ZnO nanorods grown by standard PLD (offset vertically for clarity). Temperature in Kelvin is indicated above each spectra on the left. The lowest temperature data for this particular experimental run was unfortunately lost.

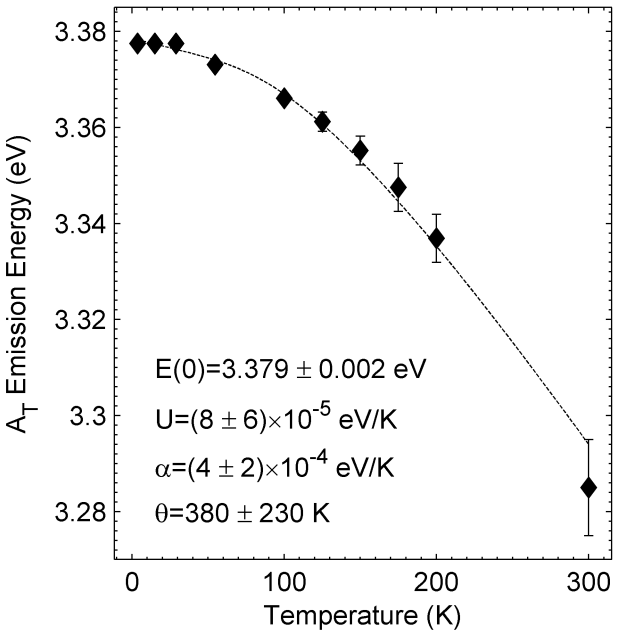

Figure 4.7: Position of the free excitonic peak in PLD grown ZnO as a function of temperature. The line is a fit to the data using equation 3.17 (page 44) with the fitted constants and 95% confidence bounds shown in the figure.

with the 95% confidence bounds. These values all agree well with the values for the free excitonic peaks in the bulk sample as listed in table 3.3 (page 46). Two LO-phonon replicas from the A_{T} peak are observed in figure 4.5 which were spaced 72 meV apart. The arrows marking the $A_{\mathrm{T}}^{1\mathrm{LO}}$ peak in figure 4.6 were calculated with equation 3.21 (page 47) with $L = 1$ using the measured A_{T} positions. This confirms the origin of the peak as $A_{\mathrm{T}}^{1\mathrm{LO}}$. Also in this region a peak around 3.335 meV was observed in the PLD grown sample and is marked SX in figures 4.5 and 4.6. Reports indicate SX is an exciton bound to dislocation loops as revealed by the spotty, localized nature of its cathodoluminescence.[11,16]

Emission from D^0X transitions dominated the PL of all the samples at low temperature. For the PLD reference sample, the line width of the D^0X emissions were too broad to resolve individual excitonic peaks. This D^0X band decayed quickly with temperature and was unresolvable by 100 K. For the EPLD grown samples, the line widths were, in general, significantly narrower than those of the PLD grown reference. A close up of the D^0X region of the [150 mTorr, 33 mm] sample is shown in the inset of figure 4.5. This sample showed some of the sharpest emission out of all the samples. The lines shown in the inset are the reported free and bound exciton positions by Meyer et al.[16] with the B_T position

taken from Syrbu et al.[24] These lines have been blue shifted by about 2 meV from reported values to line up with the data. This blue shift may be due to internal strain in the sample and/or calibration issues on absolute peak positions. Strain will effect the free and donor bound exciton energies the same,[145] and applying a constant shift is valid over the region shown in the inset of figure 4.5.

The assignments of these excitonic peaks were based on the temperature dependent PL, which is shown for the [100 mTorr, 33 mm] sample in figure 4.8. As temperature increased, the intensity of the bound excitons decayed quickly and by 75 K the free excitonic peaks dominated the spectrum. Like the bulk sample discussed in section 3.7, the LPB_A peak persisted at much higher temperatures than would be expected for an ionized donor bound exciton. Figure 4.9(a) shows an Arrhenius plot of the absolute peak intensities. Solid lines show the weighted least squares fits to the one path Arrhenius equation (3.11). Fitted activation energies along with the 95% confidence bounds are shown below each trace. All fit paramters and the χ^2_{R} values are shown in table 4.1.

Since no uncertainty in the photon counts was measured during the PL experiment, data was weighted for the fit by using $\sqrt{I(T)}$ for the uncertainties. This assumes repeated measurements of photon counts at a single wavelength would follow a Poisson distribution. Poisson distributions describe the spread of results when repeatedly counting a randomly occurring physical phenomenon with a definite average rate over a set period of time.[126] One common example is radioactive decay. Continuous wave PL experiments fit into this category when the data is taken with a PMT in photon counting mode. Experimentally this requires the fluctuations in the excitation laser power to be small. Also, since the data covers a few orders of magnitude, unweighted least squares fitting would have put significantly more emphasis on the high intensity points at low temperature. This would become a problem for extracting activation energies as the high temperature data is more important for extracting a reliable value. Weighting the fit using $\sqrt{I(T)}$ effectively balances Arrhenius fits of thermally activated PL quenching.

An activation energy of 19.4 ± 0.8 meV was obtained for the A_{T} peak using equation 3.11. This was considerably smaller than the 60 meV exciton binding energy which is supposed to be comparable to the activation energy. However, to accurately estimate the activation energy the temperature of the experiment should be raised above $E_{\mathrm{a}}/k_{\mathrm{B}}$, which is greater than 700 K for A_{T}. Also, the absolute intensities were used for the fits which do not take into account the

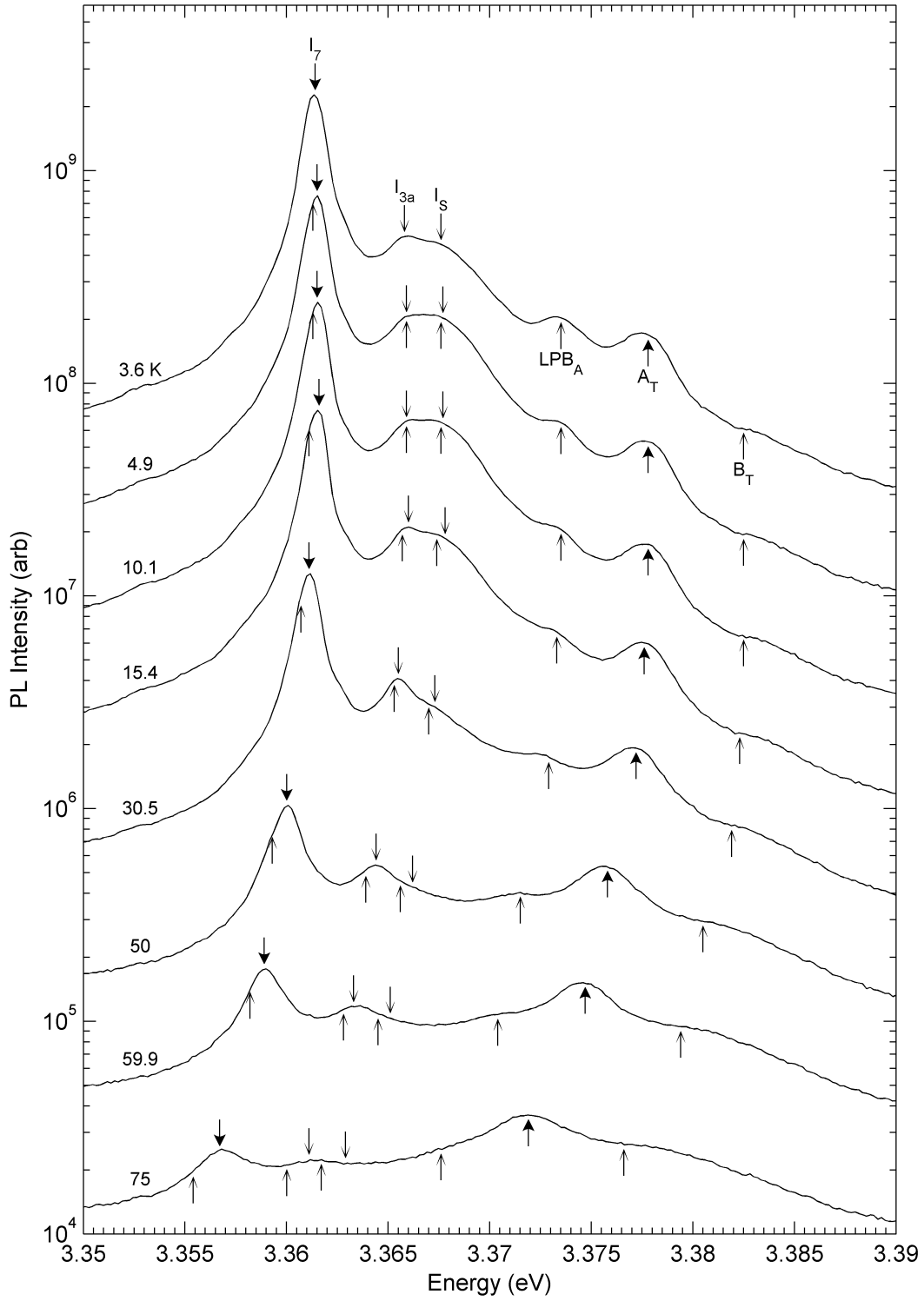

Figure 4.8: Temperature dependent PL emission from EPLD grown ZnO, deposited at an O_2 pressure of 100 mTorr with the mask at 33 mm. Arrows below the spectra were placed at constant spacings from the A_T peak while the arrows above the spectra were a constant distance from the I_7 peak.

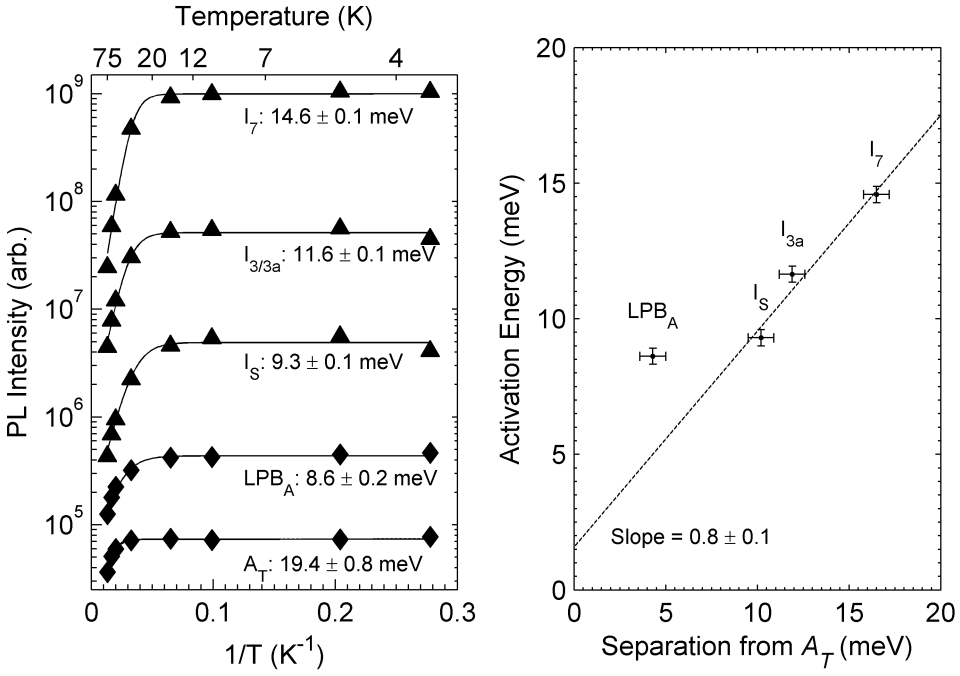

Figure 4.9: (a)Arrhenius plot of absolute peak intensities of EPLD grown ZnO ([100 mTorr, 33 mm]) showing fitted activation energies (vertically offset for clarity) (b) Comparison of the activation and localization energies of the excitonic features.

thermal broadening effect. This results in underestimates of the activation energy for all the peaks. It must be noted that essentially an identical curve could be fit to the A_{T} data by adding a second decay path to the fit with a fixed activation energy of 60 meV using equation 3.12 (page 41). This adds one parameter, B, to the fit. By adding the second path with a fixed 60 meV activation energy, a 20% reduction in χ^2_{R} was obtained for the A_{T} fit. While this may not be a very large reduction, it shows that free-exciton dissociation can describe the decay in intensity assuming the presence of a second nonradiative decay path with an activation energy of 15 ± 2 meV.

At low temperatures the $[A, E_{\mathrm{a}}]$ path was responsible for most of the PL decay. Examining equation 3.12 it can be shown that the effects of the two paths are equal at a temperature of

$$T_{\mathrm{E}} = \left[\frac{E_{\mathrm{a}} - E_{\mathrm{b}}}{k_{\mathrm{B}}}\right]\left[\ln\left(\frac{A}{B}\right)\right]^{-1} \tag{4.1}$$

which is equal to 90 ± 20 K for this sample using the data in table 4.1. Equation 4.1 only gives physical results when $B > A$ (with $E_{\mathrm{b}} > E_{\mathrm{a}}$). As temperature is

raised further, the effect of the [B, E_b] path becomes dominant. The effect of the [A, E_a] path can be considered negligible when its effect is $1/e^2$ times that of the [B, E_b] path. This happens at a temperature of

$$T_D = \left[\frac{E_a - E_b}{k_B}\right]\left[\ln\left(\frac{A}{B}\right) + 2\right]^{-1} \tag{4.2}$$

which is 130 ± 30 K for this sample. This situation will occur at finite temperatures when $\ln(A/B) < -2$ or at $T = \infty$ when $\ln(A/B) = 2$. Thus, the [A, E_a] and [B, E_b] activation paths represent the high and low temperature PL quenching mechanisms respectively.

For the LPB$_A$ peak the extracted activation energy was 8.6 ± 0.2 meV, considerably higher than the separation of this peak from A_T. Thus, this peak cannot be an exciton bound to a shallow trap (ionized donor, D^+X) and is an exciton-polariton from the lower branch of the dispersion curve. Appearance of LPB$_A$ in this spectra confirms the presence of the transverse A-exciton (A_T with Γ_5 symmetry) since only transverse excitons will couple strongly with the photons to create polaritons, as discussed in section 3.2. On the other hand, all the bound excitons show activation energies comparable to their localization energies. This is shown clearly in figure 4.9(b). A straight line with slope of 0.8 ± 0.1 can be fit through the bound exciton data with LPB$_A$ lying above the line. This is strong evidence that the I_x peaks were emission from bound excitons and the decay in emission was due to thermal dissociation from the binding center. A slope of 1 was expected in this case but the value obtained here was close. The slope value being less than 1 was due to underestimated activation energies since absolute instead of integrated intensities were used for the fits. Nonradiative recombination of the excitons may also have reduced the effective activation energies.

As revealed by the temperature dependent PL spectra of figure 4.8, the broad emission around the I_{3a} region (around 3.367 eV) was composed of two separate emission peaks. One was a sharp peak with the line width of a D^0X complex while the other had a broader nature. According to figure 4.9(b) these peaks decayed with temperature like bound excitons should. The sharp peak was identified as the I_{3a} peak based on its localization energy. I_{3a} has been attributed to interstitial Zn donors,[146] and its presence here is not surprising considering the Zn-rich growth conditions. The broader emission decayed like a bound exciton but its line width was noticeably broader than the neighboring peaks. This gave evidence that this was an exciton bound to a shallow extended structural defect,

Table 4.1: Fitted Arrhenius parameters for the intensity of the PL features from EPLD grown ZnO ([100 mTorr, 33 mm]). The top part of the table is for a one path fit (equation 3.11, page 41) and the bottom part shows the two path fit (equation 3.12, page 41) to A_{T} with the second activation energy fixed at 60 meV.

Parameter	A_{T}	LPB$_A$	I_{S}	$I_{3\mathrm{a}}$	I_7
$I(0)$ (arb.)	7.36 ± 0.03	8.75 ± 0.04	24.7 ± 0.01	26.0 ± 0.1	99.9 ± 0.01
A (arb.)	20 ± 3	8.2 ± 0.4	37 ± 1	55 ± 1	227 ± 4
E_{a} (meV)	19.4 ± 0.8	8.6 ± 0.2	9.3 ± 0.1	11.6 ± 0.1	14.6 ± 0.1
χ^2_{R}	50	260	3100	1800	3200
$I(0)$ (arb.)	7.38 ± 0.05	–	–	–	–
A (arb.)	7 ± 3	–	–	–	–
E_{a} (meV)	15 ± 2	–	–	–	–
B	$(3 \pm 1) \times 10^3$	–	–	–	–
E_{b}	60 ± 0	–	–	–	–
χ^2_{R}	40	–	–	–	–

I_{S}. These EPLD grown samples have a very high surface area due to the complex nanostructured morphology and the I_{S} peak is likely an exciton bound in a surface trap. The line width of this peak seemed comparable to the SX peak observed at 3.335 meV.

The dominating emission at low temperature from the EPLD grown samples was from a D^0X complex labeled as I_7 which has an unknown chemical origin.[16] The D^0X origin of this emission is essentially unambiguous considering its line width, localization energy, and the fact that ZnO is intrinsically n-type. The actual I_7 identification was based on the localization energy and the following two arguments. First, the peak in the bulk spectrum of figure 3.6 (page 30) which was closest to I_7 is the Al-related $I_{6\mathrm{a}}$ peak. There is no reason to believe that a significant Al concentration is present in any of these samples. No trace of Al was found in the target as reported by the manufacturer and no materials containing Al were deposited in the HV chamber in any previous deposition. Second, the other peak with a similar localization energy to I_7 is I_8 which has been attributed to excitons bound to neutral Ga.[16] Similar to Al, no trace of Ga was found in the target or placed in the chamber in any previous experiment. According to the manufacturer the main impurity in the Zn target used to deposit these samples was Pb at a concentration of 12 ppm. As such, a Pb related complex could be the origin of this I_7 emission. Further experiments such as diffusion studies,[16] magnetic resonance techniques,[147] or tracer experiments using

radioactive isotopes[148] will be required to identify the chemical origin of I_7.

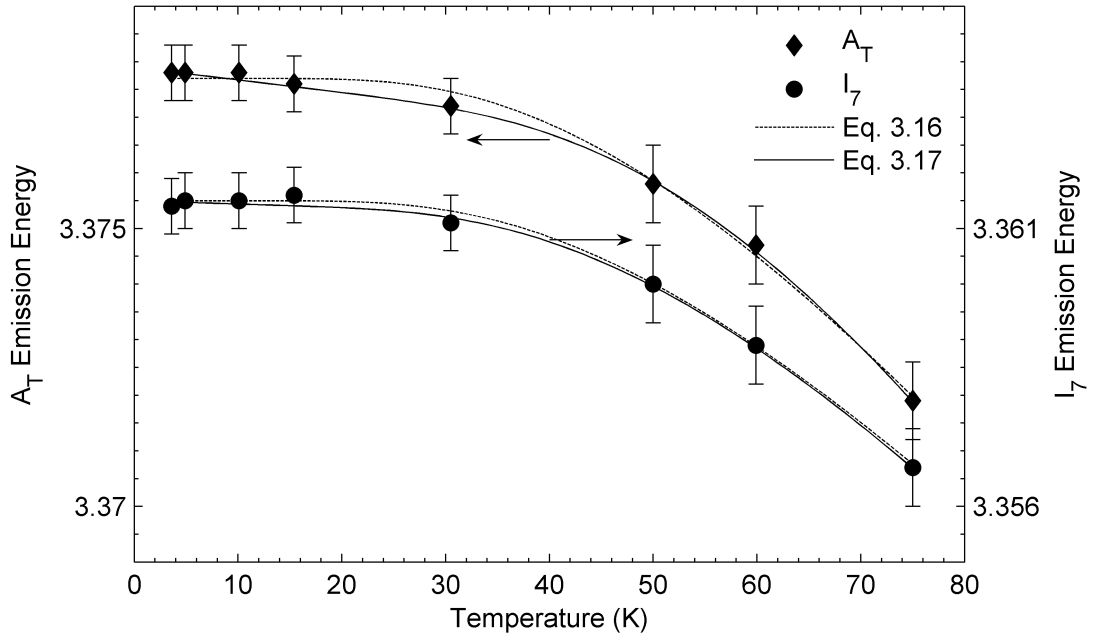

Figure 4.10: Energy shift of the EPLD emission with increasing temperature. Solid lines show the fits to the modified Manoogian equation (3.17) and the dashed lines are the fits using the Bose-Einstein equation (3.16).

Figure 4.10 shows the position of the A_{T} and I_7 peaks as a function of temperature. The positions of these two peaks were found by eye at each temperature and then used to calculate the positions of the rest of the arrows shown in figure 4.8. Those arrows below the spectra were placed by keeping a constant spacing with the A_{T} peak while the arrows above the spectra were a constant distance from the I_7 peak. As is clearly shown in the figure, the position of the bound excitons did not quite follow that of the free excitons, similar to that observed in the bulk sample of chapter 3. To study this in detail the Bose-Einstein and modified Manoogian models (equations 3.16 and 3.17) were fit to the data and are shown in figure 4.10 by the dashed and solid lines respectively. Unweighted least squares fitting, as well as weighted fitting using the uncertainties, was performed and the fitted parameters with their 95% confidence bounds are shown in table 4.2. A slightly modified form of the χ^2_{R} parameter presented earlier in equation 3.18 was used to compare the fits and is given by

$$\chi^2_{\mathrm{r}} = \frac{1}{N-P} * \sum \left(y_i - y_i^F\right)^2 \tag{4.3}$$

where again N is the number of data points, P is the number of parameters in the fit, y_i is the i^{th} data point, and y_i^F is the calculated data. χ^2_{r} is used here in order to compare the goodness of the weighted and unweighted fits since its value is independent of the weighting used. Weighting the data using the uncertainties shown in figure 4.10 resulted in essentially identical fits for both models as seen by comparing χ^2_{r} values. The only difference was much larger 95% confidence bounds on the fitted parameters, so much so that the fitted values on the weighted fits seem meaningless. Nevertheless, the values obtained for all parameters of both models for the free and bound excitonic peaks are consistent with those values obtained for bulk ZnO (see table 3.3, page 46) and the PLD grown reference sample (see figure 4.7). This is true without having to resort to the extreme limits of the confidence bounds.

Table 4.2: Fitted constants to the emission energies of the A_{T} and I_7 PL peaks in EPLD grown ZnO.

Model	Parameter	A_{T}	I_7
Bose-Einstein(3.16) unweighted	$E(0)$ (eV)	3.3777 ± 0.0002	3.3615 ± 0.0001
	α (eV/K)	$(3 \pm 1) \times 10^{-4}$	$(2.2 \pm 0.7) \times 10^{-4}$
	θ (K)	160 ± 40	160 ± 30
	χ^2_{r} ($\times 10^{-7}$)	0.39	0.14
Bose-Einstein weighted	$E(0)$ (eV)	3.3777 ± 0.0006	3.3615 ± 0.0006
	α (eV/K)	$(2 \pm 3) \times 10^{-4}$	$(2 \pm 4) \times 10^{-4}$
	θ (K)	150 ± 150	150 ± 184
	χ^2_{r} ($\times 10^{-7}$)	0.41	0.14
Manoogian (3.17) unweighted	$E(0)$ (eV)	3.3779 ± 0.0003	3.3615 ± 0.0003
	U (eV/K)	$(2 \pm 1) \times 10^{-5}$	$(6 \pm 20) \times 10^{-6}$
	α (eV/K)	$(4 \pm 2) \times 10^{-4}$	$(2 \pm 1) \times 10^{-4}$
	θ (K)	230 ± 60	180 ± 80
	χ^2_{r} ($\times 10^{-7}$)	0.096	0.15
Manoogian weighted	$E(0)$ (eV)	3.378 ± 0.001	3.362 ± 0.001
	U (eV/K)	$(2 \pm 8) \times 10^{-5}$	$(5 \pm 10) \times 10^{-6}$
	α (eV/K)	$(4 \pm 12) \times 10^{-4}$	$(2 \pm 6) \times 10^{-4}$
	θ (K)	220 ± 420	170 ± 380
	χ^2_{r} ($\times 10^{-7}$)	0.085	0.15

The $E(0)$ values for all the fits were consistent with each other for both peaks and agree well with the expected values. $E(0)$ is the only parameter which was fit with a small uncertainty since this parameter does not effect the curvature of the model functions. All the α values in table 4.2 are consistent with each other

and with the bulk and standard PLD values obtained earlier. Higher values for α were obtained for the free excitons implying stronger coupling to the LO-phonons as compared to the bound excitons. This was observed more clearly in the hydrothermally grown bulk sample. The U parameter of the Manoogian fit for this EPLD grown sample was an order of magnitude higher for the free excitons compared to that for the bound excitons. Furthermore, there was a significant decrease in the χ^2_{r} parameter for the Manoogian fit for the free excitons but not for the bound excitons. This implies lattice dilation does not effect the bound excitons as much as the free excitons in ZnO nanostructures as well as in bulk crystals.

Like the PL analysis of the bulk sample, the temperature dependence of the emission features from the (E)PLD samples revealed important information about their origin. From the intensity decay it was found that the dominant emission at low temperature was from D^0X transitions in the PLD and EPLD grown samples. It also showed that the peak labeled A_{T} was indeed the free-exciton as this feature dominated the PL at higher temperatures. Appearance of the free exciton in both the PLD and EPLD produced samples is testament to the high crystal quality which can be achieved by using a metallic Zn target for (E)PLD.

4.1.3 PL Comparison at 3.6 K

Figure 4.11 shows the 3.6 K PL spectrum from a piece of each of the 9 EPLD samples placed in the cryostat in the same experimental run. O_2 pressure during growth is shown along the top and the shadow mask distance from the target is shown down the side. Care was taken to ensure that the section of each sample with the strongest emission was picked based off the results of section 4.1.4. Each spectrum is plotted on identical x and y axes with a close up of the NBE region shown in the insets. This figure shows that the PL emission from all the EPLD grown samples was composed of the same peaks in different intensity ratios with varying widths. A clearly resolved A_{T} peak was seen in 3 of the samples and appeared as a shoulder in rest except for the [200 mTorr, 17 mm] sample. In most of the samples the dominating emission was from the I_7 donor bound exciton with $I_{3\mathrm{a}}$ or I_{S} dominating the PL from the rest.

At a given O_2 pressure the samples grown with the mask at 17 mm showed the broadest lines. Moving the shadow mask closer to the substrate resulted in a decrease in PL line width. At a given shadow mask position the samples

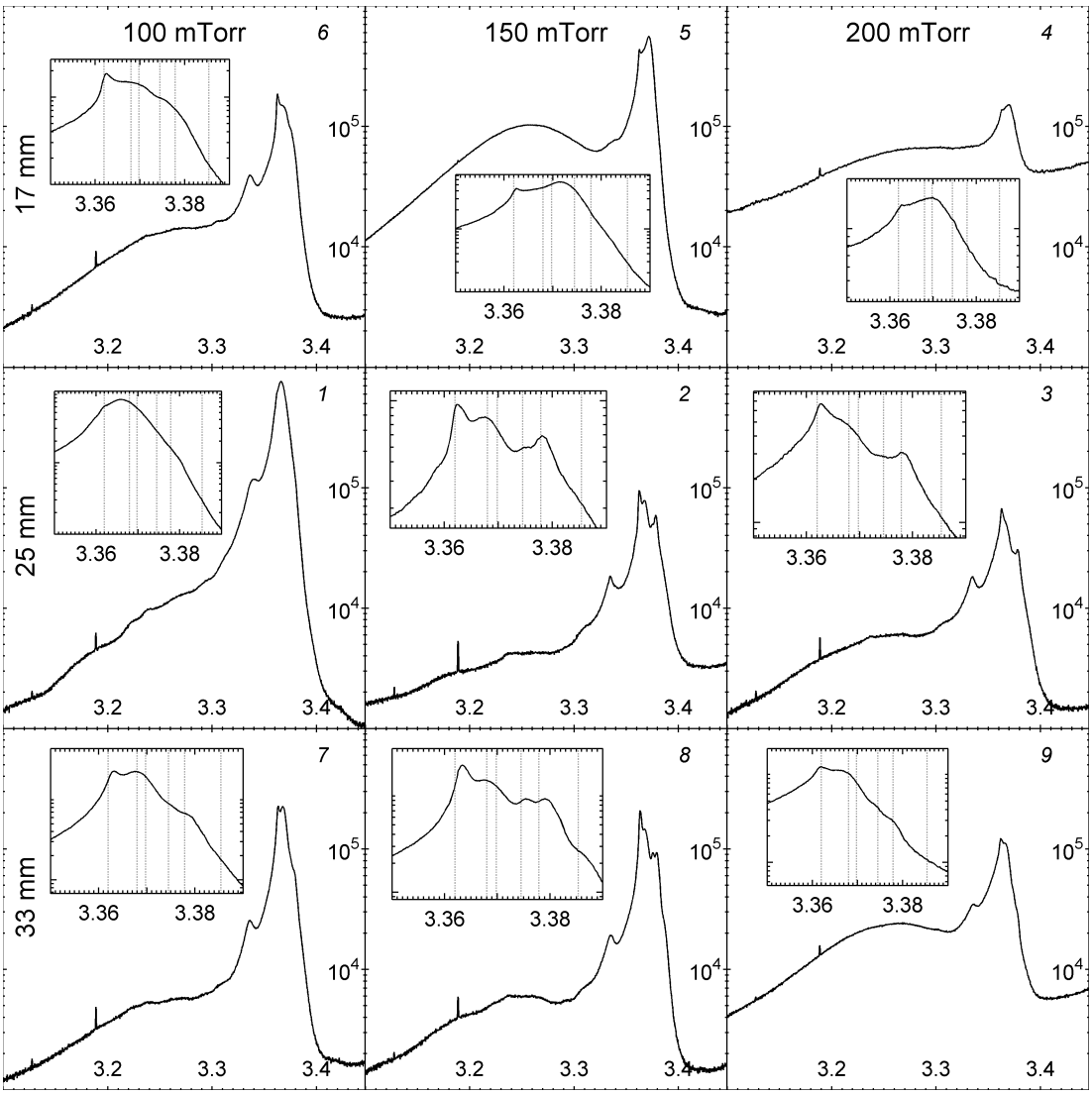

Figure 4.11: PL spectra from the 9 EPLD grown samples shown on identical x and y axes. O_2 pressure is shown along the top and shadow mask distance from target is shown down the side. The inset shows the NBE region with the lines indicating the positions of the B_T, A_T, LPB_A, I_S, I_{3a}, and I_7 peaks going from right to left (high to low energy).

grown at 150 mTorr showed the narrowest PL line widths. Line width of the PL emission correlates with crystal quality and figure 4.11 shows the samples with the highest crystallinity were the [150 mTorr, 25 mm] and [150 mTorr, 33 mm] samples. Furthermore, inspection of the insets in figure 4.11 shows that these two samples had the strongest A_{T} emission compared to the I_7 peak. This is another good indicator of the high crystallinity of these two samples. The II-VI flux ratio and growth rates of these two samples appeared to be in the optimum range for EPLD growth of high quality ZnO nanostructures from a metallic Zn target.

All samples except for the [200 mTorr, 17 mm] sample showed clear evidence of the structurally bound exciton emission, SX. This transition was probably present in the [200 mTorr, 17 mm] sample but it was not resolvable due to the broad nature of the emission and relatively weak signal. Laser scatter was a problem for this sample which was the cause for the high background photon count. A very broad peak in the violet region was clearly observed around 3.262 ± 0.005 eV in some of the samples. Defect related emission is the only way to account for such a broad emission peak. Considering the energy of this emission, it must be due to either an eA^0 or DAP transition. The emission energy of this peak is 180 ± 10 meV less than the bandgap energy, about the same as acceptor binding energies in ZnO which are typically 100-300 meV.[16,21,83,105,133] Broad emission at low temperature in the 3.26 eV region has been previously reported in nitrogen doped ZnO and was attributed to eA^0 transitions.[149,150] No significant nitrogen incorporation is to be expected in any of the samples and there is no reason to believe the [150 mTorr, 17 mm] sample would have more than the others. A native acceptor-like defect as the center of an eA^0 transition is the most likely origin for this 3.26 eV emission band. The intensity of this band did not correlate with the O_2 pressure or shadow mask position. The growth order is shown in the top right corner of the 9 graphs in figure 4.11. No correlation between the growth order and the broad 3.26 eV emission or any other feature can be seen. This shows that target degradation due to repeated growth is not an issue for EPLD grown ZnO from a Zn metal target.

Figure 4.12 shows the UV integrated intensity of all ten samples in this series. EPLD grown samples all had intensities an order of magnitude higher than the standard PLD grown sample. Furthermore, the PL line widths of the EPLD grown samples were significantly narrower than the PLD reference sample. These facts imply that the EPLD samples had improved crystallinity and stoichiometry

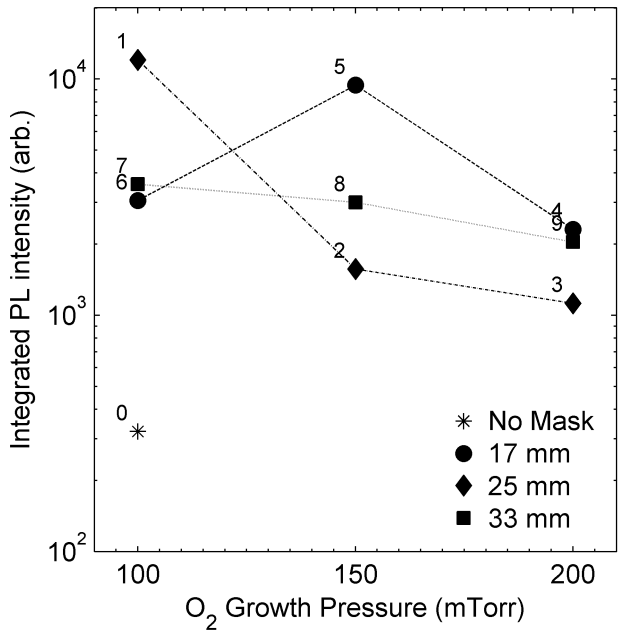

Figure 4.12: Integrated PL intensity above 3.35 eV of the PLD and EPLD grown ZnO samples. The numbers near the individual data points indicate the growth order.

compared with the PLD sample. This was not unexpected as the deposited Zn will have had several collisions with the O_2 ambient as it diffused around the shadow mask during EPLD growth. Increasing the number of collisions increases the probability of a reaction, bringing relatively more oxygen to the substrate which improves the crystal quality. However, increasing the number of collisions by simply increasing the O_2 pressure generally decreases the PL intensity (figure 4.12) and when the O_2 pressure goes above 150 mTorr the line widths increase. By blocking out the central portion of the plume, the shadow mask cut a considerable amount of Zn out of the substrate region. This brought the deposition closer to stoichiometric conditions. The shadow mask also selected the portions of the plume which most likely reacted with the O_2 ambient, improving the stoichiometry and structural quality of the EPLD grown nanostructures. Hence, EPLD is an effective way to grow high quality oxides from simple metallic targets.

4.1.4 Spatial PL Variation at Low Temperature

PLD is notorious for producing material with large variations in physical properties over relatively small areas compared to other growth techniques. Stoichiom-

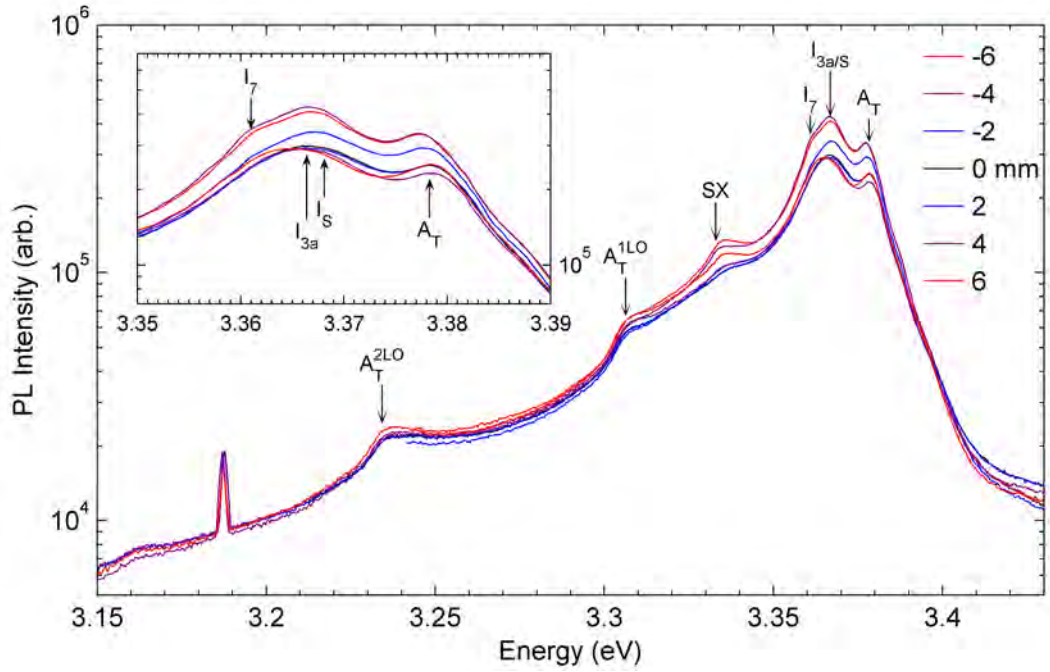

Figure 4.13: Low temperature PL as a function of position across the standard PLD grown sample. The near band edge region is shown in the inset.

etry, thickness, and roughness along with many other characteristics can vary significantly over a PLD grown sample.[53] These variations can all be traced back, in one way or another, to the angular distribution of material in the plume. PL is sensitive to many of these characteristics and the PL spectra from different spots on the PLD grown sample is shown in figure 4.13. Data was taken at 2 mm intervals with the laser spot smaller than 500 µm in diameter. The legend indicates the distance from the sample center from which the PL data was obtained. During deposition, the plume origin, center of the shadow mask, and the center of the substrate were aligned to within 1 or 2 mm.

For the sample grown by standard PLD, the shape of the emission did not drastically change across the surface. Free exciton emission was observed from all positions and was clearly resolved as a peak. Its absolute intensity varied by up to 40% across the surface. Position of A_T varied across the suface by about 1 meV which was small but still greater than the uncertainty introduced from machine reproducibility. This was verified by the 3.187 eV plasma line from the He-Cd laser which is consistent to within 0.5 meV in all the scans. Such variations likely arose from the spatial dependence of the stoichiometry. Local stoichiometric variations lead to variations in strain which can shift the A_T emission peak by the

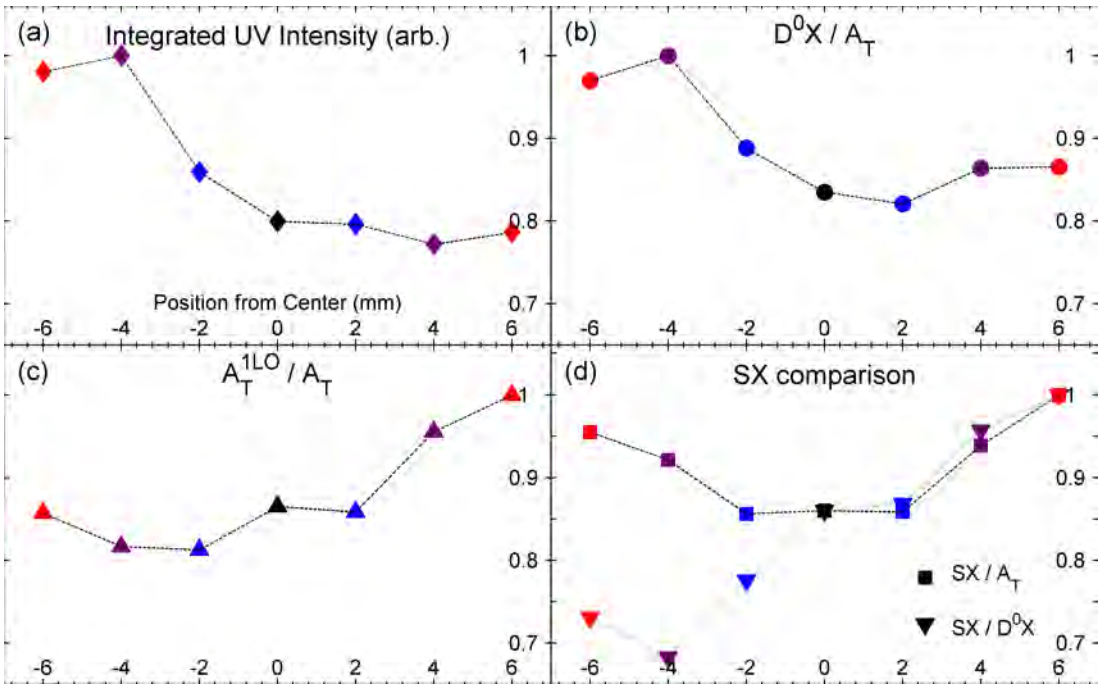

Figure 4.14: Spatial dependence of the low temperature PL emission from PLD grown ZnO. (a) UV intensity integrated above 3.35 eV (b) normalized D^0X:A_{T} ratio (c) normalized $A_{\mathrm{T}}^{1\mathrm{LO}}$:$A_{\mathrm{T}}$ ratio and (d) normalized SX:A_{T} and SX:D^0X

small amount obverved here. Figure 4.14(a) shows the UV integrated intensity (above 3.35 eV) was more or less constant across most of the sample but increased by about 25% towards one edge, the negative side of the sample. In the standard PLD case, the PL signal was more-or-less uniform over at least 6 mm which could be extended by optimization of growth conditions and geometry.

Intensity of the D^0X emission was also dependent on position and roughly followed the behavior of the free excitonic peaks. The normalized ratio of intensities between the bound and free exciton bands is shown in figure 4.14(b). Bound exciton emission was integrated from 3.35 to 3.374 eV and free exciton emission above 3.374 eV. The ratio followed the behavior of the UV integrated emission intensity, showing that the UV increase was due mainly to an increase in D^0X emission. Toward the high intensity edge of the sample the I_7 peak could be seen as a shoulder but it was unresolvable on the other side, as seen in the inset of figure 4.13. The two positions which showed I_7 most clearly were those with the highest overall integrated UV intensity. Overall structural quality will be relatively high in those spots suggesting that high crystallinity is necessary for observable I_7 emission.

Figure 4.14(c) shows the ratio of the first LO-phonon replica from the A_{T} emission to the zero phonon line. This ratio shows nearly the opposite behavior with respect to position as the D^0X:A_{T} ratio. Varying concentrations of the binding centers for the D^0X peaks can explain this. Assuming the donor concentration was proportional to the D^0X:A_{T} ratio, the positive side of the sample had a relatively smaller concentration. Free excitons were not captured by the binding centers as quickly and so they had more time to recombine via phonon assisted luminescence. The asymmetrical nature of these trends with respect to the plume center is somewhat surprising. Misalignment of the sample with the plume, the plume turning effect, and asymmetry of the laser spot on the target could all be contributing to the asymmetry.

The feature which showed the most obvious dependence on the position was the emission from SX, at 3.335 eV. Figure 4.14(d) shows the normalized SX:A_{T} integrated intensity ratio. It was lowest for the center of the sample and rose toward the edges of the samples where this feature was most pronounced. This feature is the only one which showed nearly symmetrical behavior with respect to the sample center. If the sample was cooler toward the edge during growth, dislocations may have formed more easily resulting in higher SX intensity. Also shown in figure 4.14(d) is the SX:D^0X integrated emission intensity ratio. TES emission is expected around 3.32-3.33 eV (see table 3.1, page 33) and if the 3.335 eV emission followed the D^0X emission it would be indicative of a TES origin for this peak. This was clearly not the case as the SX:D^0X ratio was not constant and actually varies more than the other ratios.

PL signal variations over the 9 EPLD grown samples are shown in figure 4.15 with the integrated UV emission intensities ($\hbar\omega > 3.35$ eV) shown in figure 4.16. For most of the samples the shape of the PL emission did not change significantly. Growth order is also shown in the figures and no obvious trends with respect to this were observed. The 3^{rd}, 6^{th}, 7^{th}, and 9^{th} samples have maximum UV emission within 2 mm of the sample center. Also, the [100 mTorr, 25 mm] sample, which was grown 1^{st}, shows strong emission across the center with intensities falling off toward the edges. Ablated Zn arriving at the center of the substrate will have had the most interaction with the background gas and hence the highest probability of reacting with the O_2. Growth rate will also be the slowest here and the combination of these two effects may have lead to the stronger PL from the central region. However, the situation was not as simple as that since the effect was not observed for all the samples. In fact, the opposite effect was observed for

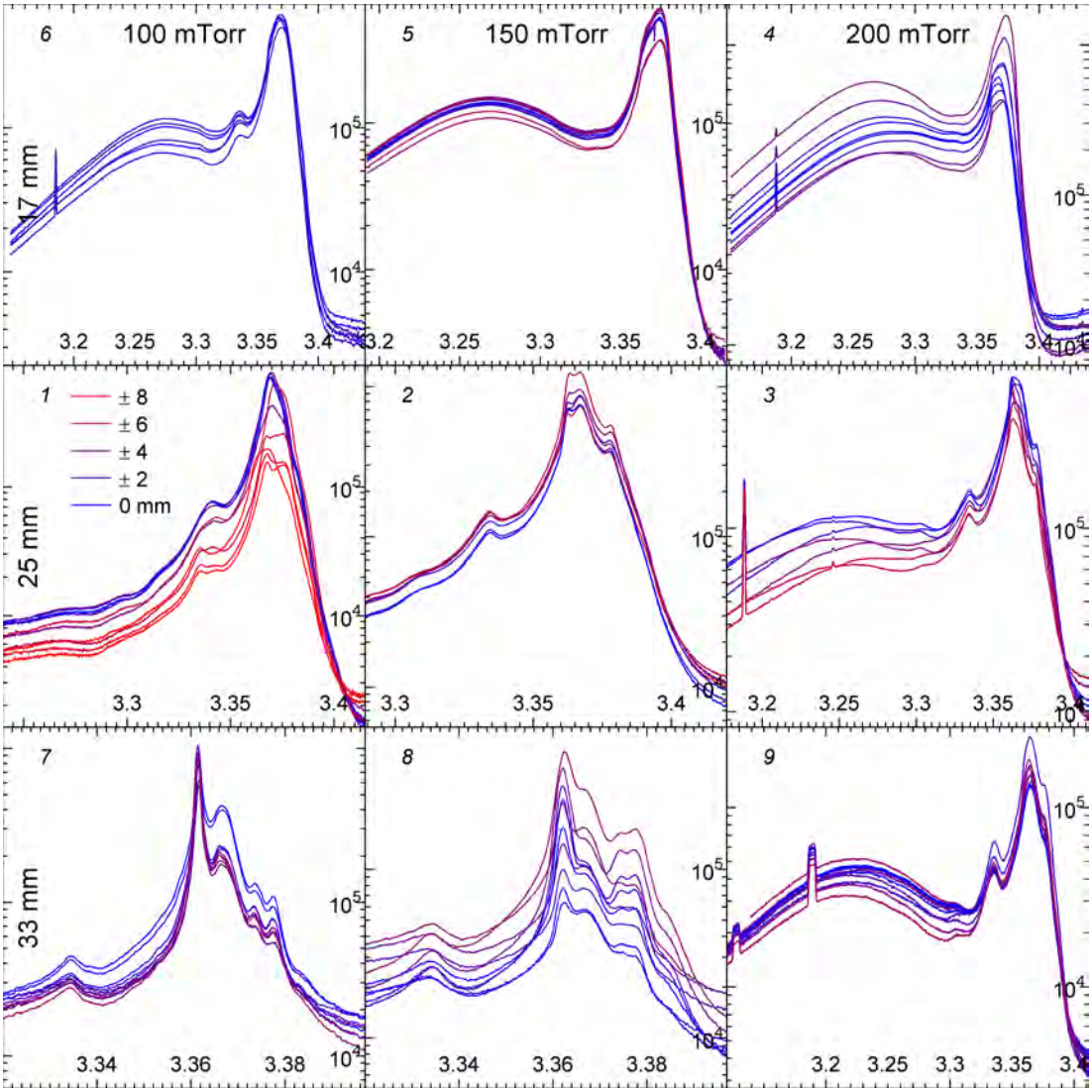

Figure 4.15: PL as a function of position across the EPLD grown samples. Spectra go smoothly from blue to red going from the center of the sample outward in both directions. Legend on the [100 mTorr, 25 mm] sample applies to all spectra and indicated position from the center. Note the different x and y scales for each of the 9 graphs.

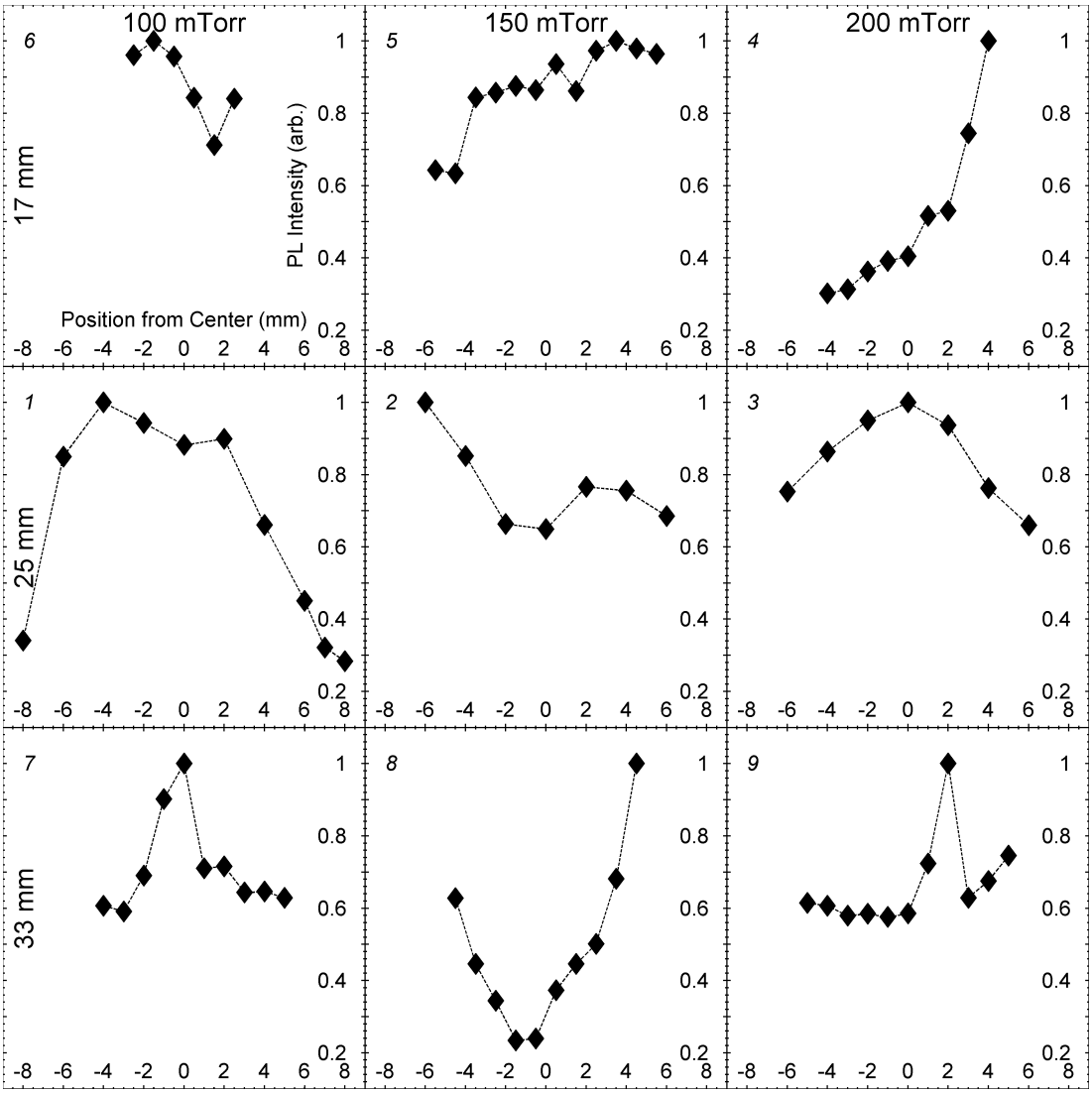

Figure 4.16: Integrated intensity of the UV emission ($\hbar\omega > 3.35\,\mathrm{eV}$) across the EPLD grown samples.

the [150 mTorr, 33 mm] sample which showed a minimum PL intensity near the center.

The broad violet emission observed from several of the samples at around 3.28 eV clearly shifted with position for the [200 mTorr, 17 mm] sample. The shift was much larger than any shift of the 3.187 eV plasma line. Emission from this region appears to be due to two components. The shift of the emission maximum was due to a change in the relative intensity of the two bands, as shown most clearly for the [200 mTorr, 25 mm] sample. The best estimates for the position of these two peaks are 3.247 ± 0.005 eV and 3.269 ± 0.005 eV as taken from the spatial dependence of the [200 mTorr, 25 mm] sample. A fairly smooth transition from one peak to the other was observed across the surface of this sample. A DAP transition and the associated eA^0 peak could account for this behavior if the concentration of the donor involved was low and it had a binding energy of about 20 meV, the energy difference between these features. Where donor concentration was the least, the eA^0 channel would be favored resulting the observed blue shift of the broad band composed of these two features.

PL from the [100 mTorr, 25 mm] sample showed a second peak at 3.343 eV was observed next to the *SX* emission at 3.335 eV. No peaks at this energy have been previously reported in ZnO. Given its width and energy, it was likely due to an exciton bound to a similar structural defect as the *SX* peak. TES emission from I_7 would be expected about 10 meV lower in energy than this peak, which also showed no correlation with I_7 emission intensity. This sample was the only one in the entire series, including the PLD grown sample, which showed this 3.343 eV peak.

Spatially resolved PL can reveal many aspects about a sample. Emission peaks that are hidden underneath stronger, near by features may be resolvable toward the edges or even just in one small localized spot. For PLD grown samples, spatially resolved PL can give an estimate of the size of the uniform region of a sample, an important aspect when considering PLD for mass production. Introduction of a shadow mask changes the spatial variations in PLD produced samples quite drastically. Optimization of growth conditions and deposition geometry could lead to EPLD grown samples with uniformities over areas significantly larger than samples grown by standard PLD.

In this study, the spatial PL dependence did not show obvious correlations with shadow mask position or O_2 pressure. This may be due to the portion

of the samples which were actually probed. Considering the $< 500\,\mu m$ spot diameter, at most the total area of the sample covered by the laser was only $10\,\mu m^2$ spread over several mm^2. A micro-PL mapping system providing full sample coverage would be a very valuable tool for these samples.[151] However, to truly find correlations a statistical study should be undertaken. For each growth condition in any controlled PLD experiment, up to 10 films should be produced (would need up to 90 samples in the '3 by 3' experiment presented here). Characterization of all the films would then allow for meaningful error bars and allow a good understanding of the correlations, or lack thereof, between growth parameters and material properties. No reports of this type were found in the literature. A statistical approach would be the only way to convincingly demonstrate stable, reproducible *p*-type ZnO grown by *any* method.

4.2 Unique Power Dependent PL

As discussed in section 3.8, the excitation intensity dependence (a.k.a. power dependence) of the PL emission can give clues as to the origin of a PL feature. Figure 4.17 shows the power dependent PL spectrum of the near band edge region of the [150 mTorr, 33 mm] sample. This sample was chosen as it showed excellent line widths and relatively strong signal intensity. Excitation intensity was varied over two orders of magnitude from 0.3 to $30\,W/cm^2$ using a set of calibrated neutral density filters to attenuate the He-Cd laser. Sample temperature was maintained at 3.6 K throughout the measurement series. The data presented in this section, as well as some of the temperature dependent study, has already been published.[2]

Starting from low laser power, the emission intensity of most of the features increased nearly linearly with excitation intensity. Integrated UV intensity of the entire region shown in figure 4.17 showed the expected $I \propto L^{\zeta}$ power law with an exponent of $\zeta = 1.05 \pm 0.02$. However, the behavior of I_7 was drastically different from the rest. Essentially nonexistent at $0.3\,W/cm^2$, the I_7 peak showed a superlinear increase with excitation intensity until it dominated the spectra at about $5\,W/cm^2$. In order to get ζ values for the individual peaks, a portion of each of the spectra was decomposed into 4 Lorentzian peaks with a constant offset. A few examples of the fits are shown in the inset of figure 4.17 and the white lines show the fits and the region which was decomposed.

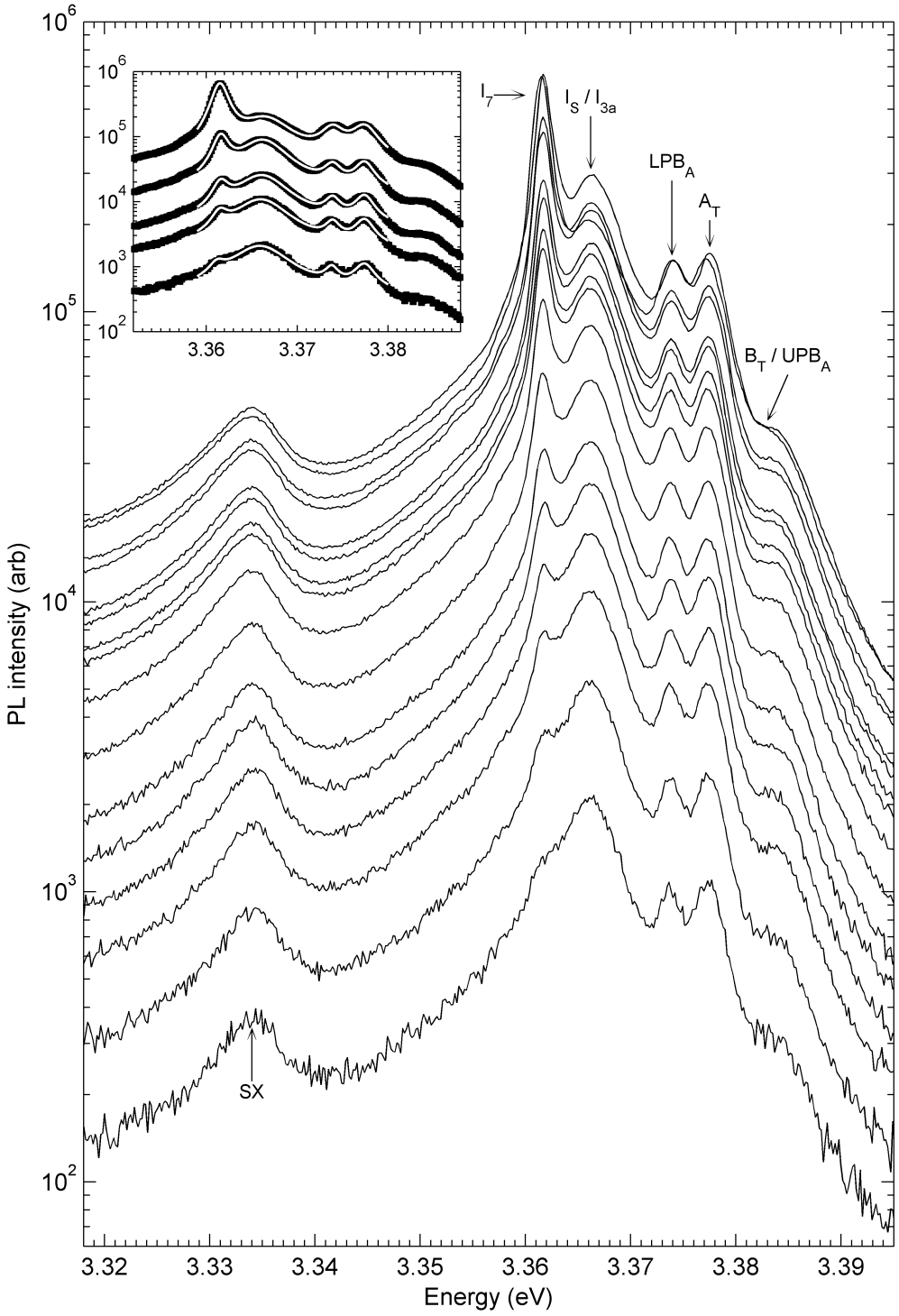

Figure 4.17: Power dependent PL of the [150 mTorr, 33 mm] sample taken at 3.6 K. The inset shows the 4 Lorentzian peak fit plus a constant baseline to a few representative spectra. Excitation intensity goes from 0.3 to 30 W/cm^2 with no vertical offset applied to the data.

Unfortunately the B_T peak could not be included reliably in any fit. Five and six peak fits were also preformed but did not produce physically reasonable results. Attempts to fit Gaussian peaks to the spectra also did not give reasonable results for 4, 5, or 6 peak fits. Lorentzian line shapes suggest a pressure broadening mechanism, hinting that weak exciton-exciton interactions govern the line shape of excitonic PL features in ZnO at cryogenic temperatures. Lorentzian peaks have been used in the past for deconvolution of PL[152,153] and Raman[154] spectra of ZnO. The most reliable, physically reasonable fit for all excitation intensities was obtained by fitting 4 Lorentzian peaks (with a constant offset) and holding the line width of the I_7 line constant at 2 meV. The implications of the constant I_7 line width will be discussed further along. Figure 4.18 shows the results of this 12 parameter fit for all the excitation intensities. Line widths and peak positions showed essentially no change with excitation power. This confirms that laser heating effects, which lead to line broadening and redshifting, were negligible over this range of excitation intensities.

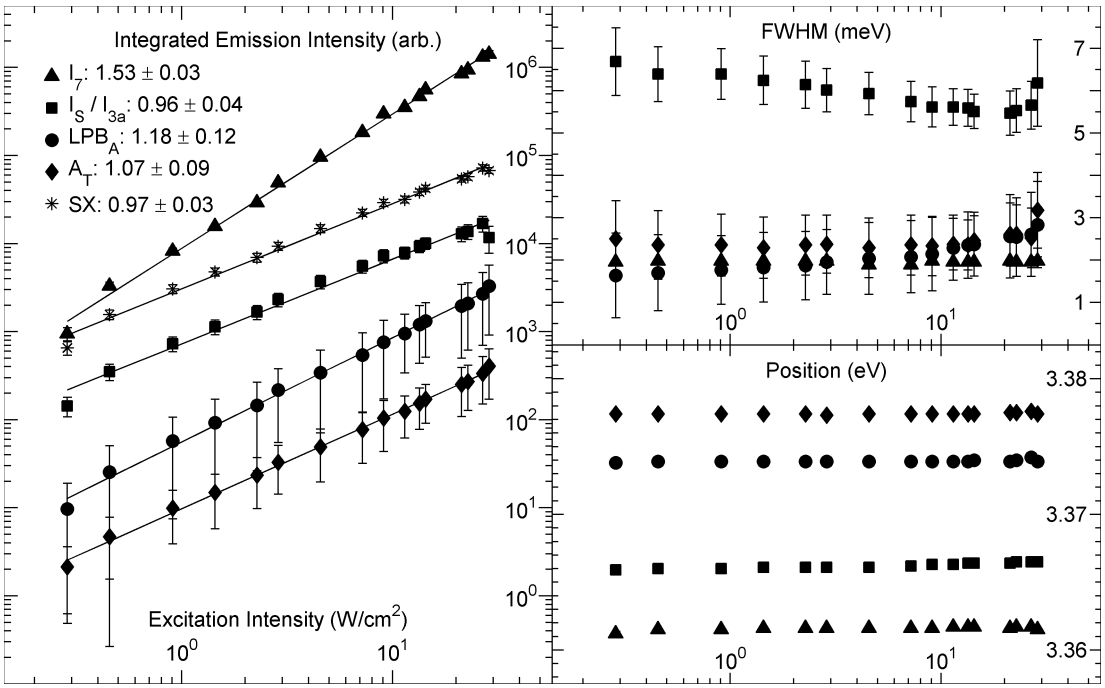

Figure 4.18: Parameters of the 4 Lorentzian peak decomposition of the power dependent PL from the [150 mTorr, 33 mm] sample. Integrated intensities have been vertically offset for clarity and ζ values are shown in the legend. Also shown in the figure on the left is the integrated intensity of the SX peak as found by a separate single peak fit. Error bars indicate the 95% confidence bounds.

Integrated emission intensity of all the fitted peaks followed clear power laws as

seen by the straight lines in the log-log intensity plot in figure 4.18. The fitted ζ values are shown in the legend. For A_{T} the exponent of 1.07±0.09 agreed well with that calculated for free excitons.[131] LPB_A emission showed a similar exponent of $\zeta = 1.18 \pm 0.12$. A higher value around $\zeta = 1.5$ was previously reported for free exciton emission in ZnO at room temperature.[117] In that study, Chen et al.[117] only studied the high temperature behavior of the emission, showing that the exponent increased up to 1.75 when going up to about 800 K. This was attributed to the dissociation of the exciton leading to band to band transitions ($\zeta = 2$) as the PL mechanism. The low temperature behavior of the free exciton power dependence would be different since many trapping processes occur. It's likely that these trapping processes could be reducing the ζ value at low temperatures. However, it should be noted that in the model proposed by Schmidt et al.[131] nonradiative pathways do not effect the ζ value and trapping of free excitons may not either.

In this 4 peak fit, the $I_{3\mathrm{a}}$ and I_{S} lines were treated as one as they were too close together to be individually resolved. Examining the temperature dependence shown in figure 4.8, it becomes apparent that the I_{S} peak was broader than the $I_{3\mathrm{a}}$ peak. Thus, the behavior of the integrated intensity of the single peak fit to both I_{S} and $I_{3\mathrm{a}}$ will be dominated by the behavior of I_{S}. The broad nature, most easily seen at low excitation intensity, and slightly lower exponent of the I_{S} peak give further evidence that it is an exciton bound to an extended structural defect. Furthermore, the fitted line width of the $I_{3\mathrm{a}}/I_{\mathrm{S}}$ was about 7 meV which was at least twice that of the other features. This peak was however much narrower than the *SX* emission, known to be due to extended defects, which showed a line width of around 16 meV. Close inspection of figure 4.17 shows this band did not change shape with excitation intensity indicating that the $I_{3\mathrm{a}}$ and I_{S} peaks have roughly the same exponent around $\zeta = 1$. Integrated intensity of the *SX* peak is also shown in figure 4.18. This data was extracted from a single peak fit of the 3.335 eV region with a constant baseline. The exponent of 0.97 ± 0.03 was very similar to that found for the I_{S} peak indicating a similar origin. An essentially linear ζ value, which is certainly larger than the $\zeta = 0.7$ or $\zeta = 0.8$ expected for free to bound or DAP transitions, confirms the excitonic origin of the *SX* emission.

Significantly different power dependence was observed for the I_7 peak compared to the rest. At low excitation intensities it was barely present but gained enough intensity to dominate the spectra at intensities around 5 $\mathrm{W/cm^2}$. An exponent of $\zeta = 1.53 \pm 0.03$ for I_7 was extracted from the log-log plots of figure 4.18

which was drastically different than the rest of the excitonic features. This ζ value strongly identifies this peak as excitonic in origin and agrees with theory and with that found for donor bound excitons in CdTe[131]. Similar ζ values have also been reported in ZnO for bound exciton emission.[133] However, Fonoberov et al.[133] did not publish their power dependent PL spectra or discuss how the intensities of the peaks were calculated. Also, they could not decompose the band edge emission into separate free and bound exciton emission so no difference in their behaviors could be observed. There are very few reports of the low temperature power dependence of the near band edge PL from ZnO[132,133] and none of them could distinguish between the power dependence of the individual excitonic features. This ζ value for I_7 was also much different from the $\zeta \approx 1$ values observed for the peaks dominating the bulk sample, discussed in section 3.8 (page 51), confirming this was not the I_{6a} or I_5 peak. The large difference in ζ values between the I_7 and I_{3a}/I_S bound excitons suggests a fundamental difference in the excitonic complex responsible for I_7 emission. Along with single impurity atoms, excitons will bind to defect pair complexes which act as neutral donors.[155] It is not unreasonable that excitons bound to these different types of donors will have different power dependencies which may depend on the defect pair separation. More information is needed on the I_7 peak from independent sources before any solid conclusions can be drawn.

As mentioned previously the FWHM of the I_7 peak was held constant for the fitting. Essentially identical looking fits were obtained when this parameter was allowed to be free. However, different behavior of the I_7 peak was extracted from this fit. Figure 4.19(a) shows the integrated intensity and FWHM of the I_7 peak for this 13 parameter fit. All the other peaks showed essentially the same behavior as in the previous fit. For this fit a threshold like behavior was observed for the intensity of the I_7 peak at $1.8 \pm 0.2\,\mathrm{W/cm^2}$ when the exponent increased from $\zeta = 0.9 \pm 0.3$ to $\zeta = 1.39 \pm 0.07$, an increase of nearly 50%. Also, the FWHM of the emission was found to decrease from 8 to 2 meV with increasing excitation intensity. This decrease was bigger than the relatvely large 95% confidence bounds of the fitted FWHM in the low excitation intensity range. Figure 4.19(b) shows the χ^2_r values (equation 4.3) of the two fits as a function of excitation intensity. A decrease in χ^2_r of about 50% was observed for the lowest excitation intensity for the 13 parameter fit.

A threshold like behavior for the integrated intensity and a decreasing FWHM are two characteristics of stimulated emission. Optically pumped stimulated emis-

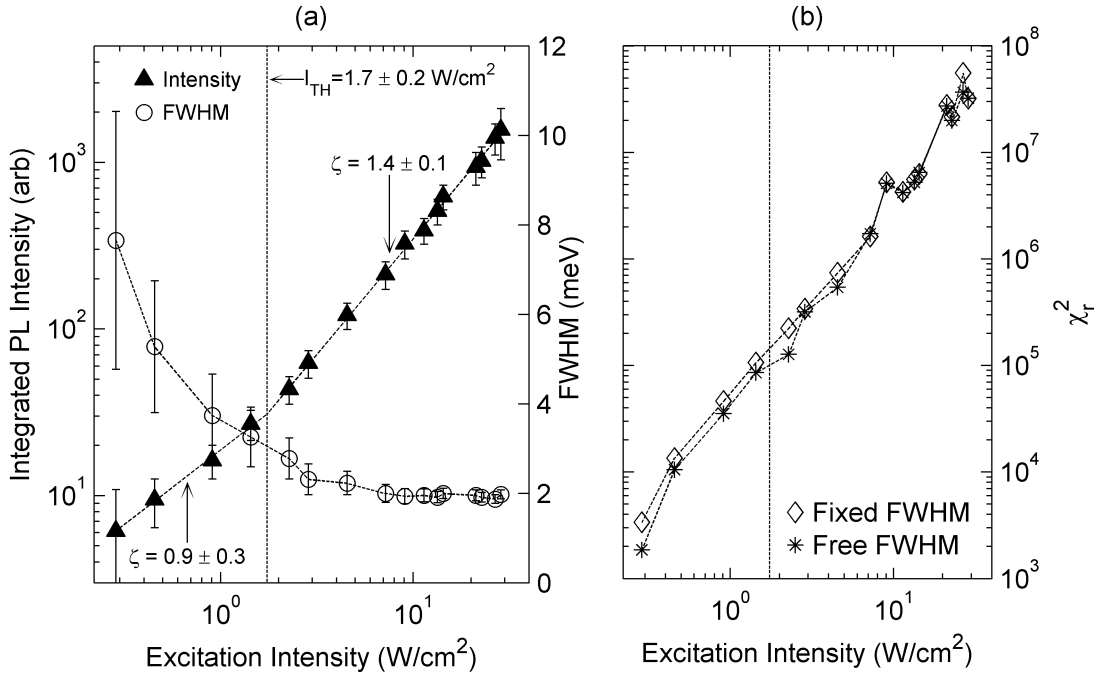

Figure 4.19: (a) Intensity and FWHM of the I_7 peak when its width was a free parameter in the fit. (b) Comparison of the χ^2_r values of the fit with a fixed FWHM of I_7 of 2 meV and the fit when the width of I_7 was a free parameter.

sion at low and room temperature has been previously observed in bulk, thin film, and nanostructured ZnO of many morphologies over a wide range of excitation conditions.[35,132,137,156–161] However, the unusual power dependence exhibited by the I_7 peak for these EPLD grown samples cannot be explained by any of the currently known mechanisms of stimulated emission in ZnO.[132,137,156] The most commonly reported stimulated emission mechanism in ZnO is exciton-exciton scattering. Two excitons in the $n_B = 1$ state will scatter off of each other. One of the excitons survives the collision and is scattered into a state with a higher n_B, usually $n_B = 2$. The other exciton is annihilated by radiatively recombining. Conservation of energy dictates that a redshifted photon is released at an energy given by[132]

$$\hbar\omega = E_g(T) - E_B\left(2 - \frac{1}{n_B^2}\right) - 3\delta k_B T \tag{4.4}$$

where $E_g(T)$ is the band gap, E_B is the exciton binding energy, n_B is the principal quantum number of the excited state which the surviving exciton scatters into, and δ is a constant which is usually taken as $\delta = 1/2$.[158–160] For ZnO at cryogenic temperatures, equation 4.4 predicts this so called P-band emission at energies around 3.32-3.34 eV. P-band emission is also characterized by a ζ value of 2 below

threshold and 4 or more above.[160,161] P-band emission can account for the experimental observations in reported studies, which show stimulated emission with thresholds as low as $7\,\mathrm{W/cm^2}$ at room temperature.[158] However, there is strong evidence refuting P-band emission as the stimulated emission mechanism under typical excitation intensities at room temperature.[156] Considering the energy of I_7, the very low apparent threshold of its intensity, and it having $\zeta < 2$ below and above threshold, P-band scattering can not explain the behavior observed in the 13 parameter fit.

Klingshirn et al.[35,81,132,156] describe several other stimulated emission mechanisms in ZnO yet none of them can explain the observed behavior of the I_7 peak. Its emission energy, and the fact that $\zeta < 2$ above and below threshold, are the main arguments against stimulated emission of the I_7 peak. For bound excitons, emission from the LO-replicas[81] and TES transitions[137] can be stimulated but there are no reports of stimulated emission from the zero phonon line. Furthermore, no physically reasonable explanation for the decreasing FWHM could be found, which shows no evidence of a threshold behavior. For these reasons the FWHM of I_7 was fixed for a 12 parameter fit. However, the fact that the behavior extracted by the 13 parameter fit can not be explained by current theories does not totally invalidate the fit. Discussion of the 13 parameter fit was included in this thesis (and in reference 2) for completeness. In any case, the drastically different power dependence of the I_7 peak compared to the other near by excitonic transitions was unique to these EPLD samples and more work is needed to understand its appearance in these nanostructures.

4.3 Helical Shadow Mask

For EPLD growth, the shadow mask geometry can have a profound influence on the properties of the deposit and their spatial fluctuations. Flat square or circular shadow masks are usually used for EPLD experiments[1,60,63,66,73,77–79] and produce excellent results for many materials. However, as mentioned in section 2.2 one major downside to EPLD using flat shadow masks is the thin spot which is usually formed in the middle of the sample. One way to combat the thin spot is to use a helical wire for the eclipsing object. A wire is twisted into a helix with a radius which increases with every turn. The increase in radius of the helix with each turn is smaller than the wire diameter resulting in a mask which is opaque when viewed down the axis. Marcu et al.[78] proposed this idea in 2000 for growth

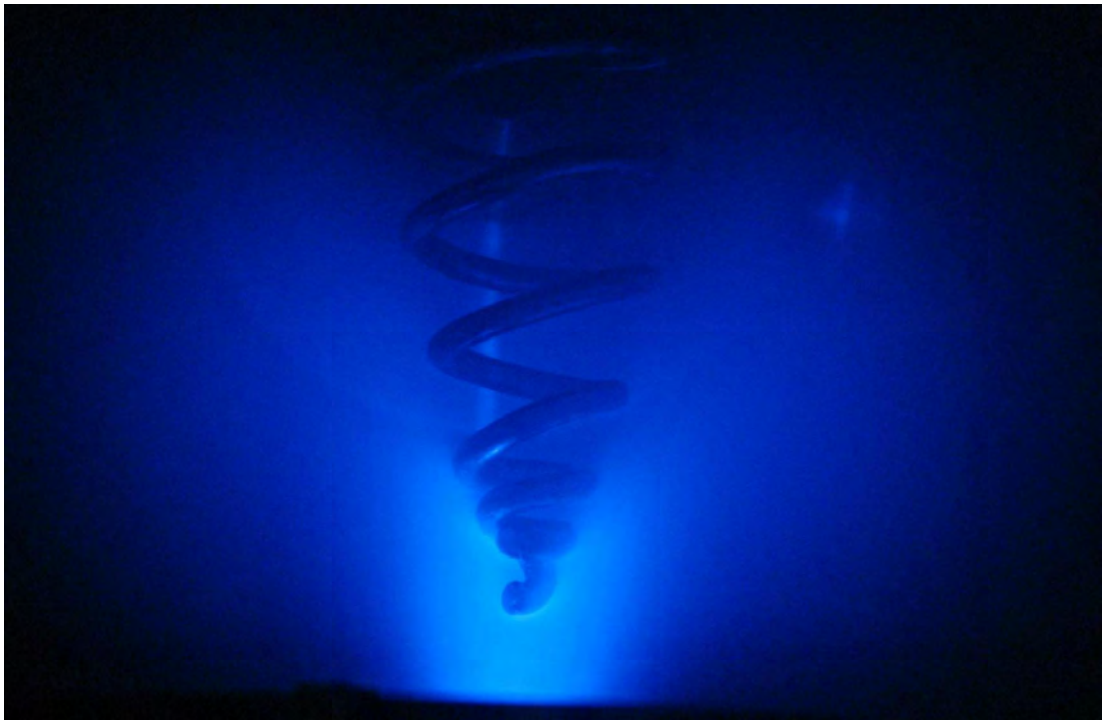

Figure 4.20: EPLD of ZnO from a metallic Zn target using a copper helix for a shadow mask.

of YBCO thin films. Figure 4.20 shows a ZnO plume propagating through a copper wire helical shadow mask in 150 mTorr O_2. The helix was made by hand-wrapping 99.995% pure copper wire with a 1.5 mm diameter around a cone with an angle of 20°. Overall length was about 40 mm with the wire placed about 5 mm from the target. As seen in figure 4.20, material clearly penetrated through the helical mask and helped to even out the growth rate across the middle of the sample. The downside to the helical wire was a significant decrease in growth rate, by factors of more than 10 compared to standard PLD.[78]

A very strange morphology was observed for ZnO growth with a helical wire shadow mask, as shown by the SEM images in figure 4.21. This sample was grown at 150 mTorr with all the other growth parameters identical to the samples discussed in the previous two sections. At first glance the low magnification images in figure 4.21(a) and (b), seem to show a very particulated surface. Higher magnification images, such as figure 4.21(e), show the surface morphology was in fact short nanorods which grew in micron sized clumps which were roughly circular and well separated from each other. Tilted SEM images shown in figure 4.21(g) and (h) show the height of the nanorods in these clumps were fairly small, likely 100 nm or less. Isolated nanostructures sitting on top of a wetting

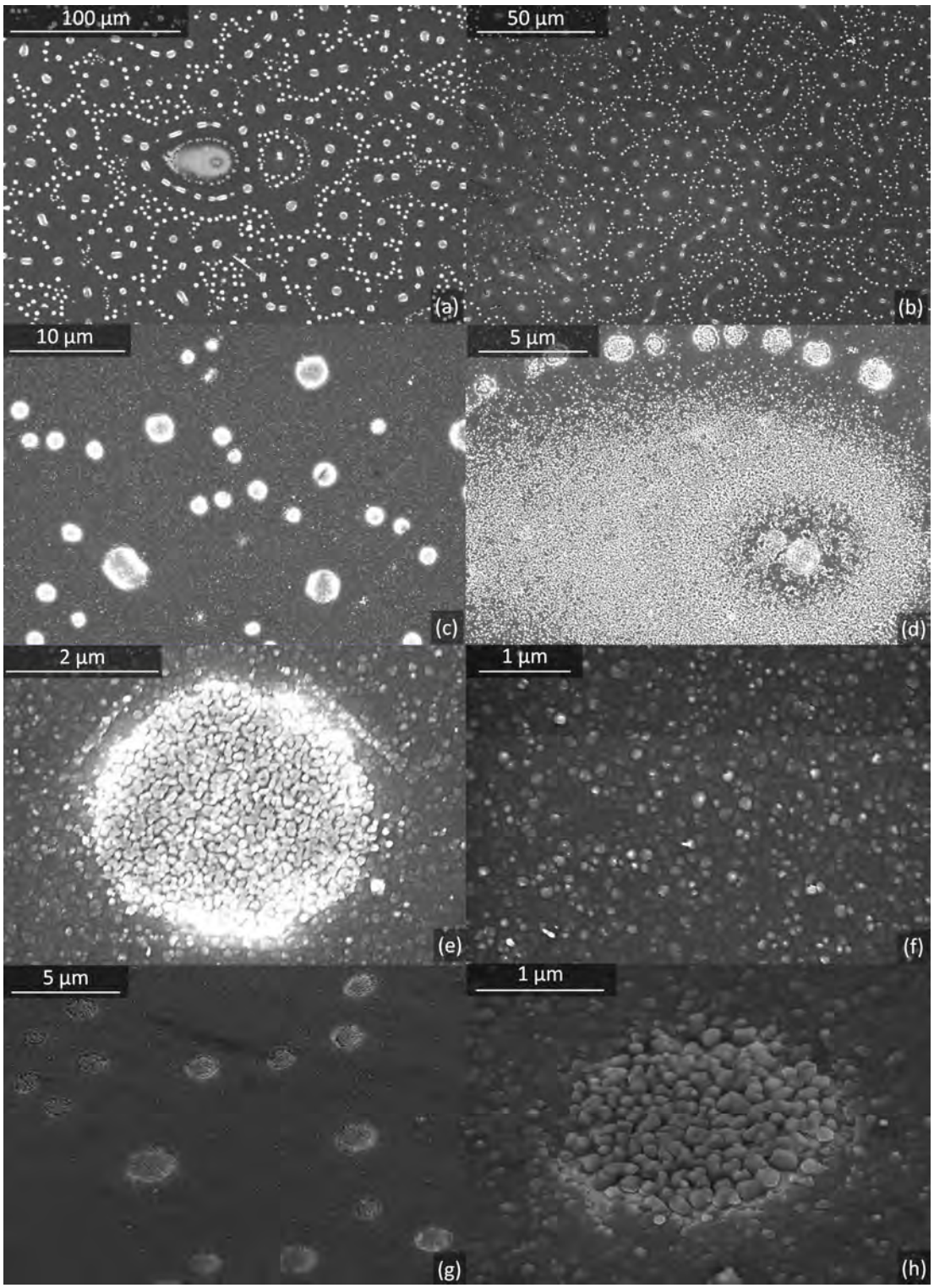

Figure 4.21: SEM images of ZnO grown by EPLD using a helical wire for a shadow mask. Images (g) and (h) were taken at 45° tilt.

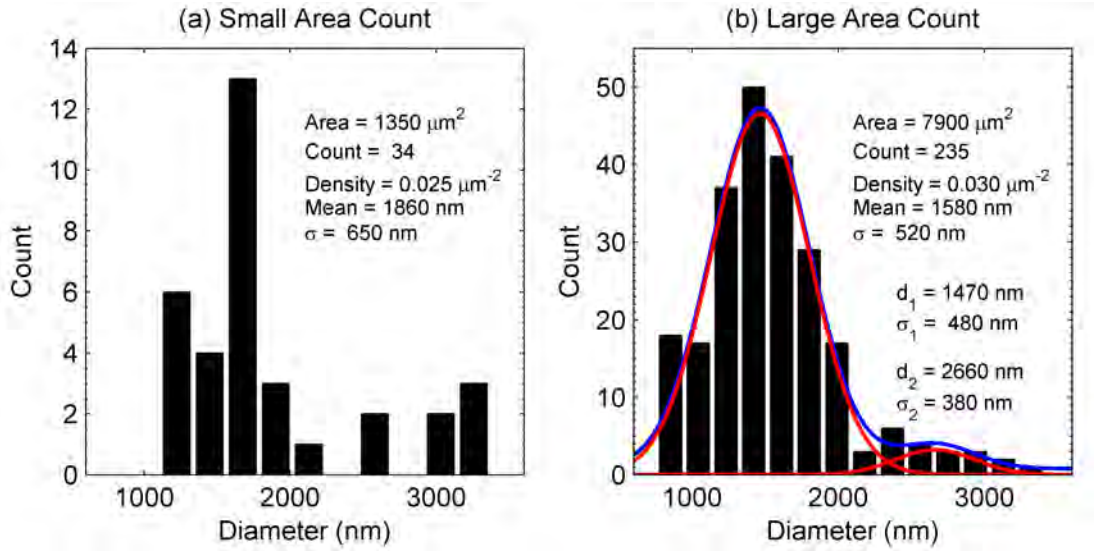

Figure 4.22: Microclump diameters from a small area (a) and large area (b) survey. σ values indicate the standard deviations in the diameters. The lines in (b) show the components of a two Gaussian fit to the distribution.

layer dotted the surface between the clumps, as shown in figure 4.21(f).

Since the helix effectively blocked the laser generated particulates, these clumps must have formed on the surface due to aggregation of atoms diffusing on the surface. Figure 4.21(f) shows a close up of the relatively clean surface in between the microclumps. Due to the significantly reduced growth rate for the helical shadow mask, the density of adatoms arriving at the surface per pulse was relatively small. Too small for liquid Zn droplets to form in the initial growth stages. This allowed the adatoms to diffuse farther on the surface before running into another adatom and binding to it. When the adatoms started to cluster the surface mobility of the unit was significantly reduced, sparking the growth of a microclump. Since the fresh adatoms arriving with each laser pulse had a high surface mobility, they could diffuse on the surface until they reached a microclump nucleation site. In this way the larger microclumps grew faster, essentially sucking up the material around them and leading to the strange morphology of this sample.

Close inspection of figure 4.21(a), (b), and (c) reveal clumps with diameters around 2-3 μm which were well separated from and surrounded by smaller clumps with diameters around 1-2 μm. Figure 4.22 shows a histogram of the radii found from a small (a) and large (b) area survey of microclump radii. Diameters were measured by eye using a Matlab script described in appendix A. The small area survey provided a more accurate measure of the individual

diameters while the large area survey gave a larger sample size for more accurate clump density and diameter distribution measurements. Comparable values for the mean clump diameter, clump density, and standard deviation were obtained from both surveys. Average clump size was around $1.7 \pm 0.2\,\mu m$ with a density of $(2.7 \pm 0.5) \times 10^6\,/cm^2$, about a hundred times less than the transistor density on Intel Core Duo processors.†

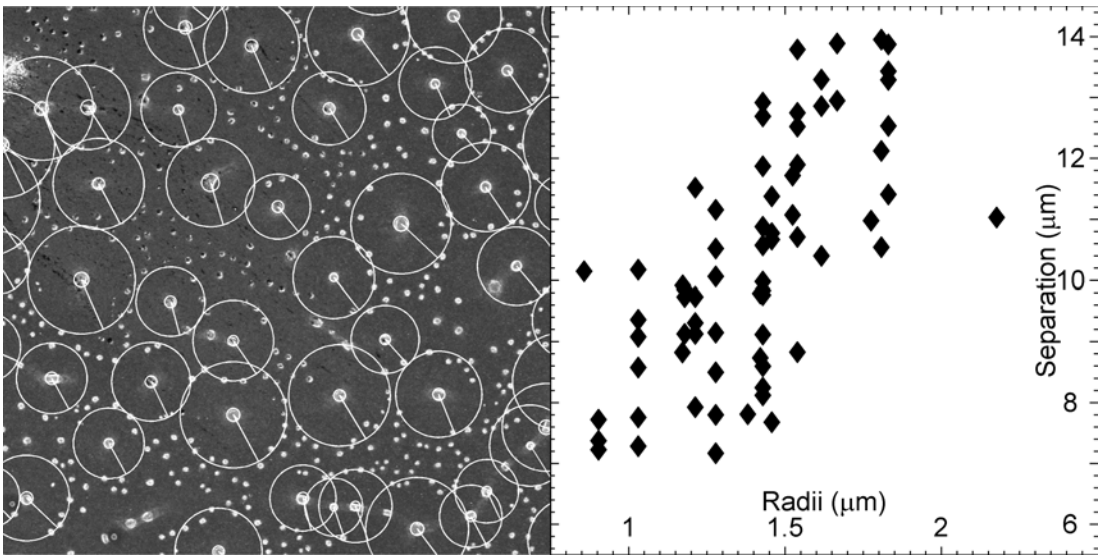

Figure 4.23: Comparison of the large microclump separations to their radii. The SEM image on the left shows a portion of the survey. Concentric circles were placed in the figure by eye to measure radii and separations.

The diameter distribution revealed by the large area survey was well fit by two Gaussian distributions peaked at 1470 and 2660 nm as shown by the red lines in figure 4.22(b). The total percentage of the sample area which was covered with the microclumps was roughly $7.0 \pm 0.5\%$. About 2.5 times more sample area was covered by clumps with diameters less than 2.1 μm than by those with larger diameters. The larger clumps were more isolated from their surroundings than the small clumps. A loose correlation was observed between the radii of the microclumps and their separations from their nearest neighbors as shown in figure 4.23. In general, the larger clumps were separated from their neighbors by larger distances, supporting the aggregation model discussed earlier. EPLD is designed to mimize particulates and this microclumping effect could lead to similar problems for devices as particulates. On the other hand, if their size, shape, and position could be precisely controlled then some interesting devices could be produced by EPLD using helical shadow masks.

†See www.intel.com

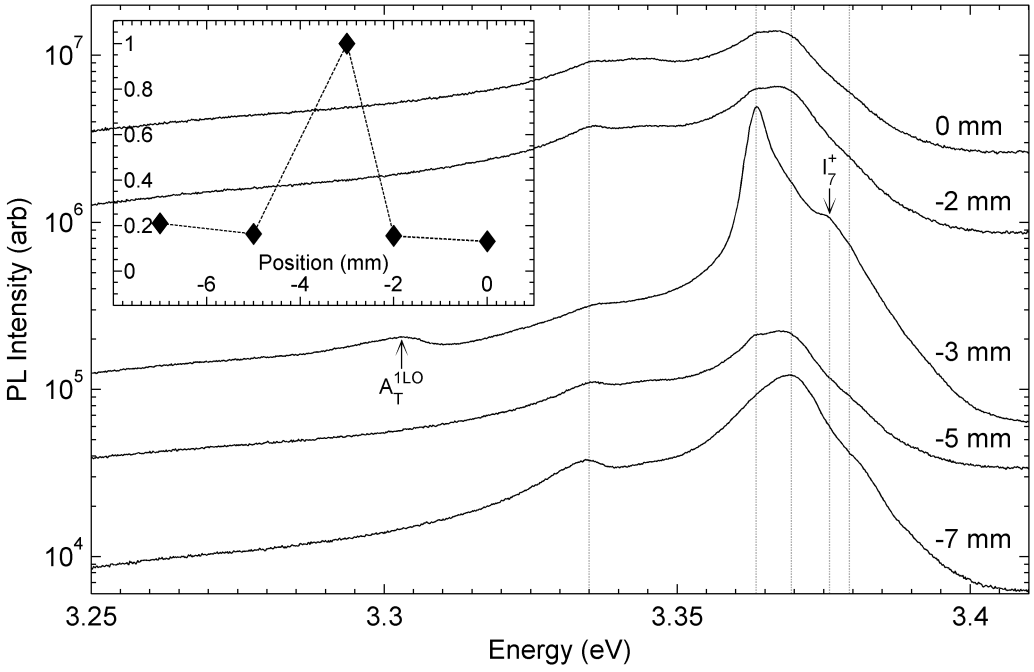

Figure 4.24: Low temperature PL from various spots on the ZnO sample grown by EPLD using a helical shadow mask. The spectra have been offset vertically for clarity. Vertical lines indicate the position of emissions from the A_{T}, LPB_A, $I_{3\mathrm{a}}$, I_7, and SX complexes going from high to low energies. The inset shows the normalized UV integrated intensity ($h\nu > 3.35\,\mathrm{eV}$).

PL emission was observed from this sample at low temperature with a relatively weak intensity from most places on the sample. Figure 4.24 shows PL spectra from different positions across the sample. A weak signal across most of the sample was not surprising due to the relatively small amount of material deposited during growth of this sample. However, the crystallinity was generally poor as line widths of the emission features were relatively broad across most of the sample. Also, free excitonic emission barely resolvable as a shoulder, further indicating degraded crystallinity. The straight lines in figure 4.24 indicate the positions of the A_{T}, LPB_A, $I_{3\mathrm{a}}$, I_7, and SX excitonic peaks going from high to low energy. All the peaks except for the SX feature have been blue shifted in position by 3.5 meV compared to the literature values[16,24] and by 2.1 meV from the [150 mTorr, 33 mm] discussed in section 4.2. Strain effects are not likely causing this shift since they should be the same for all the samples as they were all grown on c-axis sapphire. Spectrometer calibration issues are the likely origin of this shift despite seeming larger than the usual day-to-day drift of 1 meV at most. The fact that the SX peak in the helical sample occurs at nearly the same energy as the square mask samples seems surprising. However, considering that SX is an exciton bound

to an extended structural defect, its exciton localization energy may be sample dependent to within a few meV.

Applying this shift provides the best match up of peak spacings for all the positions shown in figure 4.24 and shows that emission from this sample was composed of the same features as the other EPLD grown ZnO nanostructures presented in this chapter. Domination of the spectra by I_{3a} again indicated a high concentration of Zn interstitials, not surprising since of the surface of this sample was mostly covered in a thin, textured wetting layer. SEM contrast between the microclumps and the wetting layer was large, indicating a big difference in the conductivity. Charging effects in the SEM cause a bright white color, indicating a low conductivity for the clumps. The dark color indicated and a high carrier concentration for the wetting layer, which the PL linked to Zn_i donors. Such high interstitial concentration implies poor structural quality of the wetting layer, which explains the broad emission from most parts of this sample.

At -3 mm the PL spectrum changed drastically, increasing in emission intensity by a factor of about 5 as seen in the inset of figure 4.24. This could be seen by eye during the experiment when scanning the laser across the sample. A very bright green glow came from this region and emission from the I_7 region dominated the PL at -3 mm by a significant factor. Emission line-width narrowed in this region with high emission intensity, which was localized to within a few laser spot diameters. Near the LPB_A energy a clear peak was observed which must have been due to the D^+X counterpart to the I_7 emission. It is highly unlikely for LPB_A to dominate the free excitonic part of the spectrum, except for in high quality optical resonator structures based on distributed Bragg reflectors.[162] However, emission of the free excitonic peaks did increase at -3 mm and emission from the $A_{\mathrm{T}}^{1\mathrm{LO}}$ peaks was observed along with it. Observation of a D^+X counterpart for I_7 further confirms the D^0X origin of I_7. However, only the splitting (or lack thereof) of the I_7 and I_7^+ features in a magnetic field could show this without any doubt.

From the spatially resolved PL of section 4.1.4, it was observed that the absolute and relative intensity of the I_7 peak was dependent on the region of the sample which was probed. The strong I_7 emission well localized around the -3 mm position of this sample was the epitome of this phenomena, which may be indicating a structural nature of the I_7 peak. Morphology of this sample showed a pronounced clumping effect with a small number of irregular features, as indicated by the SEM images in figure 4.21(b) and (d). Morphology at -3 mm

could be similar to that of figure 4.21(b) and (d) since such sharp, intense emission could not have been produced by the wetting layer. Unfortunately it will never be known since this region was destroyed during cleaving the sample for further investigation.

Cathodoluminescence (CL) studies of the −3 mm would have been most valuable for this strange sample. Also, power dependent measurement at −3 mm would have allowed a more accurate measure of the emission exponents for I_7. Observation of the unique power dependence presented in section 4.2 was made *after* the spatially resolved PL of this sample was performed and the sample was cleaved. It is a lesson hard-learned for PL characterization of PLD grown samples. The entire surface should be explored as thoroughly as possible. Interesting PL emission from localized regions can provide excellent clues as to their origin. Temperature dependence, and other extensions to the PL technique, should be carried out on the interesting regions *before* the samples are sectioned. Full exploration of ZnO growth by helical wires is very far from complete and could be subject of many interesting investigations. Once optimized conditions are found, helical wires and other 3D masks may provide a way to produce exotic materials with device quality over practical areas.

EPLD growth of ZnO is a good way to achieve high quality nanostructured material. However, optimized deposition conditions for a given application may be difficult to find due to the large parameter space associated with EPLD growth. Once such conditions are found, the large parameter space may become an advantage by allowing fine tuning of material properties. All these samples were grown onto bare *c*-axis sapphire which has a high lattice mismatch to ZnO. Al_2O_3 is electrically insulating which prevents an easy back contact for ZnO based devices. In the next chapter the effects of a few buffer layers on the growth and photoluminescence of ZnO grown by EPLD are presented. For device integration these buffer layers will be key to achieving the desired performance standards.

Chapter 5

Growth Using Buffer Layers

Epitaxial growth of ZnO on most surfaces is severely hindered by the large lattice mismatch it has to common substrate materials. The most common substrate for ZnO deposition is probably *c*-axis sapphire. Synthetic sapphire (Al_2O_3) is high quality, relatively cheap, and has a hexagonal structure similar to ZnO. However, there is an 18% lattice mismatch between the *a* lattice parmeters of ZnO and sapphire. A high density of dislocations would be expected to form when ZnO is grown directly onto sapphire in order to releave the strain imposed by the lattice mismatch. The closest match to ZnO is GaN with a lattice mismatch of only 2%.[163] However, bulk GaN crystals have not yet been realized and would likely be extremely expensive if they were available. Of course, using bulk ZnO crystals for homoepitaxial growth of ZnO would give the best results. Homoepitaxial ZnO films with better crystal quality and higher purity than the substrate have already been demonstrated.[107,164] ZnO substrates certainly are not as cheap as sapphire and it may be difficult to integrate devices grown onto ZnO substrates with silicon technology. To get around these difficulties, a thin buffer layer can be introduced onto a substrate with a high lattice mismatch before ZnO growth. Complex materials with high structural quality can be grown onto exotic substrates by employing the right buffer layer structure.

In this chapter the effects of different buffer layers on the EPLD growth of ZnO on *c*-axis sapphire are presented. Adding a buffer layer introduces even more growth parameters to the deposition but the extra work in optimizing them is usually worth the effort. Growth of ZnO using buffer layers has been reported extensively for several deposition techniques.[65,95,141,163,165–167] In most cases the buffer layer improved the crystallinity and optical properties of the samples considerably. For this work, platinum and thin ZnO buffer layers grown at reduced temperatures were explored. Different morphologies with interesting

PL emission were produced by each of the buffer layers. Only the tip of the iceberg was explored with regards to buffer layer growth but nevertheless, the potential for EPLD grown ZnO on various buffer layers is certainly there and should be the subject of many further investigations.

5.1 Pt Buffer Layers

A popular buffer layer choice for growth of many materials is Pt. Platinum is a stable metal which does not react with many compounds, even at elevated temperatures. It can add some interesting functionality to many materials as Pt is well known for its catalytic properties for many reactions. Pt has good electrical conductivity which makes it an attractive material for device contacting. There have been several publications regarding growth of ZnO on Pt surfaces[68,142,165,168,169] but very few on the photoluminescence emission of the material[165]. Pt is particularly well suited as a buffer layer for ZnO growth as there is a small in-plane lattice mismatch of only 1.4% between the *c*-plane of ZnO and the Pt$\langle 111 \rangle$ plane.[170] When deposited onto *c*-axis sapphire, Pt will naturally grow in the $\langle 111 \rangle$ direction[165,171] making Pt/Al_2O_3 an attractive buffer structure for ZnO epitaxy. Also, the high melting point of the Pt means it will not form a eutectic with Zn at typical growth temperatures for PLD of ZnO. This may suppress the VLS growth mechanism allowing for ZnO films as well as nanostructures to be produced by EPLD from a Zn target.

In this work a platinum layer less than 100 nm thick was deposited onto *c*-axis sapphire by standard PLD. Deposition was carried out at base pressure which was around 5×10^{-6} Torr. Substrate temperature was kept at 400 °C during the growth and the sapphire was subjected to the standard 3 step cleaning procedure before growth. With the laser aperture in place no discernible plume could be obtained, even after tightly focusing the beam and setting the laser power to maximum. Removing the aperture did not increase the fluence, it only increased the amount of material ablated per pulse by increasing the spot size and total energy incident on the target. Bright red-orange sparks were observed in the plume flying in straight lines radially away from the laser spot at all angles. Very similar behavior was observed for iridium ablation shown in figure 2.4(a) (page 15). By adjusting the laser focus during ablation it was observed that these sparks seemed to be generated as soon as a noticeable plume was observed.† Using the

†Even at base pressure a small plume was observed from other materials, such as Zn, when

$1/e^2$ laser spot size measured by the laser manufacturer, the resulting spot size on the target was estimated to be $2\,\mathrm{mm}^2$ giving a fluence around $8\,\mathrm{J/cm}^2$. A laser repetition rate of 10 Hz was used for 10 min which resulted in a 65 ± 10 nm layer as measured by Rutherford backscattering spectroscopy (RBS). RBS measurements were carried out by Dr. John Kennedy at the GNS Institute in Wellington, New Zealand using 2.2 MeV alpha particles.

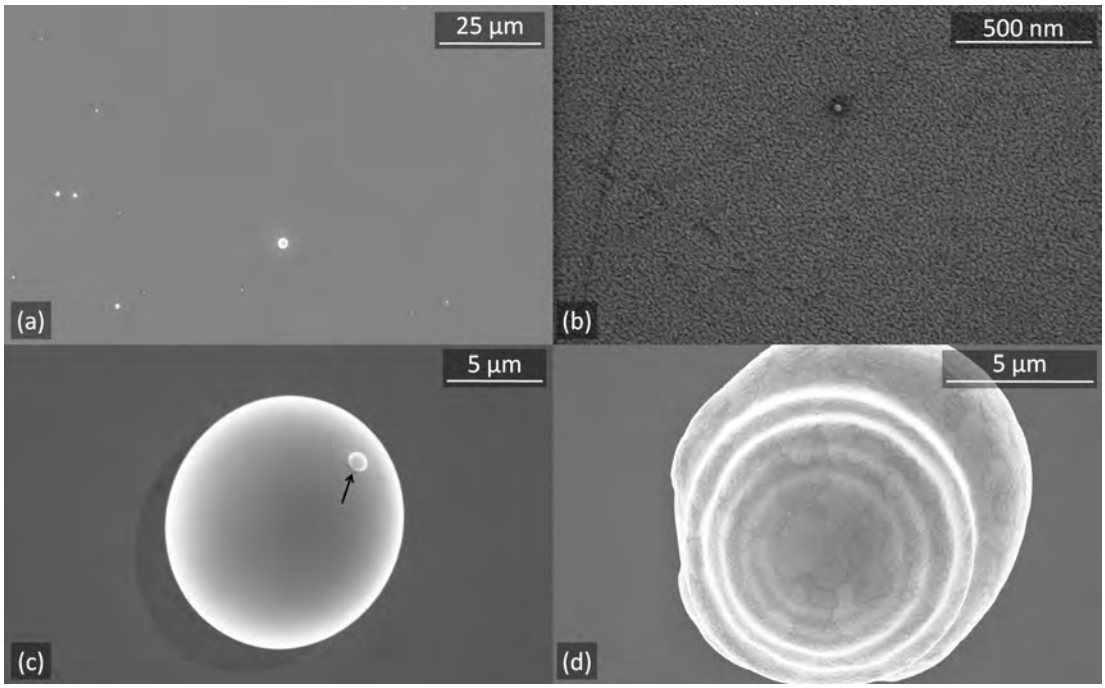

Figure 5.1: SEM images of Pt grown on Al_2O_3 by standard PLD at 400 °C.

To the eye the deposited Pt layers appeared as a smooth metallic platinum color with a high reflectivity. Figure 5.1 shows top down SEM images of the Pt layer. The bright sparks seen in the plume were large micron sized particulates which were violently ejected from the target. They could be seen over the entire substrate in concentrations similar to that observed in the low magnification figure 5.1(a). Most of the particulates were spherical in nature, with some elliptical distortions. This indicates the particles were molten upon ejection from the target, most of which solidified on the way to the substrate. Typically the diameter of the particles were between 1 and 10 µm. Figure 5.1(d) shows one of the larger particulates which was molten when it reached the substrate. Upon impact with the substrate this particulate solidified at just the right speed for the shock wave from the impact to be clearly visible on the surface. Of all the

ablation was occurring so the lack of emission in this case was not due to the lack of a buffer gas.

particulates examined with the SEM, this was the only one showing a frozen wave. Evidence for the collisions between the large particulates in the plume is shown by the particulate displayed in figure 5.1(c). The small arrow indicates a small fragment from a collision with another particulate which most likely happened within the plume. There must be a multitude of uses for micron sized Pt spheres and laser ablation of Pt in a liquid could prove quite effective at producing them in practical volumes. A close up of the surface in between the particulates is shown in figure 5.1(b). A highly textured surface was observed which appeared porous. These pores were quite small, significantly smaller than 50 nm. Porous platinum is known to be especially well suited for catalytic applications due to the drastic increase in available surface area.[172] A nanoporous layer may not be the ideal buffer layer for subsequent depositions but if high quality material can be grown on top, the porous Pt can be taken advantage of for gas sensing applications.

Optimization of the growth parameters for Pt layers destined for subsequent ZnO growth is beyond the scope of this thesis. The best approach would be to optimize the growth conditions of the Pt and ZnO layers *to each other*. Conditions producing the 'best' Pt layer on its own may not give the optimum surface for ZnO growth. Also, its likely that optimized ZnO growth conditions will be different for Pt/Al_2O_3 substrates than bare sapphire. It was not the point of this study to optimize the growth conditions of the $ZnO/Pt/Al_2O_3$ system, just to explore its potential. Pursuing this endeavor would likely lead to some interesting devices and rewarding physics.

5.1.1 ZnO Growth and Morphology

ZnO was grown onto Pt/Al_2O_3 structures by PLD and EPLD from the same Zn target used to grow the samples discussed in chapter 4. After the Pt layer was deposited the sample was removed and sectioned. One piece was placed back into the chamber, another piece saved for SEM measurements, and one piece was stored for the next growth. Since the HV chamber was not equipped with a multiple target holder the vacuum needed to be broken before the ZnO could be deposited. Contamination of the interface may have been an issue and ideally the HV chamber should be equipped with a 2 or 3 target carousel so multi-layer materials can be grown without breaking vacuum. Oxygen pressure for both PLD and EPLD growth was 100 mTorr with the substrates held at 600 K. For EPLD growth the shadow mask was placed 33 mm from the target since this was

found to produce samples with strong, sharp PL when grown onto bare sapphire. Laser conditions were replicated as nearly as possible to the samples discussed in chapter 4. A fluence of 4 J/cm^2, spot size of 1.5 mm^2 and repetition rate of 10 Hz over 2 h, was used on the same excimer laser through the same lens which was in roughly the same position.

Significantly different morphology was observed for the samples grown on the platinum buffer layer compared to the samples grown on bare sapphire. Figure 5.2 shows the morphology of ZnO grown on top of the PLD grown Pt buffer layer. Instead of the clumps of nanorods and isolated nanohexamids, these samples were grown in a thin film form. Standard PLD resulted in a continuous film with pronounced grains separated by surface cracks. Typical grains were about 150 nm across with some as large as 300 or 400 nm. Close inspection of some grains in figure 5.2 show a hexagonal structure indicating growth was along the *c*-axis, as expected for ZnO growth onto Pt $\langle 111 \rangle$.[68,142,165] Morphology of the EPLD grown ZnO/Pt/Al_2O_3 is shown in figure 5.2(b), (d), (f), and (h). A brain-like morphology was the result with a high density of nanoscale pores. The surface appeared to have an underlying step-terrace type structure as indicated in the tilted figure 5.2(f). This can also be seen in the top down figure 5.2(d) by the varying contrast between the some of the regions. Appearance of pores in the EPLD sample was due to the low growth rate. The small number of atoms arriving with each pulse had a large surface mobility. Adatoms were able to move around the surface and mimic the porous structure of the underlying Pt layer. For the PLD sample, the growth rate per pulse was too high and the adatoms did not move far on the substrate once they were deposited. Instead of pores, the observed cracks were formed. As with the bare Al_2O_3, morphology of the ZnO grown on Pt/Al_2O_3 is highly dependent on the growth rate.

Many sharp spikes with smooth crystal faces were seen pointing off of the sample grown by standard PLD as shown in the titled SEM image shown in figure 5.2(e). Typical spike lengths were between 500 and 1000 nm with diameters near the ZnO surface of around 200-300 nm. All the spikes appeared to be tilted with respect to the substrate normal. On the edge of the sample where the substrate was cleaved from the wafer, a dense grouping of these spikes were observed as shown in the inset of figure 5.2(c). This suggests that they form off of defects on the crystal surface. Spike density on the surface was comparable to the particulate density of the buffer layer. The smaller Pt particulates could be the source of the defects which act as nanospike nucleation sites. The gradual

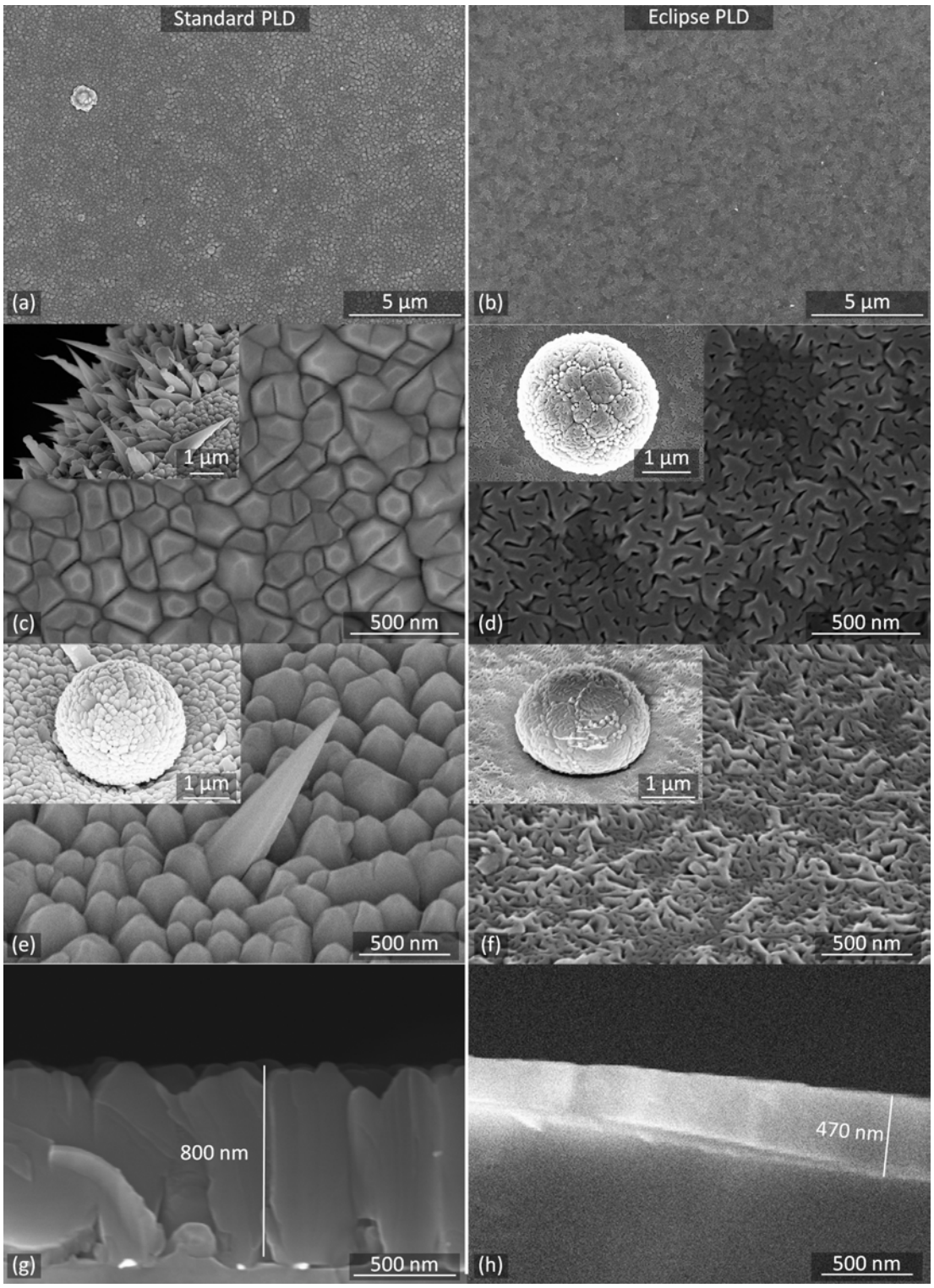

Figure 5.2: SEM images of ZnO grown on top of Pt/Al_2O_3 by standard and eclipse PLD. Images (e)-(h) were taken at a 45° tilt.

tapering may be suggesting a vapor-solid (VS) growth mechanism which would be expected since there are no reports of a Pt-Zn eutectic point. Furthermore, the growth temperature was well below the melting point of Pt. However, a self catalyzed VLS process could be responsible for the shape with the gradual taper due to the high growth rate for the PLD geometry. This would lead to less dramatic tapering than the EPLD grown nanohexamids, resulting in nanospike formation. TEM of one of the nanospikes would reveal a VS or VLS growth mechanism by the absence or presence of a capping particle respectively.

ZnO growth occurred on top of the large Pt droplets with a similar morphology to the flat regions, as shown in the insets of figure 5.2(d)-(f). Some of the particulates, such as that shown in the inset of figure 5.2(f), underwent clear deformation upon impact with the substrate. The larger Pt particles showed the most deformation (see figure 5.1). Larger particulates will retain their heat longer due to the lower surface area to volume ratio. They may still be molten by the time they reach the substrate and will not solidify as fast upon impact as the smaller ones. ZnO/Pt microspheres would have some interesting catalytic properties and may allow for some interesting devices if they can be removed from the substrate or formed in a solution. The porous nature of the ZnO layer grown by EPLD would allow the reagents to penetrate the ZnO and interact with both the ZnO and the underlying Pt microsphere.

Despite the rough nature of the surfaces, both the PLD grown and EPLD grown ZnO on Pt/Al_2O_3 were optically smooth and interference fringes were clearly observed by eye. Figure 5.3 shows the normal incidence reflectance from the two samples as measured by the OceanOptics USB2000 spectrometer and reflectance probe. Clear interference fringes were observed for both samples. The tighter fringe spacing (in wavelength) of the PLD grown sample was due to its larger thickness. Film thickness, d, can be extracted from fringe spacing using[173]

$$d = \frac{m}{2\left(\frac{1}{\lambda_i} - \frac{1}{\lambda_f}\right)\sqrt{n^2 - \sin^2\theta}} \tag{5.1}$$

were n is the refractive index, θ is the angle of incidence from the normal, and m is the (integer) number of fringes between wavelengths λ_i and λ_f. For normal incidence equation 5.1 reduces to $d = m/(2n(1/\lambda_i - 1/\lambda_f))$. For best accuracy it was found that correcting the reflectance spectra with the wavelength dependent refractive index produced the best results. Refractive index over the wavelength region shown in figure 5.3 was calculated using the Sellmeier equation.

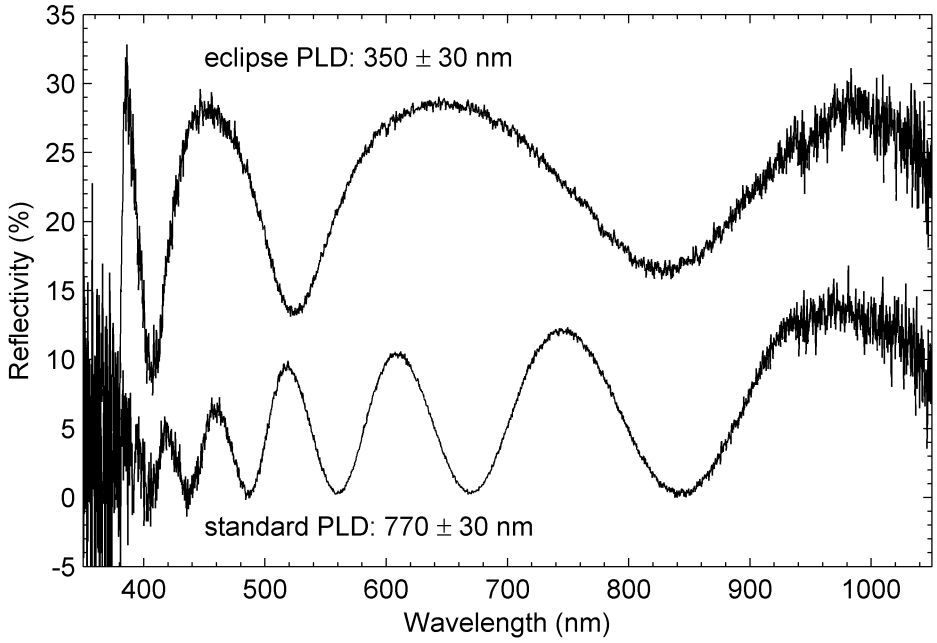

Figure 5.3: Normal incidence reflectance of ZnO/Pt/Al_2O_3 grown by standard and eclipse PLD showing clear thin-film interference patterns. Thickness extracted from the fringe spacing is shown above each spectra.

Sellmeier constants were taken as those reported for ZnO grown epitaxially onto *c*-axis sapphire by PLD.[64] The *n*-values were then used to convert the measured wavelengths to the values *inside* the ZnO layer. Thickness was then extracted with equation 5.1 by setting $n = 1$ since the wavelengths were already been corrected for n. Thicknesses of 770 ± 30 nm and 350 ± 30 nm were calculated by this method for the PLD and EPLD grown samples respectively.

For the PLD grown sample this thickness value agrees well with the cross-sectional SEM of figure 5.2(g). The thickness extracted from reflection for the EPLD grown sample well agrees with the 350 ± 20 nm determined by RBS. Since these samples were films with two independent thickness measurements, growth rates could be easily compared between the PLD and EPLD geometries. A decrease in growth rate of at least a factor of 2 was obtained in this experiment when the shadow mask was placed between the target. This decrease in growth rate is small compared to that observed in the literature for other material systems,[60,77,78] indicating that Zn can easily diffuse around the shadow mask by the O_2 ambient during EPLD.

5.1.2 Photoluminescence

Strong UV photoluminescence was observed from both the EPLD and PLD grown ZnO layers on the Pt/Al_2O_3 structure at low temperature. Figure 5.4 shows the 3.6 K PL spectrum of the samples grown on Pt/Al_2O_3 as well as the EPLD [150 mTorr, 33 mm] sample and a standard PLD grown sample on bare sapphire (offset vertically for clarity). A small wavelength shift was applied to each spectrum to line up the free exciton position with that reported by Meyer et al.[16] as indicated to the right of the figure. Each of the spectra in figure 5.4 were taken on different days and the variation in the shift is mostly due to the spectrometer calibration since this shift aligns the laser plasma lines at 3.185 eV to within 0.5 meV. Before correction, most were offset by about -1.5 to -2 meV to the values reported for bulk by Meyer et al.[16]. This is most likely due to differences in calibration techniques since the bulk sample studied in chapter 3 also showed emission about 1.5 meV higher in energy than observed by Meyer.

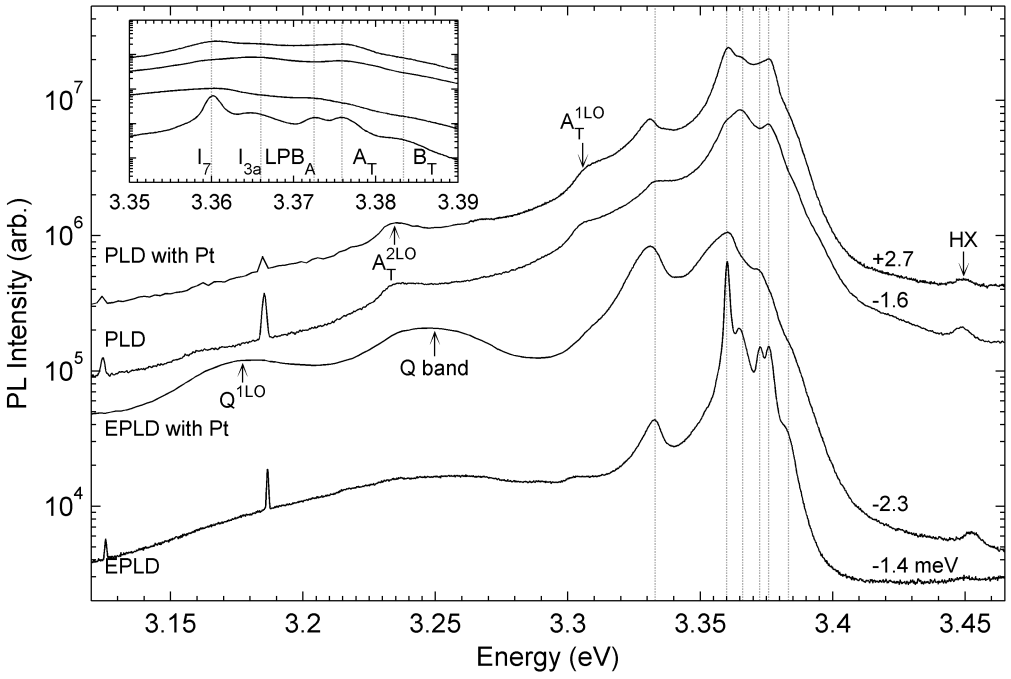

Figure 5.4: Low temperature PL from PLD and EPLD grown ZnO both with and without a Pt buffer layer (offset vertically for clarity). Each spectra has been shifted by 1 or 2 meV to line up with the reported values of the free exciton. Vertical lines indicate the position of the B_T, A_T, LPB_A, I_{3a}, I_7, and SX peaks going from right to left.

NBE luminescence from all the samples was composed of the same emission peaks, as seen in the inset of figure 5.4. Samples grown on Pt/Al_2O_3 had I_7 as

the dominant exciton, similar to the EPLD grown sample on bare sapphire. I_{3a} emission was resolvable from the samples grown on Pt/Al_2O_3 but was hidden by the large line widths and large background from I_7. A_T was the strongest free excitonic feature for the PLD sample on Pt/Al_2O_3 while LPB_A was the strongest free excitonic feature for the EPLD sample on Pt/Al_2O_3. Exciton-photon coupling, which causes the formation of the polaritons, is strongest in polar materials like ZnO and appears to have been stronger in the $ZnO/Pt/Al_2O_3$ compared to the unbuffered sapphire. The more or less continuous nature of the $ZnOPt/Al_2O_3$ samples, compared to the highly structured ZnO/Al_2O_3, may be the reason for this.

All four samples shown in figure 5.4 produced distinct *SX* emission. The EPLD grown sample on Pt/Al_2O_3 showed *SX* emission intensity which was nearly 80% of the dominant I_7 emission intensity. *SX* originates from dislocation loops,[11] which were present in the EPLD grown sample on Pt/Al_2O_3 in a high concentration. A dislocation loop forms when two screw-type dislocations with opposite orientations merge.[174] SEM revealed the EPLD grown $ZnO/Pt/Al_2O_3$ had a brain-like morphology with nanoscale holes which were not present in the PLD grown $ZnO/Pt/Al_2O_3$. The dislocation loops were likely connected with the pores, which could easily induce screw-type dislocations throughout the ZnO layer. For both the PLD and EPLD grown $ZnO/Pt/Al_2O_3$, the *SX* band was redshifted slightly. The size of the dislocation loop will govern the exciton localization energy, with the smaller loops localizing the excitons the strongest. Stronger localization means a redshift in the emission. Thus, individual dislocation loops in the $ZnO/Pt/Al_2O_3$ were smaller than those in the ZnO/Al_2O_3, but they were present at a higher concentration.

In the violet region the two PLD grown samples have very similar emissions. Essentially the only features present were the 1 and 2LO-phonon replicas from A_T which were on a weak background. The story is much different for the EPLD grown $ZnO/Pt/Al_2O_3$ which showed a strong emission in the violet region, labeled as the *Q*-band as shown in figure 5.4. *Q*-band emission showed a clear LO-phonon structure. The zero phonon line appeared to be at 3.25 eV which is roughly the same energy as the weak background peak observed in the PL from the EPLD grown sample shown in figure 5.4. Figure 4.11 (page 81) and figure 4.15 (page 87) show EPLD grown samples on bare sapphire with strong, broad emission around 3.25 eV. Despite the lack of LO-phonon structure the origin of the broad emission in those samples grown on bare sapphire could be the same as the *Q*-band of the

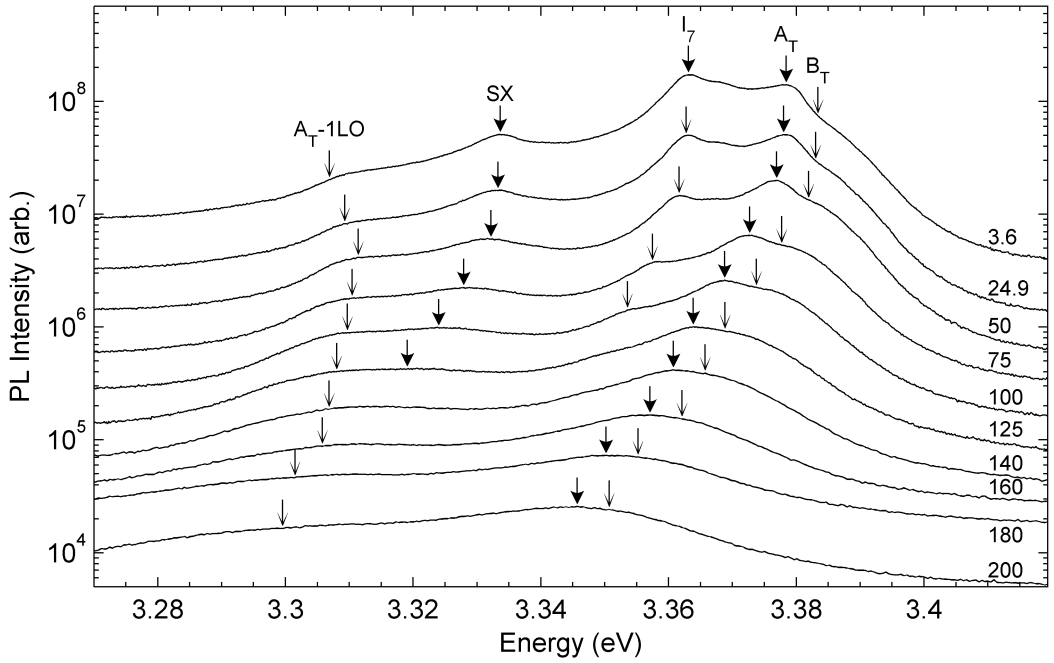

Figure 5.5: Temperature dependent PL emission from the PLD grown $ZnO/Pt/Al_2O_3$ (offset vertically for clarity). Temperature in Kelvin is shown to the right of the figure.

EPLD grown $ZnO/Pt/Al_2O_3$. Phonon structure of the Q-band in the ZnO/Al_2O_3 could have been washed out by inhomogeneities in the nanostructures. Defect related emission of the free to bound or DAP type are candidates for the origin of the Q-band, which by its line shape and energetic position, was not the LO-replica band of any of the observed excitonic transitions.

Figure 5.5 shows the temperature dependent PL emission from the PLD grown $ZnO/Pt/Al_2O_3$ (vertically offset for clarity). At low temperatures the spectra was dominated by the I_7 exciton which died out by 125 K as expected. Its emission energy followed the temperature dependence of the A_T transition, in contrast to the bulk and EPLD grown ZnO/Al_2O_3 from a Zn target. By 50 K the free excitonic emission dominated the spectra which was persistent up to room temperature. Laser scattering effects became a problem for higher temperatures and this data is not shown in figure 5.5. A_T^{1LO} was clearly seen in this sample and it followed the expected shift with temperature predicted by equation 3.21 (page 47) with $L = 1$. An Arrhenius plot of the A_T emission is shown in figure 5.6(a). A_T emission intensity decayed with typical Arrhenius behavior and the solid line in the figure shows the $\sqrt{I(T)}$-weighted least squares fit of the two path Arrhenius decay (equation 3.12, page 41) with E_b fixed at 60 meV. The relatively small 95%

confidence bounds indicate a good fit to the two path model. The [A, E_a] path, representing the nonradiative recombination of the free exciton, has an activation energy around 5 meV. This is two to three times smaller than the E_a values of the two path fit for the EPLD grown ZnO/Al_2O_3. The [A, E_a] path was the main PL quenching mechanism up until $T_E = 154.0 \pm 0.3$ K when the effect of the two paths were equal. [B, E_b] represents the thermal dissociation of the free exciton and it dominated the PL quenching at $T_D = 301.1 \pm 0.8$ K according to equation 4.2.

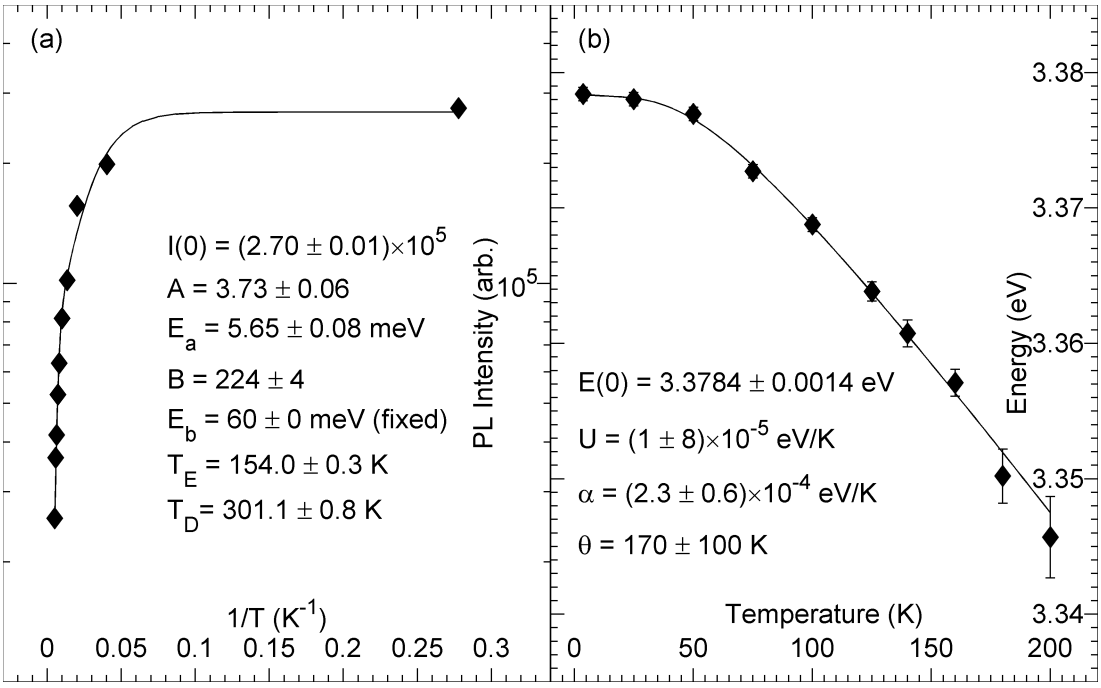

Figure 5.6: (a) Arrhenius plot of the PL intensity of the A_T peak in PLD grown $ZnO/Pt/Al_2O_3$. The solid line shows the $\sqrt{I(T)}$-weighted least squares fit of the two path Arrhenius decay (equation 3.12, page 41) with E_b fixed at 60 meV. (b) A_T emission energy as a function of temperature. The solid line is the weighted least squares fit to the modified Manoogian equation (3.17, page 44).

Arrhenius fitting was not carried out on the I_7 or SX peaks since they were only present in 5 spectra. More data points at lower temperatures would be needed to get reliable fits to the bound exciton emissions. Unfortunately this data was not gathered the first time and all of the (E)PLD grown samples showed significant degradation of the PL over time. All the PL data presented in this thesis was taken shortly after growth, within one or two weeks and sometimes the next day. ZnO is very sensitive to atmospheric conditions and will absorb many species from the environment. Surface contamination builds up over time, quenching the PL and preventing measurements on the samples after extended

periods. A more sophisticated sample storage system may be able to overcome this issue. Regrowing samples is an option but there are many issues regarding reproducibility for PLD. Usually, techniques to reproducibly grow useful materials will get patented, preventing publication of the recipe or the underlying physics.

Typical redshift of the exciton emission energies was observed as temperature was increased. Figure 5.6(b) shows the A_{T} position as a function of temperature. As mentioned previously, the shift of the other excitonic peaks (not including A_{T}^{1LO}) directly followed the A_{T} behavior. The modified Manoogian equation (3.17, page 44) provided a good fit as shown by the solid line in the figure which is the weighted least squares fit. Also shown are the fitted parameters with the 95% confidence bounds. Lattice dilation does not appear to effect this sample as the U parameter has a very large relative uncertainly. Furthermore, a fit using the Bose-Einstein equation (3.16, page 43), which does not include the U term yeilds essentially the same curve and α and θ values. Both the α and θ values are smaller than those found for the bulk ZnO sample and the (E)PLD grown ZnO/Al_2O_3. The relatively small number of data points which go only up to 200 K is the likely reason for the smaller θ value in this case.

Evolution of the PL from the EPLD grown $ZnO/Pt/Al_2O_3$ was very similar to the PLD grown $ZnO/Pt/Al_2O_3$ and is shown in figure 5.7. Emission at low temperature was dominated by the I_7 exciton, which decayed quickly with temperature and was unresolvable by 125 K. Similar decay was observed for the SX peak. In between $SX$and I_7 a faint peak was observed which was truly unresolvable by 25 K. It was 35 meV below the A_{T} peak which lies just below the energy range where acceptor bound exctions would be expected in ZnO.[21] Such a fast decay with temperature indicates that this peak was not excitonic and was likely due to some unknown defect. At 40 K the LPB_A peak dominated the PL emission which appeared to be taken over by A_{T} and B_{T} at 200 K. This sample was the only one out of all the samples grown by the author to show emission dominated by LPB_A at any temperature. This implies a strong exciton photon coupling in this sample which may have something to do with the unique morphology which has not been previously reported. Such strong exciton-photon coupling would make this type of material ideal for polariton experiments in optical resonator structures. However, it would be difficult to produce a high quality distributed Bragg reflector required for high optical confinement on the rough, brain like morphology of this sample.

Arrhenius fits to the intensity of the A_{T}, I_7, and SX excitons are shown in

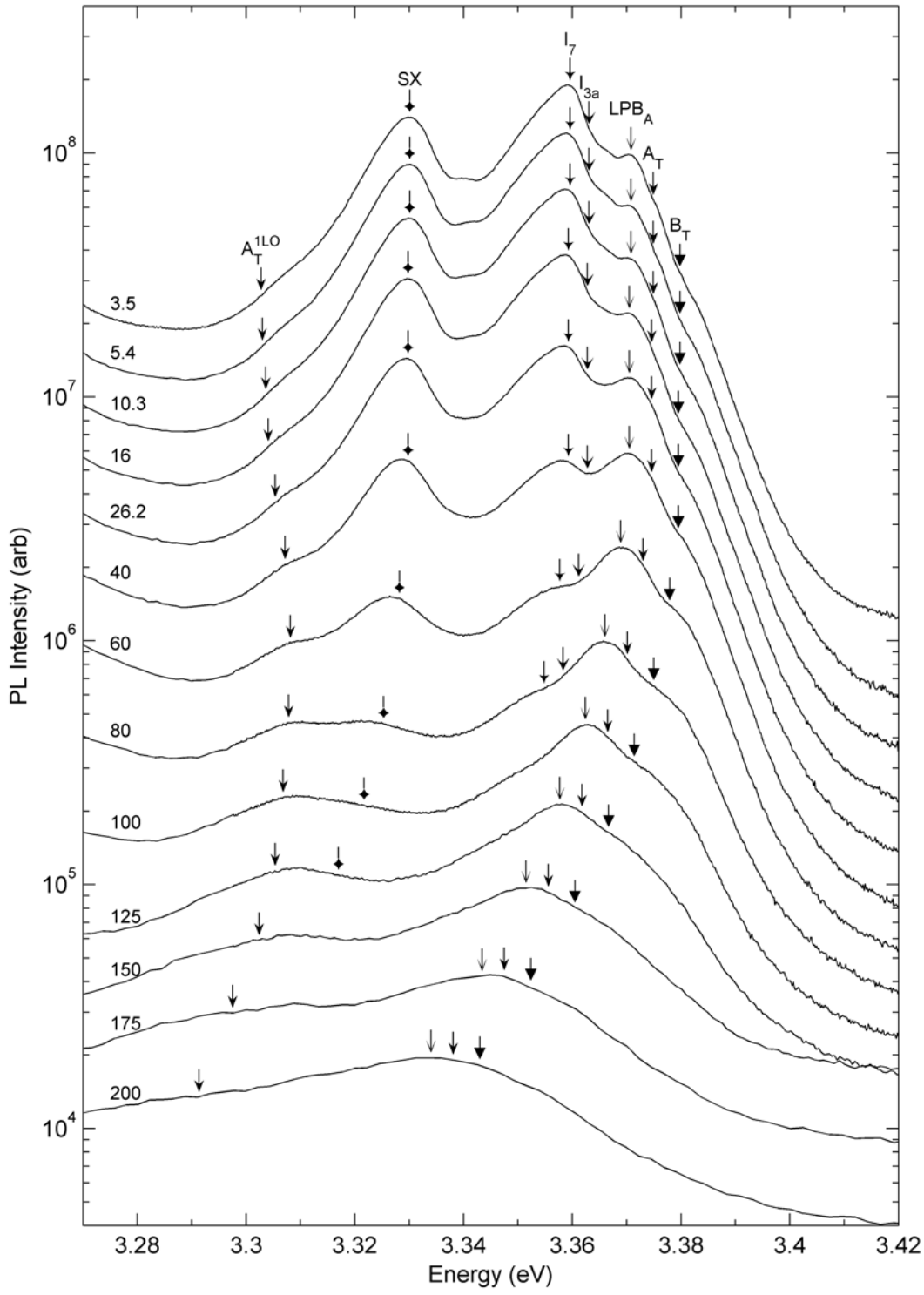

Figure 5.7: Temperature dependent PL from the near band edge region of EPLD grown ZnO/Pt/Al_2O_3 (offset vertically for clarity). Temperature in Kelvin is indicated to the left of the figure. Arrows were calculated from the position of the LPB_A peak using the energy spacings measured at 3.5 K

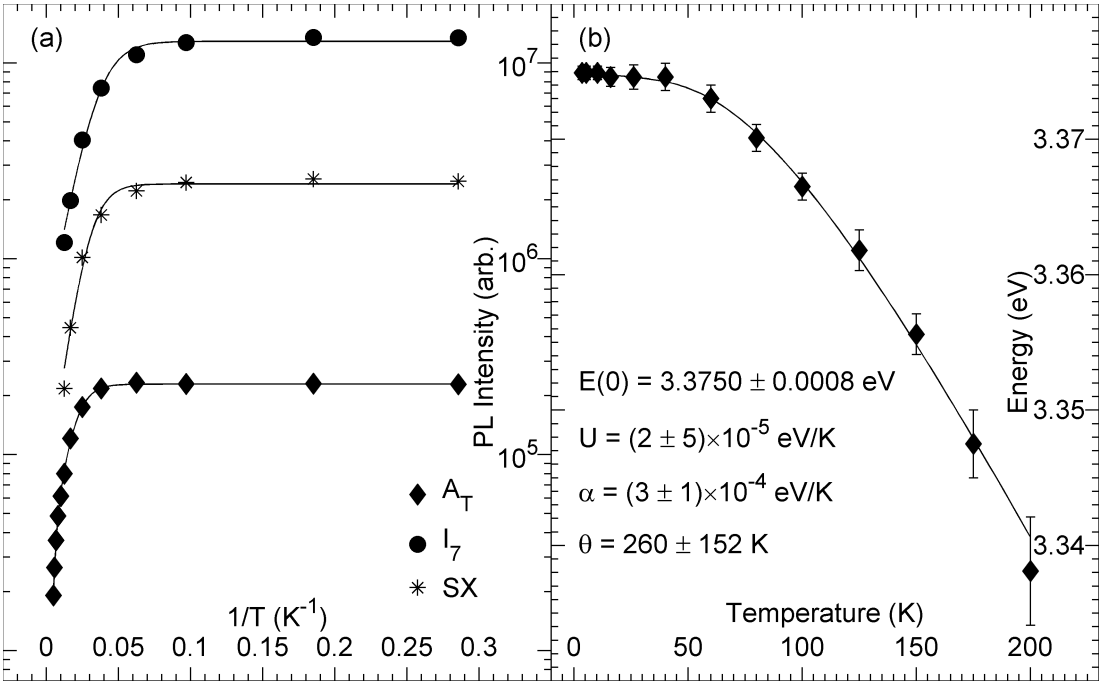

Figure 5.8: (a) Arrhenius plot of the PL intensity of the A_{T} and I_7 peaks in EPLD grown ZnO/Pt/Al_2O_3. A_{T} was fit with a two path Arrhenius decay (equation 3.12 page 41) while I_7 was fit with a single path (equation 3.11 page 41). (b) A_{T} emission energy as a function of temperature. The solid line is the weighted least squares fit to the modified Manoogian equation (3.17, page 44) with the uncertainties used for the weighting.

figure 5.8(a). Again, the data was weighted by the $\sqrt{I(T)}$ for both the A_{T} and I_7 fits. The two path Arrhenius decay (equation 3.12 page 41) was fit to the A_{T} intensity, providing an excellent fit with small confidence bounds as shown in table 5.1. For A_{T}, E_{b} was fixed at 60 meV, representing the thermal dissociation of the exciton. According to equation 4.2 (page 76), thermal dissociation of the exciton does not dominate the PL quenching for this sample until $T_{\mathrm{D}} = 632 \pm 9\,\mathrm{K}$, close to the temperature corresponding to $kT = 60\,\mathrm{meV}$. Non radiative recombination, with an activation energy of $E_{\mathrm{a}} = 9.8 \pm 0.2\,\mathrm{meV}$, was relatively efficient in this sample compared to the other (E)PLD grown samples. The nanopores seen on this sample could be inelastic scattering centers which induce nonradiative recombination of the A_{T} excitons though phonon emission. For the I_7 and SX bound excitons, a one path Arrhenius decay (equation 3.11 page 41) provided good fits. Activation energy of the I_7 peak was about half of its localization energy of 15 meV. This in contrast to the other samples grown from the same target on bare sapphire which had activation energies about 80% of the localization energy. The situation is even worse for the SX peak which had an activation energy

Table 5.1: Fitted constants to the decay and emission energies of the A_{L}, I_7, and SX PL peaks in EPLD grown ZnO/Pt/Al_2O_3. Energy shift of the I_7 and SX peaks followed that of A_{T}.

Model	Parameter	A_{T}	I_7	SX
Arrhenius (3.11 & 3.12)	$I(0)$ (arb.)	2.298 ± 0.0005	6.45 ± 0.01	4.83 ± 0.01
	A (arb.)	3.73 ± 0.06	26.2 ± 0.3	35.3 ± 0.6
	E_{a} (meV)	9.8 ± 0.2	8.04 ± 0.04	10.46 ± 0.06
	B (arb.)	176 ± 5	–	–
	E_{b} (meV)	60 (fixed)	–	–
Bose-Einstein (3.16)	$E(0)$ (eV)	3.3748 ± 0.0006	–	–
	α (eV/K)	$(3 \pm 1) \times 10^{-4}$	–	–
	θ (K)	230 ± 70	–	–
	χ^2_{R}	0.17	–	–
Manoogian (3.17)	$E(0)$ (eV)	3.3750 ± 0.0008	–	–
	U (eV/K)	$(2 \pm 5) \times 10^{-5}$	–	–
	α (eV/K)	$(3 \pm 1) \times 10^{-4}$	–	–
	θ (K)	260 ± 152	–	–
	χ^2_{R}	0.14	–	–

only about 25% of its localization energy. Non-radiative decay of the bound excitons, as opposed to delocalization from the binding center, is likely skewing these results. The SX exciton, being localized to the extended structural defects, would be effected more by nonradiative recombination if these defects were indeed inducing nonradiation excitonic recombination in the first place.

Redshifting of the excitonic peaks followed the expected trend as shown in figure 5.6(b). Energy of the free exciton was taken as the LPB_A energy minus 4.1 meV, since LPB_A was much easier to resolve in this sample. Error bars in the figure thus represent the uncertainty in obtaining the position of the LPB_A peak and were used to weight the least squares fits. Both the Bose-Einstein equation (3.16, page 43) and modified Manoogian equation (3.17, page 3.17) were fit to the data with fitted parameters and reduced χ^2_{R} values calculated with equation 3.18 (page 45) shown in table 5.1. $E(0)$ values for the two fits agree very well with each other and the values obtained for the bulk and (E)PLD grown samples presented in the previous two chapters. α and θ values for the two fits agree to within their uncertainties. This fact, along with the minimal reduction in χ^2_{R} value when adding the U parameter, implies that lattice dilation did not significantly effect the excitonic bandgap in this sample as well as the PLD grown ZnO/Pt/Al_2O_3.

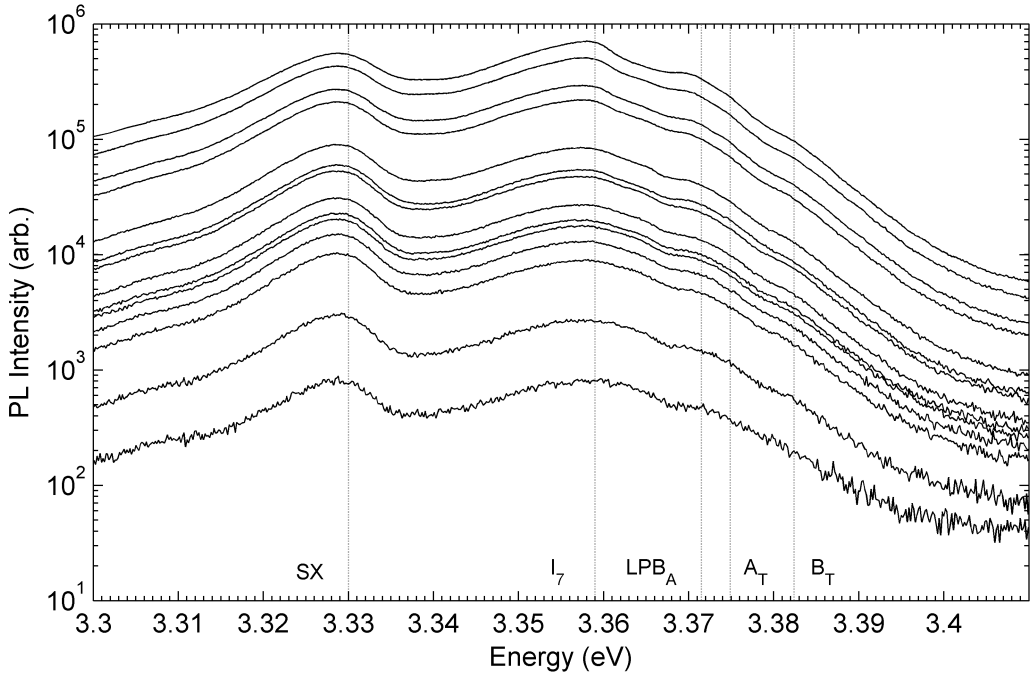

Figure 5.9: Low Temperature power dependent PL from the near band edge region of the EPLD grown ZnO/Pt/Al_2O_3.

Low temperature power dependent PL from the near band edge of this sample is shown in figure 5.9. Integrated intensity of the UV emission band showed linear dependence on the excitation intensity. Unfortunately, deconvolution of the spectrum into component peaks was not reliable. Close inspection of the figure shows the *SX* emission dominating at low excitation intensities, which eventually was overtaken by the I_7 emission as excitation intensity increased. This was not unexpected since I_7 showed a superlinear increase with excitation intensity in the ZnO/Al_2O_3. At the highest excitation intensities, the I_7 emission stared to sharpen up and appeared to be gaining intensity faster then the free excitons. Compared to the ZnO/Al_2O_3, the emission exponent for the I_7 peak would have been smaller in this sample. This indicates a fundamental difference in the dynamics of the I_7 exciton for the two different morphologies.

Some unusual PL emission was observed from the ZnO/Pt/Al_2O_3 at energies above the free excitons. Figure 5.10 shows this region for the EPLD grown ZnO/Pt/Al_2O_3 which had two weak, narrow peaks at 3.452 and 3.525 eV. The peak at 3.452 eV was observed in the (E)PLD grown samples on bare sapphire using the same metallic Zn target. These two peaks were separated from each other by 72.6 meV which is the LO-phonon energy in ZnO.[4] At low temperature

the 3.452 eV peak was also 72.6 meV above the B_{T} peak which, at first, suggested that these emissions were anti-Stokes LO-replicas, which have been observed in ZnO[110] and CdS[112]. However, these two high energy, weak peaks do not shift with temperature like the excitonic features do as indicated by the B_{T} arrows in figure 5.10. Anti-Stokes peaks should follow the energy dependence of their zero-phonon lines with the appropriate thermal corrections. Also, there are no features from the He-Cd laser in this energy region. Plasma lines from the laser are extremely sharp, like the one at 3.189 eV which shows up in several of the PL spectra presented in this thesis. The only origin for these two high energy peaks which is consistent with the emission energies and temperature dependence is hot exciton emission.[175]

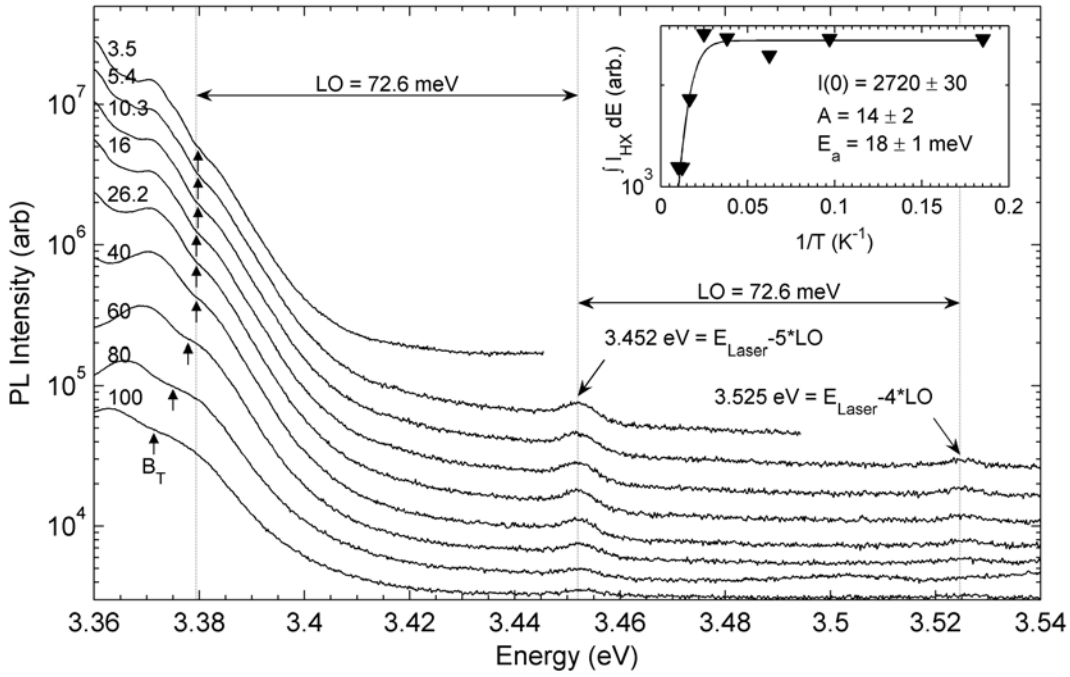

Figure 5.10: Temperature dependent PL from above the free exciton energy showing 2 peaks due to hot exciton emission (offset vertically for clarity). Temperature in Kelvin is indicated to the left of the figure. The inset shows an Arrhenius plot of the integrated intensity of the $HX_{5\mathrm{LO}}$ hot exciton as found from a Lorentzian peak fit with a cubic baseline.

Hot exciton emission is observed from excitons which have not yet thermalized with the lattice. When a photon from the He-Cd laser is absorbed in ZnO, an exciton with an energy of $E_{ex} = 3.815\,\mathrm{eV} - \hbar\omega_{LO}$ is created high up in the conduction band. $\hbar\omega_{LO}$ is the energy of the LO phonon which is simultaneously produced to conserve momentum, bringing the exciton to the correct part of its

dispersion curve. One way for the exciton to quickly thermalize with the lattice is to emit LO-phonons. This is due to their relatively high energy compared to most other phonons and the strong Frölich coupling in ZnO. In samples where the excitonic lifetime is short, radiative recombination of the exciton can occur before the exciton reaches thermal equilibrium with the lattice. This results in a series of small emission peaks, $HX_{m\mathrm{LO}}$, which are separated from the laser excitation energy by integer multiples, m, of the LO-phonon energy. By setting the LO-phonon energy to 72.6 meV, the two high energy peaks in the EPLD grown ZnO/Pt/Al_2O_3 were placed 4 and 5 LO-phonon energies below the laser to within 0.3 meV. Since the laser energy does not change, these peaks will not shift with temperature, as was clearly observed in figure 5.10. Thus, these two peaks were from the $HX_{4\mathrm{LO}}$ and $HX_{5\mathrm{LO}}$ recombinations. Photoluminescence excitation (PLE) spectroscopy would have provided unambiguous assignment of these $HX_{m\mathrm{LO}}$ but a tunable UV laser in the appropriate energy range was not available.

Hot exciton emission has been previously observed in bulk ZnO which was subjected to mechanical polishing.[152] Point defects were introduced by the polishing which decreased the radiative lifetime of the exciton by increasing the probability of nonradiative recombination. In the experiment by Hamby et al.[152] excitation was carried out with the 3.532 eV line from an Ar^+ laser which resulted in three narrow hot exciton peaks, $HX_{1-3\mathrm{LO}}$, with FWHM values of about 3 meV. In the EPLD grown ZnO/Pt/Al_2O_3, the FWHM of the $HX_{5\mathrm{LO}}$ peak was roughly 4 meV and its intensity was stronger than the $HX_{4\mathrm{LO}}$ peak, ruling out Raman scattering as the origin of these two features. Raman scattering could give peaks which are integer multiples of the LO-phonon energy below the excitation energy, but the 4^{th} order LO peak would be more intense than the 5^{th} order peak. Investigation of the high order Raman lines of ZnO by Kunert et al.[176] showed no 3^{rd} or 4^{th} order LO peaks. The tailing signal toward high wavenumbers in their study suggests 5^{th} order Raman peaks were also absent. Furthermore, Raman peaks are not expected to decay with increasing temperature,[154] which was not the case for the $HX_{4,5\mathrm{LO}}$ peaks in the ZnO/Pt/Al_2O_3. The inset of figure 5.10 shows an Arrhenius plot to the integrated intensity of the $HX_{5\mathrm{LO}}$ peak. A single Lorentzian peak on a cubic background was used to fit the $HX_{5\mathrm{LO}}$ peak to get the integrated intensities. A steep fall off in intensity was seen around 60 K and a single path Arrhenius decay (equation 3.11, page 41) with an activation energy of 18 ± 1 meV provided a decent approximation to the decay. Hamby et al.[152] show a similar decay in $HX_{m\mathrm{LO}}$ emission intensity but do not fit the data with any model.

According to Permogorov,[175] $HX_{m\mathrm{LO}}$ luminescence decays with temperature due to an increased probability of nonradiative recombination. This type of decay with increasing temperature is analogous to the [A, E_{a}] path of the two Arrhenius decay channel model for the free exciton discussed throughout this thesis.

For this EPLD grown sample the exciton lifetime must have been shortened by the high density of nanopore defects, allowing the $HX_{m\mathrm{LO}}$ peaks to be observed. A short free exciton radiative lifetime can explain the relatively high free exciton to donor bound exciton PL intensity ratio which was observed in all of the (E)PLD grown ZnO presented in this thesis so far. The free excitons simply did not have enough time to find a binding center before they radiatively recombine. Time resolved PL on these samples would be most useful but would require a pico or femtosecond laser, which was not available. So far only Hamby et al.[152] have observed $HX_{m\mathrm{LO}}$ luminescence in ZnO. However, $HX_{m\mathrm{LO}}$ peaks have been observed in several material systems,[152,177–179] with some groups using quantum well structures to increase the $HX_{m\mathrm{LO}}$ emissions.[177,179] It was found, by PLE, that when the laser excitation was an integer number of LO-phonon energies above an excitonic peak the emission of that peak was enhanced.[178] This could also be enhancing the free excitonic luminescence in the (E)PLD grown samples since the B_{T}/UPB$_A$ peak is 6 LO-phonon energies below the He-Cd laser (to within 0.5-1 meV).

It should be noted here that recent optical-pump THz-probe experiments on hydrothermally grown bulk ZnO indicate that excitons form after the photoexcited carriers cool until they are close to the excitonic bandgap.[180] Acoustical phonon scattering then relaxes the excitons down to the band minimum. This was deduced from the time dependence of the conductivity which is related to the time-dependent electric field strength and modulation of the THz probe pulse which transmits through the sample. Exciton formation in this manner would preclude the appearance of hot exciton emission indicating that exciton formation dynamics are different in the bulk ZnO studied by Hendry et al.[180], the mechanically polished bulk studied by Hamby et al.[152], and the ZnO samples produced by (E)PLD in this thesis. PLE, time resolved photoluminescence, and dephasing measurements using four wave mixing[179] would allow for truly unambiguous identification of the $HX_{m\mathrm{LO}}$ peaks. Such experiments would help to uncover the nature of the different exciton formation mechanisms in different ZnO morphologies.

In the blue/violet region this sample showed a strong, broad, and structured

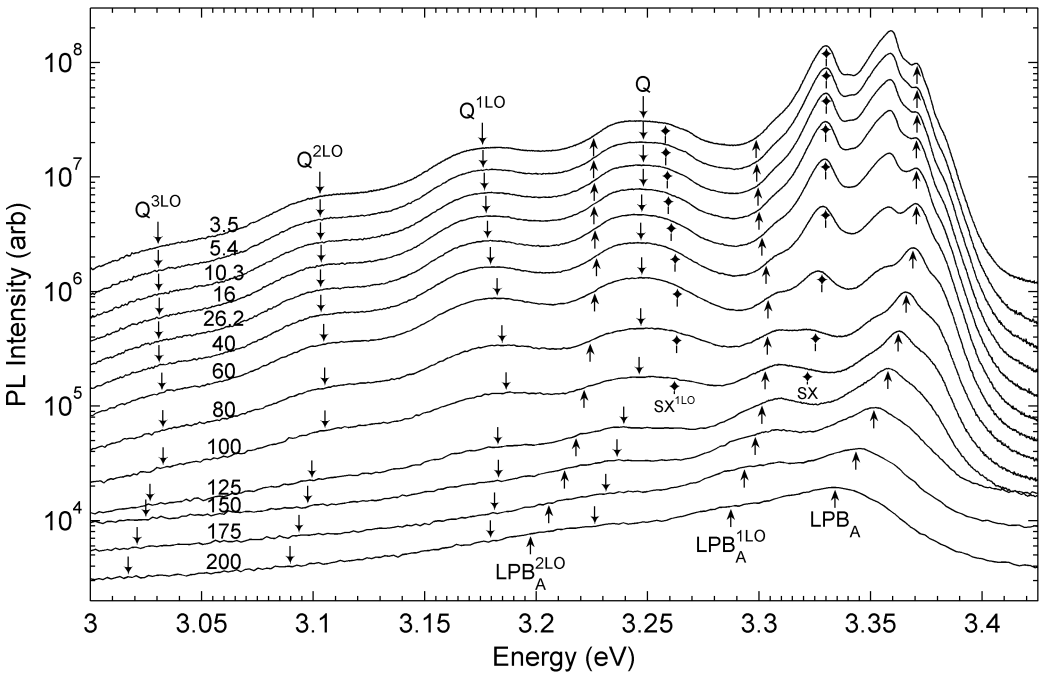

Figure 5.11: Temperature dependent PL from the blue/violet region of the EPLD grown ZnO/Pt/Al_2O_3 (vertically offset for clarity). Positions of LPB_A, SX, and their 1LO-phonon replicas are indicated below the graphs showing that zero-phonon line of the Q-band emission is not a phonon replica.

emission band as seen in the temperature dependent PL shown in figure 5.11. What appears to be a zero-phonon line was centered at 3.245 ± 0.005 eV at 3.5 K which was accompanied by 3 clear LO-phonon replicas. It showed anomalous behavior with respect to temperature and excitation intensity and is labeled as the Q-band. At low temperature the line shape of this transition resembled a flattened Gaussian suggesting the presence of more then one emission component to the band. As temperature was increased the flattened nature of the peak became slightly rounded. Position of the SX^{1LO} peak is indicated in figure 5.11 which may have been one of the components of this Q-band. Blueshifting and decay of this high energy component could cause the rounding of the band at higher temperatures. Position of the Q-band did not directly follow the bandgap, showing essentially no shift until the temperature was raised above 100 K as shown in figure 5.12(a). Energetically, the Q-band was in the DAP region of ZnO with several reports of violet DAP emission in ZnO.[16,152,181,182] However, DAP emissions are expected to blueshift initially with increasing temperature due to redistribution of carriers to short-lived, close pairs and thermal hopping processes.[183] For this EPLD grown ZnO/Pt/Al_2O_3, the bandgap shrinking with

increasing temperature could balance such an initial blueshift until the redshifting dominated at higher temperatures. Such a balancing act is dependent on donor and acceptor concentrations and would be expected to vary from sample to sample.

Variation of the bandgap, with and without a thermal correction term are shown by the dotted lines in figure 5.12(a). Decent agreement to the shift of the DAP peak was obtained by adding $k_{\mathrm{B}}T/2$ to the shift from the bandgap. This thermal correction is the same as that for eA^0 peaks which accounts for the kinetic energy of the free electrons in the conduction band. An eA^0 origin for this 3.25 eV peak, could account for its emission energy and the observed shift with temperature. This would imply an acceptor binding energy of 190 meV which is close to the substitutional N_O binding energy measured in sputtered N:ZnO films[150]. However, an eA^0 origin of this peak is unlikely as the sample was not intentionally doped and there is a large donor concentration as indicated by the intense D^0X emission. As such, the presence of acceptors in naturally n-type materials like ZnO would usually lead to DAP emission before an eA^0 peak is observed. In fact it is quite likely that the $k_{\mathrm{B}}T/2$ correction is simply a coincidence and the Q-band is neither a common DAP nor a free-to-bound transition.

An Arrhenius plot of the absolute PL intensity of the Q-band emission is shown in figure 5.12(b). A single channel Arrhenius decay (equation 3.11, page 41) provided a nice fit with the solid line in the figure showing the $\sqrt{I(T)}$-weighted least squares fit. An activation energy of $E_{\mathrm{a}} = 24.3 \pm 0.3$ meV was extracted which is considerably smaller than the 50-70 meV expected for DAP emission in ZnO. Ionization of the shallow impurity is the channel which usually quenches DAP luminescence with increasing temperature[81] and for ZnO the donor is the shallow impurity with binding energies in the 50-70 meV range.[4,16,21,152,184]. The measured activation energy is also significantly smaller than the 190 meV expected for an eA^0 peak at this energy. Temperature broadening will result in an underestimated activation energy when using absolute intensities but this Q-band did not seem to broaden significantly and errors should be minimal.

The three LO-replicas from the Q-band followed the expected energy shift with temperature according to equation 3.21 (page 47) with $L = 1, 0$, and 0 for the 1^{st}, 2^{nd}, and 3^{rd} LO-phonon replicas. A Huang-Rhys factor of $S = 0.6 \pm 0.2$ at $T = 3.5$ K was calculated by fitting equation 3.8 (page 36) to the normalized intensities of the zero phonon line and its 3 LO-replicas. S increased slightly to

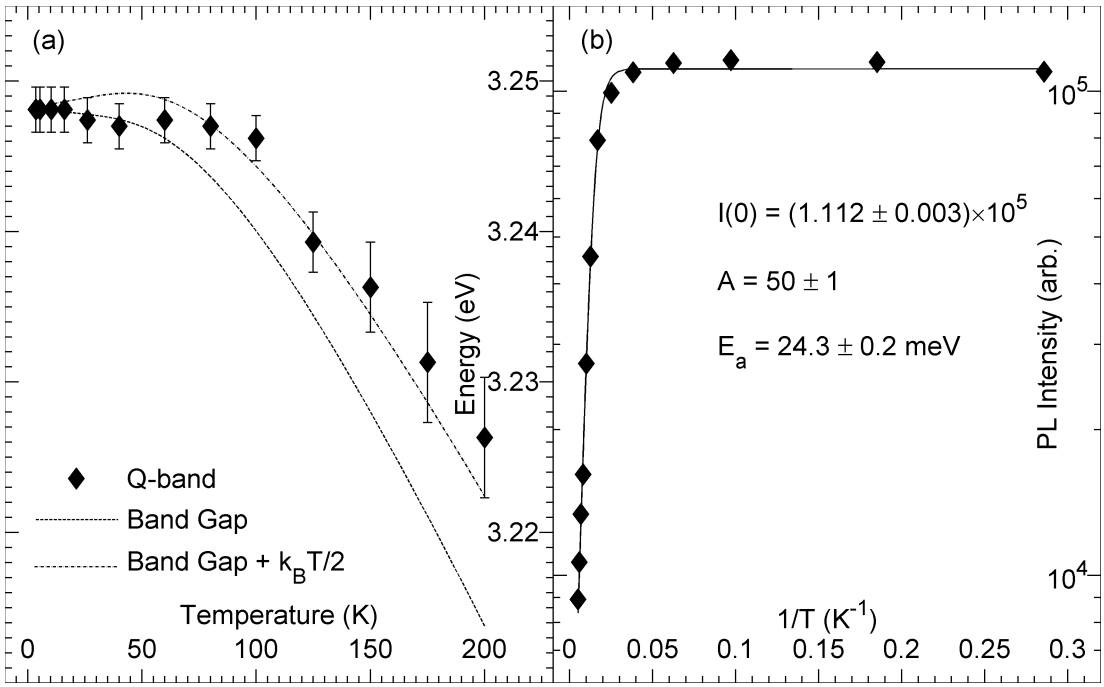

Figure 5.12: (a) Emission energy of the Q-band. The bandgap variation with and without a thermal correction term are also shown.(a) Arrhenius plot of the Q-band emission. The solid line is the $\sqrt{I(T)}$-weighted least squares fit to the one channel Arrhenius decay (equation 3.11, page 41). Fitted parameters and 95% confidence bounds are shown.

0.8 ± 0.2 as temperature was raised to 200 K (uncertainties are the 95% confidence bounds). Absolute intensities were used for calculation of S but the value and uncertainty did not change at all when integrating the spectra over windows as large as 40 meV. This S-factor was comparable to $S = 0.41 \pm 0.01$ reported for DAP emission at 3.21 eV by Hamby et al.[152] Their calculation was based solely off the intensity of the zero phonon line and the first LO-replica using $S = I_1/I_0$. However, no comment was made about wether integrated intensities were used or how the very low uncertainty was estimated. In this study, the intensity distribution of the zero-phonon line and 3 LO-replicas were used in a least squares data fitting algorithm. S-factors calculated in this way may give a large uncertainty which is realistic since S is calculated from 4 independent data points as opposed to just one. Combining this least squares technique with proper line-shape fitting (such as that in reference 185), would give the most realistic estimate of S. However, the complex shape of the Q-band and its unknown origin prevented such a line fitting proceedure.

PL as a function of excitation intensity of the blue/violet emission from the

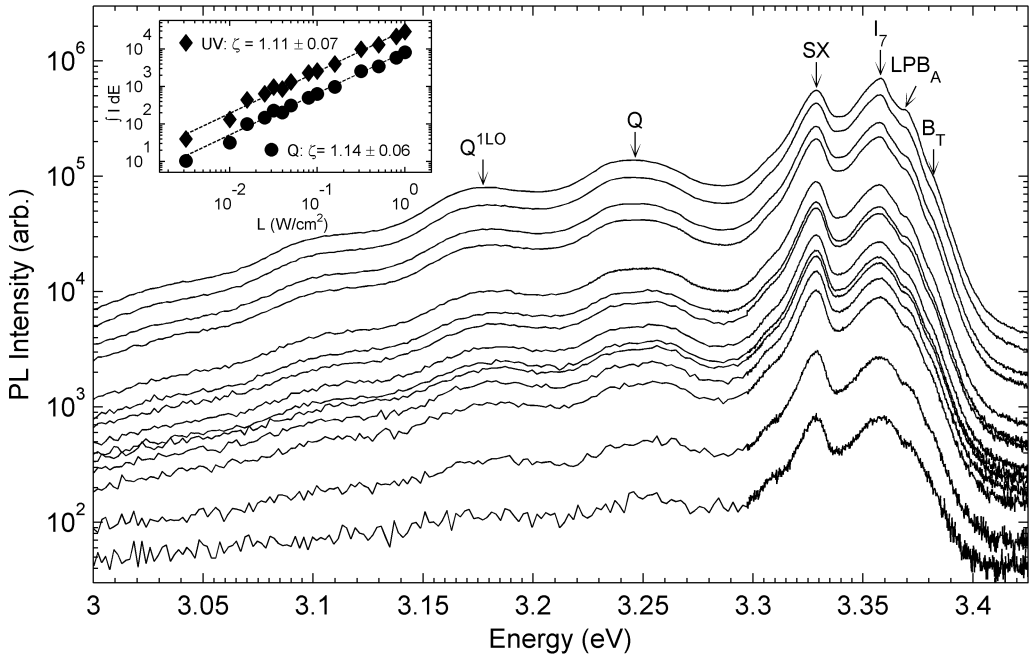

Figure 5.13: Power dependent PL from the EPLD grown ZnO/Pt/Al_2O_3. Integrated intensity of the UV and Q-band as a function of excitation intensity, L, is shown in the inset. Both show typical power law behavior with surprisingly similar exponents.

EPLD grown ZnO/Pt/Al_2O_3 is shown in figure 5.13. There was no noticeable blueshift of the Q-band with increasing excitation intensity. This is more evidence against a DAP origin of this emission but is still not enough to rule it out completely. As discussed in section 3.8, emission of DAP peaks will usually blueshift with increasing excitation intensity and emission intensity typically follows the usual $I \propto L^{\zeta}$ power law with an exponent $\zeta < 1$.[116,131] Hamby et al.[152] and Thonke et al.[181] both report DAP emission in the 3.2-3.25 eV range for undoped bulk ZnO but surprisingly neither group reported on the power dependence. Jiao et al.[186] report DAP emission at 3.26 eV which does shift in N-doped ZnO epilayers grown by MBE. If the Q-band had a classic DAP origin, a low concentration of compensated donor-acceptor-pairs may have lead to a vanishing blueshift with increasing excitation intensity. With a low concentration of compensated donor-acceptor pairs, the lowest laser power may have photoneutralized most of the donor-acceptor pairs. Hence, increasing the laser power further would not noticeably decrease the average distance of the pairs. Also, DAP emission has been observed to shift by substantially different amounts with laser power for different samples as observed for GaAs implanted with various impurities.[183] Yu et al.[183] showed a correlation between the amount the DAP band shifted and the

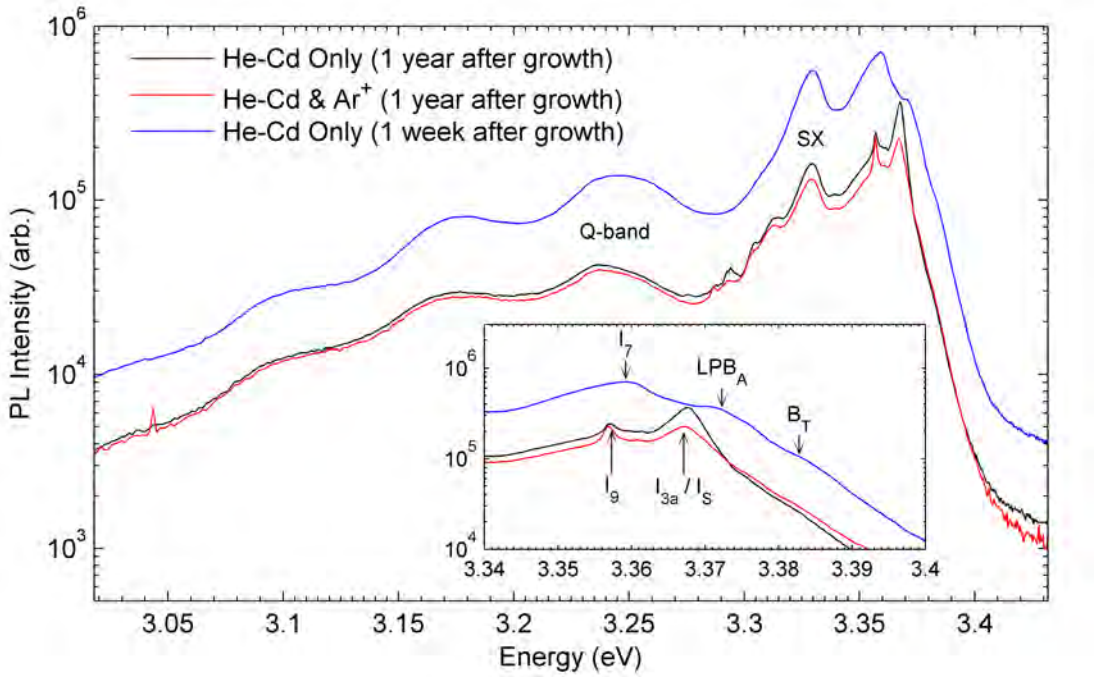

Figure 5.14: Effect of age and simultaneous below-gap optical pumping using 400 mW of the 515.4 nm line from an Ar^+ laser. Unfortunately, simultaneous pumping with the Ar^+ laser was only attempted for the later experiment.

impurity concentration; the more impurities the larger the blueshift with some of the purer samples showing blueshifts of only 1 meV per order of magnitude increase in excitation intensity.

However, with such a low concentration of compensated donor-acceptor pairs, the intensity of the DAP peak would be expected to saturate quickly with increasing excitation intensity. This was clearly not the case for the Q-band as shown in the inset of figure 5.13. Q-band emission from the EPLD grown ZnO/Pt/Al_2O_3 increased roughly linearly ($\zeta = 1.14 \pm 0.06$) with excitation intensity. This is most surprising as exponents between 1 and 2 usually indicates excitonic behavior.[131,132] Unfortunately, Yu et al.[183] did not report on the emission intensity of the GaAs samples which showed a large range of blueshifts with increasing excitation intensity. Nor did Jiao et al.[186] report on the emission intensity of the DAP peak observed in their PL study. Considering the broad width and low energy, an excitonic origin for the 3.25 eV emission in this sample is highly unlikely.

Further evidence that Q-band emission is not excitonic is seen in figure 5.14 which shows the PL when simultaneously pumping the sample with below-gap

photons. As with the bulk sample, 400 mW of 515.4 nm light from an Ar^+ laser was used to create additional free carriers in this EPLD grown ZnO/Pt/Al_2O_3. Ar^+ laser scatter was more of an issue for this sample then the bulk and its full background was removed from the data. No luminescence features were observed from solely Ar^+ pumping. As discussed in section 3.9 (page 54), bound excitons are screened by the free carriers created by the Ar^+ laser. A clear decrease in the D^0X emission due to the Ar^+ laser can be seen in the inset of figure 5.14. Integrated intensity of the D^0X band decreased to 83% of its value without Ar^+ excitation. A small redshift of 0.25 meV was observed due to bandgap renormalization from the free carriers. On the other hand, the Q-band retained 95% of its intensity when the sample was subjected to Ar^+ laser light, ruling out the possiblilty of a very deeply bound excitonic origin for the Q-band.

The anomalous behavior with respect to temperature, excitation intensity, and below-gap excitation of the Q-band point toward to an unconventional origin. Neither DAP nor eA^0 transitions can adequately explain the observed behavior. Isolated impurity transitions, such as those seen for Er-doped ZnO [187] also cannot account for the Q-band emission due to the broad width and strong coupling to the LO-phonons. Simultaneous below-gap pumping shows this Q-band is not excitonic, as the power dependence would indicate, and must be due to a defect related transition. The slightly superlinear dependence of the Q-band intensity could perhaps be explained by DAP or eA^0 transition involving a defect center which is created optically. Photoionization of neutral defects could be occurring due to the He-Cd laser and the Q band could be due to a charged DAP or eA^- transition involving double donors and/or double acceptors. Such transitions have not been reported in the literature. However, pumping with the below-gap Ar^+ line should create enough free carriers to neutralize the ionized defects, quenching luminescence of such a peak. Considering all the anomalies, the origin of the Q-band remains questionable at this time. Spatially and temporally resolved PL measurement may be able to shed some light on such anomalous PL emission bands.

Aging effects of the low temperature PL from the EPLD grown ZnO/Pt/Al_2O_3 are also shown in figure 5.14. Simultaneous pumping with the below-gap Ar^+ laser was carried out nearly a year after growth. A relatively strong PL signal was still obtained after such a long time but there was a profound change in the features near the band edge. Free excitonic emission could no longer be resolved after a year indicating degraded crystal structure. Emission from the I_7 transition

disappeared, leaving behind a clear peak in the I_{3a}/I_S region and a peak near the I_9 energy. Indium donors are the origin of the I_9 emission,[16] and its surprising to see an indium signature from this sample after a year. No indium at all was introduced into the HV chamber and none was detected by the manufacturer of the Zn target. A different origin is possible for this peak, which likely occurred in all the samples grown from the metallic target. It was simply overwhelmed by the I_7 emission in all cases. To understand the effect of age on EPLD grown ZnO and why the I_7 peak disappeared, a controlled experiment studying the effect of aging on the PL spectrum of various ZnO samples would be required. Storage of the samples under different conditions along with periodic PL measurements may reveal interesting impurity and defect dynamics occurring over large time scales. This information would be valuable for improving the lifetime of ZnO based gas sensors or other applications where the ZnO is exposed directly to the environment.

Platinum buffer layers are a viable option for ZnO growth by (E)PLD onto sapphire. Unique morphologies were observed which showed strong, sharp UV luminescence. Emission from the samples deposited on Pt/Al_2O_3 was composed of essentially the same emission features as those deposited on bare sapphire. Hot exciton emission was identified in these samples, which was also present in the ZnO/Al_2O_3 samples. This is evidence for a short excitonic radiative lifetime which can explain the high free excitonic emission intensity in all the (E)PLD grown samples. Anomalous emission was observed from the EPLD grown $ZnO/Pt/Al_2O_3$ in the violet region. This so called Q-band emission has a questionable origin and has yet to be observed in any other sample. Understanding this emission may be key to improving the quality of the EPLD grown $ZnO/Pt/Al_2O_3$. Only the surface of EPLD grown $ZnO/Pt/Al_2O_3$ was scratched in this study and optimizing this material system will undoubtedly yield interesting physics and novel devices.

5.2 Low Temperature ZnO Buffer Layers

Of course, the best surface to grow ZnO on is high quality bulk ZnO wafers. Thin ZnO films with purity and crystal quality exceeding that of the ZnO substrate have already been realized.[107] Fortunately, ZnO bulk wafers produced by various means from several different suppliers are readily available. This is not always going to be the case for a given material. Also, homoepitaxial growth has the

obvious disadvantage of being limited to that particular substrate which could be relatively expensive and hard to integrate into devices. Perhaps the next best thing to homoepitaxial growth of any material is the use of a thin buffer layer of that material grown at a reduced temperature. By using these low temperature (LT) buffer layers, growth of a wide range of materials can be achieved on unconventional substrates.

At low growth temperatures, adatoms depositing on the substrate will not have a high mobility and a high concentration of point defects will be generated in the layer. The effect will be enhanced for systems with a high lattice mismatch. When subsequent growth proceeds at an elevated temperature, the strain at the interface between the LT-buffer layer and the new growth is most easily released by generation of dislocations in the defect ridden LT-buffer layer. This was clearly observed by Chen et al.[188] when growing $Si_{1-x}Ge_x$ on top of Si using an LT Si-buffer layer. TEM observations after annealing of the sample showed propagation of threading dislocations through the LT-buffer layer toward the substrate and no dislocations were observed in the $Si_{1-x}Ge_x$. For ZnO growth, it was reported that employment of an LT ZnO buffer layer resulted in a decrease in dislocation density of an order of magnitude for samples grown by plasma-assisted MBE.[189] As a result, significant improvement in the electron mobility was observed for the sample grown on the LT-buffer but there was a lot of room for improvement.

For this thesis, employment of a LT-buffer for ZnO grown by (E)PLD from a Zn target is discussed. Buffer layers were grown in situ by simply ablating the target for a short while with the substrate at a reduced temperature. O_2 pressure for all growths discussed in this section was maintained at 100 mTorr for buffer and main layer growth and during the temperature ramp in between. Laser spot size was kept at 1.5 mm^2 using the circular aperture plate and the fluence for all growths was 4 J/cm^2. Substrate to target distance remained unchanged at 53 mm. For the EPLD growths the shadow mask was placed half way between the target and substrate. All the samples discussed in this section were grown from a different metallic Zn target than those discussed in chapter 4 and section 5.1 since the surface of that target was very heavily used. This is not normally a problem for EPLD growth as the increased particulate concentration originating from a well-used surface gets blocked by the eclipsing object. However, samples grown by standard PLD were required for comparative purposes and these samples would be adversely effected by a well-used surface. The two targets were from the same supplier but the target used to grow the LT-buffer layer samples had a

higher Pb impurity concentration of around 30 ppm. Aside from this difference, growth conditions for these LT-buffer samples were very similar to the previously discussed (E)PLD grown samples.

For comparison between PLD and EPLD growth of ZnO using a LT-buffer layer, a series of 4 samples was grown. For each method, two samples were grown using LT-buffers deposited at 300 and 400 °C. In order to get layers of similar thickness, the PLD samples were grown for 1 h and the EPLD samples were grown for 2 h. Buffer layer growth took place for 1 min for the PLD grown sample and 2 min for the EPLD grown samples. Figure 5.15 shows SEM images from this sample series. Images (a)-(d) were from the two samples grown by standard PLD and (e)-(h) show the EPLD grown samples. Growth temperature of the buffer layer is indicated in the bottom left of the images.

A much different morphology was observed for the LT-buffer samples as opposed to those grown on unbuffered Al_2O_3 or the Pt/Al_2O_3. For both PLD grown samples the particulate density was surprisingly small as indicated in figure 5.15(a) and (c). Cross-section of the PLD grown sample shown in figure 5.15(c) revealed the $T_{BL} = 300\,°C$ PLD grown sample was deposited as a continuous film with a rough, nanorod-like surface. Thickness after a one hour growth was roughly 380 nm as shown in figure 5.15(b). This gave a growth rate of 0.12 Å/pulse (6 nm/min). This is comparable to the PLD produced $ZnO/Pt/Al_2O_3$ growth rate of and 0.09 Å/pulse (5.6 nm/min) observed for the PLD growth on unbuffered Al_2O_3. Sharp crystal edges and hexagonal shaped features were seen on some of the surface structures indicating a good degree of crystallinity. The highly textured surface is characteristic of a 3D growth mode. As such, the film would be expected to be polycrystalline with a high density of grain boundaries. As seen in figure 5.15(c) and (d), increasing the buffer layer temperature to 400 °C for the PLD grown ZnO did not seem to significantly effect the morphology. The only change was quite subtle with the $T_{BL} = 400\,°C$ PLD grown sample perhaps showing less voids on the surface and more contact between the surface nanostructures.

SEM images from the EPLD grown samples in figure 5.15(e)-(h) show a dense array of nanorods was formed in the EPLD geometry. With $T_{BL} = 300\,°C$, the nanorods grew off the substrate at angles of about 30° with respect to the substrate normal. Top down images show the in plane orientation of the nanorods was along 3 principle directions separated equally by 120° as indicated by the black arrow in the inset of figure 5.15(e). Thickness of this layer of tilted nanorods

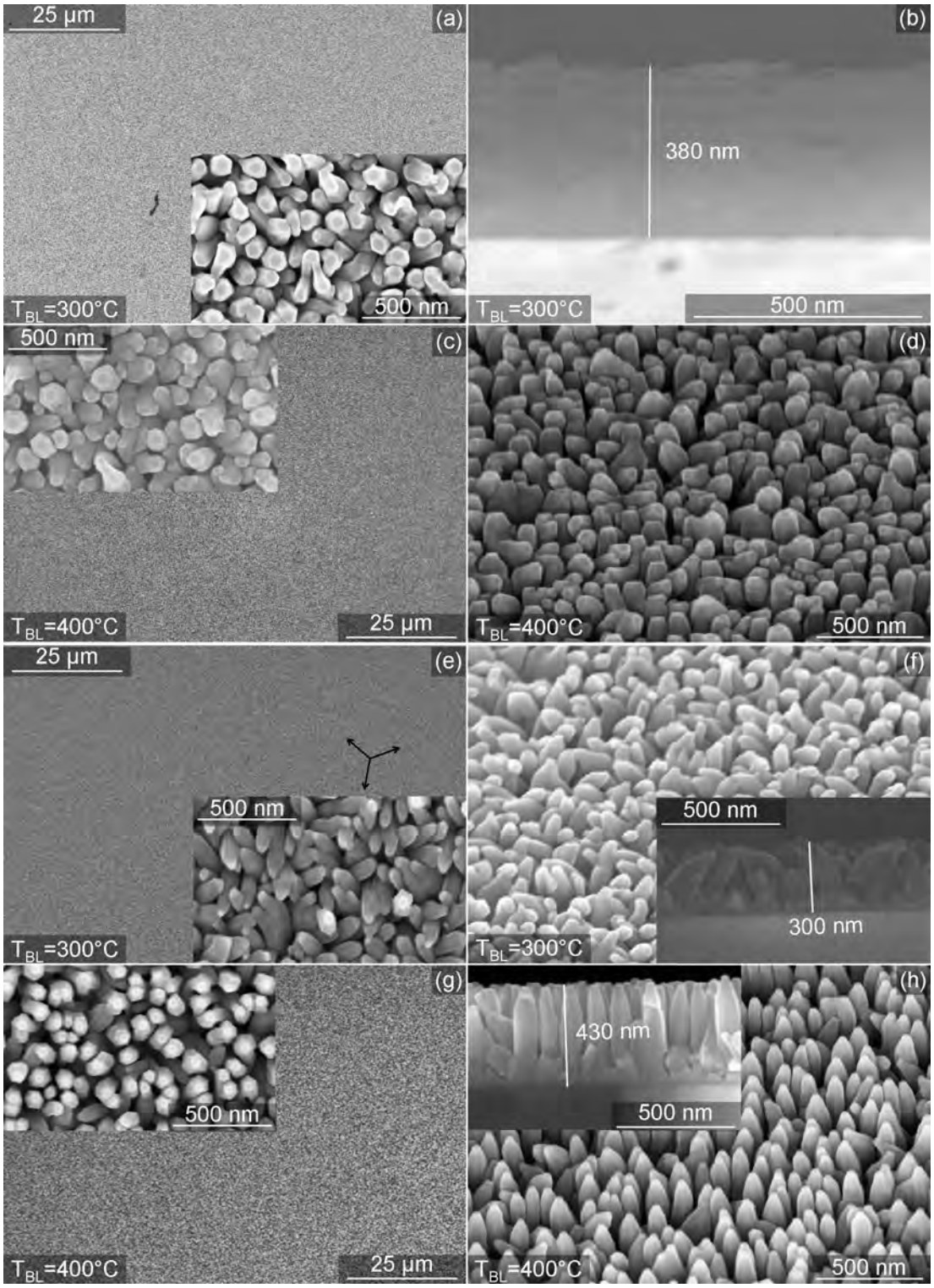

Figure 5.15: SEM images of PLD grown (a-d, top 4 images) and EPLD grown (e-h, bottom 4 images) ZnO using low temperature ZnO buffer layers. Buffer layer growth temperature is shown at the bottom left. Tilted images (d,f,h) were taken at a 45° angle and (b) shows a cross-section.

was roughly 300 nm as seen in the SEM cross-section, increasing by .04 Å/pulse (2.5 nm/min). Increasing the buffer layer growth temperature to $T_{BL} = 400\,^{\circ}C$ had a profound effect on the orientation of the nanorods. In this case the rods preferentially grew perpendicular to the substrate with a few pointing in similar directions to the tilted $T_{BL} = 300\,^{\circ}C$ array. Nanorod length for $T_{BL} = 400\,^{\circ}C$ was about 430 nm, noticeably longer and thinner than the tilted array grown at $T_{BL} = 300\,^{\circ}C$. Growth rate of these rods was about .06 Å/pulse (3.6 nm/min). Rod number density was about $75\,/\mu m^2$, similar to that for the PLD grown nanorod array on unbuffered Al_2O_3. Mass deposition rate for the two EPLD LT-buffer growths were essentially identical and the difference in orientation and aspect ratio of the nanorods between the two EPLD grown samples accounts for the large difference in layer thickness of these samples.

Close inspection of the top down and tilted SEM images of figure 5.15(e)-(h) show the presence of small capping particles. This implies a VLS growth mechanism, similar to growth by EPLD on unbuffered sapphire. Such capping particles were not easily observed for the PLD grown LT-buffer samples but were still seen on the end of several of the surface structures. Introduction of a low temperature ZnO buffer layer has been shown to efficiently suppress the VLS growth mechanism for ZnO nanorods grown on Si by PLD from a ZnO target.[65] Sun et al.[65] proposed that the low temperature buffer layer created a high density of ZnO nanocrystallites which acted as nucleation sites for vapor-solid (VS) growth. The difference here is likely due to the use of a Zn metallic target which produced a more Zn rich growth environment. The LT-buffer layers grown from the metallic Zn target were likely composed of thin solid films of ZnO_x with x noticeably less than 1. Heating the buffer layers from 300 to 600 °C in the oxygen ambient would have crystallized them into solid ZnO layers with stoichiometry closer to one to one. Subsequent growth at 600 °C in Zn-rich conditions would have produced liquid Zn droplets. These droplets may have been attracted to individual nanocrystallites in the LT-buffer layer, organizing themselves into a dense arrangement on top of individual grains in the buffer layer. VLS growth would proceed from these droplets leading to the observed nanorod morphologies. For the PLD grown samples, the lateral growth rate was sufficiently high enough for these rods to conglomerate together into a nanocrystalline film. At $T_{BL} = 400\,^{\circ}C$, the grains in the PLD grown film would have grown into a columnar shape with good alignment along the c-axis, giving a film with less voids and defects. This was likely due to a larger spacing between the initial Zn-droplets which had no nanocrystallite ZnO layer to use as a template.

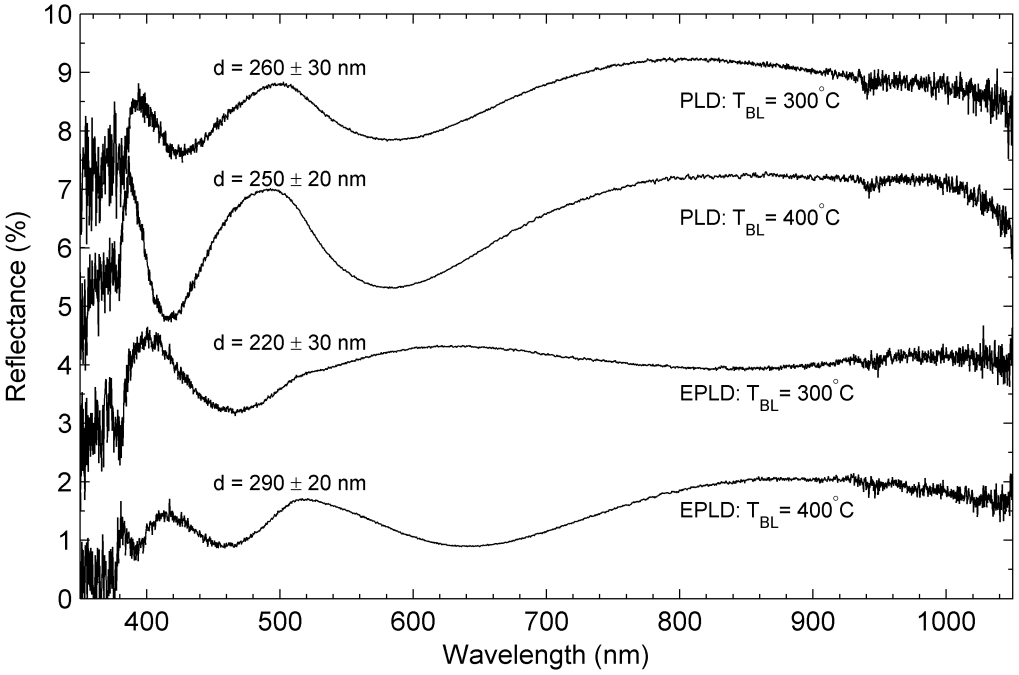

Figure 5.16: Normal incidence reflectivity of PLD and EPLD grown ZnO using LT-buffer layers (offset vertically for clarity). Thickness estimates from equation 5.1 are shown above the spectra.

Thin-film interference patterns were easily observed by eye on all 4 of the samples in this series. Figure 5.16 shows the normal incidence reflectance as measured by the OceanOptics reflectance probe (spectra offset for clarity). Reflectance values were less than 3% for all samples across the visible range, implying low absorption and high transmittance of visible light as expected for high quality ZnO. Reflectance was taken at several positions over each sample, with the PLD $T_{\mathrm{BL}} = 300\,^{\circ}\mathrm{C}$ sample showing the largest variation in signal over the surface. Thickness from equation 5.1 (page 111) is shown above each spectra and was calculated using the same method outlined in section 5.1.1. The uncertainty represents the variation in the signal over the sample, showing roughly 10% deviation over the surface. These thickness values were consistently about 70% less than those determined by cross-sectional SEM (xSEM) for both the PLD and EPLD grown samples. Examination of equation 5.1 shows that an overestimated refractive index leads to an underestimated thickness and decreasing the refractive index by 75% across the spectrum equates the thicknesses from reflectance to the xSEM values.[†] Such a large variation in refractive index would be quite surprising. Voids in the sample could reduce the effective refractive index but

[†] n effectively changes from 2 to 1.5 at 500 nm and from 2.7 to 2 at 300 nm.

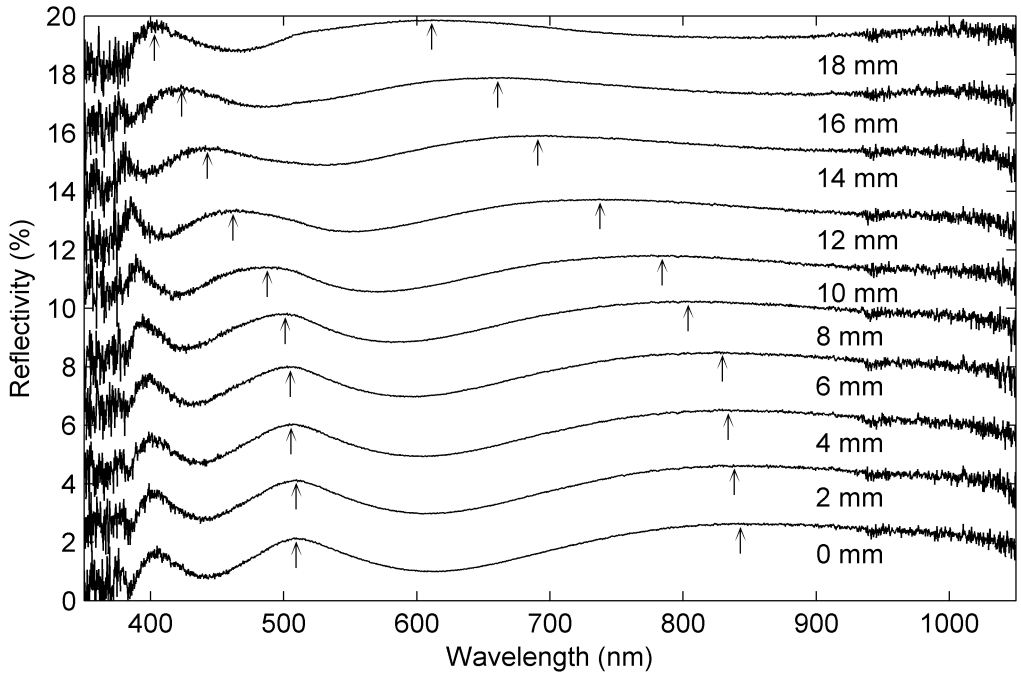

Figure 5.17: Normal incidence reflectivity across the EPLD grown $T_{\mathrm{BL}} = 300\,^{\circ}\mathrm{C}$ sample (offset vertically for clarity). Position from the left hand side of the sample is shown to the right of the figure. Thickness was measured using the fringe indicated by the arrows as this was the only one present across the entire sample.

the effect should be significantly more pronounced for the EPLD grown samples. However, the high density of grain boundaries in the PLD grown samples may also be reducing the effective refractive index by playing a similar role to the voids in the EPLD grown samples.

As mentioned previously, the PLD grown sample with $T_{\mathrm{BL}} = 300\,^{\circ}\mathrm{C}$ showed the most variation in reflectance across the sample. Figure 5.17 shows the reflectance as a function of position on the PLD $T_{\mathrm{BL}} = 300\,^{\circ}\mathrm{C}$ sample. Fringe-spacing decreased going from left to right indicating an increase in thickness toward the right hand side. Arrows in the figure show the evolution of a single fringe, measured from maxima to maxima, across the sample. This fringe is the only one visible in every scan. Thickness as a function of position based off of this fringe is shown in figure 5.18. Experimental geometry is shown to the right of the figure indicating the orientation of the sample with respect to the incoming laser beam on the right hand side (RHS). The laser spot on the target was aligned with the center of the substrate to within 1-2 mm with careful note of which side of the sample was the right and which was the left.

The observed variation in thickness was a direct result of the angular distribution of the material in the plume. For laser induced plumes the angular distribution of material is described by $f(\theta) = \cos^p(\theta)$ where $1 < p < 20$ for most materials ablated under typical PLD conditions and θ is the angle indicated in the diagram of figure 5.18.[53] Higher p values mean a narrower distribution and a more forward-directed plume. When depositing the plume onto a flat substrate, which is the usual PLD geometry as indicated in figure 5.18, the thickness of the film is described by $T(\theta) = f(\theta)\cos^3(\theta)$ since the plume flux in a small solid angle element, $d\Omega$, is deposited on a substrate-area element $dA = (d_{TS})^2 d\Omega/\cos^3(\theta)$.[53] Thus, thickness distributions would be expected to have a $T(\theta) = \cos^{p+3}(\theta)$ form on the substrate. However, figure 5.18 shows an asymmetric distribution about $\theta = 0$ meaning a $T(\theta) = \cos^{p+3}(\theta)$ type distribution can not be fit to the data. Plume steering toward the laser, as mentioned in section 2.2, was the origin of the asymmetry.

In the simplest case, plume steering by an angle ϕ will result in an angular material distribution of the form $f(\theta) = \cos^p(\theta - \phi)$. Including a normalization constant D_0, the film thickness can then be described by

$$T(\theta) = D_0 \cos^p(\theta - \phi)\cos^3(\theta). \tag{5.2}$$

Even if normalized distributions are used for fitting the D_0 constant is necessary for a proper fit since $\cos^n(\theta - \phi)\cos^3(\theta)$ never reaches 1 for $\phi \neq 0$. The solid line in figure 5.18 is a weighted least squares fit of equation 5.2. Uncertainties in the thickness measurements represent the spread in measured thickness values when considering the uncertainty in the position of the reflectance maxima. The plume distribution factor was found to be $p = 5 \pm 3$ indicating a rather diffuse plume compared to many materials cataloged in reference 53. Angular distribution of the plume is highly dependent on many of the growth parameters such as fluence, spot size, laser-pulse width, ablation wavelength, target composition and ambient gas pressure.[53,190] Simulations show that by varying the laser parameters alone p can be varied from 2 to 12.[190]

A plume turning angle of $\phi = 7 \pm 1^\circ$ was extracted which represents the effective turning angle as the plume turned throughout the growth. The maximum steering angle is thought to be half of the incident angle of the laser as measured from the target normal.[53] At the beginning of the growth the plume will steer quickly and then slowly approach the maximum angle, in this case 22.5°. This

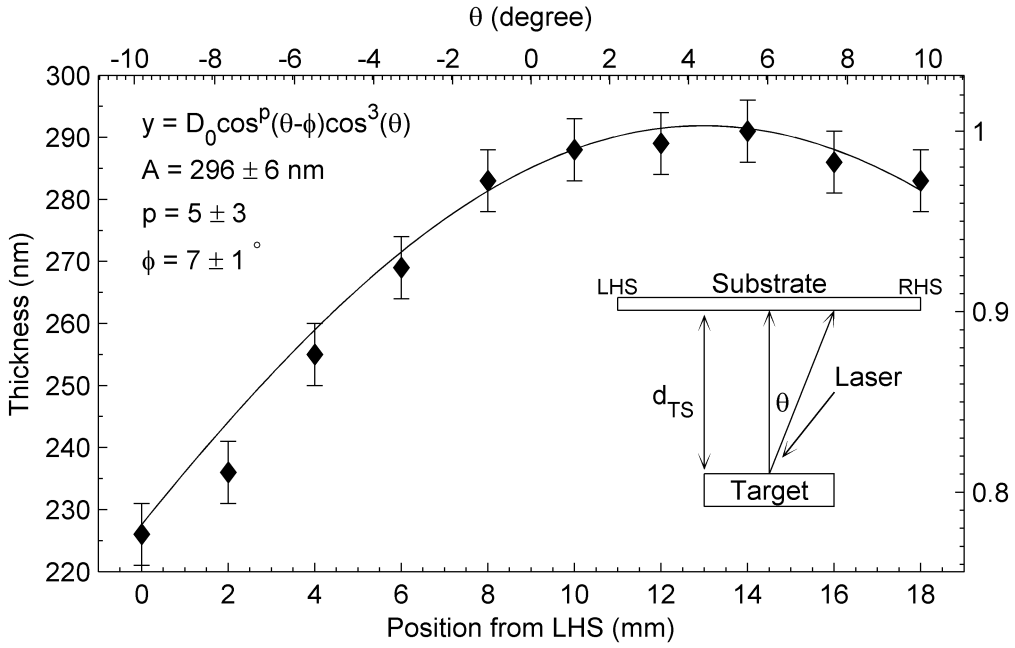

Figure 5.18: Thickness across the PLD $T_{\mathrm{BL}} = 300\,^{\circ}\mathrm{C}$ sample as found from reflectance. Solid line shows the fit of equation 5.2 with the fitted parameters and 95% confidence bounds listed to the left. Deposition geometry is shown to the right indicating the angle θ and direction of incoming laser beam. Right hand y-axis shows the normalized thickness.

sample was the first sample grown from the fresh target face indicating that after one hour of ablation the plume steered by a third of its maximum. Typically, PLD is carried out for one hour or more emphasizing the need to take plume steering into account when optimizing PLD for thickness uniformity. Equation 5.2 could also be applied to the tilted PLD technique which places the substrate at a non-normal angle with respect to the plume propagation direction.[191] In that case ϕ would represent the acute angle between the plume propagation direction and the substrate normal. Exploration of the model described by equation 5.2 for both on and off-axis PLD would provide a quick measure of the optimum geometry which leads to maximum uniformity. More sophisticated integral techniques more closely simulating the process would be the best,[190] but a simple model makes it much easier to find good starting parameters for optimization experiments.

All samples showed strong UV photoluminescence at low temperature as shown in figure 5.19. At 4 K the samples glowed a violet color with a bit of an orange hint under UV excitation with very little green emission observed by the eye or PMT. Orange emission is not easily observed with the Spex1700 spectrometer

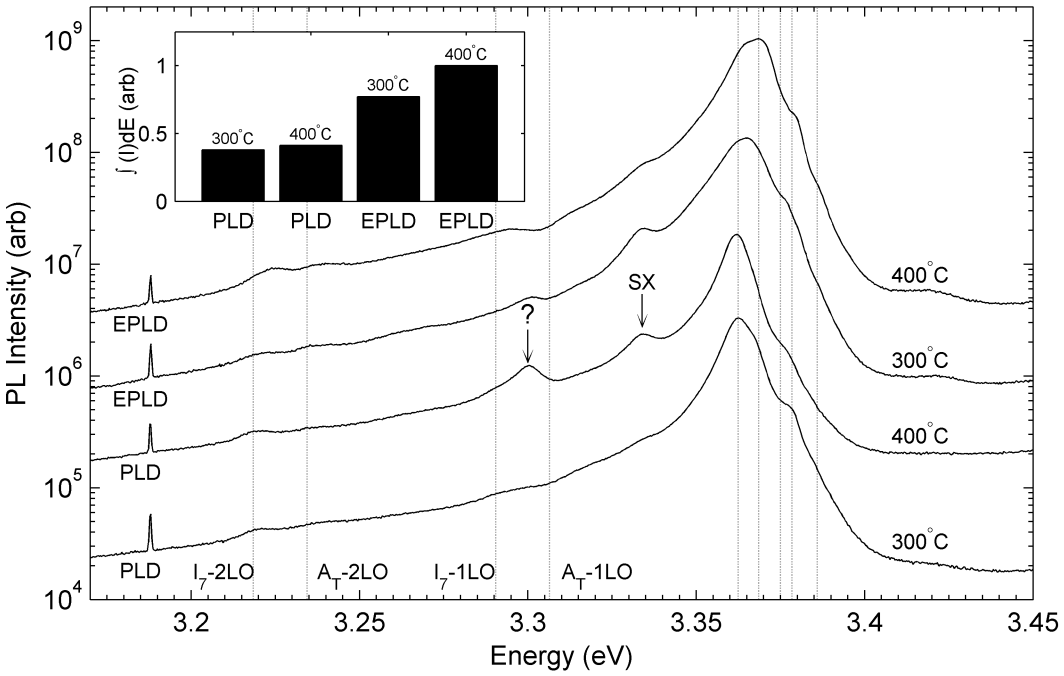

Figure 5.19: Photoluminescence at 4 K from ZnO grown by PLD and EPLD with LT-buffer layers (offset vertically for clarity). Buffer growth temperature is indicated above each spectra to the right. Dotted vertical lines at high energies show the positions of the B_{T}, A_{T}, LPB_A, $I_{3\mathrm{a}}$, and I_7 excitons.

due to second order diffraction of the laser and NBE PL features. Integrated intensity of the UV emission is shown in the inset of the figure. As with growth on the unbuffered sapphire, the EPLD produced samples with significantly higher UV emission intensities than PLD. In this case the increase was only by a factor of 2 as compared to the order of magnitude increase for unbuffered Al_2O_3 shown in figure 4.12 (page 83).

For both the PLD and EPLD geometries, the integrated PL intensity of the $T_{\mathrm{BL}} = 400\,^{\circ}\mathrm{C}$ samples was higher than that for the $T_{\mathrm{BL}} = 300\,^{\circ}\mathrm{C}$ samples. In the PLD case the increase was only by 8% compared to the nearly 30% increase for the EPLD geometry. This can be explained by the different effect the buffer layer had on the morphology of the PLD and EPLD grown samples. Morphology of the PLD grown LT-buffer samples was relatively unchanged when changing the buffer layer growth temperature. Compare this to the profound impact that T_{BL} had on the alignemnt of the EPLD grown nanorods. The better alignment achieved with $T_{\mathrm{BL}} = 400\,^{\circ}\mathrm{C}$ for EPLD grown ZnO would have reduced the number of defects introduced when two tilted rods grew into each other. A decrease in the relative intensity of the SX band was observed for the EPLD grown samples when

$T_{BL} = 400\,°C$, showing a reduced number of dislocation loops. Such dislocation loops may have been the result of collisions between nanorods during growth, which were suppressed by the hotte buffer layer. Line width of the PL from the EPLD grown ZnO decreased for $T_{BL} = 400\,°C$ and free excitonic emission was more easily resolved. This further indicates an improved crystallinity for the hotter buffer layer in the EPLD geometry.

The story seems the opposite for the PLD grown self-buffered ZnO. Despite the small increase in integrated PL intensity, the appearance of the SX and another unknown peak at 3.301 eV when PLD growth was on top of a $T_{BL} = 400\,°C$ buffer layer indicates a degraded crystal structure. These peaks were not seen in emission from the PLD $T_{BL} = 300\,°C$ samples. Furthermore, the relative intensity of the free excitonic shoulder compared to the D^0X band in the PLD $T_{BL} = 400\,°C$ sample was significantly less than that for the PLD $T_{BL} = 300\,°C$ sample. Kinetic energy distributions of the adatoms as they reach the substrate and the substantially different growth rates may play a key-role in the difference in PLD and EPLD growth dependence on T_{BL}. For now, this phenomena was merely observed and understanding its true nature would require many more experiments and a wider range of characterization techniques.

Figure 5.20 shows the emission from the EPLD $T_{BL} = 300\,°C$ and the unbuffered EPLD grown [150 mTorr, 33 mm] sample. These samples were chosen for comparison as they have the sharpest lines from each sample series. The inset of figure 5.20 shows that the emission from the LT-buffer samples was composed of the same peaks as the unbuffered samples, which is to be expected. However, in order to line up the near-band-edge peaks a -1.5 meV shift had to be applied to the LT buffered sample. This shift was not due to calibration error as the 3.189 eV plasma line from the He-Cd laser lined up between scans to within 0.3 meV. This shift meant the peak positions of the buffered sample were blueshifted by 3 meV compared to the bulk, twice as much as the unbuffered samples. Strain effects, which can cause such a blueshift, should be *less* pronounced in the LT-buffer samples. A different mechanism is likely responsible for the blueshift in the EPLD grown ZnO. A Moss-Burstein band filling effect [192] can cause a blueshift but this is only observed in intentionally doped. ZnO [193] Also, bandgap renormalization due to a high carrier concentration may counteract the Moss-Burstein effect in ZnO. Quantum size effects, another cause of blueshifted PL in nanostructures, should also be minimized in all the (E)PLD grown samples due to the small excitonic Bohr radius in ZnO. [4]

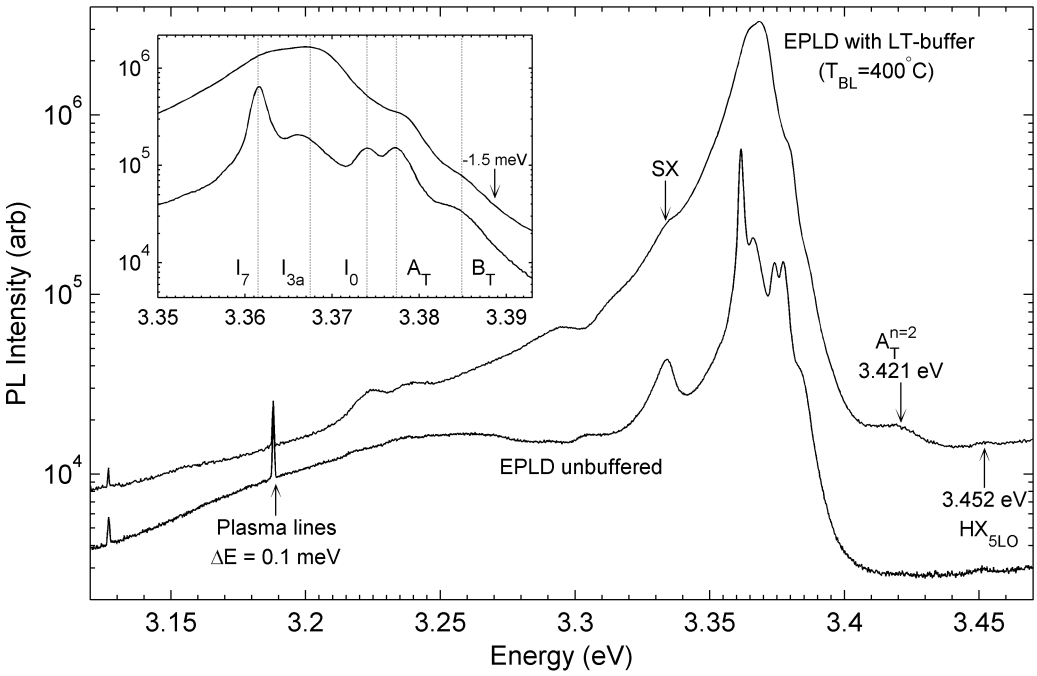

Figure 5.20: Low temperature PL of EPLD grown ZnO with and without a LT buffer layer (offset vertically for clarity). The unbuffered sample is the [150 mTorr, 33 mm] and the buffered sample is the EPLD $T_{\mathrm{BL}} = 400\,^{\circ}\mathrm{C}$ sample. Inset shows a magnification of the band edge with a -1.5 meV shift to line up the emission peaks. No shift was applied to the main graph.

Room temperature PL was observed from all the samples as shown in figure 5.21. For these measurements the spectrometer slits were opened to 250 μm and a 2400 lines/mm diffraction grating was used. This gave a sampling bandwidth of about 1.5 Å. The use of such wide slits in room temperature scans will often pick up a UV peak at 3.51 eV which has been observed from excitation of the Ag-paste used to mount the samples to the cold fingers. It is surprising that this emission can be measured since the substrates were only polished on one side. Plus, the absorption of 3.51 eV photons in ZnO is quite strong as they are above the bandgap. This peak was identified during attempts to measure PL from a nanocluster film of SnO_2 deposited on double-sided quartz. PL emission from the ZnO in the UV range was peaked at 3.30 eV and was due to free excitonic emission along with a phonon side band, as has been previously observed in ZnO.[127,156,185] Free exciton emission at room temperature from these samples is an indication of good quality ZnO.

Weak green emission around 2.45 eV was observed in three of the samples. This green emission was not seen by eye and the samples looked an eerie violet-

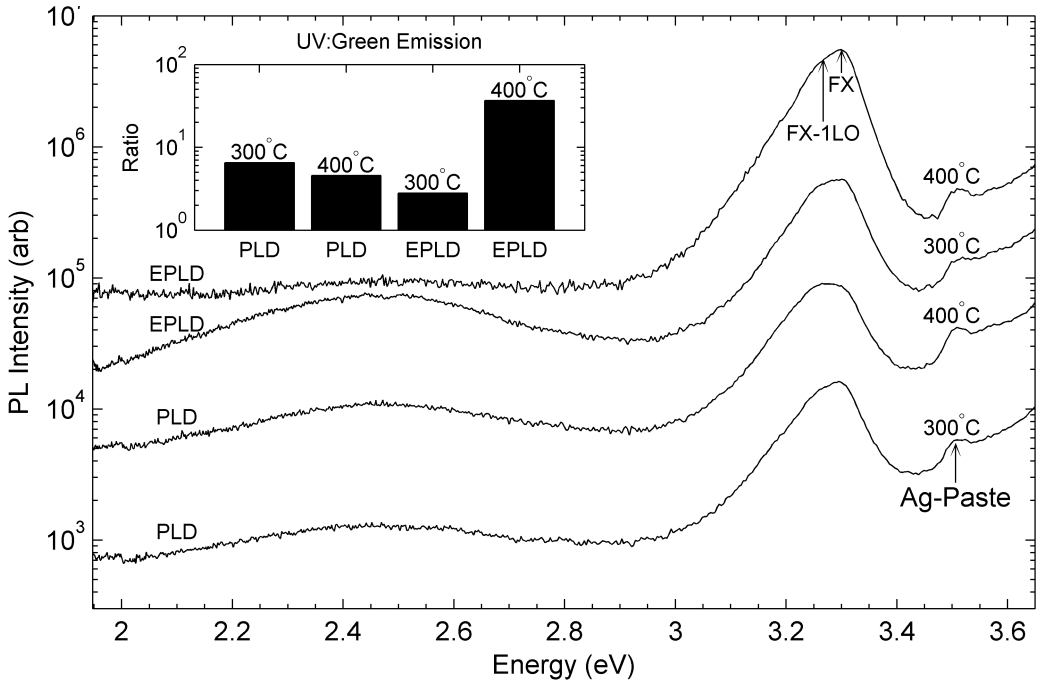

Figure 5.21: Room temperature PL from ZnO grown by (E)PLD using LT-buffer layers (offset vertically for clarity). Buffer layer temperature is indicated to the right of the figure. Inset shows the ratio of the integrated UV to green band emission after laser scatter was removed.

orange color under UV excitation. Essentially no emission was detected in the visible region from the EPLD $T_{\mathrm{BL}} = 400\,^{\circ}\mathrm{C}$ sample. Visible emission in ZnO, and in all wide-gap semiconductors, is due to defect states and usually has a free-to-bound or DAP type character.[14,25] The UV to visible emission intensity ratio can give a measure of the relative quality between samples analyzed with identical optical arrangements. All four samples shown in figure 5.21 were placed in the cryostat simultaneously with no change in the arrangement of any of the optics or spectrometer slit widths. The inset of the figure shows this ratio for each of the samples (note the log scale). Laser scatter, which was responsible for the high energy tail, was removed for this calculation by fitting of the tail end of a Gaussian centered on the laser energy to the data above the Ag-paste emission.

The UV:green ratio decreased with increasing T_{BL} for the PLD growth and increased with T_{BL} for EPLD growth. Like the low temperature results, this suggests that a hotter buffer layer is good for EPLD growth but not for PLD growth. The EPLD $T_{\mathrm{BL}} = 300\,^{\circ}\mathrm{C}$ sample showed the lowest ratio indicating that the defects causing the green emission in these samples can be induced by collisions between rods during the growth. Alternatively, the defects may be a

result of the same unknown phenomenon which causes the rods to tilt in the first place. The situation is complicated by the fact that there are several known origins for the green emissions in ZnO.[14] Confidently assigning them to a particular transition requires excellent correlations to independent measurements such as TEM, deliberate doping studies, or measurements of impurity concentrations. In any case, both the low and room temperature PL suggest that hotter buffer layers are good for EPLD growth but not for PLD grown ZnO from a metallic target.

Low temperature buffer layers had a profound effect on the morphology and light emission from (E)PLD grown ZnO. PLD growth led to continuous films with a high density of grain boundaries and a rough nanorod-like surface. Optically smooth layers were produced by both PLD and EPLD as evidenced by thin-film interference fringes observed by eye and in the reflectance spectra. For the EPLD geometry, a dense array of nanorods was formed whose alignment was dependent on the temperature the LT-buffer layer was deposited at. For $T_{\mathrm{BL}} = 400\,^{\circ}\mathrm{C}$ the nanorods grew perpendicular to the substrate with excellent overall alignment. At $T_{\mathrm{BL}} = 300\,^{\circ}\mathrm{C}$ the rods were tilted colliding with each other during growth which lead to an increase in emission from the *SX* defect-bound exciton. Deep level emission was also suppressed for EPLD growth when using the hotter buffer layer. The opposite was true for PLD growth where the low and room temperature PL suggested the cooler buffer layer led to better structural quality. Hence, what works for one technique does not necessarily produce the best results for another very closely related method. In this study, only a small fraction of the possibilities for buffer layers was explored. Essentially an endless supply of investigations into buffer layer structures can be conceived and picking the right experiments is necessary for timely progress toward a given application.

Chapter 6

Pb-implanted Bulk ZnO

6.1 Motivation and Implantation

Despite being studied for nearly 50 years, there are still many mysteries regarding the origin of the various sharp features in the excitonic spectrum of ZnO. Identifying the chemical origin of these features has been the subject of several investigations involving diffusion studies[16], doping studies using epitaxial films[194], and ion-implantation into bulk crystals[195]. Knowing the origin of specific excitonic features makes PL spectroscopy a powerful tool for quick, non destructive impurity analysis. Sensitivity as high as one part in 10^{10} has been reported for various impurities in Si.[196] For the bulk sample discussed in chapter 3, assignments of essentially all the peaks in the near band edge region was achieved by matching localization energies with the accepted literature values (see reference 16). Applying the same technique to the EPLD samples showed that the I_7 exciton dominated the PL of most of the samples produced from the Zn metallic target. So far the chemical origin of I_7 has not yet been identified and the EPLD grown samples may provide a clue into discovering it.

According to the manufacturer, the dominant impurity in the Zn targets used for (E)PLD growth of ZnO in this thesis was lead. The majority of the samples were grown from a target with 12 ppm Pb, giving samples with 0.001 at % Pb. Those flims which were presented in section 5.2 were grown from a Zn target having a Pb concentration of 30 ppm (0.003 at %). Considering this, it seems likely that a Pb-related complex could be responsible for the I_7 bound exciton. To date there have been several investigations into Pb incorporation into ZnO, in both unintentionally[197] and deliberately[198–201] doped samples. However, the low temperature PL spectrum of the near band edge region of intentionally Pb-doped ZnO has not yet been reported.

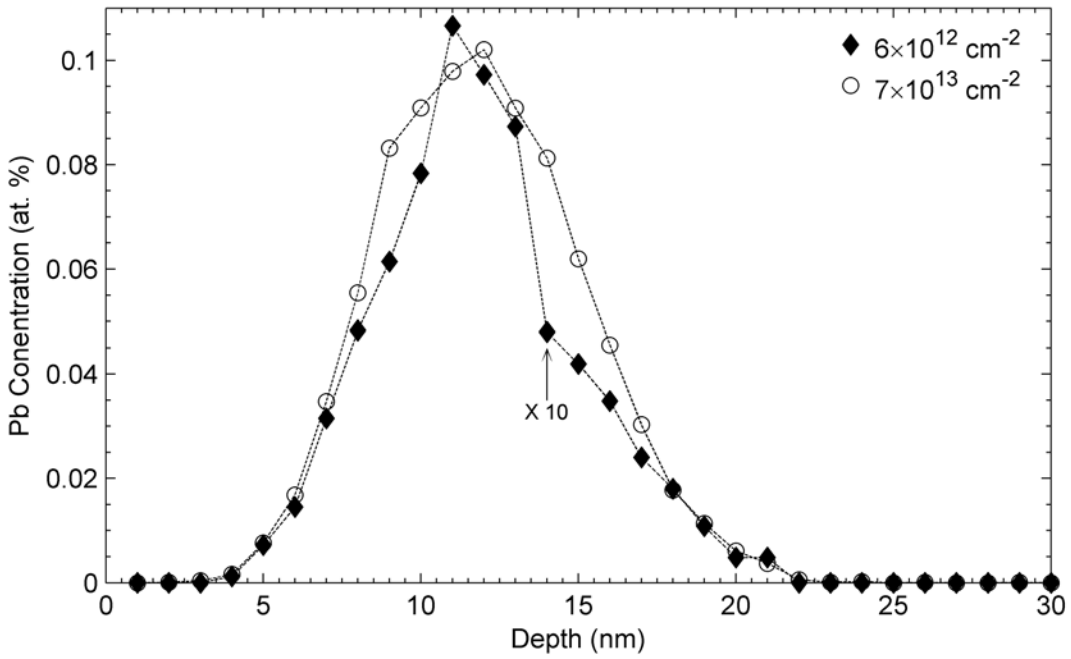

Figure 6.1: Dynamic TRIM simulation of the Pb concentration in the implanted samples. The trace for the lower dose, shown by the closed diamonds, has been multiplied by 10 for comparison.

In order to determine if Pb is connected to the I_7 donor-bound exciton, hydrothermally grown bulk ZnO crystals were implanted with $^{207}Pb^+$ at the GNS Institute in Wellington, New Zealand.† Pieces from the same wafer which was used for the PL of chapter 3 were used for the experiments. Implantation was done in vacuum at room temperature using the system described in reference 202. Two samples were implanted using a beam energy of 30 keV at doses of 6×10^{12} and 7×10^{13} ions/cm^2. Implantation profiles as found by the TRIM simulation [203] are shown in figure 6.1. Peak concentration for both samples was found at depths around 11 nm where the two concentrations were 0.01 and 0.10 at % for the 6×10^{12} and 7×10^{13} ions/cm^2 doses respectively. Essentially all of the Pb was contained within 25 nm of the surface, which is about half of the penetration depth of the 325 nm He-Cd laser line. Ion implantation is known to cause many structural defects to the wurtzite lattice.[33] After implantation, both Pb-implanted samples were annealed in O_2 at 600 °C for 1 h to repair the damage caused by the ion beam. The samples were placed on a quartz holder with the implanted sides face up. Previous experiments on hydrothermally grown ZnO from Tokyo Denpa showed this annealing recipe to be effective at narrowing the low temperature

†Many thanks to Dr. John Kennedy for carrying out the implantation.

near band edge PL features.

Growth of the EPLD samples were all done with the substrate at 600 °C, resulting in similar thermodynamic conditions between the implanted and EPLD grown samples. Due to the shadow mask and interactions with the O_2 ambient, the ablated plume would have been significantly cooled before reaching the substrate.[204] Thus, the biggest difference in the thermodynamic conditions would have arisen from the ambient O_2 pressure along with the different intrinsic defects and impurity concentrations. These differences may have had a profound effect on the incorporation of Pb into ZnO and the optical activity of its related emission centers.

6.2 Low Temperature Photoluminescence

Low temperature PL emission in the NBE region from the two implanted samples along with the unimplanted, unannealed piece from chapter 3 is shown in figure 6.2. All three samples were placed in the cryostat at the same time for accurate comparison of intensities and to reduce relative calibration uncertainties. Spectrometer slit widths for the undoped samples were set to 25 µm and then opened to 60 µm for the implanted samples. Taking PL from the Pb-implanted samples with 25 µm slits showed the intensity was increased by a factor of 25 when opening the slits to 60 µm. Spectra are shown only for the implanted samples after annealing as PL emission from implanted and unannealed samples is all but destroyed. This is due to significant surface damage, which PL is highly sensitive to. After annealing, both Pb-implanted samples showed strong PL with narrow line widths. However, compared to the undoped sample, PL intensity integrated over the region shown in figure 6.2 was cut down by factors of 60 and 170 for the 0.01% Pb and 0.10% Pb samples respectively (after taking the factor of 25 from the different slit widths into account). Sharp lines along with a substantial decrease in PL intensity indicate that defects introduced during implantation were substantially reduced by annealing but were not completely eliminated.

Dominant PL emission from both implanted samples was still from the Al-related I_{6a} exciton. Annealing is not expected to substantially reduce the Al concentration and may even help it to substitute more efficiently onto the Zn site. The I_{6a}^{B} and I_{6a}^{+} peaks also survived the annealing step showing their connection to the dominant I_{6a} exciton. Intensity of the neutral donor bound excitons I_4

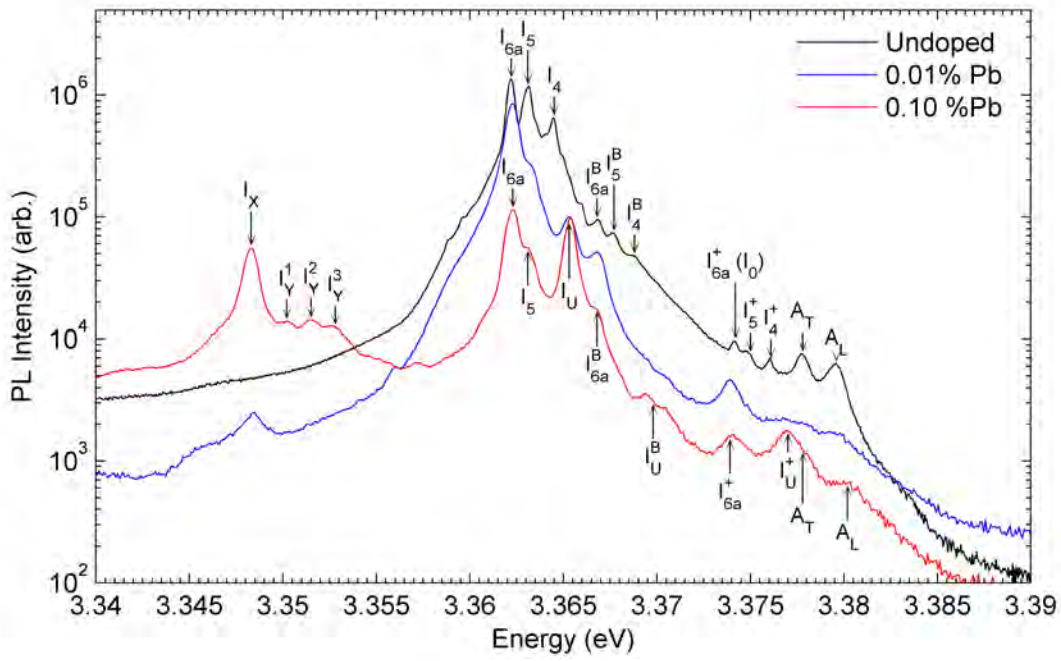

Figure 6.2: Low temperature (5 K) PL from the NBE region of Pb-implanted bulk ZnO.

and I_5 were reduced in both samples due to the annealing. Their B-exciton and D^+X counterparts also diminished giving more confidence to their assignment. Free excitonic emission was observed in the Pb-implanted samples at a reduced intensity with significantly broadened lines. Line width of the free excitons are more susceptible to lattice disorder than the bound excitons due to their extended wavefunctions. Optimizing the annealing conditions may help to decrease the lattice disorder and assist the substitution of Pb into the lattice.

A quick look in the I_7 region shows no sign of a peak in the Pb-implanted samples. While this is strong evidence against Pb being the origin of I_7, it cannot be completely ruled out. Thermodynamic and chemical differences when Pb was incorporated into the bulk and EPLD grown samples could have led to different Pb-related complexes. However, two striking new features were observed in the near band edge region in the Pb doped samples and are labeled I_{U} and I_{X} in figure 6.2. The I_{U} peak, at 3.365 eV, was in the D^0X region with a localization energy of 12.4 ± 0.4 meV which is in between the reported values of the I_{3a} and I_4 excitons[16]. The ratio of the intensities of I_{U} and I_{6a} tracked the Pb concentration, increasing from 0.12 to 0.85 when increasing the Pb concentration from 0.01 to 0.10%. I_{U} is either absent in the undoped bulk crystals or it is very weak and

hidden by the other intense, nearby peaks. Clearly this feature is Pb related and, based on its position, is most likely a D^0X complex. The appearance of the B-exciton and D^+X counterparts of I_U (I_U^B and I_U^+) in the PL from the Pb-implanted samples support the D^0X assignment of I_U since these corresponding peaks were observed for all 3 dominating D^0X transitions in the undoped sample.

Another new and perhaps more interesting emission was observed at 3.348 eV in the Pb-implanted samples and is labeled as I_X in figure 6.2. I_X was not observed in the undoped bulk and there are no reports of such intense, sharp emissions at this energy from ZnO in the literature. Like I_U, intensity of this peak tracked the Pb concentration. However, the effect was even more pronounced for I_X with the I_X to I_{6a} intensity ratio going from 0.003 to 0.490 when the Pb concentration increased from 0.01 to 0.10%. Accompanying I_X in the 0.10% Pb sample were several less intense, sharp peaks at 3.350, 3.352, and 3.353 eV labeled as I_Y^{1-3}. These small peaks may be connected with I_X considering their close proximity and correlated intensity with I_X and Pb concentration. Energetically, I_X and the I_Y^i complexes are in the neutral acceptor bound exciton region. However, an A^0X origin for these peaks is unlikely when considering that Pb is usually incorporated in ZnO on the Zn site and acts as a double donor.[197,201]

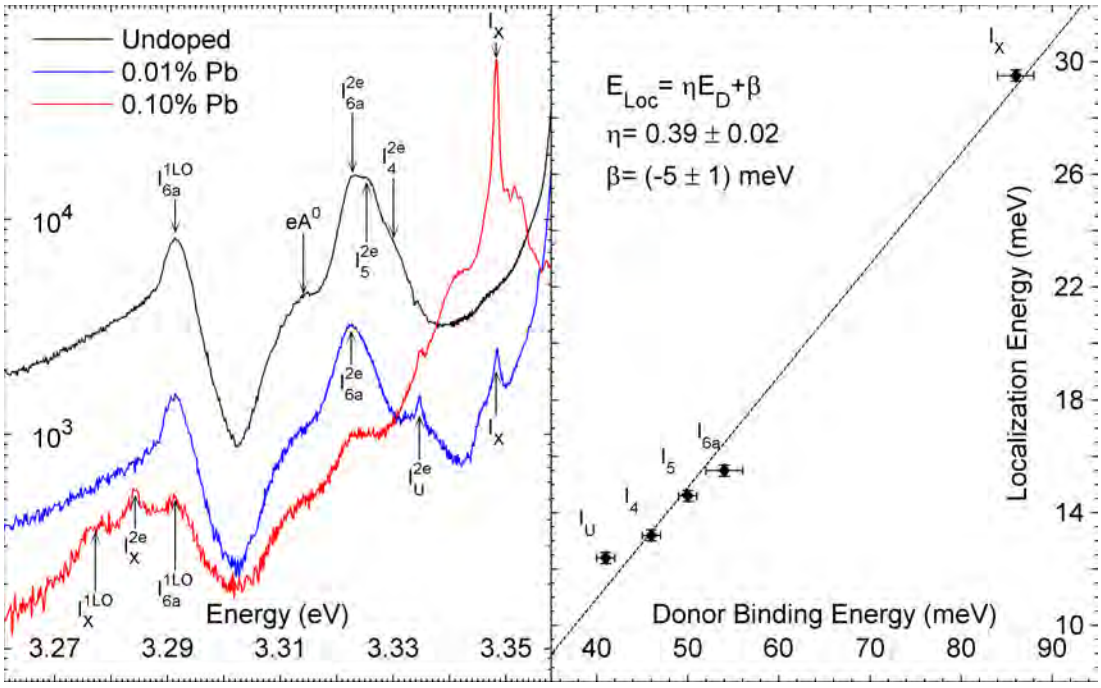

Figure 6.3: (a) Low temperature (5 K) PL from the TES region of Pb-implanted bulk ZnO. (b) Haynes rule plot.

Strong evidence that both the I_U and I_X peaks are donor bound excitons was seen in the two electron satellite (TES) region shown in figure 6.3(a). Two new peaks were introduced in the spectra at 3.335 eV and 3.284 eV in the Pb-implanted samples. They are assigned here to the TES transitions of the I_U and I_X peaks respectively. TES emission is only observed from D^0X transitions and no corresponding satellite transitions for A^0X complexes have ever been reported, even in samples with A^0X emission dominating.[205] Following the lines of section 3.4 (page 32), the donor binding energy, E_D, for the centers binding the I_U and I_X excitons were calculated as 41 ± 1 meV and 86 ± 2 meV respectively. Table 6.1 summarizes this data. Figure 6.3(b) shows a Haynes rule plot for the Pb-implanted samples including the I_4 and I_5 data points from the undoped sample. All the data in the figure lies on a straight line with a slope of $\eta = 0.39 \pm 0.02$, showing that all 5 peaks are D^0X complexes and follow Haynes rule. The value of η extracted here agrees reasonably well with the 0.30 ± 0.09 value obtained in section 3.4 for the undoped bulk sample and 0.37 value reported by Meyer et al.[16,103] The small discrepancy between these values may be a result of the simple effective mass approximation used to calculate E_D. TES transitions are useful for identifying D^0X complexes and their appearance in the Pb-implanted samples confirms Pb was incorporated as a donor in these implanted bulk ZnO samples.

Table 6.1: PL peak positions and localization energies along with TES position, separations, and calculated donor binding energies for the Pb-implanted bulk ZnO.

Peak	E_{PL}[a](eV)	E_{Loc}[b](meV)	E_{TES}[c](eV)	ΔE_{TES}[c](meV)	E_D[c](meV)
$I_{6/6a}$	3.362	15.5	3.322	40	54
I_U	3.365	12.4	3.334	31	41
I_X	3.348	29.5	3.284	64	86

[a] ± 1 meV on absolute peak positions due to calibration fluctuations
[b] ± 0.2 meV on differences in peak positions for two sharp peaks
[c] $\pm(< 2)$ meV calculation and/or eyeball error

Low temperature PL emission over the full UV/visible spectrum from the Pb-implanted bulk samples is shown in figure 6.4. Fano resonance, causing the dip on the high energy side of I_{6a}^{1LO}, was seen in both implanted samples indicating that structural quality was not significantly degraded in the implanted ZnO. In the 0.01% Pb sample 3 LO-replicas from the I_{6a} peak were observed with 2 LO-replicas from I_{6a} seen clearly in the 0.10% Pb sample. Also seen in the 0.10% Pb sample were 2 LO-replicas from the I_X peak showing simlar phonon coupling

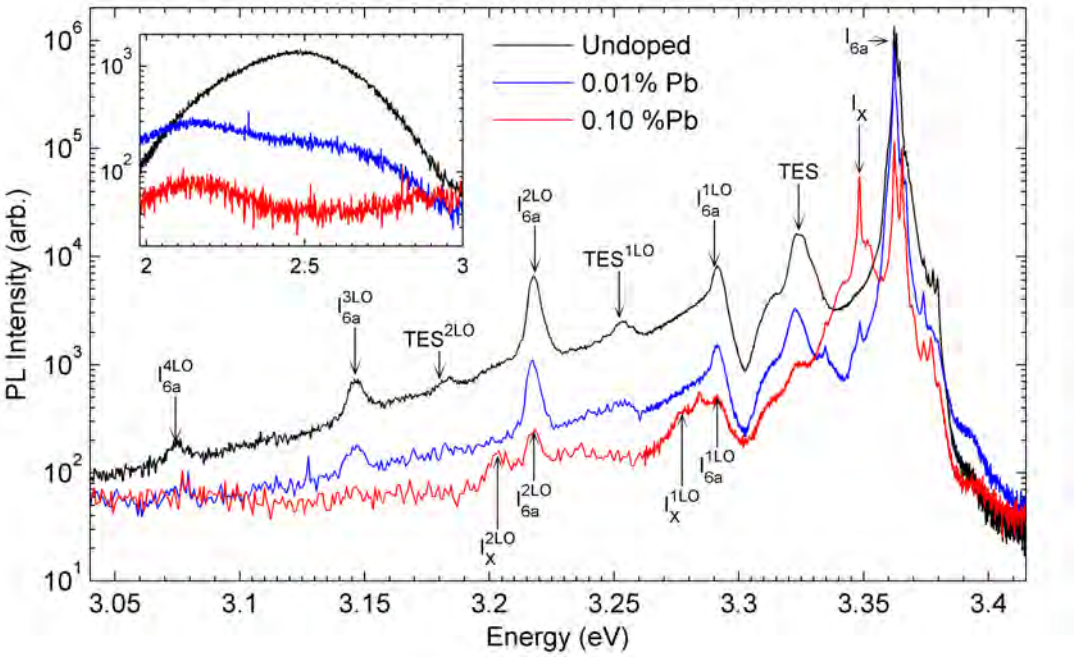

Figure 6.4: Low temperature (5 K) PL from the violet and visible region of Pb-implanted bulk ZnO. Inset shows the deep level defect emission band.

strengths for I_{6a} and I_X. This also gives more evidence that structural integrity remained mostly intact after the Pb implatation and annealing.

Visible emission is shown in the inset of figure 6.4 and was significantly reduced from the implanted samples. Taking into account the correction for varying spectrometer slits widths, the visible emission intensity was cut down by factors of 100 and 330 for the 0.01% and 0.10% Pb samples repectively. The green component of the visible emission, centered, around 2.45 eV may be due to oxygen vacancies[14], V_O, and may have been reduced due by the annealing step performed in an O_2 atmosphere. However, compared to the orange component, the green emission is quenched more effectively in the 0.10% Pb sample than in the 0.01% Pb sample. Pb impurities could be moving to the vacant oxygen sites, forming Pb_O, centers which would help to reduce V_O and the green emission. Alternatively, charge transfer processes between Pb_{Zn} and V_O centers could be occuring which have been previously observed in Pb-doped ZnO.[197,198] Such processes may be changing the charge state of the V_O centers which could further quench the 2.45 eV emission band. Fully understanding the effect of Pb doping on the visible emission first requires good knowledge of its origin in the undoped sample. A significant amount of independent data is needed to identify their origin and understand the

interactions of these deep centers in the Pb-implanted ZnO.

6.3 Temperature Dependent PL

To further explore the nature of the Pb related emission peaks, temperature dependent PL was carried out on the 0.10% Pb sample. Figure 6.5 shows the PL as a function of temperature from the NBE region. Positions of the arrows marking the peak positions were measured by eye if marked with a thick-head or calculated from one or two of the measured positions if marked with a thin-head. The first peaks to die out were the ionized donor bound excitons I_{6a}^{+} and I_{U}^{+} which both became unresolvable above about 30 K. Such quick decay is characteristic of $D^{+}X$ transitions due to their small localization energies, showing these peaks are not free excitonic or from the polariton branches.

Position and intensity of the I_{6a}^{B} and I_{U}^{B} peaks tracked their A-exciton counterparts reasonably well with temperature. The arrows indicating the position of these B-exciton peaks were placed 4.5 meV below their A-exciton counterparts. Some discrepancy was observed between the arrow placement and apparent peak positions for the bound B-excitonic transitions with the I_{U}^{B} transition showing instability above 20 K. Close examination of the nearby features shows no instabilities, ruling out spectrometer errors as the source. Emission from the I_{U}^{B} region was actually composed of two peaks which appeared to have the same temperature dependences. As of now, the reason for a doublet in this region and its instability with temperature are unknown. The B-exciton counterpart to I_{U} is even more evidence that I_{U} is a $D^{0}X$ complex and shows it has a similar nature to the I_{6a} emission. It is also possible that I_{U}^{B} was incorrectly assigned as a B-exciton complex. Either way its still another feature introduced by the Pb-implantation.

At low temperature the NBE emission was dominated by the I_{6a} with I_{U} as a close second. As the temperature was raised the I_{6a} peak decayed slightly faster than I_{U}, which became the dominant emission between 50 and 80 K. This is surprising as the I_{U} peak would be expected to decay faster than I_{6a} due to its smaller localization energy. This could clearly be observed for the I_{5} emission, which was no longer resolvable at 50 K. Similarly, the I_{X} peak died away quicker than both I_{6a} and I_{U} despite having a localization energy a factor of two greater. Arrhenius plots of the intensity of several important emission features are shown

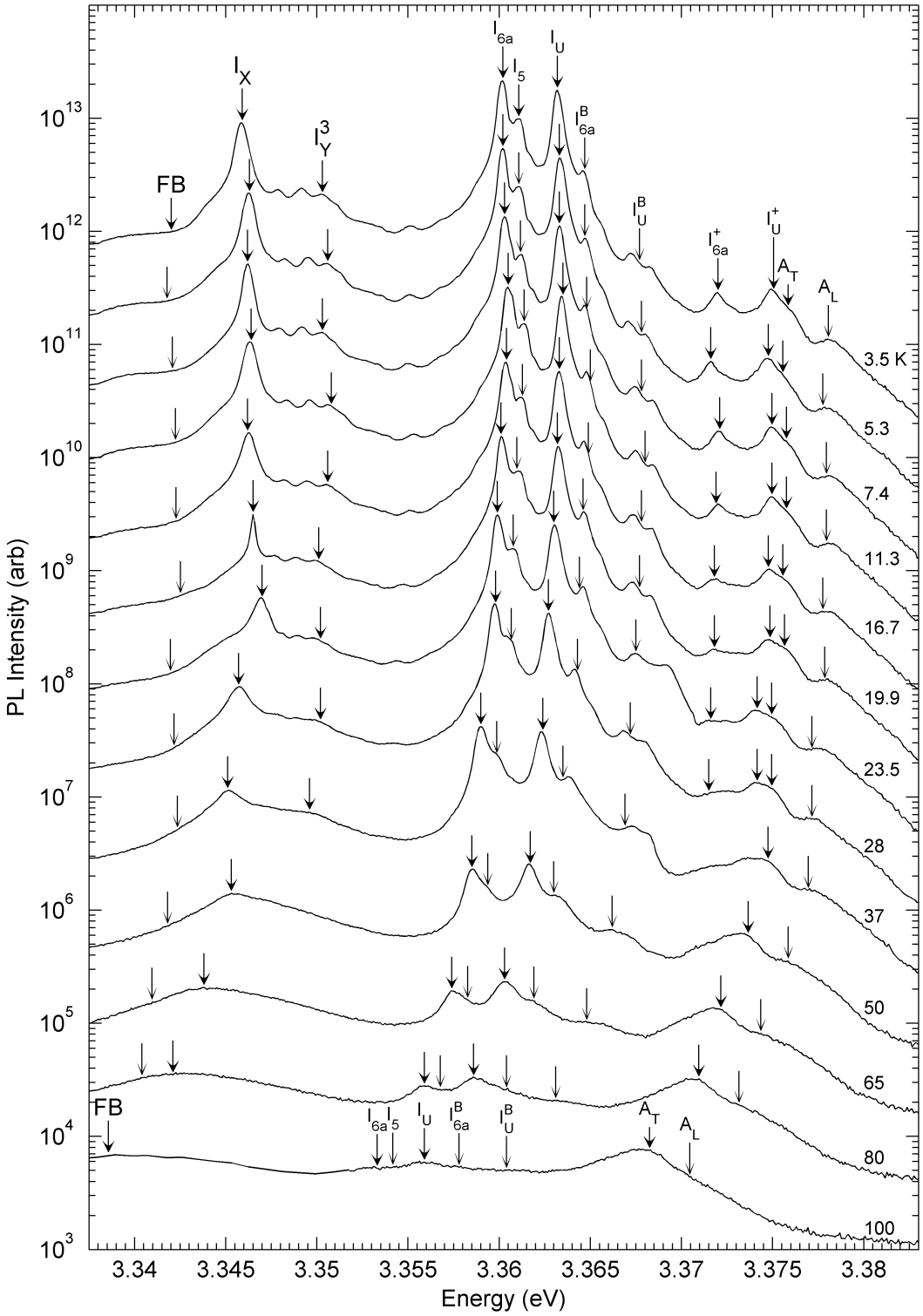

Figure 6.5: Temperature dependent PL from the NBE region of ZnO implanted with 0.10% Pb (offset vertically for clarity). Thick-headed arrows were placed by eye and then the position of the thin headed ones were calculated from their complementary measured peak.

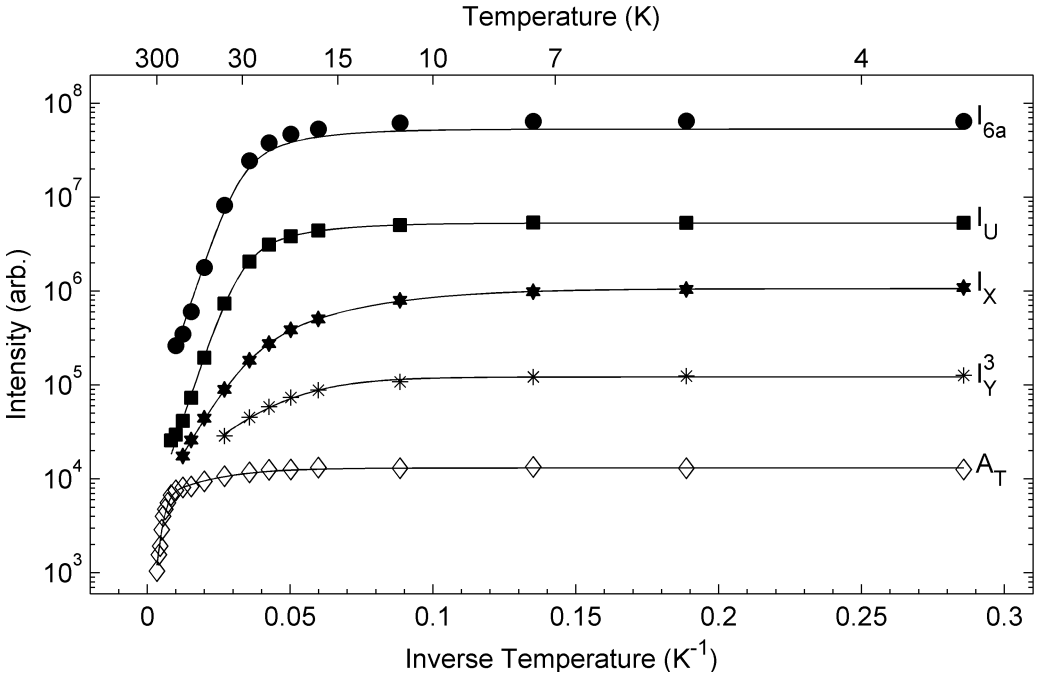

Figure 6.6: Arrhenius plot of the absolute intensity of the PL emission features in the NBE region of ZnO implanted with 0.10% Pb (offset vertically for clarity). Solid lines are the $\sqrt{I(T)}$-weighted least squares fit of the two path Arrhenius decay (eq. 3.12, page 41). E_b for the A_T peak was fixed at 60 meV.

in figure 6.6. Solid lines are the $\sqrt{I(T)}$-weighted least squares fit of the two path Arrhenius decay (eq. 3.12, page 41). Fitted parameters along with the 95% confidence bounds are shown in table 6.2. Expected behavior was observed for the A_T peak, with a good fit obtained by setting the activation energy of the second path to 60 meV. A value of $E_\mathrm{b} = 80$ meV was obtained for A_T when it was allowed to be free. This may have been due to laser scatter, which increased above temperatures around 200 K. For data above 200 K, a small constant was subtracted but this may have not completely removed the laser background.

Unlike the undoped bulk sample, the Arrhenius data for the 0.10% Pb sample could not be satisfactorily fit with a single decay channel for the free or donor bound excitons. The necessity to add the effects of a second decay path indicates deteriorated crystallinity in the 0.10% Pb sample since decay channels with low activation energies (≈ 5 meV) represent nonradiative recombination of the excitons. Crystal defects are a ready source of such nonradiative recombination pathways. Optimizing the annealing conditions could reduce the effect of these pathways and is something which should be explored in detail.

Table 6.2: Arrhenius parameters of the PL from the 0.10% Pb-implanted ZnO as found by a $\sqrt{I(T)}$-weighted least squares fit using two decay channels(eq. 3.12, page 41). Uncertainties represent the 95% confidence bounds.

Parameter	A_{T}	I_{U}	$I_{6\mathrm{a}}$	I_{X}	$I_{\mathrm{Y}}^{3\,\mathrm{b}}$
$I(0)$(arb.)[a]	1.31 ± 0.01	106.5 ± 0.1	128.7 ± 0.1	53.3 ± 0.1	12.24 ± 0.01
A (arb.)	1.32 ± 0.08	4.7 ± 0.3	5.2 ± 0.3	8.0 ± 0.4	16.6 ± 0.6
E_{a} (meV)	5.4 ± 0.4	4.5 ± 0.1	4.6 ± 0.1	3.02 ± 0.06	5.44 ± 0.08
B (arb.)	90 ± 3	1680 ± 40	1840 ± 50	261 ± 8	–
E_{b} (meV)	60 (fixed)	18.4 ± 0.1	18.7 ± 0.1	11.2 ± 0.1	–
T_{E} (K)[c]	150.2 ± 0.2	27.4 ± 0.2	27.9 ± 0.2	27.1 ± 0.4	–
T_{D} (K)[d]	286 ± 1	41.6 ± 0.4	42.3 ± 0.4	64 ± 1	–

[a] $\times 10^4$
[b] One Path Fit (equation 3.11, page 41)
[c] Calculated by equation 4.1 (page 75)
[d] Calculated by equation 4.2 (page 76)

Essentially identical Arrhenius fits were obtained for the $I_{6\mathrm{a}}$ and I_{U} peaks with $I_{6\mathrm{a}}$ having slightly higher activation energies for both nonradiative decay channels. As temperature was raised, $I_{6\mathrm{a}}$ died out before I_{U} (see figure 6.8) implying that I_{U} should have a higher activation energy for the [B, E_{b}] decay path. The close proximity and very similar behavior of the $I_{6\mathrm{a}}$ and I_{U} peaks made it too difficult for the fitting algorithm to accurately tell the difference. The 95% confidence bounds on the fits are quite small and more realistic uncertainties may be as much as 10 times the values listed in table 6.2. A slower decay with temperature for the I_{U} peak compared to the other D^0X transitions could mean excitons were being released from a deeper trap and recaptured into the I_{U} level. It could also be caused by an increase in the concentration of the centers which bind I_{U} when the temperature was raised. Either effect would not have to be large in order to slow the thermal quenching of I_{U} by the small amount observed. In any case, both of the activation energies of the [B, E_{b}] paths were comparable to the localization energies. This implies thermal release of the excitons from the binding centers (creating free excitons) was the main PL quenching mechanism above about 30 K. Unlike the unimplanted bulk, there was no observed increase in the free exciton emission intensities as the temperature was raised initially. Thus, in the Pb-implanted sample there was an increased probability of nonradiative recombination once the excitons were thermally released from the neutral donors. Again, this is another effect of the disorder in the lattice introduced by the implantation process.

Unexpected behavior with respect to temperature was observed for the intensity of the I_X and I_Y^i recombinations. Both sets of peaks died out quicker than the higher energy D^0X transitions. Activation energies for I_X and I_Y^3 extracted from the least squares fits were much lower than their localization energies, smaller by at least a factor of 4.[†] As such, quenching of these peaks could not have been due to thermal release from the binding centers. Such low activation energies for the nonradiative decay channels implies that the centers which bound the I_X and I_Y^i excitons were destroyed as temperature increased or, that they had substantially higher nonradiative lifetimes than the other bound excitonic transitions.

Close inspection of the Arrhenius plots in figure 6.6 shows that I_X decayed noticeably faster than I_Y^3. This is also evident when carefully studying the PL spectra themselves. It becomes very clear when comparing the E_a values from the two fits. For I_Y^3, the two path Arrhenius equation (3.12) could not be fit to the data. A singular matrix error always resulted despite several attempts using different initial guesses. This was most likely due to the small number of data points available for I_Y^3. Comparison to the $[A,\ E_a]$ path of the I_X transition is appropriate as this path dominates the PL quenching below about 30 K, above which I_Y^3 was unresolvable. Difference in the quenching of the I_X and I_Y^3 peaks suggests that they were separate, unconnected emissions which coincidentally had similar energies. It certainly rules out the I_Y^i series from being some sort of excited state of the I_X emissions, which may have been able to explain the appearance of the I_Y^i lines in the first place. Nevertheless, the I_Y^i lines were another feature introduced by the Pb-implantation.

Around 80 K I_X and the I_Y^i lines merged together with a free to bound transition marked as FB in figure 6.5. Merging was the result of the initial blueshift of the FB emission and the redshift of the I_X and I_Y^i peaks. Emission from FB recombination was at 3.342 ± 0.001 eV at 3.5 K. This gave a donor/acceptor binding energy of $E_{D,A} = 94$ meV using equation 3.1 (page 19) and taking the band gap as 60 meV above the A_T energy. The binding energy of FB was close to the 86 ± 2 meV binding energy of the donor which traps I_X as determined by the relative position of the I_X^{2e}. As such, the FB transition could be either an eA^0 involving a shallow acceptor or an hD^0 transition involving a deep donor.

Shifting of the emission energy of the important spectral features with temperature is shown in figure 6.7. Solid lines show the least squares fit of the Modified

[†] I_Y^3 was chosen as it was the farthest away from I_X meaning it was not sitting on a significant background from I_X.

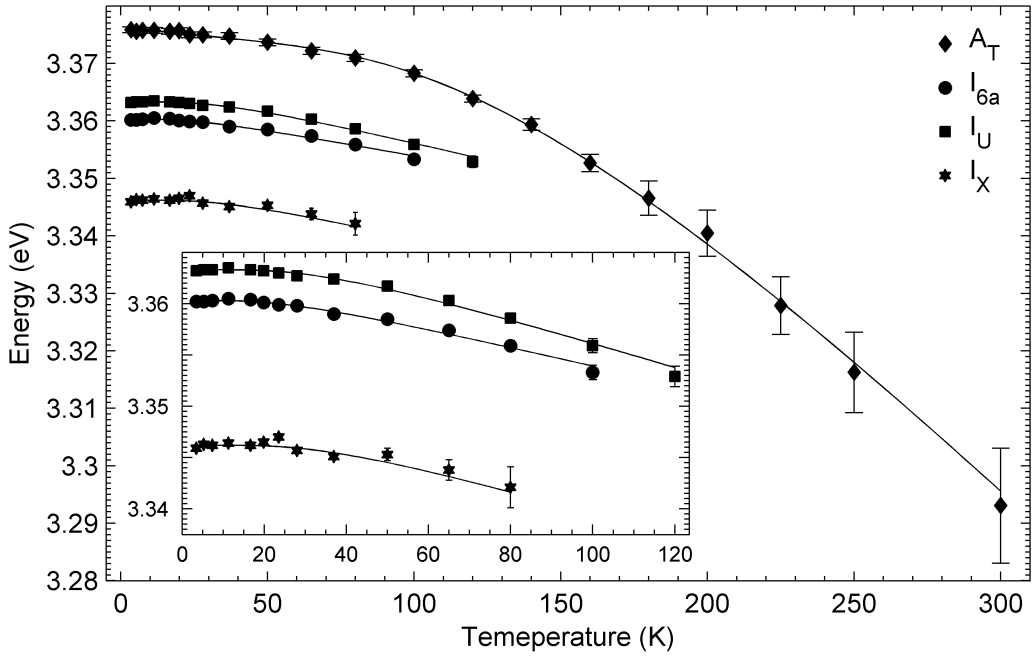

Figure 6.7: Energy shift of the PL spectral features from Pb-implanted ZnO with temperature. Solid lines are the least squares fit of the modified Manoogian equation (3.17, page 44) with $U = 0$ for the bound excitons.

Manoogian equation (3.17, page 44). For A_{T}, the extracted α, U, and θ values agree well with those found for the undoped bulk shown in table 3.3 (page 46). Essentially, this experiment was an independent measurement of the band-gap shift of the bulk ZnO to that presented in section 3.7 despite the fact that the Pb-implanted piece came from the same wafer. The good agreement indicates the validity of the 4-parameter modified Manoogian model and its capability to reproduce the parameter values.

Table 6.3: Parameters of the uncertainty-weighted least squares fit of the modified Manoogian equation (3.17, page 44). Uncertainties represent the 95% confidence bounds.

Parameter	A_{T}	I_{U}	$I_{6\mathrm{a}}$	I_{X}	I_{Y}^3
$E(0)$(eV)[a]	3.376	3.3633	3.3603	3.3462	3.351
U (meV/K)	0.05 ± 0.02	0 (fixed)	0 (fixed)	0 (fixed)	0 (fixed)
α (meV/K)	0.5 ± 0.1	0.12 ± 0.03	0.05 ± 0.03	0.1 ± 0.1	0.07 ± 0.2
θ (K)	432 ± 103	100 ± 30	74 ± 30	110 ± 70	70 ± 170

[a] ± 1 of the last listed decimal place

Fits to the bound excitons were not as successful as the free exciton fit,

showing high relative uncertainties. Based off of the temperature dependence presented throughout this thesis, the U parameter was fixed to zero. This reduces the modified Manoogian model to the Bose-Einstein model (eq. 3.16, page 43). The best fit was obtained for the I_{U} peak which must have been due to the larger number of data points and the higher temperature at which this peak was resolvable. Both the α and θ values fit to the I_{U} exciton agree well with the values obtained for $I_{6\mathrm{a}}$ in the undoped bulk. For the undoped sample, the $I_{6\mathrm{a}}$ peak was resolvable up to 120 K while in the Pb-implanted sample it was only observed up to 100 K. Effect of the nonradiative recombination of the bound excitons in the Pb-implanted sample was responsible for this. Such nonradiative recombinations were not needed to describe the intensity decay in the undoped bulk. This independent measurement of the bound exciton shift verifies the $U = 0$ assumption in the modified Manoogian model for bound exciton complexes.

Emission from the violet region is shown in figure 6.8. All the features below the FB transition can be accounted for by assuming they are either LO-replicas or TES transitions of the main band edge peaks. Positions of the LO-replicas were calculated using equation 3.21 (page 47) with $E_{LO} = 72\,\mathrm{meV}$ and $L = 1/L = 0$ for the 1/2LO-replica. Excellent agreement was seen between the calculated LO-replica positions and the corresponding peaks in the spectrum. Two LO-replicas were clearly observed from the $I_{6\mathrm{a}}$ and I_{X} peaks at similar intensity ratios to their zero-phonon lines, indicating similar coupling to the LO-phonons for these transitions. LO-replicas from I_{U} were also seen but just appeared as a high energy shoulder on the $I_{6\mathrm{a}}^{\mathrm{mLO}}$ due to the close proximity of the zero-phonon lines. Good agreement between the expected TES positions with temperature were also observed by assuming that their spacing with the zero-phonon line remained constant with temperature. TES spacing was measured at 3.5 K and this was then used to calculate the positions at the higher temperatures. This assumption is really stating that the donor binding energies do not change with temperature, which is a reasonable assumption over the 0-300 K range. To know for sure would require temperature dependent IR photoconductivity measurements at temperatures low enough to prevent ionization of the donors. In any case, this assumption seems to account for the TES positions, became unresolvable around 30 K. This fact is strong evidence that these are indeed TES transitions as they are expected to die out with temperature before the zero phonon lines.

These temperature dependent measurements were quite useful at solidifying the assignment of the I_{U} and I_{X} transition as donor-bound-excitons. I_{U} behaved

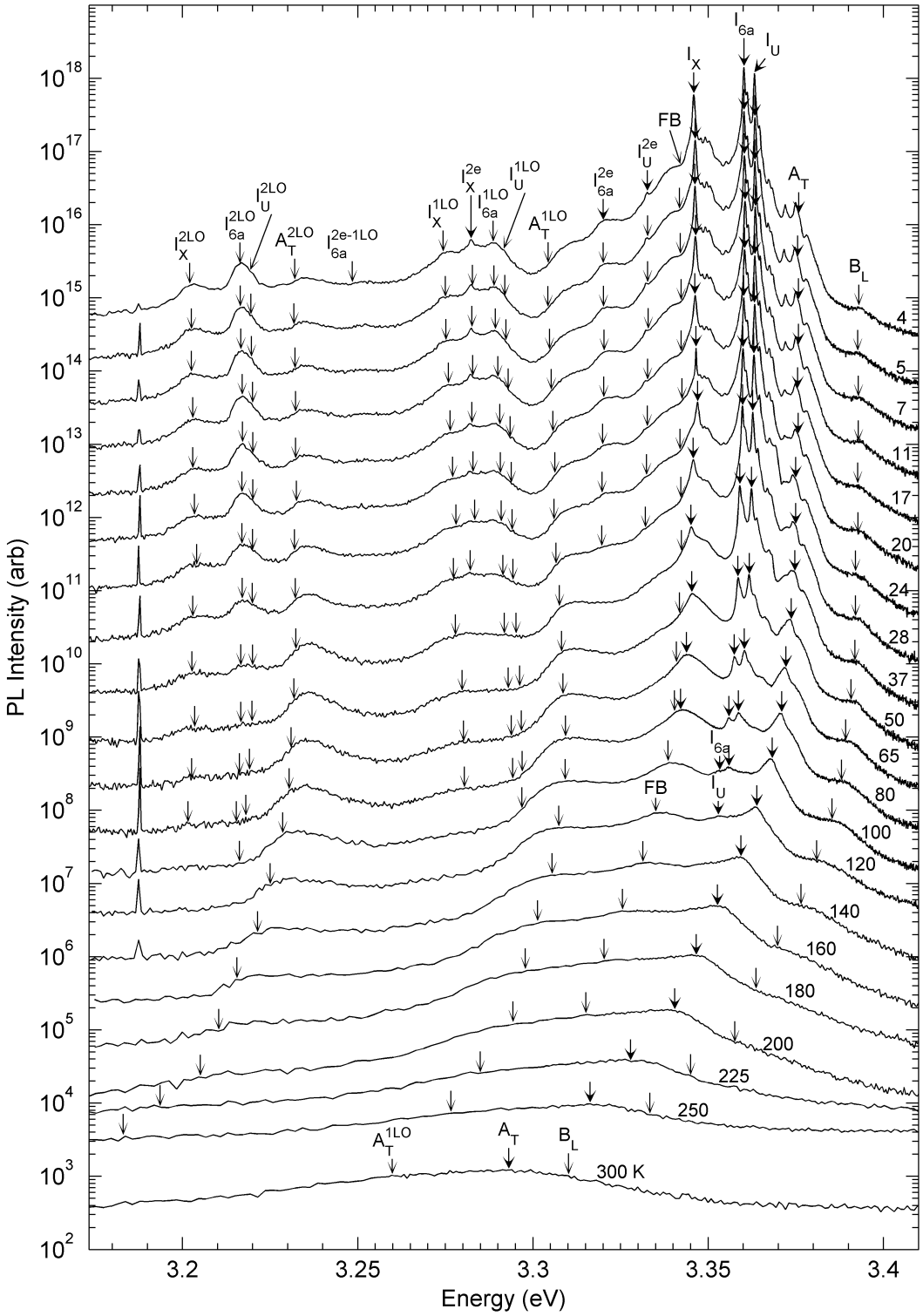

Figure 6.8: Temperature dependent PL in the violet region from ZnO implanted with 0.10% Pb (offset vertically for clarity). Thick-headed arrows were placed by eye and then the position of the thin headed ones were calculated from their complementary measured peak.

just like a typical D^0X transition, showing all the expected features of a D^0X complex which manifest in the I_{6a} and other standard, known D^0X complexes in ZnO. On the other hand, interesting behavior was observed for the I_X and I_Y^i lines which implied a temperature dependent binding center concentration or some interaction of these peaks with other close by defect levels. Many useful observations were made with this temperature dependent PL study but it could not possibly reveal all the secrets behind the PL of the Pb-implanted ZnO.

6.4 Power Dependent PL

Low-temperature power dependence of the PL from the 0.10% Pb implanted ZnO was performed on the exact same spot on the sample as the temperature dependence of the previous section. Optical arrangement was not changed at all and the spectra were gathered on consecutive days in the lab. Figure 6.9 shows the spectra taken at various excitation intensites with the sample at 5 K. Spot size was for this experiment was roughly 0.6 mm^2 with the laser intensity varied over 3 orders of magnitude, from 3 to 0.003 W/cm^2, using a set of well calibrated filters. These excitation conditions were very similar to those used for the excitation intensity dependence performed on the undoped bulk sample presented in section 3.8 (page 51). However, they did not quite reach the same intensities as those reached during the power dependence of the EPLD grown samples presented in section 4.2 (page 90). This was due to the difficulties in reproducing the laser spot size since the optics get changed frequently in the heavily-used optics lab at the University of Canterbury. Measuring the laser spot size is also quite tricky in the first place, usually done by scanning the laser over the edge of the sample using micrometer driven translation stages. Exact location of the edge of the laser spot is hard to determine, leading to an uncertainty as high as 20 to 30% on the absolute value of the unattenuated laser intensity. However, the relative uncertainties between two different intensities were much smaller due to the high accuracy and known performance of the laser filters.

The shape of the emission did not dramatically change with the excitation intensity as shown in figure 6.9 and its inset. All the peaks showed the expected $I \propto L^{\varsigma}$ power law (see section 3.8, page 51) as shown by the plot of the absolute intensities of the features in figure 6.10. Emission lines did not appear to broaden with temperature meaning the absolute peak intensities followed the same power law with the same exponent as the integrated emission intensities. Some error was

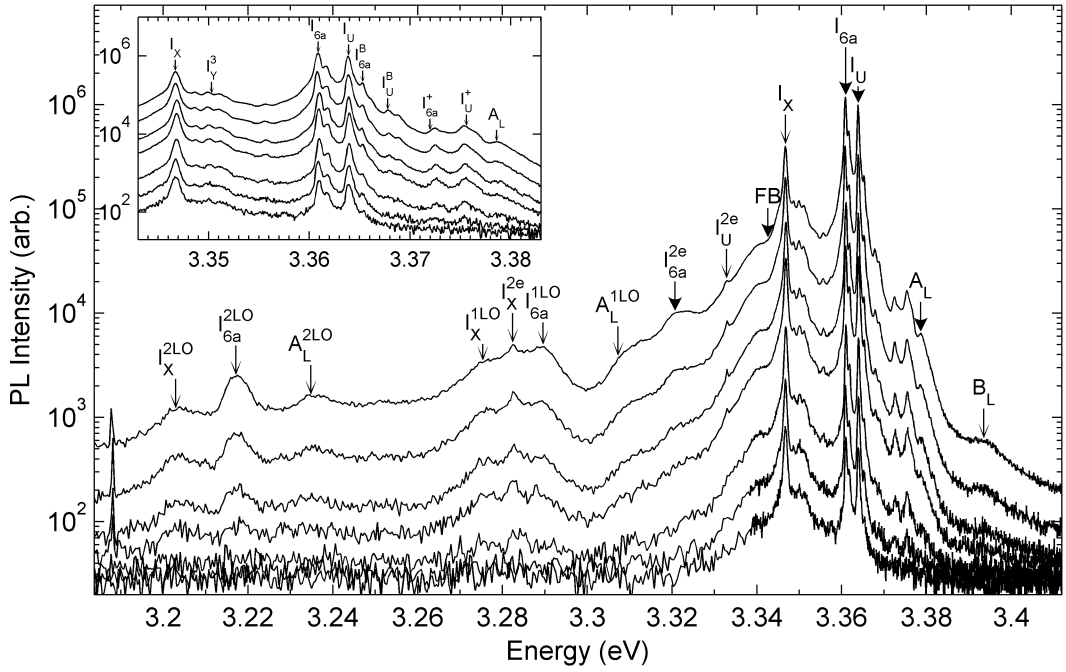

Figure 6.9: Power dependent PL from the ZnO implanted with 0.10% Pb. Thick-headed arrows were placed by eye and then the position of the thin headed ones were calculated from their complementary measured peak.

introduced by the background from neighboring peaks but it was minimal since all the features showed nearly linear exponents. The most error from neighboring peaks was for the I_{6a}^{1LO}, I_X^{2e}, and I_X^{1LO} recombinations due to their close proximity compared with their broad widths.

Recombinations characteristic of the undoped hydrothermally grown ZnO from Tokyo Denpa, namely the B_L, A_L, I_{6a}, and I_{6a}^{mLO} transitions, showed the expected behavior. Emission exponents of the free excitons, B_L and A_L, were close to one and agree with each other to within their uncertainties. Exponent of the I_{6a} emission was just above one, typical of D^0X transitions[131,133,134], but much less than the 1.5 value observed for the I_7 transition in the EPLD grown nanohexamids discussed in section 4.2. No indication of the highly nonlinear behavior was observed in this Pb-implanted bulk sample, implying that the Pb impurities were not interacting with the I_{6a} peak causing it to show superlinear behavior. If this was the case then the dominant emission from the EPLD samples would have been from the I_{6a} exciton. However, the excitation intensities used for the EPLD grown nanohexamids went half an order of magnitude above those used in this one. Despite this, the unique effect observed for I_7 would have still been seen if it was occurring for I_{6a} in the Pb-implanted bulk. At least one order of magnitude

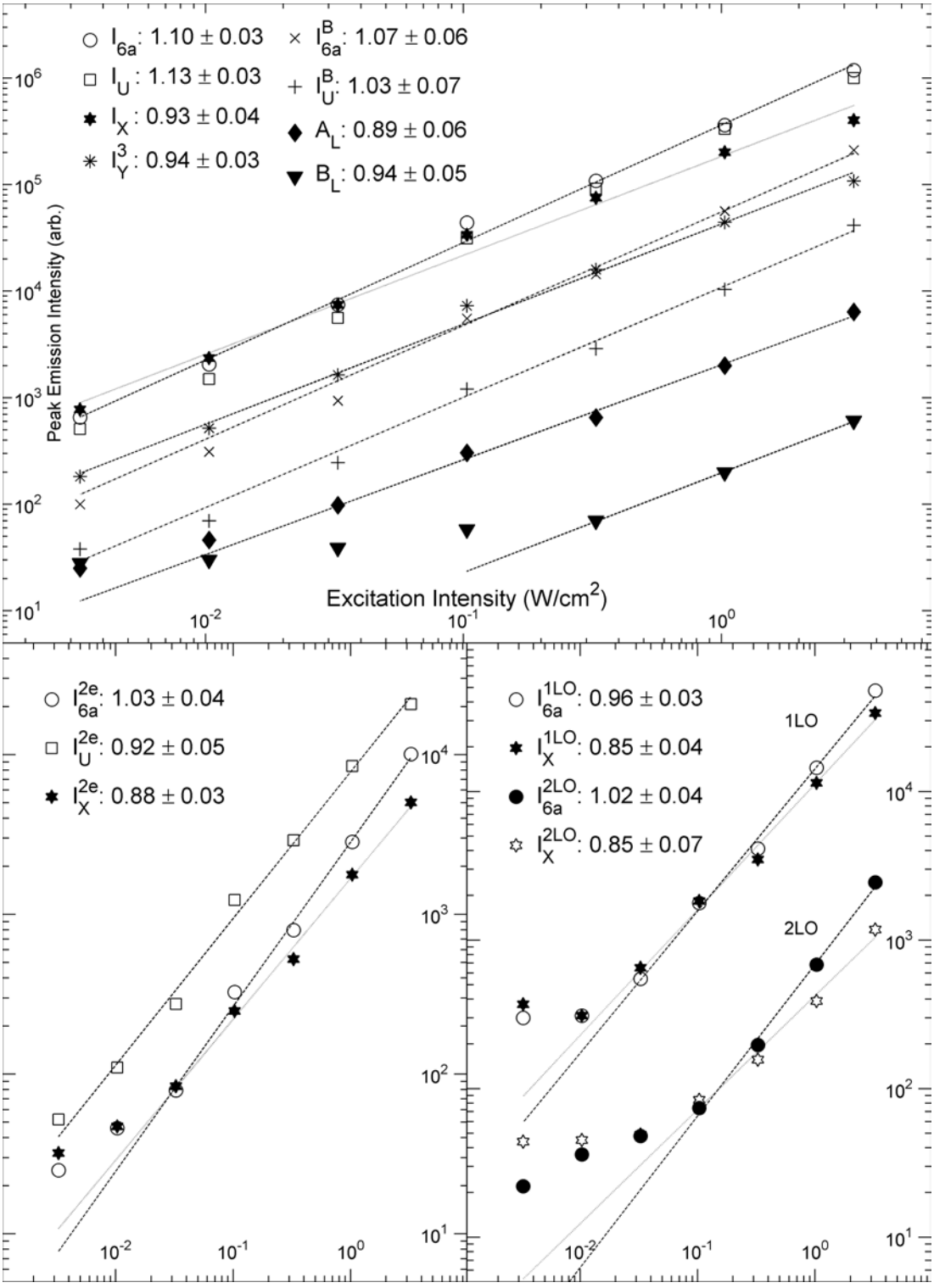

Figure 6.10: Power dependence of the absolute peak intensities of the PL features from 0.10% Pb implanted ZnO. Only the data for the $I^{1LO}_{6a,X}$ peaks has been offset for clarity. Legends indicate the exponent of the $I \propto L^{\zeta}$ power law and their 95% confidence bounds from least squares fits.

of excitation intensity was common between the two experiments and the I_7 peak showed its unique behavior at the lowest intensities probed in the EPLD study.

Emission from the I_{U} peak, and its complementary B-exciton and TES recombinations, showed essentially identical behavior to that observed for the $I_{6\mathrm{a}}$ peak. Emission exponent of the zero-phonon line of I_{U} agreed with that of $I_{6\mathrm{a}}$ to within the listed uncertainties. The same went for the B-exciton counterparts, with exponents that were both very comparable to the A-exciton complexes. Exponents for the TES transitions were also similar. Again, this was more solid evidence that I_{U} was a typical D^0X transition which shared the same nature as the I_4, I_5, and $I_{6\mathrm{a}}$ excitons in the undoped bulk sample.

The same cannot be said about the I_{X} and I_{Y}^3 lines which showed noticeably smaller exponents compared to the $I_{6\mathrm{a}}$ and I_{U} recombinations. Compared with the listed uncertainties, the $\zeta \approx 0.9$ measured for these transitions is well separated from the $\zeta \approx 1.1$ values measured for the $I_{6\mathrm{a}}$ and I_{U} peaks. Looking closely, the difference can be seen in the inset of figure 6.9 which shows the I_{X} peak dominating at $0.003\,\mathrm{W/cm^2}$ and the $I_{6\mathrm{a}}$ peak dominating at higher intensities. Similarity of the I_{X} and I_{Y}^3 emission exponents shows a connection between the two complexes. However, these measurements may have been clouded by emission from the close-lying FB transition. Reduced exponents were also seen for $I_{\mathrm{X}}^{2\mathrm{e}}$ and I_{X}^{mLO} compared to the ζ values of $I_{6\mathrm{a}}^{2\mathrm{e}}$ and $I_{6\mathrm{a}}^{mLO}$. This fact solidifies the ties between the I_{X}, $I_{\mathrm{X}}^{2\mathrm{e}}$, and I_{X}^{mLO} and is confirmation of the assigned relationship.

Like the temperature dependence, the PL dependence on excitation intensity separates the I_{U} and I_{X} emission peaks. Both are clearly bound excitons resulting from the Pb impurities but the exact nature of these bound excitons is still unclear. So far, I_{U} has shown all the behavior characteristic of D^0X transitions while I_{X} has only shown some of these characteristics. Specifically, I_{X} showed a TES recombination line and LO-phonon replicas. However, the quick decay with temperature and sublinear exponent suggest extra interactions were occurring for the I_{X} exciton and/or its binding center which are not seen for typical D^0X transitions in bulk ZnO. One might suggest that the sublinear behavior observed for I_{X} is due to the limited concentration of binding centers. If this was the case, then the concentration of the I_{X} binding centers would be significantly less than the I_{U} binding centers, which did not show any saturation effects. As both peaks are likely due to Pb, this is evidence that I_{U} could be due to interstitial Pb impurities and the I_{X} peak was from substitutional Pb_{Zn} centers. Implantation is expected to produce a high concentration of interstitials and only a small portion

may be reaching the Zn sites after annealing.

6.5 Simultaneous Above- and Below-Gap Excitation

Simultaneous above- and below-gap excitation was carried out on the 0.10% Pb-implanted ZnO to see the effects of free carrier interactions with the new PL features introduced by the Pb impurites. Figure 6.11(a) shows the spectra at varying below-gap excitation (BGE) intensities. For this experiment the above-gap excitation was provided by the 325 nm He-Cd laser line at an intensity of about 3 W/cm^2. BGE was done with the 515 nm line of an Ar^+ laser, focused to a slightly larger spot. Beam power of the 515 nm line was 400 mW and the excitation intensity was varied from 6 to 60 W/cm^2 by attenuating the beam with calibrated filters. Inspection of the spectra shows no broadening of the sharp NBE features indicating the Ar^+ laser was not heating or damaging the sample. No PL emission in the NBE region was detected from the samples using just BGE. A constant background offset from the Ar^+ laser was subtracted from the spectra to bring the noise level at 3.422 eV down to the value measured without any Ar^+ light on the sample.

Emission from the excitonic peaks characteristic of the undoped, hydrothermally grown bulk ZnO showed the expected decay, or lack thereof, in intensity and small redshift with increasing BGE intensity. The redshift was about 0.3 meV for the highest BGE, just barely measurable in the PL system used for the experiment. Peak intensities normalized to the values with no BGE are shown in figure 6.11(b). Straight lines are the least squares fit to a simple exponential decay $I = I_0 \exp(-\gamma L_{\mathrm{BG}})$ where I is the PL intensity, L_{BG} is the BGE intensity, and γ is a constant. By no means were the exponential fits very good or based off a physical model. They are more of a guide to the eye and a simple way to quickly quantify the non-linear intensity decay with BGE. Uncertainties in the γ values represent the uncertainty due to the scatter in the data points about the fitted lines. Plotting this data on a log-log scale and fitting a power law did not provide as good of a fit as the exponentials. Developing a physical model to use for data fitting would be best done by converting the BGE intensities into carrier concentrations as measured by low temperature Hall experiments under identical BGE conditions. A He-cooled optical cryostat with variable magnetic field and electrical feed throughs would provide valuable information as the carrier concentrations are likely a nonlinear function of the BGE intensity. Small samples

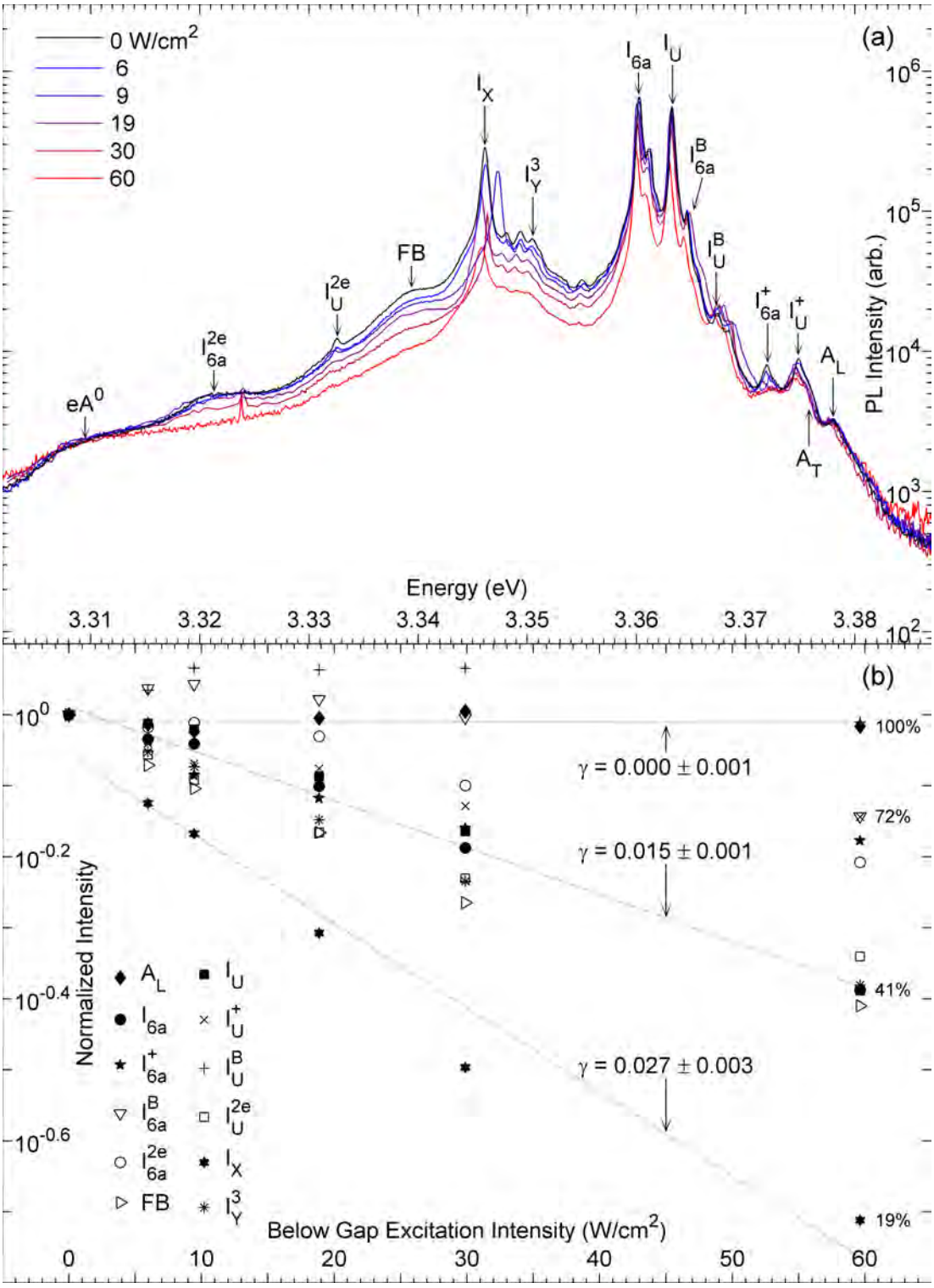

Figure 6.11: (a) Simultaneous above- and below-gap pumping effects on the 4 K PL from 0.10% Pb-implanted ZnO. Numbers in the legend indicate the intensity of the 515 nm line from an Ar^+ laser used for below-gap pumping ($h\nu = 2.41$ eV). (b) Peak intensities normalized to the value with no BGE.

and a large spot size for the BGE source would be required for the best results.

Intensity of the A_{L} free exciton showed essentially no dependence on the BGE. Unfortunately nothing could be said about the B_{L} exciton due to its low intensity compared to the noise introduced by the Ar^+ laser scatter. The I_{6a} peak showed nearly exponential decay in intensity with increasing BGE, dropping to 41% of its initial value at the highest BGE intensity. Emission from the I_{6a}^{+} and I_{6a}^{2e} recombinations followed essentially the same behavior as the I_{6a} principal recombination line, further strengthening their connection. At the highest BGE intesity the I_{6a}^{+} peak was efficiently screened and the nearly 70% normalized intensity measured at $60\,\mathrm{W/cm^2}$ Ar^+ intensity was due to the background from the unscreened LPB_A recombination.

Figure 6.11(b) shows the behavior of I_{U} and its TES and D^+X counterparts was essentially identical, with respect to the BGE intensity, to the corresponding recombinations in the I_{6a} family. In this case the background from the unscreened A_{T} peak is what caused the overestimated intensity of I_{U}^{+} at $60\,\mathrm{W/cm^2}$ BGE intensity. Emission from the I_{6a}^{B} and I_{U}^{B} excitons was also similar to each other, both increasing in emission intensity with increasing BGE intensity before reducing to at or below their initial intensity. This is more clear evidence that the free carriers created by the Ar^+ laser do not efficiently screen the interaction of the free B-excitons with the binding centers. Free carriers may even promote B-exciton capture at the right BGE intensities. It is also more evidence that I_{U}^{B} was in fact the B-exciton counterpart of the I_{U} recombination. Indeed, I_{U} behaved just like I_{6a} and the other typical D^0X transitions in unintentionally doped ZnO and can now be unambiguously identified as a D^0X transition.

Like increasing the temperature or above-gap excitation intensity, the I_{X} exciton showed strikingly different behavior to the rest of the peaks when subjected to BGE. Intensity of I_{X} dropped to 19% of its initial intensity when the BGE intensity was $60\,\mathrm{W/cm^2}$, quenched much more efficiently than all the other peaks. This includes the I_{Y}^{3} line, which dropped to about 40% of its initial intensity under the highest BGE intensity just like the typical D^0X transitions. Similar to the temperature dependence, the BGE dependence separates the I_{X} and I_{Y}^{i} lines into different basic origins. Intensity of I_{X} showed close to an exponential behavior with $\gamma = 0.027 \pm 0.003$, twice as large as the other D^0X transitions and their TES and D^+X counterparts. Since I_{X} was a D^0X transition, it would have been subjected to essentially the same quenching due to screening as I_{U} and the other typical D^0X peaks. Thus, quenching to 40% of the initial intensity of I_{X} was due

to screening and the rest was due to another process which was photosensitive to visible radiation. Destruction of the binding center of I_X by the 2.41 eV photons or by the capture of the carriers which have been photoexcited by the BGE must have been occuring to explain such drastic quenching. This is a big piece of the puzzle hiding the origin of the I_X emission, which as discussed in the next section, is most likely due to an exciton bound to Pb substituting on a Zn site. More precisely, I_X is an exciton bound to substitional Pb^{2+} which sits on a Zn^{2+} site and acts as a neutral donor.

6.6 Discussion

All the PL data gathered so far on the Pb-implanted ZnO is needed to build a clear picture of how the Pb was incorporated into the hydrothermally grown bulk ZnO. From the low temperature data alone, the chemical origin of the I_U, I_X, and I_Y^i peaks can be assigned to Pb-complexes. These three transitions all showed clear intensity correlations with implanted Pb concentration. Studying a larger data set of Pb-concentrations would be helpful to strengthen this assignment but nevertheless, the correlations here are clear. The low temperature PL data also provided strong evidence that I_U and I_X peaks are both D^0X transitions due to their narrow line widths and the appearance of their complementary TES recombinations. However, behavior of the I_U and I_X peaks with respect to temperature, excitation intensity, and BGE showed striking differences which indicate fundamentally different structural origins for these two Pb-related peaks.

I_U, with a localization energy of 12.4 ± 0.2 meV, shows all the behavior of typical D^0X transitions and its intensity correlates with the Pb-concentration. In most respects it behaves just like I_{6a} and the one exception is the slightly slower intensity decay with increasing temperature. Assigning the I_U peak to interstitial Pb defects, Pb_i, can account for all of its behavior. First off, implantation of Pb into ZnO is likely to produce a high concentration of interstitial defects as the ions are stopped by the lattice. In order for Pb to be incorporated onto a Zn substitutional site in high quality ZnO with good stoichiometry, a Zn atom needs to be displaced from its lattice site during bombardment. Pb then has to diffuse to the Zn vacancy before the displaced Zn does. Pb has a large atomic (180 pm)[206] and ionic radius (119 pm for Pb^{2+})[207] meaning it has a low diffusion rate in ZnO. EPR measurements on deliberately Pb-doped ZnO powders show only a small fraction (about 0.1%) of the Pb was incorporated into substitutional

crystal sites.[198] In these implanted samples, the fraction could be signifiantly smaller as incorporation onto substitutional sites is significantly more efficient when the impurity is added during the crystal growth. Furthermore, implantation experiments with transition and rare earth metals show that full lattice recovery of ZnO does not occur until the samples have been annealed above 1000 °C,[34] much higher than the 600 °C used in this study. However, annealing at temperatures above 900 °C causes diffusion of the implanted ions toward the surface,[208] significantly altering the concentration profile and encouraging clustering.

Appearance of I_{U} in the 0.01% Pb-implanted ZnO is very strong evidence that it is due to interstitial Pb. If the efficiency of the Pb substitution was as efficient as the deliberately doped powder,[198] the concentration of the substitutional Pb at 0.01 at % Pb would be less than 0.1 ppm. It is likely less than that, perhaps even by orders of magnitude. Concentrations in this range are certainly detectable by PL[196] but this depends on the impurity and the host. In any case, it would be suprising to see I_{U} at such high intensity in the 0.01% Pb sample if it was due to substitutional Pb. Interstitial impurities will usually act as donors, even when the impurity atom is normally incorporated as an acceptor when it's on the substitutional site. This has been verified by electron paramagnetic resonance (EPR) and electron nuclear double resonance (ENDOR) experiments for Li and Na interstitials in deliberately doped ZnO nanoparticles.[209] It is one of the reasons why ZnO, and every other semiconductor, is 'intrinsically' n-type. Pb occurs in oxidation states of +2, +3, and +4 and would readily donate electrons from its outer $6s$ and/or $6p$ shell when incorporated interstitially. Narrow line width of the I_{U} exciton rules out Pb-clusters as the origin of the I_{U} peak. The distribution in the cluster sizes would inhomogeneously broaden the transition, which was not observed.

Pb_i as the origin of the I_{U} may also be able to account for the slightly slower decay in temperature than the Al-related $I_{6\mathrm{a}}$ peak. The high concentration of implanted Pb would provide a large number of traps for the excitons thermally released from the $I_{6\mathrm{a}}$ binding center as temperature is raised. Being interstitial with a high concentration, Pb_i centers would come into very close proximity to the substitutional Al impurities responsible for $I_{6\mathrm{a}}$. Interaction of the the $I_{6\mathrm{a}}$ and I_{U} traps, which are close in energy, could lead to thermal transfer of the exciton from the Al_{Zn} center to Pb_i. Such processes have not been reported in the literature as direct evidence would be extremely hard to obtain. It's possible that other Pb-related complexes are responsible for the I_{U} emission, but the Pb_i

origin is the simplest and most likely.

I_X, with a localization energy of 29.5 ± 0.2 meV, shows some behavior of typical D^0X transitions and, like I_U its intensity also correlated with the Pb-concentration. The significant quenching of this peak with BGE compared to the typical D^0X transitions is good evidence that this peak is due to substitutional Pb^{2+} sitting on the Zn^{2+} lattice sites. Due to its multivalent nature, Pb will act as a double donor when substituted on the Zn site in ZnO.[198] It was found by EPR and optically detected magnetic resonance (ODMR) that the Pb^{2+} center can be photoionized into the paramagnetic Pb^{3+} state by photons with energies above 1.35 eV.[197] In the BGE experiment, the 2.41 eV photons from the Ar^+ laser would have ionized the Pb^{2+} centers, further quenching the I_X emission under BGE. However, even at the highest BGE intensity the total destruction of the Pb^{2+} was prevented since the Pb^{3+} centers capture the photoexcited electrons produced by the BGE. A steady state concentration of substitutional Pb^{2+} and Pb^{3+} centers would have been produced by the laser at a given intensity, ensuring that the I_X peak would survive under high intensity BGE.

Dependence of the I_X peak on the above-gap excitation, as presented in section 6.4, also supports the Pb^{2+}_{Zn} origin of I_X. A smaller exponent on the power law relation was observed for the I_X peak compared to the rest, implying that its intensity was being saturated at the higher laser powers. The relatively small concentration of Pb^{2+}_{Zn} centers in these samples can account for that. Furthermore, the Pb^{2+} centers could also be photoionized by the 3.815 eV photons from the He-Cd laser, leading to the observed sublinear dependence on above gap excitation intensity for the I_X exciton. On the other hand, a Pb^{2+}_{Zn} origin cannot explain the fast decay with temperature observed for the I_X peak. Thermal ionization of the Pb^{2+}_{Zn} center would only be significant at temperatures where bound exciton emission would not be observed in the first place. Clearly, another interaction is going on for the Pb^{2+}_{Zn} centers which leads to efficient thermal quenching and may be a result of the nearby I^i_Y lines. These lines show anomalous behavior and no speculations to their origin have been made at this time. Despite the anomalous temperature dependence, the PL data points toward Pb^{2+}_{Zn} as the origin of I_X.

Laiho et al.[197] estimate the first donor level of Pb, corresponding to the Pb^{2+} to Pb^{3+} transition, to be 1.35 eV below the conduction band based on the spectral dependence of the photosensitivity of the paramagnetic Pb^{3+} EPR signal. This is much larger than the 86 ± 2 meV donor binding energy for the I_X trapping center as measured by the TES separation in this study. However, measuring donor

binding energies by photo-EPR is not nearly as reliable as the measurements from the TES separations. The photoionization cross section of the Pb^{2+} likely varies with photon energy, making direct extraction of the donor binding energy impossible. The threshold measured by Laiho et al.[197] at 1.35 eV may be more closely related to the ionization cross section than the donor binding energy itself. On the other hand, the TES separation is a direct measurement of the energy separations of the excited states of the donor electron. This can be tied directly back to donor binding energies using simple effective mass approximations, being only slightly improved by correcting for the chemical shift induced by the impurity.[16] Hence, the 86 ± 2 meV binding energy extracted in this study is a much better estimate of the donor binding energy of Pb^{2+} and is in the range of other commonly measured donor binding energies in ZnO.

Assigning I_U to excitons bound to interstitial Pb and I_X to excitons bound to substitutional Pb^{2+} can account for their relative energetic positions. Interstitial Pb will not be strongly bonded to the lattice and its electrons would be easily removed, leading to a low donor binding energy for Pb_i. For substitutional Pb, two of the valence electrons get snapped up by the Pb-O bonds which effectively leaves the Pb in a +2 charge state. Donor electrons of the Pb^{2+} center are more strongly bound, effectively seeing a +2 charge from the Pb ion. Thus, the donor binding energy of Pb_{Zn}^{2+} would be expected to be higher than Pb_i. According to Haynes rule,[106] I_X should have a higher localization energy than I_U, as was observed in these Pb-implanted samples.

One possible problem with the proposed assignments of the origins of I_X and I_U were their relative PL intensities. Intensity of I_X was less than I_U in both the Pb-implanted samples, emitting at 3% of the I_U intensity in the 0.01% Pb sample and at 60% of the I_U intensity in the 0.10% Pb-implanted sample. Such a drastic increase in the relative intensity of the I_X peak with Pb concentration sheds some doubt on the Pb_{Zn}^{2+} origin. Incorporation of the Pb onto the Zn sites during the annealing process should not be so strongly dependent on the Pb concentration. However, when considering their relatively large size, the Pb impurities would not be able to move far at 600 °C during the annealing. The order of magnitude higher concentration of the impurity in the 0.10% Pb samples would significanlty reduce the distance between the Pb impurities and the Zn vacancies, where they could be easily incorporated into a Zn site. This increases the chance of each Pb ion reaching a substituional site, which would increase the efficiency of the substitutional incorporation. Another possible explanation of the

relative intensities may be differences in the radiative lifetime of the I_X and I_U recombinations. I_X could have a significantly shorter radiative lifetime than I_U. The result would be a stronger time-integrated PL signal for the I_X peak than the I_U peak if they had the same binding center concentrations. Time resolved PL would open up a wealth of information about the exciton dynamics in these Pb-implanted ZnO samples.

Pb implantation into ZnO resulted in several new and interesting emission features in the NBE region of the ZnO photoluminescence spectrum. Two sharp peaks were assigned to D^0X complexes, originating from interstitial Pb and Pb_{Zn}^{2+} centers. So far there are no reports of excitons bound to double donors in the literature and they may be quite different to excitons bound to standard single donors. With single donors, Haynes rule shows the D^0X complex can be thought of as a hole bound to a positive donor ion by an electron-pair bond.[106] For excitons bound to double donors, there are three electrons, one hole, and the positive donor ion. The extra electron from the double donor may upset the electron-pair bond and result in different behavior to standard D^0X complexes. Such behavior might also be able to account for the I_Y^i lines if it led to splitting of the Pb_{Zn}^{2+} energy level. Truly unambiguous assignment of the PL features discussed in this chapter will require more data than what has been presented. Magnetic field dependence of the PL emission along with time resolved measurements, EPR studies, and a larger sample size using several more Pb-concentrations would provide a complete data set. Dependence on the implantation and annealing conditions could also yield valuable information into the incorporation of the Pb into its various complexes inside the wurtzite ZnO structure. Nevertheless, confident assignments of I_U to interstitial Pb and I_X to Pb_{Zn}^{2+} centers have been made. Due to its interesting interactions with above and below gap excitation, Pb-doping may prove useful for optoelectronic devices. Before this can happen, more work needs to be carried out to understand all of the effects that Pb has on the excitonic spectrum of ZnO.

Chapter 7

EPLD growth of other oxides

7.1 Noble Metal Oxides

The success of EPLD for ZnO deposition from a metallic Zn target suggests that other simple oxides can be grown by this technique. Of particular interest are the oxides of the noble metals such as Ir, Pt, Pd, and Ru. These metals and their oxides have many interesting properties which make them ideal for a wide range of applications. Extreme conditions are required to oxidize the noble metals, easily obtainable by reactive laser ablation using high powered excimers. EPLD proved successful at producing Ir, IrO_x, Pt, PtO_x, Pd, and PdO_x thin films on room temperature substrates by ablating metallic targets in an O_2 atmosphere. This work was initially motivated by research into noble metal Schottky contacts to bulk ZnO and was in collaboration with Dr. Martin Allen of the Electrical and Computer Engineering department. EPLD grown noble metal oxides produced remarkable rectifying characteristics on bulk ZnO,[3] emphasizing the viability of EPLD for oxide growth from metallic targets.

Iridium is a heavy element with unique properties. It is the second densest element on the periodic table and when the Earth was still molten, most of the Iridium sank into the core where it still resides today.[210] It is 4 times rarer than gold in the Earth's crust but is present in much higher concentrations in meteors. A thin layer of 65 million year old Ir found across the globe is what Alvarez et al.[211] used to suggest an asteroid caused the cretaceous-tertiary extinction, killing the dinosaurs. Of all the known pure metals, Ir is the most resistant to corrosion.[212] Ir also has a very high melting point, the 11^{th} highest out of all the elements. It finds a multitude of uses for microelectronics including bulk acoustic wave resonators[213] and even organic LED's[214]. Iridium usually oxidizes into IrO_2, which has a rutile structure with a tetragonal primitive cell.[72] Highly-conductive

single crystals of IrO_2 can be grown by chemical transport techniques at high temperatures.[215,216] Thin-films have been grown by several techniques including DC sputtering,[217] spray pyrolysis[218], chemical vapor deposition,[219] and standard PLD[72,220]. Applications for IrO_2 are wide ranging and include electrochromic devices,[221] microscopic pH sensors,[222] and now Schottky diodes[3]. Exploration of EPLD growth of this material and other oxides of iridium may produce unique morphologies with a wide range of applications.

Ruthenium is another noble metal with interesting characteristics. Ru is one of the three naturally occurring elements which is less abundant in the Earth's crust than Ir. It has been used to harden titanium alloys,[223] in dye-sensitized solar cells,[224] and as electrodes for DRAM cells[225]. Oxides of Ru include Ru_2O_3, RuO_4, and RuO_2. Like IrO_2, single crystal RuO_2 can be grown by chemical transport techniques.[215,226] It also has a rutile structure and finds similar uses as IrO_2. Thin films of RuO_2 have been used in electrochromic devices,[227] microscopic pH sensors,[228] and they show similar high-conductivity at room temperature as IrO_2[229]. They can be deposited by chemical vapor deposition,[229] sputtering,[230] and PLD[231,232]. For PLD growth, RuO_2 sputter targets are usually used and are commercially available.[231,232] However, oxide targets are typically more expensive than pure metals and so far there are no reports of PLD from metallic Ru targets.

Iridium and ruthenium are two elements in the so called platinum group metals.[210] Platinum itself is one of the most useful metals on the periodic table, finding applications from catalytic converters in automobiles[233] to holding the diamonds which impress the ladies. Platinum is another material which is notoriously hard to oxidize but under extreme conditions crystalline PtO, Pt_2O_3, and PtO_2 along with amorphous platinum oxide layers can be produced.[234,235] These oxides have been shown to have a semiconductor character with both a direct and an indirect bandgap.[235,236] Due to their catalytic and optical properties, the platinum oxides will find many uses in novel sensors and microelectronic components. Palladium is another member of the platinum group which also has a wide range of uses. Recent interest in palladium-deuterium based cold-fusion has rekindled hope in work which was pioneered in the late 1980's and then quickly dismissed.[237]

Oxides of all of these platinum group metals show unique properties which will lead to some innovative device architectures. For this thesis, oxides of Pt, Ir, Pd, and Ru were deposited from metallic targets by EPLD in an O_2 atmosphere. Fully oxidized material was not achieved but the layers showed striking differences

when deposited in an O_2 or an Ar ambient. It is not the goal of this chapter to present fully characterized samples of each of these oxides. Instead, the viability of EPLD for growth of these materials is presented, epitomized by the remarkable characteristics of EPLD grown oxidized noble metal Schottky contacts to bulk ZnO.

7.2 EPLD Growth

Compared to the Zn target, all the noble metal targets were considerably harder to ablate. Figure 7.1 shows images of the resulting noble metal plumes in an oxygen ambient of 50-100 mTorr. During the Pt ablation, fast moving orange sparks were seen flying off the target at all angles which are not clear in the plume image. The same was true for the Ir and Ru plumes where the sparks were more pronounced and were captured clearly in the photographs. As shown in figure 5.1 (page 107) these sparks are micron sized molten particulates caused by violent subsurface explosions. Such sparking was not observed during Pd ablation. An iridescent green Pd plume was created by the UV laser, a color not observed for any other material deposited in the HV chamber. Unfortunately no optical emission spectra could be recorded from any of these plumes using the OceanOptics CCD system. When ablated in Ar, the plumes looked essentially the same although a turquoise color could be seen which was not present in O_2, presumably due to Ar transitions. Thorough study of the spatially and temporally resolved optical emission spectra from these plumes would yield some useful information.

PLD growth of Ir[238], IrO_2,[72,220], RuO_2,[231,232], Pt,[239] and Pd[240,241] thin films has been previously reported. However, there are no reports on standard PLD growth of Ru films or the oxides of Pt or Pd. Reported fluences for ablation of Ir are as high as $20\,J/cm^2$,[72] while Pt fluences were reported much lower at around $5\,J/cm^2$.[68] For Pd there is a wide spread in the reported fluences, ranging from $5\,J/cm^2$ (references 240,242) to $25\,J/cm^2$ (reference 241). In this work, fluences of 15, 15, 7, and $15\,J/cm^2$ were used for the Ir, Pt, Pd, and Ru targets respectively. To achieve these fluences, the circular aperture was removed from laser path and the full beam was used for ablation. The laser spot size on the target was estimated at around $2\,mm^2$. During initial tests with each target it was found that the sparking accompanied the plume for all fluences above threshold. The exception was the first minute or so of ablation from a fresh target. In some cases no sparks were observed until a few minutes of ablation. Necessity for such

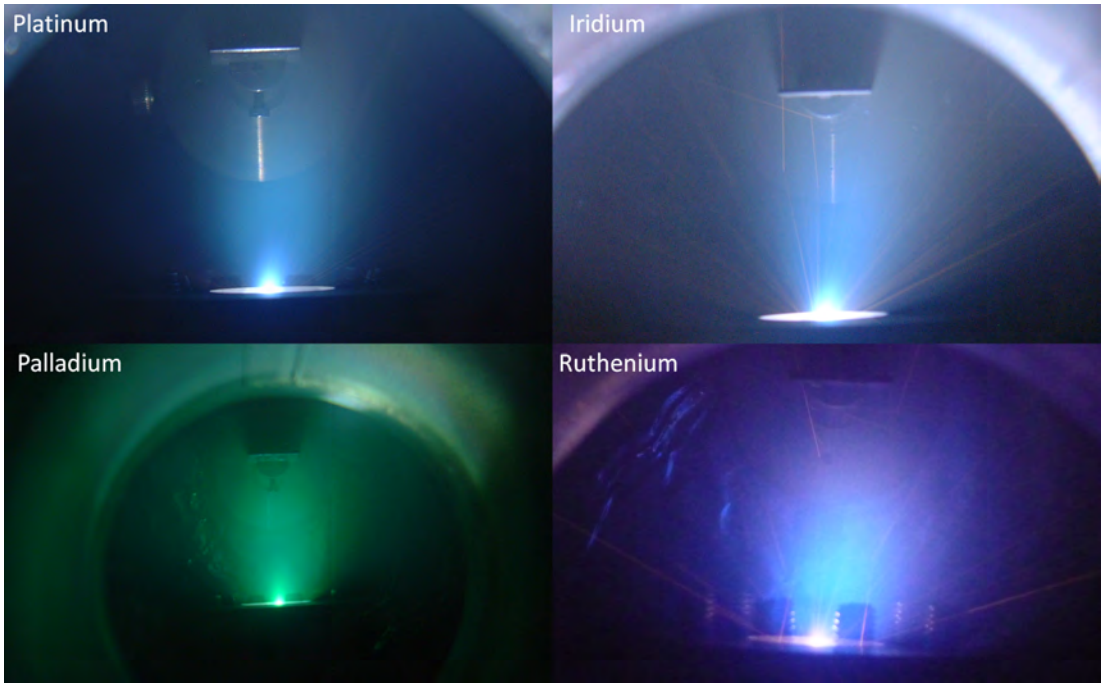

Figure 7.1: Images of laser-induced plumes from noble metal targets taken through the top view port of the HV chamber. All plumes were in 100 mTorr except for the palladium which was ablated in 50 mTorr

high laser fluences is one down side to PLD growth of the noble metals and their oxides, especially from the industrial viewpoint.

Films of the noble metals and their oxides were grown by EPLD onto quartz and the Zn- and O-polar faces of hydrothermally grown ZnO from Tokyo Denpa. Growth of the pure metals was done in 50-100 mTorr of Ar and the oxides were deposited in 50-100 mTorr O_2 ambient. Target to substrate distance was 53 mm. The shadow mask was a $10 \times 10\,\mathrm{mm}^2$ stainless steel square placed $2/3^{rds}$ of the way from the target to the substrate. Laser repetition rate was 10 Hz and growths were done for 1 h. Thickness of the samples, as measured by profilometry, was between 50 and 150 nm. All depositions were done at room temperature. The main motivation for room temperature growth came from previous experiments trying to sputter or evaporate Ir contacts to bulk ZnO. Ir is extremely tough with a high melting point and heating from the source was annealing the ZnO. This reduced the carrier concentration and resulted in poor quality diodes. No such problem exists for EPLD growth and this method is particularly well suited for growth of noble metal oxides onto temperature sensitive substrates.

After deposition of all the metals in an O_2 ambient, the substrate holder (heater

with no current) was covered with a black coating with no metallic-like reflectance. At 100 mTorr O_2 pressure this coating could be easily scraped off the holder with a razor. The samples appeared smooth to the eye and were partially transparent. Some showed thin-film interference patterns, especially the IrO_x deposited on quartz and the sample deposited on Si shown in figure 2.4(c) (page 15). Those samples deposited in Ar showed a metallic looking surface with a high reflectivity but still slightly transparent. Trying to remove the metallic deposits from the substrate holder proved quite difficult indeed.

Due to the room temperature substrate and the resistance of some of these noble metals to oxidation, fully oxidized material was not likely formed by ablation in non-activated O_2. X-ray photoelectron spectroscopy (XPS) was performed on an IrO_x sample which indicated an O/Ir fraction of around 0.22.[3] However, its possible that O atoms were preferentially removed during an in situ sputtering step designed to penetrate below the heavily oxidized and contaminated surface layer before XPS measurements. XPS also indicated a continuous density of states above the Fermi energy, showing metallic like behavior or perhaps a degenerate semiconductor-like electronic structure. XRD data would shed light on the oxidation of the noble metal oxides and is key to a full understanding of this material.

SEM images of IrO_x grown by EPLD on top of the quartz substrate with an O_2 ambient of 100 mTorr is shown in figure 7.2. Despite the shadow mask, a high density of particulates was present on the sample as shown in figure 7.2(a). Most of these particulates were around 1 or 2 μm in diameter but some were in the 100-200 nm size range. Collisions between the particulates within the plume can diffuse them around the shadow mask. Also, during growth particulates could clearly be seen bouncing off the top and bottom of the HV chamber and making it around the shadow mask. It's hard to say which process leads to more particulates and the problem could be solved by using a chamber with a larger volume with more space between the substrate and walls. Another idea is to put the substrate directly on the backside of the shadow mask. A smooth looking deposit was grown on the back of the shadow mask after a few growths. The drastic cut in growth rate for this geometry might be worth it to obtain smooth, particulate free films for a given application.

Under high magnification, the IrO_x/quartz sample was ripped apart along the apparent grain boundaries. These images were taken with a beam energy of 10 kV. Figure 7.2(b) shows an extreme close up of the IrO_2 surface. In the time it took to

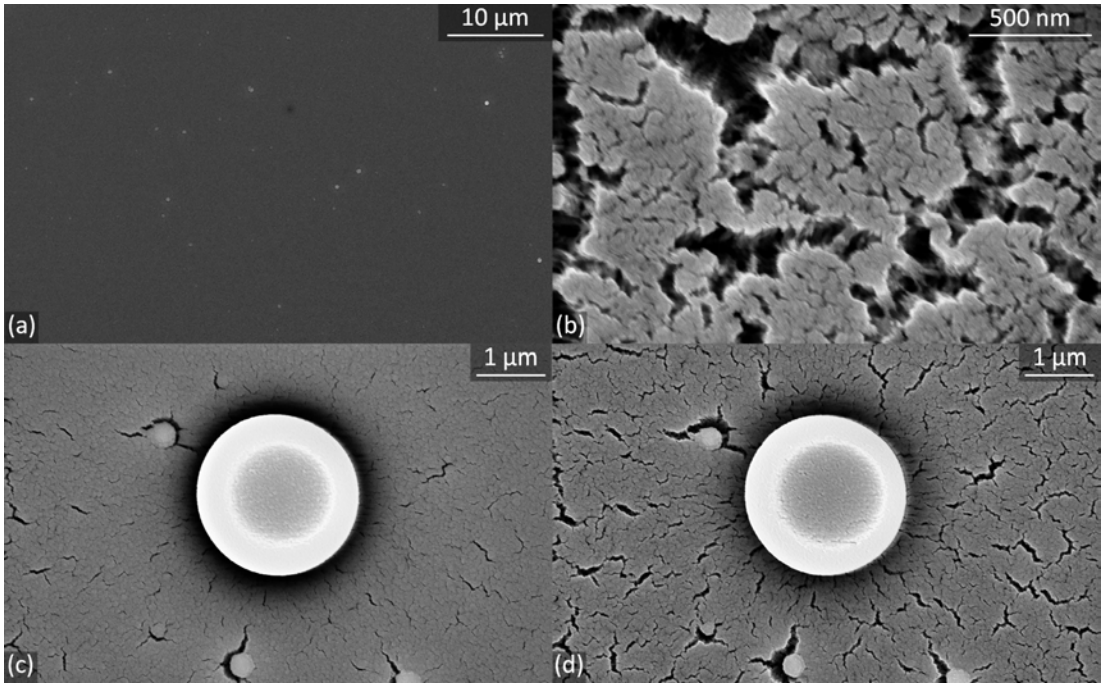

Figure 7.2: SEM images of IrO_x grown on quartz at room temperature. (a) Low magnification image. (b) Close up showing tearing of the surface by the SEM. (c) Particulate and the start of surface tearing. (d) Same spot as the image in (c) after 1 minute exposure to the SEM electron beam.

raster the beam across the sample (about 20 s), pronounced cracking of the IrO_2 occurred. This was tearing of the film and not evaporation or sputtering. The process could be easily watched by eye with the SEM in a faster scanning mode. The surface would look normal at first, then the grain boundaries became more pronounced, then cracks started to form, and finally they started to spread open. Once formed these cracks were permanent and did not relax after the electron beam was moved. Figures 7.2(c) and (d) show two moderate-magnification SEM images taken one minute apart of the exact same spot on the sample. At this magnification, the cracking would stop after about 1 min. A particulate is shown in the images and some small cracks can be seen on it after 1 min exposure to the electron beam. The reason for the tearing is unknown at this stage. Its possible that surface charges were building up on the grain boundaries and the Coulomb repulsion was strong enough to rip the samples apart.[†] Some evidence of charging can be seen as the white regions at the edge of the fissures. Alternatively, thermal annealing from the electron beam may also be ripping the layer apart as oxygen gas is lost from below the surface. A controlled study of this phenomena would

[†]This idea was suggested by Gary Turner.

yield important information about the durability of this material.

7.3 Optical Transmission

All the samples produced, whether grown in O_2 or Ar, were somewhat transparent since they were all less then 150 nm thick. Figure 7.3 shows the optical transmission from the noble metals and their oxides deposited by EPLD onto double polished quartz. This data was gathered using a Cary spectrophotometer and was corrected for the transmission of the quartz substrate. Oxidized samples were more transparent than the pure metallic ones, something which was easily observed by eye and shown clearly in figure 7.3. One or two interference fringes were clearly observed in the transmission of the IrO_x, indicating an optically smooth surface despite the particulates. Except for the RuO_x, the oxidized samples showed a semiconductor-like transmission onset around 300 or 400 nm. The lamp output and detector response of the Cary spectrophotometer starts to fall off at these wavelengths, but the low noise and smooth curves attest to the reliability of the data in this region. More importantly, a relatively flat response was observed for the pure metals across the UV/visible spectrum, as expected for light with frequencies far from the plasma frequency. Clearly, the EPLD technique produces at least partially oxidized noble metals when depositing onto room temperature substrates.

There have been several theoretical studies of the band structure of some of the noble metal oxides. Among the most commonly investigated are the various oxides of Pt along with PdO.[236,243–246] In most cases, the platinum and palladium oxides are treated as semiconductors with direct and/or indirect bandgaps. The same is true for IrO_2,[217] and so far there are no theoretical reports on the band structure of RuO_2 or the other oxides of Ru. Experimental studies show a relatively large range of direct and indirect optical bandgaps for these materials, ranging from 0.7 to nearly 4 eV.[232,235,247] The semiconductor-like transmission observed for the PtO_x, IrO_x, and PdO_x suggests that these EPLD grown samples also have optical bandgaps. According to the Tauc relation, the optical bandgap is related to the absorption coefficient α_c by[248]

$$\alpha_c = \frac{C(h\nu - E_g)^n}{h\nu} \tag{7.1}$$

where C is a constant, E_g is the optical bandgap, $h\nu$ is the photon energy, and

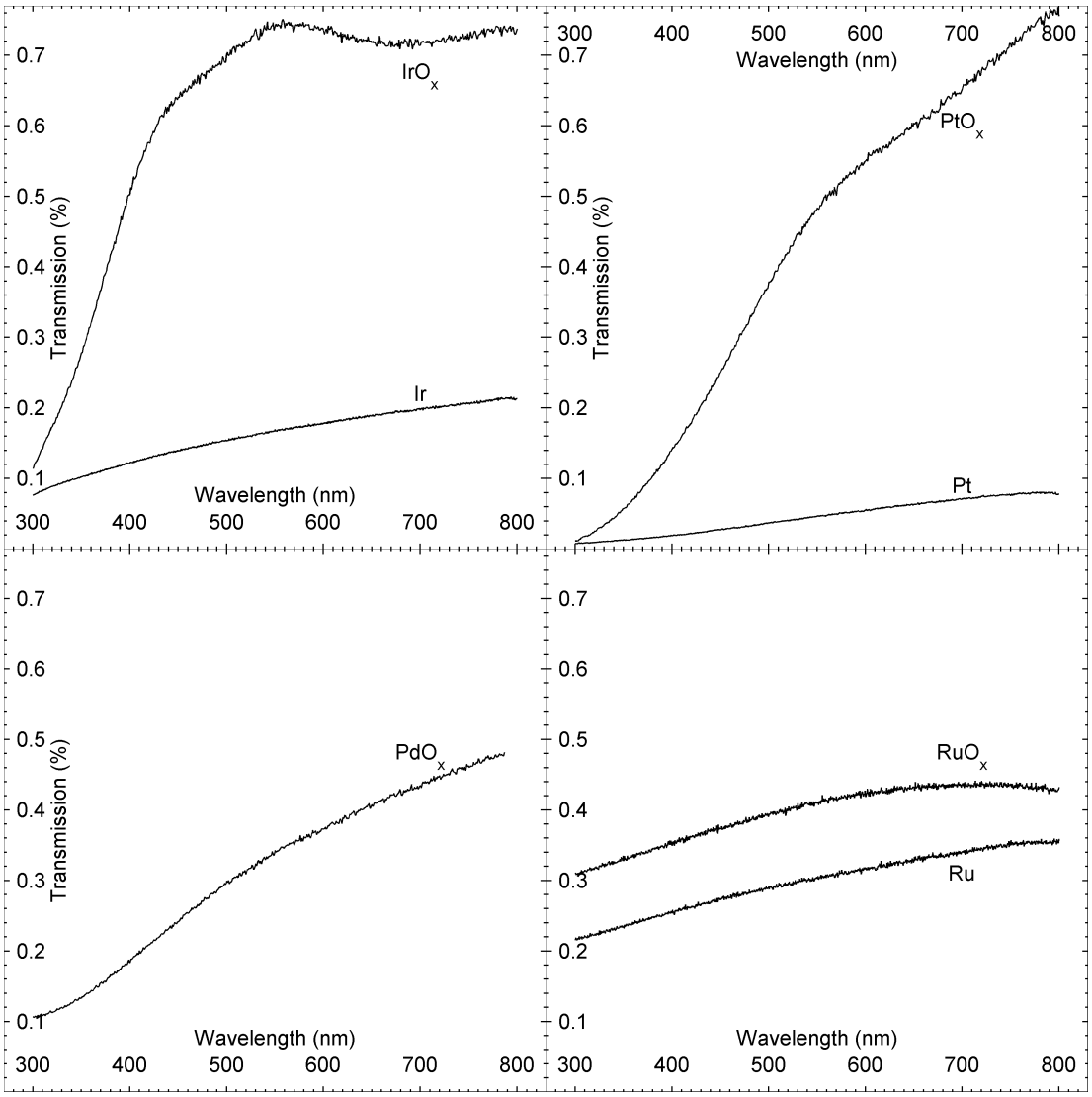

Figure 7.3: Optical transmission of noble metals and their oxides.

$n = 1/2$ for a direct gap or $n = 2$ for an indirect gap. According to equation 7.1, the bandgap can be extracted as the x-intercept of a plot of $(\alpha_c h\nu)^{1/n}$ vs $h\nu$. α_c is related to the transmission T by[249]

$$\alpha_c d = -\ln\left[\frac{T}{(1-R)^2}\right] = A \tag{7.2}$$

where R is the reflectivity and d is the film thickness. Defining the absorbance, A, as $A = \alpha_c d$ allows bandgap extraction using the Tauc relation without knowing the film thickness. This is because multiplying a straight line by a constant does not change the x-intercept, it simply rescales the y-axis about $y = 0$. Equation 7.2 shows that extraction of A from the transmission requires knowledge of the

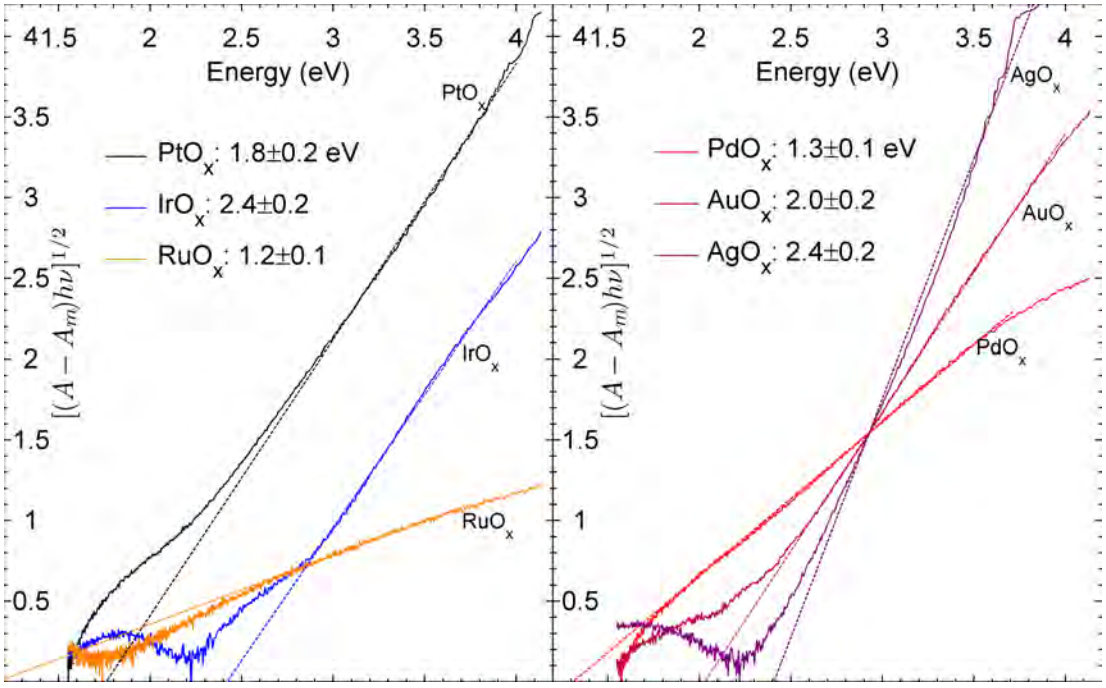

Figure 7.4: Determination of the indirect bandgap of the noble metal oxides using an approximate Tauc relation.

reflectivity. This data was not gathered simultaneously with the transmission in the Cary spectrophotometer. Using the OceanOptics reflectance probe to get R is unreliable at wavelengths shorter than 400 nm and absolute values are hard to measure with that system. Trial and error combined with examination of equation 7.2 and the Tauc relation shows that a flat reflectivity response will not change the x-intercept of the $(Ah\nu)^{1/n}$ vs $h\nu$ plot. Only a strongly wavelength dependent R will shift the extracted bandgaps. Also, the important data for E_g measurements using A comes from the above gap data where the reflectivity should be a smooth function with relatively small variations. Again, trial and error shows that no more than a 10% error in extracted bandgaps should be present when assuming $R = 0$ or some other constant. Such an error is smaller than the spread in measured bandgaps for the noble metal oxides and transmission measurments are a simple way to extract their bandgaps.

Following the lines of Sirohi et al.[250], direct and indirect bandgaps were extracted from plots of $[(A - A_m)h\nu]^{1/n}$ vs $h\nu$ where A_m is the minimum measured absorbance.[†] Figure 7.4 shows the indirect bandgap calculations for the EPLD grown noble-metal oxides. Data for EPLD grown AuO_x and sputtered AgO_x

[†]There is a typo in the third paragraph of section 3.1 of the report by Sirohi: $[(\alpha - \alpha_1)h\nu]^n$ should read $[(\alpha - \alpha_1)h\nu]^{1/n}$ as can be verified by the y-axes in figures 1 and 2 of that report.

is also shown. Both of these samples were deposited at room temperature on double polished quartz. Uncertainties in the figure represent an error of roughly ±10% due to the approximation that R does not strongly depend on $h\nu$ above the bandgap as discussed earlier. All of the oxides show linear behavior in figure 7.4 over ranges from about 2.5 to 4 eV indicating indirect gaps are present in these oxides. The measured indirect gap for PtO_x is not far off the 1.5 eV value measured for α-PtO_2 films deposited by sputtering.[235] It is in good agreement with the 1.8 eV bandgap measured by optical absorbance and scanning tunneling spectroscopy by Zhensheng et al.[251], but no comment about its direct or indirect nature was made. Some α-PtO_2 might be present in these samples but it was likely mixed in with other phases and amorphous regions. In either case, the good agreement with literature values shows the noble metals are oxidized during EPLD. Agreement also shows that transmission can be used to get a reasonable estimate of E_g without accounting for the reflectance.

An indirect gap of 2.4 ± 0.2 eV was calculated for the IrO_x sample. So far there are no reports of indirect gaps measured for IrO_2. El Khakani et al.[252] report on the transmission of PLD grown IrO_2 and observed similar transmission curves to that shown here. They observed transmission as high as 45% at $\lambda = 500$ nm for samples 80 nm thick grown on quartz at 450 °C. The EPLD grown IrO_x showed roughly 70% transmission at 500 nm and was 75% for 570 nm. Thickness of this sample was around 60 nm. Such high transmission for room temperature growth attests to the ability of EPLD to produce high quality noble metal oxide thin films. For PdO_x an indirect gap of 1.3 ± 0.1 eV was extracted with good linearity seen in the indirect Tauc plot of figure 7.4. Most reports consider PdO to be a direct gap semiconductor with a large spread in reported E_g values.[236,243,244] Perhaps the most reliable is the 0.8 eV value extracted from a full Kramers-Kronig analysis of the optical transmission of PdO thin films.[253] The indirect gap extracted for PdO_x in figure 7.4 is not far off this value and must be located between different points in the Brillouin Zone than the direct gap at the M-point.[236,244] RuO_2 is also treated as a direct gap semiconductor with reported bandgaps around 2.7 eV.[232,254] The linearity of the indirect Tauc plot of RuO_x in figure 7.4 suggests the presence of an indirect gap of 1.2 ± 0.1 eV somewhere in the Brillouin zone. More detailed studies of the band structure of the oxides of Ru should be undertaken to understand this observed indirect optical bandgap.

Tauc plots were also produced for oxides of Ag and Au with indirect gaps of 2.4 ± 0.2 and 2.0 ± 0.2 eV extracted for AgO_x and AuO_x respectively. The

AgO_x sample was grown by DC sputtering of a metallic Ag target in an oxygen ambient. Silver oxidizes into many forms such as the commonly observed Ag_2O, AgO, Ag_2O_3 , Ag_3O_4, and even Ag_4O_4. Nanostructured Ag_4O_4 has recently been grown by PLD from pure metallic Ag targets in an oxygen atmosphere.[255] Photoelectron spectroscopy of Ag_2O shows a gap at the Γ-point of 1.1 eV,[256] much smaller than than the indirect gap of 2.4 ± 0.2 eV extracted from the indirect Tauc plot of the sputtered AgO_x. Of all the plots in figure 7.4 the straight line fit to the AgO_x data is the worst, indicating that the AgO_x does not have an indirect gap.

Of all the noble metals, and in fact of all the naturally occurring elements, gold shows the most resistance to oxidation. Au_2O_3 can be formed under highly nonequilibrium conditions but is unstable even at room temperature.[257] Oxidized gold samples have been previously produced by PLD by ablating a metallic gold target in an oxygen atmosphere.[258] In this study the AuO_x was grown by EPLD in an oxygen ambient using a fluence of $15\,J/cm^2$ with the substrate at room temperature. Oxygen content of this film was likely quite low but an absorbance onset resembling that of a semiconductor was observed and indicated an indirect optical gap of 2.0 ± 0.2 eV. The high fluence would have created the nonequilibrium conditions required for oxidation of the Au. Room temperature substrates prevented the thermal decomposition and the shadow mask protected the surface from damage from the laser induced plasma. EPLD is thus a very viable way to produce oxidized gold samples.

Plots of $[(A - A_m)h\nu]^2$ vs $h\nu$ were used to extract direct bandgaps for these oxides as shown in figure 7.5. For both the direct and indirect gap calculations the data above 4 eV was not included in the fits as the machine response becomes questionable in this region. A few of the spectra have been multiplied by a constant for clarity as indicated by the arrows. For PtO_x the extracted gap was 3.3 ± 0.3 eV but the fit was not all that great suggesting there is no direct gap for this material. The same is true for the AuO_x and AgO_x which have similar extracted bandgaps to the PtO_x. On the other hand, the fits for the IrO_x and RuO_x direct gaps were good fits and indicate direct bandgaps of 3.4 ± 0.3 and 2.9 ± 0.3 eV for IrO_x and RuO_x respectively. Density functional theory calculations predict a direct bandgap of 3.1 eV for IrO_2 which is close to the value extracted in figure 7.5.[217] Previous reports of optical absorption measurements of IrO_2 indicate a slightly smaller bandgap around 2.7 eV.[232] Reported bandgap of RuO_2 films grown by PLD was 2.7 eV, in good agreement with the value shown

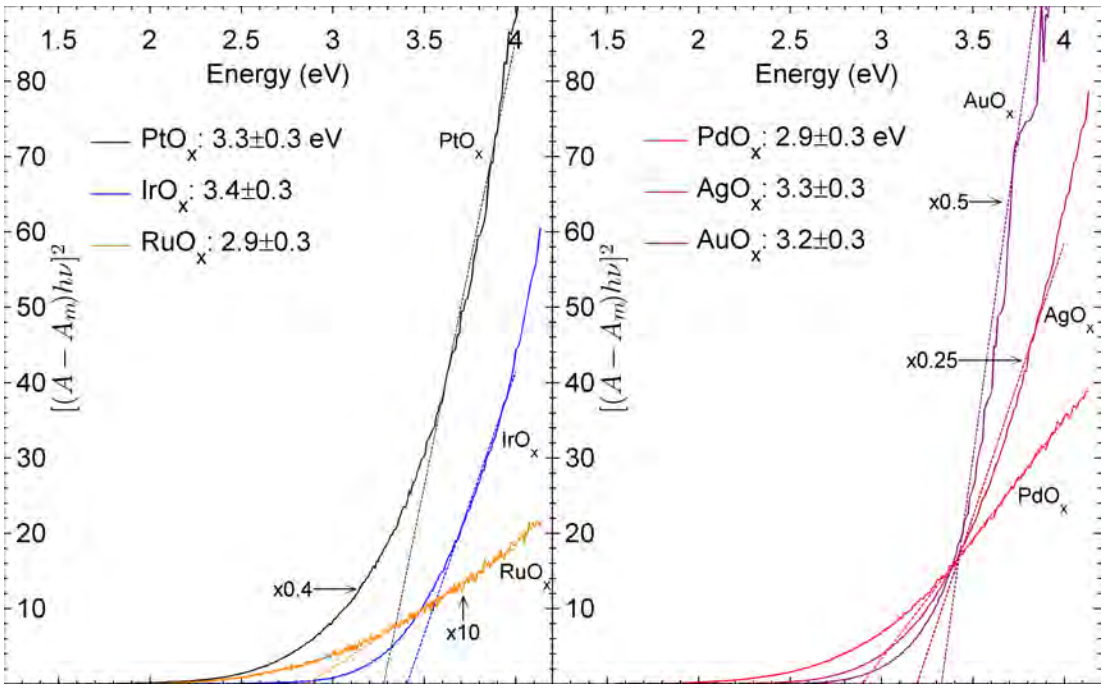

Figure 7.5: Determination of the direct bandgap of the noble metal oxides using an approximate Tauc relation. Arrows indicate those lines which have been multiplied by a constant (which does not change the x-intercept) for clarity.

in figure 7.5. Perhaps the best fit was for the PdO_x which showed a direct gap of $2.9 \pm 0.3\,\text{eV}$. However, this value was much larger than $E_g = 0.8\,\text{eV}$ extracted from a Kramers-Kronig analysis of the transmission of PdO thin film.[253] XPS and XRD studies on these samples would complement this data nicely and give insight into the connection between the electronic structure and optical properties of these noble metal oxides.

7.4 Schottky Diodes onto bulk ZnO

As mentioned previously, growth of the noble metal oxides was motivated by research into Schottky contacts onto ZnO. Dr Martin Allen produced silver oxide Schottky contacts onto ZnO by sputtering.[259] Barrier heights as high as 1.20 eV were demonstrated, the largest reported for n-type ZnO. It is the high work function of Ag and the other noble metals which make them attractive for Schottky contacts to ZnO. However, sputtering proved to produce poor quality contacts when using Ir and Pt. High temperature of the sputtering source was thought to heat the ZnO and effectively anneal out some of the free carriers. Damage

to the interface by the sputtering plasma may also have degraded performance of the diodes. EPLD does not suffer from either one of those problems. The laser ablation takes place in a very small region and does not lead to significant residual heating of the target, let alone the substrate placed 53 mm away. High energy species in the plume are effectively blocked by the eclipsing object and a low energy, diffuse flux of adatoms reaches the ZnO. Noble metal oxide/ZnO Schottky contacts deposited by this method showed excellent characteristics,[3] further demonstrating the merits of EPLD for simple oxide growth.

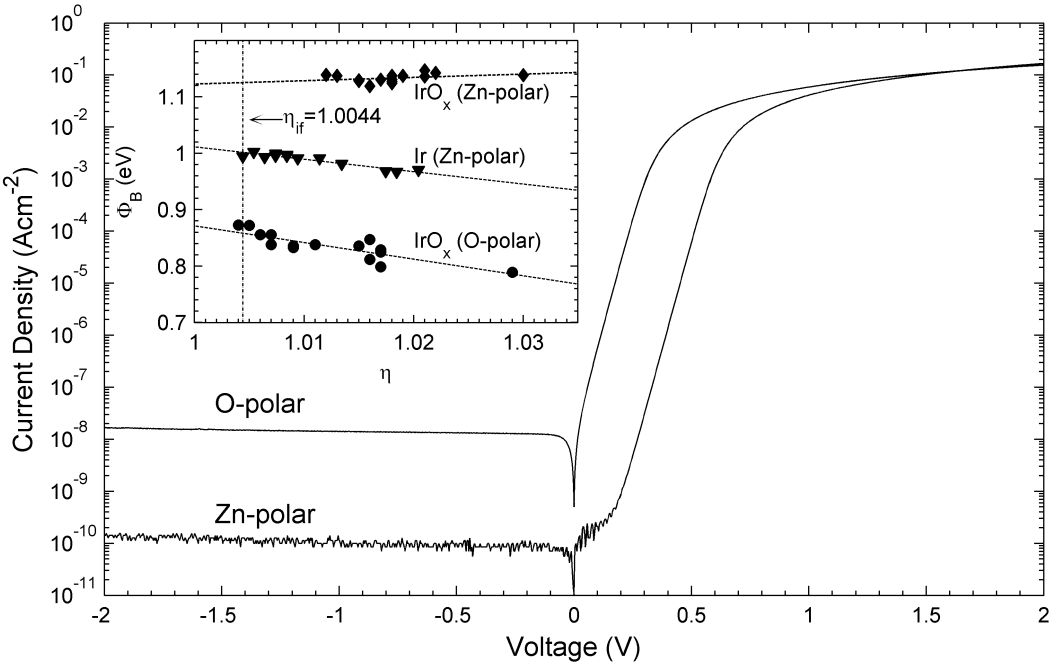

Figure 7.6: Current-voltage diagram of IrO_x/ZnO Schottky diodes. The inset shows the barrier heights Φ_B as a function of the ideality η, which approaches the image-force-controlled limit for laterally homogeneous interfaces η_{if}.

Typical current-voltage plots of the IrO_x diodes on Zn- and O-polar ZnO are shown in figure 7.6. Highly rectifying behavior was observed with essentially no back current up to -2 V. Forward to reverse current ratios at ± 1.5 V were about 10^9 and 10^7 for diodes on the Zn- and O-polar faces respectively. Barrier heights for the diodes on the Zn-polar face were larger than those deposited on the O-polar faces as shown in the inset of figure 7.6. All the noble metal oxide Schottky contacts showed excellent characteristics with incredibly low ideality factors as indicated in the inset of figure 7.6. η and Φ_B were calculated from the forward bias region using standard thermionic emission theory.[260] Ideality factors approached the image-force-controlled limit for laterally homogeneous interfaces,

η_{if}, which indicates a high degree of lateral homogeneity in the EPLD produced Schottky contacts.[261]

So far this thesis was focused solely on the fundamental physics of the ZnO and noble metal oxides produced by EPLD and these high-quality diodes show an application of the EPLD technique to device fabrication. Optimization of the diodes has only just begun and the characteristics are just going to improve from here. Further investigation of EPLD grown noble metal oxides will not only give better Schottky diodes, but uncover some useful fundamental physics regarding the electronic band structure of these strange and useful materials.

Chapter 8

Conclusion

ZnO has many useful properties which make it a rewarding material system for fundamental studies on the physics of highly crystalline direct-gap semiconductors. As far as light emitters go, no other semiconductor shows as rich of a photoluminescence spectrum as ZnO. High intensity UV emission with many sharp excitonic features at low temperature inspires thousands of publications about PL of ZnO every year. Essentially all the processes which lead to light emission from semiconductors can be observed from commercially available bulk ZnO substrates and high quality nanostructures. From polaritons, to excitonic-polarons, to Fano resonance, PL from ZnO also demonstrates the quantum mechanical nature of the fundamental excitations in a solid. This makes ZnO an ideal material for teaching students of all levels about light-matter interactions in an ordered semiconductor.

There is, however, a downside to working with materials with such beautifully structured PL emission as ZnO. More than 20 excitonic features have been reported in the near band edge region of ZnO. Several of these transitions overlap, washing out the fine structure and complicating their identification. One of the best ways to get around this limitation is to look at the temperature dependence of the PL emission. Peaks decay and shift differently with temperature and this can be used to separate the peaks and identify their origins. In this thesis it was shown that the free and bound excitons redshift differently with temperature. By using a modified from of a model describing the band gap variation with temperature, this difference was attributed mainly to the effect of lattice dilation. Bound excitonic peaks did not seem to be affected by the lattice dilation due to their localized wavefunctions compared to the free excitons. This phenomenon was clearly observed in the EPLD grown ZnO as well. More investigation into this aspect of excitonic emission is needed before solid conclusions about the effect of lattice dilation can be made.

Power dependent PL is another useful extension to the PL technique but caution must be made when interpreting the results. Intensity of excitonic PL peaks will usually show a superlinear dependence on excitation intensity. A sublinear dependence is expected for defect peaks. However, when essentially linear behavior is observed the results are ambiguous and usually do not reveal any new information. This said, power dependent PL is still a valuable characterization technique. It can show interesting phenomena, such as stimulated emission or the unique power dependence observed in the ZnO nanohexamids grown by EPLD. Altering the free carrier concentration with simultaneous below gap excitation adds another dimension to the analysis, easily separating the D^+X transitions from the LPB_A feature in the bulk ZnO presented in chapter 3. A single low temperature PL spectrum is essentially useless unless its dependence on these parameters is explored. Time resolved PL and magneto-PL can be added to the mix to truly explore the nature of the PL from ZnO. These techniques would be invaluable to the optics lab and solid state research at the University of Canterbury.

Standard and eclipse PLD produced high quality ZnO films and nanostructures from ablation of a Zn target in an oxygen atmosphere. Nanorods nearly a micron long were produced by standard PLD via a vapor-liquid-solid (VLS) growth mechanism due to the highly Zn-rich growth conditions and high substrate temperature. Introducing the shadow mask cut the Zn flux down considerably and a complex morphology resulted. Nanorods grown by vapor-solid (VS) growth mechanism were clumped together into well separated micron sized regions. In between the microclumps were isolated nanohexamids with 6-fold symmetry and clear capping particles, indicative of self catalyzed VLS growth. Appearance of both VS and VLS grown nanostructures in EPLD grown ZnO from a Zn target lead to a unique morphology. Introduction of the eclipsing object also lead to a decrease in particulate concentration but did not eliminate them completely. Collisions between the larger particulates can guide them around the shadow mask. The shadow mask also selected only those adatoms which had collided at least once with the background gas. This increased the probability of a reaction between the deposited Zn and the O_2 ambient. This aspect helped to balance the stoichiometry and improve the crystallinity.

Low-temperature PL emission from the NBE region of EPLD grown ZnO was strong and sharp. All the samples showed emission from $I_{3\mathrm{a}}$ which has been attributed to interstitial Zn atoms. This Zn_i signature is indicative of the highly

Zn rich growth conditions for ablation of a Zn target. The ratio of free to bound excitonic emission was an order of magnitude higher in the (E)PLD grown ZnO than it was in the bulk sample. Bound excitonic line widths were as small as 2 meV, noticeably larger than those of the bulk emission but comparable to those reported from high-quality heteroepitaxial films. Polariton emission from the lower branch was clearly observed in the EPLD grown samples and was identified by its slow decay with increasing temperature. EPLD grown ZnO showed UV PL emission intensities at least an order of magnitude higher than those samples grown by standard PLD under similar conditions. These aspects are testament to the high optical quality of ZnO produced by EPLD from a Zn target.

Shadow mask position and oxygen pressure had a profound effect on the PL emission from these samples. These variables are the two main parameters effecting the growth rate. Higher background pressure lead to higher mass deposition rates and material could make it around the mask most easily when it was half way between the target and substrate. In general, higher PL intensities were observed for lower growth pressures and the transitions were sharper when the shadow mask was closer to the target. This was caused by the slower growth rate for these geometries, which is known to generally lead to higher structural quality.

Perhaps the most interesting observation made on the EPLD samples was the unique behavior of the PL with respect to excitation intensity. The I_7 exciton dominated the PL of most of the samples produced in this thesis and clearly showed superlinear behavior with respect to excitation intensity. While this is expected for D^0X complexes, the emission exponent of around $\zeta = 1.5$ for I_7 was significantly larger than those of all the other features in the NBE region. Such a big difference in power dependence between individual D^0X complexes has not been previously reported in ZnO or other material systems. This behavior may help to identify the chemical and structural origin of I_7, which still remains a mystery.

I_7 emission showed strong variations across each of the samples. This was most pronounced for the sample grown with a helical shadow mask, showing overwhelming I_7 emission from a small region on the sample. Emission from I_7 seems to be intimately connected to the unique morphology of these samples. Dominating emission from I_7 has not been previously reported in ZnO and more information is needed before the origin of I_7 can be unambiguously identified. When it is finally discovered, this feature may uncover new and interesting physics

behind the light-matter interaction in ZnO and other nanostructured materials.

Morphology and structural quality of materials grown by EPLD, or any other deposition technique, are profoundly influenced by buffer layer structures. ZnO has a high lattice mismatch with most common substrate materials, resulting in a high dislocation density in heteroepitaxially grown samples. Inserting a thin layer of another material between the substrate and main layer can reduce the lattice mismatch and absorb the dislocations. For this study, use of a Pt buffer layer was explored and it had a significant effect on the morphology and PL emission of the ZnO deposited on top. Pt has a high melting point, which helped suppress the VLS growth mechanisms. Continuous films with pronounced grains, clearly visible by SEM, were deposited by standard PLD. A brain like morphology was the result of EPLD growth on the Pt/Al_2O_3 with the surface showing a high concentration of nanoscale pores. The difference in the morphology between PLD and EPLD grown $ZnO/Pt/Al_2O_3$ was again linked to the difference in growth rates. The Pt buffer layer was shown to be porous and the low growth rate of the EPLD technique allowed the adatoms to mimic the underlying structure. Such porous samples may be ideal materials for the next generation of gas and chemical sensors.

PL emission was also affected by the Pt buffer layer. The $ZnO/Pt/Al_2O_3$ showed similar UV PL intensities to the ZnO/Al_2O_3 but had slightly broadened lines. Emission was composed of the same basic features as the unbuffered ZnO, showing free excitonic emission along with strong Zn_i signatures. Emission was once again dominated by the I_7 exciton, even for the PLD grown ZnO/Al_2O_3. Emission from hot excitons was clearly observed from the $ZnO/Pt/Al_2O_3$ and several of the ZnO/Al_2O_3 samples. Hot exciton emission indicates a short radiative lifetime of the free excitons. A short excitonic radiative lifetime in the (E)PLD grown ZnO can also explain the high free excitonic to bound excitonic intensity ratio. The shorter the free exciton radiative lifetime, the smaller the probability of being captured by a defect before recombination.

In the EPLD grown $ZnO/Pt/Al_2O_3$, a strange emission around 3.25 eV was observed along with 4 LO-replicas. DAP recombinations have been observed in ZnO near this energy but the so called Q-band emission from these samples did not show characteristics of DAP emission. There was no blueshift with increasing excitation intensity. Furthermore, its emission intensity showed a power law with an exponent of just over one, much greater than the 0.6-0.8 expected for DAP recombination. Free carrier concentration, as induced by simultaneous

BGE, also did not affect the Q-band emission. No such behavior has been reported for a broad peak at this energy in ZnO, giving it a questionable origin. LO-phonon structured Q-band emission was only observed in the EPLD grown ZnO/Pt/Al_2O_3 but may have been present as a very broad, unstructured band in some of the EPLD grown ZnO/Al_2O_3. Time resolved emission may help to resolve the origin of the Q-band emission, which remains a mystery at this time. Pt is a viable buffer layer for growth of ZnO by any method, reducing strain from lattice mismatch and providing a back contact for optoelectronic device fabrication.

Essentially all of the ZnO grown by EPLD from metallic Zn targets had I_7 as the dominant PL emission feature at low temperatures. Pb was the main impurity in the Zn targets so a Pb-related complex is a likely origin of I_7. Bulk ZnO wafers, grown hydrothermally by Tokyo Denpa, were implanted with $^{207}Pb^{1+}$ to see if I_7 emission could be induced. After implantation the samples were annealed at 600 °C in 1 atm O_2 to repair the damage from the implantation. PL emission from the Pb-implanted samples was cut down by factors of up to 170 compared to the undoped bulk but the line widths were essentially preserved. As such, defects from the implantation were reduced but not completely eliminated by the implantation.

No peak in the I_7 region was observed in the Pb-implanted bulk. This casts doubt on Pb as the chemical origin of I_7 but does not rule it out. (E)PLD growth is a nonequilibrium process and its likely the Pb incorporated in different complexes in the implanted bulk and the EPLD grown samples. Different annealing conditions or Pb concentrations may induce I_7 emission in the bulk. The residual impurities in the bulk sample are also different than the (E)PLD grown samples. Pb is known to interact with these impurities via charge transfer processes and this could be destroying the I_7 binding center in the implanted bulk. More experiments will be needed to confidently rule out a Pb-complex as the origin of the I_7 bound exciton.

Pb-implantation did however induce other peaks in the NBE region of the low temperature PL. A peak with a localization energy of 12.4 ± 0.2 meV, labeled as I_U, was introduced by the Pb-implantation. This peak showed all the typical behavior of a D^0X complex. The only exception was the slightly slower decay in intensity with increasing temperature compared to the other D^0X complexes. TES emission from I_U was observed and indicated a donor binding energy of around 40 meV for the I_U binding center. Pb would have been initially implanted interstitially and only a small percentage would have moved to substitutional sites

after annealing due to its large ionic radius. Considering its low donor binding energy, typical D^0X behavior, and appearance in the sample implanted with a small Pb flux, I_{U} was tentatively assigned to excitons bound to interstitial Pb.

Another sharp excitonic feature was introduced by the Pb-implantation at a lower energy, having a localization energy of 29.5 ± 0.2 meV and labeled as I_{X}. TES emission was observed from this peak, identifying it as a D^0X complex bound to a donor with a donor binding energy of around 90 meV. Its emission intensity showed sublinear dependence on the excitation intensity, which is unusual for a D^0X peak. This sublinear dependence indicates the center which binds I_{X} was present at a low concentration in these samples. I_{X} also showed significant quenching when the implanted samples were subjected to simultaneous BGE, affected twice as much as all the other peaks. Along with the sublinear power dependence, such photosensitivity gave strong evidence that I_{X} is an exciton bound to substitutional Pb^{2+} sitting on the Zn site. Pb acts as a double donor in ZnO and can be photoionized with photons with energies greater than 1.4 eV. BGE destroys the Pb^{2+} centers, but recapture of the BGE-induced free electrons by Pb^{3+} ensures the I_{X} peak will survive at high BGE intensities. Relative intensity of the I_{X} may have been stronger than that expected for a low binding center concentration and time resolved measurement would be most useful for understanding this phenomena.

Several other sharp features were observed a few meV higher in energy from I_{X}, with intensities about 4 times less than I_{X} and labeled as the I_Y^i lines. Strange behavior was also observed for the I_Y^i lines, which were not photosensitive like the I_{X} peak. Origin for the I_Y^i lines remains a mystery but it is clearly related to the Pb-implantation. In any case, Pb-implantation introduced easily detectable excitonic peaks in the low temperature PL spectrum. Behavior of the I_{U}, I_{X}, and I_Y^i lines is sufficiently unique that their appearance in the low temperature PL spectrum from a ZnO sample is a clear indication of Pb impurities.

EPLD proved to be an effective technique to produce high quality ZnO samples from a metallic target. It was also successful at depositing other simple oxides from metallic targets. Pt, Ir, Pd, and Ru metallic targets were ablated in an oxygen atmosphere and deposited on quartz and ZnO substrates. XPS indicated the samples were not fully oxidized but nevertheless, they showed transmission characteristic of semiconducting oxides. Laser fluences for these growths were much higher than the Zn fluence of $4\,\mathrm{J/cm^2}$, and violent splashing was observed for the Pt, Ir, and Ru depositions. Growth onto ZnO was motivated by Schottky

diode fabrication and the resulting diodes showed high barriers with excellent ideality. A clear increase in the barrier height for diodes deposited in oxygen was observed compared to those deposited in an Ar environment. These materials are hard to deposit by other growth techniques and optimizing the EPLD conditions could result in some high performance diodes. EPLD is not a new growth technique but comparatively little has been reported on its results. It is the author's hope that this thesis and the reports published during its creation help to revive this technique. Many interesting EPLD experiments can be devised and will one day lead to some truly exotic materials and devices.

8.1 Future Work

Of course, questions inevitably lead to more questions and the work undertaken in this thesis is only the tip of the iceberg as far as EPLD growth of simple oxides from metallic targets is concerned. For ZnO, some progress has been made but reproducibility issues have inhibited more investigations of the I_7 exciton and its appearance in the EPLD grown nanostructures. A barrage of experiments should be undertaken to reproduce the morphology and PL of the nanohexamids which show I_7 and the unique power dependence. Once this is achieved then spatially resolved cathodoluminescence along with time resolved PL should be undertaken. This will shed light on the structural origin of I_7 and the dynamics which lead to the drastically different power dependence compared to the other peaks. Understanding this behavior will uncover important physics behind light-matter coupling in nanostructured ZnO.

Growth of all the samples in this thesis was done with the substrate at 600 °C. Substrate temperature has a profound effect on the morphology and structural quality of the samples. Surface mobility of the adatoms is highly dependent upon the substrate temperature. Initial experiments show the clumping effect observed for the EPLD grown nanorods on bare sapphire was dependent on the substrate temperature. Lower temperatures gave less clumping at the cost of structural quality. Balancing the substrate temperature with a post growth annealing process may give some control over the size and density of the nanorod clumps while maintaining a high crystallinity.

Only one variation on the shadow mask shape was explored in this thesis and a very unusual sample was grown when using a helical wire as a shadow mask.

Exploration of the effect of the helix size, pitch, wire diameter, and placement would surely result in some interesting morphology with many potential applications. Shadow mask size, shape, and position all have an impact on the thickness profile of the samples. Designing shadow masks with unconventional shapes and sizes may allow for engineering of the thickness profile of the deposited sample. The best way to do this is by comparing experimental data with simulations until a useful model of the diffusion around a shadow mask during EPLD is discovered. Composition of the shadow mask could also play a role and may be a possible way to achieve low concentration doping. Ablating through a grid of thin wires composed of material which is susceptible to interactions with the plume may lead to inclusions in the sample. There is almost a limitless number of possible experiments exploring the shadow mask geometry, many of which would reveal some fundamental physics in the PLD field.

Buffer layers were found to have a profound effect on the morphology and light emission from the EPLD grown ZnO. Samples deposited on Pt/Al_2O_3 showed a continuous morphology, much different to the highly nanostructured surface grown on bare sapphire. SEM revealed a high density of nanoscale pores in the Pt layer. For subsequent EPLD growth of ZnO, these pores lead to a brain-like morphology for the ZnO deposited on top. Eliminating the pores in the buffer layer is likely only a matter of optimizing its growth rate and substrate temperature, something which should be done for (E)PLD grown Pt layers anyway. Gaining control over the pore size and density would also prove useful for catalytic applications.

Low temperature ZnO buffer layers proved to be effective at increasing the structural quality of the samples. Dependence of the main layer on the buffer layer thickness needs to be explored as well as more buffer layer temperatures. A two-parameter study, similar to the shadow mask position and O_2 pressure experiment presented in section 4.1, covering buffer layer temperature and thickness would be most interesting. Double buffer structures should also be considered such as $ZnO/LT\text{-}ZnO/Pt/Al_2O_3$, or several LT-ZnO layers grown at different temperatures with different thicknesses. Adding buffer layers at least doubles the number of controllable parameters for EPLD growth growth and would provide enough work for several thesis students.

While it did not induce I_7 emission, implantation of Pb into bulk ZnO resulted in several previously unreported sharp excitonic lines in the low temperature PL spectrum near the band edge. These samples were characterized thoroughly

by temperature and power dependent PL along with simultaneous below-gap excitation. However, the dynamics of these emission peaks are still unknown and time resolved luminescence would help to understand their nature. Dependence on an external magnetic field would also help to solidify the peak assignments and may shed some light on the mysterious I_Y^i lines induced by the Pb-implantation.

Its possible that the I_7 emission can be induced by Pb-implantation into the bulk if the right annealing procedure is found. A controlled experiment looking at different annealing procedures for Pb-implanted ZnO should also be carried out. Double-donors are not commonly reported and excitons bound to these type of impurities may show intrinsically different behavior to excitons bound to standard donors. A theoretical treatment of excitons bound to double donors is well beyond the scope of this thesis but would prove useful for ZnO and other light emitting semiconductors. Implantation of other possible double donors into bulk ZnO with the same oxidation states as Pb, such as Sn from the same group or one of the transition metals like Pd, would prove valuable for comparison to these Pb-implanted samples.

EPLD proved useful for growing high quality ZnO as well as oxides of the noble metals. Full characterization of the EPLD grown noble metal oxides was certainly not achieved by this thesis. XRD data would fill a huge gap in the analysis of the noble metal oxides, providing phase information as well as grain sizes and epitaxial relationships. Before a detailed investigation of the noble metal oxides is undertaken, quick and easy access to an X-ray diffractometer optimized for thin films must be secured. XRD data would also help to understand the ZnO samples grown by EPLD and this piece of equipment must be secured by the University of Canterbury. Once access to XRD is sorted out then detailed investigations of EPLD grown noble metal oxides would be possible. Electrical measurements should be taken and correlated with optical transmission. Reflectance data should also be taken from these samples, preferably at the same time as the transmission from the same spot on the sample. This may be possible by modification of the Cary Spectrophotometer or use of two CCD systems with good UV responses. Such a set up would allow for accurate absorption spectra and more reliable bandgap measurements. With some luck, any of the above experiments will further the understanding of the EPLD process and its application to simple metal oxides. This thesis was all about the fundamental physics behind the materials. Fully understanding these fundamentals would take several lifetimes and is enough to keep research groups around the world busy and well funded.

Appendix A

Some Matlab Scripts

Large amounts of data can be generated relatively quickly with today's experiments. Compared to the > 10 terabyte/day of data anticipated from the Large Hadron Collider, the data produced in the photoluminescence experiments presented in this thesis was tiny. Nevertheless, it was still more data than could be easily handled using simple graphical-user-interface (GUI) based programs such as Microsoft Excel. The Matlab software package provides an ideal platform for handling medium to large size data sets. By making use of its command-line-based control and programming constructs, such as *if* statements and *for* loops, many of the tedious steps of an analysis algorithm can be streamlined and automated.

Aside from the data analysis, Matlab also provides the tools necessary to create publication-quality figures which present the results in a clear manner. Nearly every aspect of the figures can be controlled by the user, from the color of the individual axes to the length and direction of the tick marks. Pie charts, bar graphs, and a slew of three dimensional plots can be produced by Matlab and even integrated into animations. Figures can be exported as all the standard graphics formats with control over the size and resolution. This allows for graphs to be introduced into documents without any resizing, ideal for sending images to publishers when the column width is known. All of the graphs produced in this thesis were created by Matlab and the code creating them can be easily modified for use with future data.

Perhaps one of the biggest advantages to using Matlab is the large amount of prewritten code available online through the Matlab Central File Exchange.[†] Matlab code for essentially every basic data analysis technique and many very complex tasks have already been written and are available online. The online

[†]http://www.mathworks.com/matlabcentral/fileexchange/

Matlab community is large and new code appears in the database every week. Of course, a good understanding of the algorithm is necessary when using code written by others to ensure correct implementation and meaningful results. Helpful user comments and reviews are available which aid in understanding the algorithms and provide possible extensions and solutions to errors. The time taken to learn the Matlab programming environment is well worth it, enabling quick yet complex analysis of a wide variety of data sets. In this appendix, a few simple tasks preformed in Matlab are outlined and the code is included for reference.

A.1 Iterative Line Fitting with Uncertainties in x and y

A.1.1 Theory

Least squares (LS) data fitting is an important tool for any experimental scientist. It allows for accurate determination of the physical parameters of a system provided the correct model is applied. There are many algorithms for LS data fitting, each one providing an advantage in certain situations. The most complex algorithms are reserved for nonlinear LS fitting, i.e. when the model contains a nonlinear relationship between the *parameters* as is the case for equations 3.13 (page 41) and 3.17 (page 44). For this type of fitting the IGOR software package provides perhaps the best platform, allowing the users to easily find a good starting value for the fitting algorithm. The IGOR multipeak fitting package, used for deconvolution of PL spectra, is the shining example. The Matlab routines for nonlinear fitting, including the ones found online, are much harder to use and rarely allow for a GUI-based initial guess. Also, the uncertainties are not as reasonable as those found by IGOR, especially for weighted LS fits. In fact, IGOR was used for all the nonlinear data fitting in this thesis.

Through appropriate substitutions, many models can be linearized and a much simpler LS fitting algorithm can be used. For example, fitting of the exponential relationship $y = Ae^{\alpha x}$ is simplified by fitting a straight line to a plot of $\ln(y)$ vs x. Other examples of models which can be linearized are power laws and the Tauc relation (equation 7.1, page 179). Fitting of straight line relations does not require an iterative algorithm, but things can get complicated when trying to account for uncertainty in the measurements. There are complicated mathematical techniques involving Hessian and Jacobian matrices to deal with

these uncertainties but they do not seem to produce physically reasonable results. They tend to grossly over or underestimate the uncertainties. In response, an iterative method was developed which provides reasonable uncertainties to the slope and intercept of a straight line fit.

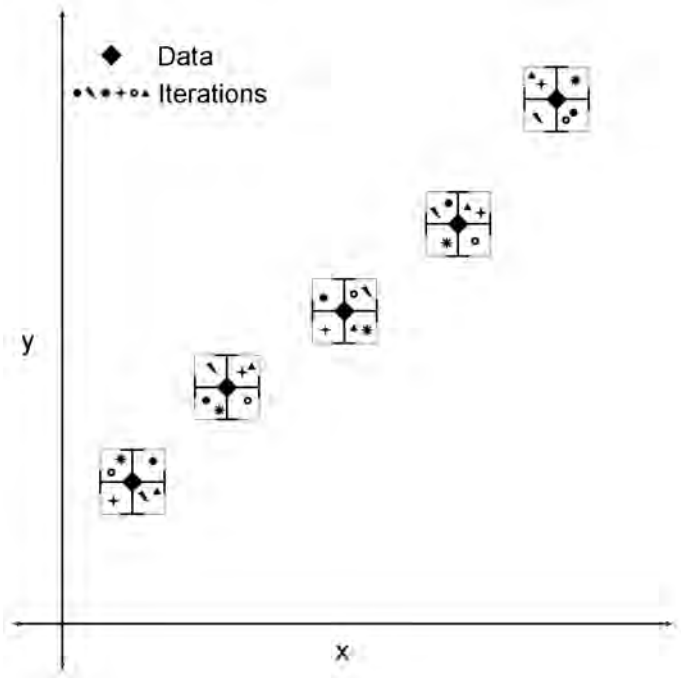

Figure A.1: Schematic of iterative least squares fitting of a straight line relation.

Figure A.1 shows a mock data set of a linear relationship including x and y uncertainties. Each data point is really a data box because of these uncertainties. Assuming the uncertainties represent the random uncertainties in the measurements, its equally likely that the actual value is anywhere within the data box. This variation will be random from data box to data box. The best way to account for this is to use an iterative Monte-Carlo style process. At each iteration a random point is chosen within each of the data boxes. A straight line gets fit to the randomly selected points and the slope and intercept are cataloged. A new set of random points within the data boxes are selected for the next iteration, as shown in figure A.1, and then the process repeats many times. The average value of the slope and intercept are taken as the best fit parameters. The uncertainties, representing the 90% confidence bounds in the measurement, are given by 1.645σ where σ is the standard deviation in the measurements. For straight line fitting 90% confidence is usually sufficient as opposed to the 95% confidence bounds presented in this thesis.

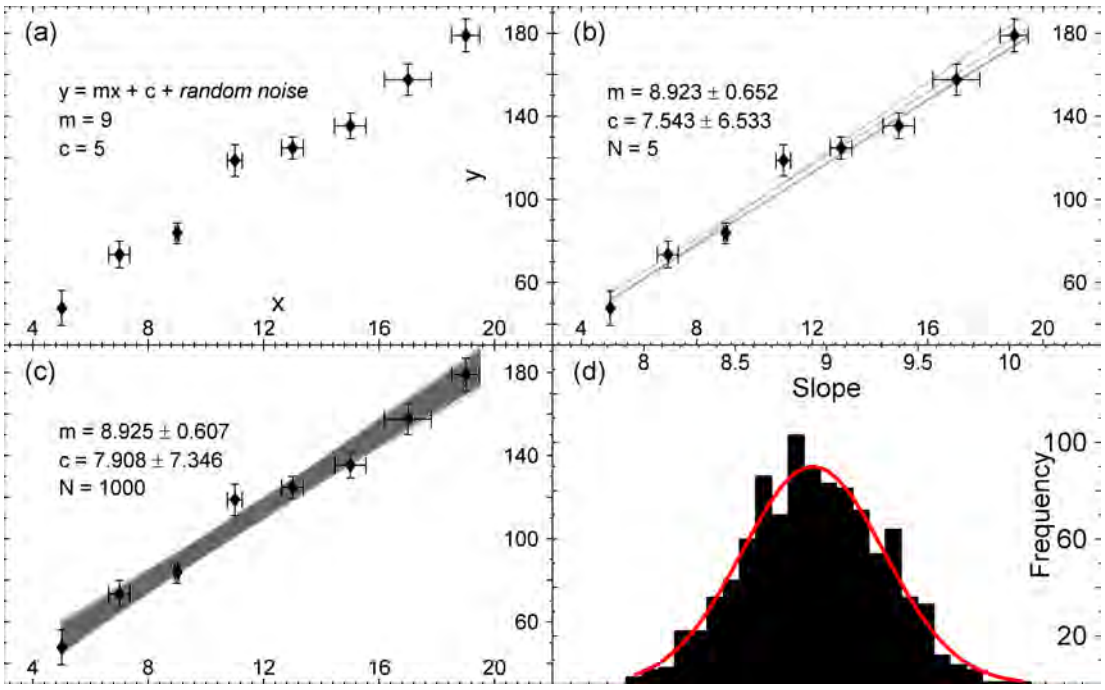

Figure A.2: Example of the iterative straight line fitting using simulated data. (a) A noisy straight line relationship with random uncertainties was generated. (b) Fit using 5 iterations. (c) Fit using 1000 iterations. (d) Distribution of measured slopes and Gaussian fit.

An example of the algorithm on simulated data is shown in figure A.2. Random noise was added to a straight line described by $y = 9x + 5$. Uncertainties of random magnitude were then generated for each of the data points resulting in the data set shown in figure A.2(a). Fits using 5 and 1000 iterations are shown in figures A.2(b) and (c), both of which extract reasonable values for the slope and its uncertainty. High relative uncertainties are typically found for the y-intercept as it can be highly dependent on small changes to the slope. Figure A.2(d) shows a histogram of the measured slopes for the 1000 iteration fit. A Gaussian curve usually provides a good fit to the distribution for fits with 500 or more iterations. All the straight line fits presented in this thesis were fit by this method. Systematic uncertainties are not taken into account by this algorithm and should always be minimized or corrected for when possible. Modifications to this algorithm could account for these uncertainties and for situations when the probability of the correct measurement is not equal over the entire data box. The code is listed below and can be cut and pasted from the pdf version directly into the Matlab editor or notepad with minimal character error.

A.1.2 Code

```
function [varargout]=slsquxy(x,y,dx,dy,N,p);
%
%Callings: [m,dm,c,dc,mvals,cvals]=slsquxy(x,y,dx,dy);
%                                  =slsquxy(x,y,dx,dy,'plot');
%                                  =slsquxy(x,y,dx,dy,N);
%                                  =slsquxy(x,y,dy,dy,N,'plot');
%Purpose: To compute the slope and intercept of a straight line along with
%         thier uncertainties when uncertainty in the x and y data are
%         known. It does not use some fancy mathmatical Hessian hoobajoob.
%         Random uncertainties evenly distributed within the errors
%         provided are added to the data and a slope is calculated.
%         This process is repeated N times. The average slope and
%         intercept are taken as the best fit with 1.645*standard deviation
%         as the uncertainty. This means 90% of the calculated slopes and
%         intercepts lie within the uncertainties calcualted.

%Input Variables:
%   x -- independent data
%   y -- dependent data
%  dx -- symmetric error in x data
%  dy -- symmetric error in y data
%   N -- Number of iterations
%   'plot' -- including this string produces a plot
%
%Output Variables: (any number can be output in above order)
%   m -- slope of the best fit line
%   dm -- uncertainty of the slope
%   c -- y-intercept of the best fit line
%   dc -- uncertainty in the y intercept
%   mvals -- vector containing slopes of all the fitted lines used for
%            uncertainty determination
%   cvals -- vector containing y-intercepts of the all the fitted lines
%
%Author: R. J. Mendelsberg
%
%Version: 1.00 -- 6 August 2008

%Check input arguments
switch nargin
    case 4
        p=0;
        N=1000;
```

```
    case 5
        if isequal(N,'plot')
            p=1
            N=1000;
        else
            p=0;
        end
    case 6
        p=1;
    otherwise
        error('Incorrect number of inputs.')
end
if size(x)~=size(y) | size(x)~=size(dx) | size(y)~=size(dy)
    error('Data and uncertainty must be the same size')
end

%Initialize
mvals=zeros(N,1);
cvals=zeros(N,1);

%Take a random walk through data N times
for ii=1:N
    %Generate random noise for x and y within specified uncertainty
    ux=dx.*(1-2*rand(size(x)));
    uy=dy.*(1-2*rand(size(y)));
    %fit noisy data
    [mvals(ii),cvals(ii)]=slsqf(x+ux,y+uy);
end
m=mean(mvals);
c=mean(cvals);
dm=1.645*std([mvals]);
dc=1.645*std([cvals]);

%Make sure error due to scatter in data is not larger than these errors
n=length(x);
if n>2
    xbar=sum(x)/n;
    yfit = m*x +c;
    alpha = sqrt( sum( (y-yfit).^2 ) / (n-2) );
    deltam=alpha / sqrt( sum(x.^2) - n * xbar^2 );
    deltac=alpha / sqrt( n - sum(x)^2/sum(x.^2) );
    if deltam>dm
        dm=deltam;
        disp('Uncertainies in slope due to scatter in data.')
    end
```

```
    if deltac>dc
        dc=deltac;
        disp('Uncertainies in intercept due to scatter in data.')
    end
end

%Organize outputs
outs={m dm c dc mvals cvals};
varargout=deal(outs);

%Optional plot
if p
    figure
    errorbar(x,y,dy,'kd','markerfacecolor','k')
    hold on
    h=herrorbar(x,y,dx,'k.');
    set(h,'marker','none')
    if size(x,1)==1;
        yy=mvals(1)*x'+cvals(1);
        for ii=2:length(mvals)
            yy=[yy mvals(ii)*x'+cvals(ii)];
        end
    else
        yy=mvals(1)*x+cvals(1);
        for ii=2:length(mvals)
            yy=[yy mvals(ii)*x+cvals(ii)];
        end
    end
    hold on
    plot(x,yy,'k--')
    hold off
    title([sprintf('m = %4.3f',m) '\pm' sprintf('%4.3f',dm) ',...
     ' sprintf('c = %4.3f',c) '\pm' sprintf('%4.3f',dc) ])
end



function [m,c]=slsqf(x,y);
% Calculate the best fit
n=length(x);
xbar=sum(x)/n;
ybar=sum(y)/n;
m = sum( (x-xbar).*(y-ybar) ) / sum( (x-xbar).^2 );
c = ybar-m*xbar;
```

```
function hh = herrorbar(x, y, l, u, symbol)
%   This code is based on ERRORBAR provided in MATLAB.
%   See also ERRORBAR
%   Jos van der Geest
%   email: jos@jasen.nl
if min(size(x))==1,
    npt = length(x);
    x = x(:);
    y = y(:);
    if nargin > 2,
        if ~isstr(l),
            l = l(:);
        end
        if nargin > 3
            if ~isstr(u)
                u = u(:);
            end
        end
    end
else
    [npt,n] = size(x);
end

if nargin == 3
    if ~isstr(l)
        u = l;
        symbol = '-';
    else
        symbol = l;
        l = y;
        u = y;
        y = x;
        [m,n] = size(y);
        x(:) = (1:npt)'*ones(1,n);;
    end
end

if nargin == 4
    if isstr(u),
        symbol = u;
        u = l;
    else
        symbol = '-';
    end
end
```

```
if nargin == 2
    l = y;
    u = y;
    y = x;
    [m,n] = size(y);
    x(:) = (1:npt)'*ones(1,n);;
    symbol = '-';
end

u = abs(u);
l = abs(l);

if isstr(x) | isstr(y) | isstr(u) | isstr(l)
    error('Arguments must be numeric.')
end

if ~isequal(size(x),size(y)) | ~isequal(size(x),size(l)) | ~isequal(size(x),size(
    error('The sizes of X, Y, L and U must be the same.');
end

%tee = (max(y(:))-min(y(:)))/100; % make tee .02 x-distance for error bars
yrange=get(gca,'ylim');
yrange=yrange(2)-yrange(1);
tee=0.025*yrange;

% changed from errorbar.m
xl = x - l;
xr = x + u;
ytop = y + tee;
ybot = y - tee;
n = size(y,2);
% end change

% Plot graph and bars
hold_state = ishold;
cax = newplot;
next = lower(get(cax,'NextPlot'));

% build up nan-separated vector for bars
% changed from errorbar.m
xb = zeros(npt*9,n);
xb(1:9:end,:) = xl;
xb(2:9:end,:) = xl;
xb(3:9:end,:) = NaN;
```

```
xb(4:9:end,:) = xl;
xb(5:9:end,:) = xr;
xb(6:9:end,:) = NaN;
xb(7:9:end,:) = xr;
xb(8:9:end,:) = xr;
xb(9:9:end,:) = NaN;

yb = zeros(npt*9,n);
yb(1:9:end,:) = ytop;
yb(2:9:end,:) = ybot;
yb(3:9:end,:) = NaN;
yb(4:9:end,:) = y;
yb(5:9:end,:) = y;
yb(6:9:end,:) = NaN;
yb(7:9:end,:) = ytop;
yb(8:9:end,:) = ybot;
yb(9:9:end,:) = NaN;
% end change

[ls,col,mark,msg] = colstyle(symbol); if ~isempty(msg), error(msg); end
symbol = [ls mark col]; % Use marker only on data part
esymbol = ['-' col]; % Make sure bars are solid

h = plot(xb,yb,esymbol); hold on
h = [h;plot(x,y,symbol)];

if ~hold_state, hold off; end

if nargout>0, hh = h; end
```

A.2 Measurement of Circular Features in Images

Image processing techniques can save a lot of time but are relatively complex and usually require expensive software. Matlab has image processing capabilities but this toolbox is not available to all Matlab users and requires knowledge of the fine details of the process. In many cases, picking features out of images is best done by eye but this usually precludes getting quantitative information. One example is finding and measuring circular features in images, such as the alaysis of the ZnO microclumps shown in figure 4.23 (page 100). Such analysis is certainly possible using automated image processing techniques but a simpler (and slower) approach was used in this thesis which keeps the user in the loop.

A Matlab routine was developed which allows the user to draw circles on top of an image or a graph using the mouse. Fine adjustment of the position and radii of these circles can then be made using the keyboard. Radii are then scaled from pixels to real world units by inputing the scale conversion manually. This is accomplished by identifying a feature with a known size in the image, such as the scale bar in SEM images. The code for this algorithm was based on a file found on the Matlab file exchange but many modifications were needed to make it useful for extracting real world measurements. One of the main modifications was the ability to generate concentric circles, which was critical for the analysis presented in figure 4.23. The following code is an excellent example of how to manipulate Matlab figures using object oriented programming.

```
function [R,C]=MeasureImageCircles(filename,NOP);
%
%Callings: [R,C]=MeasureImageCircles
%          [R,C]=MeasureImageCircles(filename)
%          [R,C]=MeasureImageCircles(NOP)
%          [R,C]=MeasureImageCircles(filename,NOP)
%
%Purpose: To measure circular features using the mouse and keyboard on
%         images and graphs plotted with Matlab. Originally created to
%         measure circular features manually in AFM images. Now modified to
%         handle image files containing a feature with known size.
%
%Input Variables:
%   NOP -- number of points to use to graph the circles. Triangles can be
%          plotted by setting this variable to 3, diamonds by setting it to
%          4, hexagons by setting it to 6, etc. Unspecified uses 500.
%   filename -- name of the file containing the image, must be a string
%
%   NOTE: No inputs are given a dialog box comes up.
%
%Output Variables:
%   R -- Radius of circles in axes units
%   C -- Center point of circles in axes units
%
%   NOTE: If the image command is used to plot an image file the axes units
%         are pixels and this is what R and C will be in.
%
%Mouse functions
%   left click -- left click where you want the center and hold and drag to
%                 draw the circles. Let go of the mouse button when desired
```

```
%                radius is reached. Use the keyboard functions described
%                below to adjust the circle after drawing it.
%  right click -- use a right click to draw a circle concentric with the
%                previously drawn circle
%
%Keyboard functions
%   Enter or Return -- Ends the program. Press one of these buttons when
%                      finished to pass control back to command line or the
%                      calling function. Closing the window will do the
%                      same.
%
%   Delete or Backspace -- deletes the last circle drawn. Holding shift and
%                          pressing these keys deletes all circles.
%
%   arrow keys -- Use the arrow keys after the circle is drawn to move the
%                 circle around. Holding shift will increase the step,
%                 holding shift+ctrl increases it even more and holding
%                 shift+ctrl+alt increases it even more again.
%
%   k -- decreases the radius. Increase the step by using the
%        shift, ctrl, and alt keys just like with the arrows
%
%   l -- increases the radius. shift, ctrl, and alt keys increase the step
%
%Author: Rueben Mendelsberg (roomend@hotmail.com) Oct 2008
%
%Acknowledgements to J.A. Disselhorst for writing createcircle.m and
%posting it on the Matlab Central File Exchange. This program was inspired
%by createcircle.m.

%Check Inputs
switch nargin
    case 0
        NOP=500;
        [filename, pathname, filterindex] = uigetfile( ...
            {'*.jpg;*.png;*.tif;*.bmp;*.gif', 'Supported Image Files (*.jpg, *.png, *.ti
            '*.*',  'All Files (*.*)'}, ...
            'Pick a file');
        filename=fullfile(pathname,filename);
    case 1
        if ischar(filename)
            NOP=500;
        else
            NOP=filename;
            [filename, pathname, filterindex] = uigetfile( ...
```

```
                {'*.jpg;*.png;*.tif;*.bmp;*.gif', 'Supported Image Files (*.jpg,
                '*.*',  'All Files (*.*)'}, ...
                'Pick a file');
            filename=fullfile(pathname,filename);
        end
end
handles.NOP=NOP;
handles.NOC=1;

%Load and produce image
IMG=imread(filename);
IMGinfo=imfinfo(filename)
ff=figure;
imshow(IMG)
axis equal

%Get scale information
hold on
retry=1;
while retry
    retry=0;
    uiwait(msgbox('Click on scale boundaries','','modal'));
    [x0(1),y0(1)]=ginput(1);
    sh1=plot(x0(1),y0(1),'bx');
    [x0(2),y0(2)]=ginput(1);
    sh=plot(x0(2),y0(2),'bx',x0,y0,'b');
    set(ff,'pointer','arrow')
    S1=sqrt((x0(1)-x0(2))^2+(y0(1)-y0(2))^2);
    S2=inputdlg('Enter real world scale distance:');
    if isempty(S2)
        delete(sh)
        delete(sh1)
        retry=1;
    else
        S2=str2num(S2{1}); %Convert from cell to string to number
        if isempty(S2)
            error('Scale Distance Must Be a Number')
        end
    end
end
Scale=S2/S1; %scale ratio
hold off

% -Save state of figure, and adjust----------------------
handles.CCaxes = gca;
```

```
handles.CCfig = ancestor(handles.CCaxes, 'figure');
handles.r=[];
handles.center=[];
handles.rho=[];
handles.CCline2=line('visible','off');
old_db = get(handles.CCfig, 'DoubleBuffer');
old_close=get(handles.CCfig,'CloseRequestFcn');
state = uisuspend(handles.CCfig);
original_modes = get(handles.CCaxes,...
      {'XLimMode', 'YLimMode', 'ZLimMode'});
lims=[xlim ylim];
handles.dx=diff(xlim)*[1/100 1/200 1/400 1/800];
handles.dy=diff(ylim)*[1/100 2/200 1/400 1/800];
original_userdata=get(handles.CCfig,'UserData');
set(handles.CCfig, 'Pointer', 'crosshair', ...
    'WindowButtonDownFcn', {@ButtonDown,handles},...
    'DoubleBuffer','on',...
    'WindowButtonUpFcn',{@ButtonUp,handles},...
    'KeyPressFcn',{@KeyPress,handles},...
    'CloseRequestFcn',{@CloseFcn});
set(handles.CCaxes,'XLimMode','manual', ...
    'YLimMode','manual', ...
    'ZLimMode','manual');
figure(handles.CCfig);

errCatch = 0;    %Wait for the function to complete.
try
    %waitfor(handles.CCline2(end), 'UserData', 'Completed');
    uiwait
catch
    errCatch = 1;
end

if (errCatch == 1)          % error
    errStatus = 'trap';
else                        %succes.
    handles=get(handles.CCfig,'UserData');
    if isfield(handles,'close')
        delete(gcf)
    end
    errStatus = 'ok';
    R=[handles.r]*Scale;
    C=[handles.center]*Scale;
end
```

```
% Restore the figure state
if (ishandle(handles.CCfig))
    uirestore(state);
    set(handles.CCfig, 'DoubleBuffer', old_db)
    set(handles.CCfig,'UserData',original_userdata)
    set(handles.CCfig,'CloseRequestFcn',old_close)

    if ishandle(handles.CCaxes)
        set(handles.CCaxes,...
            {'XLimMode','YLimMode','ZLimMode'}, original_modes);
        axis(lims)
    end
end

% Check for errors
if errCatch
    % An error was trapped during the uiwait
    error('Interruption During Mouse Selection')
end

function ButtonDown(src,eventdata,handles)
point = get(handles.CCaxes,'CurrentPoint');
if handles.NOC>1 && isequal(get(handles.CCfig,'SelectionType'),'alt')
    center_x=get(handles.CCline1(handles.NOC-1),'XData');
    center_y=get(handles.CCline1(handles.NOC-1),'YData');
    handles.center(handles.NOC,:)=handles.center(handles.NOC-1,:);
else
    center_x=[point(1,1) point(1,1)];
    center_y=[point(1,2),point(1,2)];
    handles.center(handles.NOC,:)=[point(1,1) point(1,2)];
end

handles.CCline2(handles.NOC) = line(,...
    'Parent', handles.CCaxes, ...
    'XData', zeros(1,handles.NOP), ...
    'YData', zeros(1,handles.NOP), ...
    'Clipping', 'off', ...
    'Color', 'r', ...
    'LineStyle', ':', ...
    'LineWidth', 1);

handles.CCline1(handles.NOC) = line('Parent', handles.CCaxes, ...
    'XData', center_x, ...
    'YData', center_y, ...
    'Clipping', 'off', ...
```

```
    'Color', 'r', ...
    'LineStyle', ':', ...
    'LineWidth', 1);

set(handles.CCfig,'WindowButtonMotionFcn',{@ButtonMotion,handles},...
    'WindowButtonDownFcn',{@ButtonMotion,handles},...
    'WindowButtonUpFcn',{@ButtonUp,handles},...
    'KeyPressFcn',{@KeyPress,handles},...
    'CloseRequestFcn',{@CloseFcn,handles});

function ButtonUp(src,eventdata,handles)

set(handles.CCfig, 'WindowButtonMotionFcn', '')
handles.NOC=handles.NOC+1;
set(handles.CCfig,'WindowButtonMotionFcn','',...
    'WindowButtonDownFcn',{@ButtonDown,handles},...
    'KeyPressFcn',{@KeyPress,handles},...
    'CloseRequestFcn',{@CloseFcn,handles});

function ButtonMotion(src,eventdata,handles)
point = get(handles.CCaxes,'CurrentPoint');
xdata = get(handles.CCline1(handles.NOC), 'XData');
ydata = get(handles.CCline1(handles.NOC), 'YData');
xdata(2) = point(1,1); ydata(2) = point(1,2);
set(handles.CCline1(handles.NOC), 'XData', xdata, 'YData',ydata);

xdif = xdata(2)-xdata(1);
ydif = ydata(2)-ydata(1);
handles.r(handles.NOC)=sqrt(xdif^2+ydif^2);
THETA=linspace(0,2*pi);
handles.rho(handles.NOC)=atan2(ydif,xdif);
X=handles.r(handles.NOC)*cos(THETA)+xdata(1);
Y=handles.r(handles.NOC)*sin(THETA)+ydata(1);
set(handles.CCline2(handles.NOC), 'XData', X, 'YData',Y);
set(handles.CCfig,'WindowButtonUpFcn',{@ButtonUp,handles},...
    'KeyPressFcn',{@KeyPress,handles},...
    'CloseRequestFcn',{@CloseFcn,handles});

function KeyPress(src,eventdata,handles)
key = get(handles.CCfig, 'CurrentCharacter');
if  ~isempty(key) && handles.NOC>1 %Theres at least 1 circle drawn
    switch double(key)
        case 28
            %move circle left
            xdata1=get(handles.CCline1(end),'xdata')...
```

```
            -handles.dx(length(eventdata.Modifier)+1);
        xdata2=get(handles.CCline2(end),'xdata')...
            -handles.dx(length(eventdata.Modifier)+1);
        set(handles.CCline1(end),'Xdata',xdata1);
        set(handles.CCline2(end),'Xdata',xdata2);
        handles.center(end,:)=handles.center(end,:)...
            -[handles.dx(length(eventdata.Modifier)+1) 0];
    case 29
        %move circle right
        xdata1=get(handles.CCline1(end),'xdata')...
            +handles.dx(length(eventdata.Modifier)+1);
        xdata2=get(handles.CCline2(end),'xdata')...
            +handles.dx(length(eventdata.Modifier)+1);
        set(handles.CCline1(end),'Xdata',xdata1);
        set(handles.CCline2(end),'Xdata',xdata2);
        handles.center(end,:)=handles.center(end,:)...
            +[handles.dx(length(eventdata.Modifier)+1) 0];
    case 30
        %move circle up
        xdata1=get(handles.CCline1(end),'ydata')...
            +handles.dy(length(eventdata.Modifier)+1);
        xdata2=get(handles.CCline2(end),'ydata')...
            +handles.dy(length(eventdata.Modifier)+1);
        set(handles.CCline1(end),'Ydata',xdata1);
        set(handles.CCline2(end),'Ydata',xdata2);
        handles.center(end,:)=handles.center(end,:)....
            +[0 handles.dy(length(eventdata.Modifier)+1)];
    case 31
        %move circle down
        xdata1=get(handles.CCline1(end),'ydata')...
            -handles.dy(length(eventdata.Modifier)+1);
        xdata2=get(handles.CCline2(end),'ydata')...
            -handles.dy(length(eventdata.Modifier)+1);
        set(handles.CCline1(end),'Ydata',xdata1);
        set(handles.CCline2(end),'Ydata',xdata2);
        handles.center(end,:)=handles.center(end,:)...
            -[0 handles.dy(length(eventdata.Modifier)+1)];
    case {11,75,107}
        %Decrease radius
        THETA=linspace(0,2*pi);
        handles.r(end)=handles.r(end)...
            -1/2*handles.dx(length(eventdata.Modifier)+1);
        X=handles.r(end)*cos(THETA)+handles.center(end,1);
        x=handles.r(end)*cos(handles.rho(end))+handles.center(end,1);
        Y=handles.r(end)*sin(THETA)+handles.center(end,2);
```

```
        y=handles.r(end)*sin(handles.rho(end))+handles.center(end,2);
        set(handles.CCline2(end),'Xdata',X,'Ydata',Y)
        set(handles.CCline1(end),'Xdata',[handles.center(end,1) x],...
            'Ydata',[handles.center(end,2) y])
    case {12,76,108}
        %Increase radius
        THETA=linspace(0,2*pi);
        handles.r(end)=handles.r(end)...
            +1/2*handles.dx(length(eventdata.Modifier)+1);
        X=handles.r(end)*cos(THETA)+handles.center(end,1);
        x=handles.r(end)*cos(handles.rho(end))+handles.center(end,1);
        Y=handles.r(end)*sin(THETA)+handles.center(end,2);
        y=handles.r(end)*sin(handles.rho(end))+handles.center(end,2);
        set(handles.CCline2(end),'Xdata',X,'Ydata',Y)
        set(handles.CCline1(end),'Xdata',[handles.center(end,1) x],...
            'Ydata',[handles.center(end,2) y])
    case {8 127}
        %Delete
        if length(eventdata.Modifier)...
            && isequal(eventdata.Modifier{1},'shift')
            %Holding shift and pressing a delete key deletes them all
            delete(handles.CCline1)
            delete(handles.CCline2)
            handles.CCline1=[];
            handles.CCline2=[];
            handles.r=[];
            handles.center=[];
            handles.rho=[];
            handles.NOC=1;
        else
            %Delete last one
            delete(handles.CCline2(end))
            delete(handles.CCline1(end))
            handles.CCline2(end)=[];
            handles.CCline1(end)=[];
            handles.r(end)=[];
            handles.center(end,:)=[];
            handles.rho(end)=[];
            handles.NOC=handles.NOC-1;
        end
    case {13 3}
        %Finished drawing circles.
        % return control to line after waitfor and pass along data
        set(gcf,'UserData',handles)
        uiresume
```

```
    end
else
    %No circles drawn
    if key==char(13) | key==char(3)
        set(gcf,'UserData',handles)
        uiresume

    end
end

set(handles.CCfig,...
    'WindowButtonDownFcn',{@ButtonDown,handles},...
    'WindowButtonMotionFcn','',...
    'WindowButtonUpFcn',{@ButtonUp,handles},...
    'KeyPressFcn',{@KeyPress,handles},...
    'CloseRequestFcn',{@CloseFcn,handles});

function CloseFcn(src,eventdata,handles)
handles.close=1;
set(gcf,'UserData',handles)
uiresume
```

Appendix B

Photoluminescence of Ag Doped ZnO grown by MBE

B.1 Ag Doped ZnO

Difficulty in obtaining stable p-type material is currently the biggest hurdle to overcome in development of ZnO based technology. Only recently has p-type material been reproducibly grown,[150,184] but the poor structural quality and low mobility of the carriers must be remedied before efficient devices can be made. Despite this, ZnO based p-n junctions have been recently demonstrated,[105] paving the way for LED's and diode lasers. As a result of these advancements, there is a renewed search for new ways to reliably dope acceptors into wurtzite ZnO.

One candidate for p-type doping is Ag. The most common oxidation state of Ag is +1 meaning Ag will act as an acceptor when sitting on the Zn site. The ionic radius of Ag^{+} is 114 pm, which is larger than the ionic radius of 74 pm for Zn^{2+}. Thus, Ag inclusions will distort the lattice significantly and may result in low hole mobilities. A recent first principles study of Ag-doped ZnO suggests oxygen rich growth environments will promote p-type behavior in Ag-doped ZnO.[262] Furthermore, the study indicates that Ag prefers the Zn site and self compensation effects from interstitials should be minimum. However, Wan et al.[262] concluded that it is difficult to achieve p-type conductivity by using Ag alone due to the very deep nature of the Ag_{Zn} acceptor.

Despite these difficulties, several groups have reported on the growth of Ag-doped ZnO.[104,263] Following suit, a whole series of Ag-doped ZnO was grown by molecular beam epitaxy (MBE) at the University of Canterbury. Growth was carried out by Jessica Chai as part of her PhD project. Photoluminescence experiments were carried out on many of these samples, which usually showed

strong UV luminescence. Over time the quality of the material improved, which was clearly evident in the progression of the PL spectra. PL experiments at low and room temperature on some of the last films grown as part of the Ag-doped ZnO series are presented in this section. Evidence of acceptors can show up clearly in PL measurements, even for deep acceptors which remain neutral up to and above room temperature.

B.2 Experimental

Silver doped ZnO samples were grown by MBE in near stoichiometric and near oxygen rich environments. Growth details are shown in table B.1 which shows Ag concentrations estimated by the Ag flux during growth. All samples were placed together in a cryostat in one experimental run and scanned with identical optics. For low temperature scans the slit-width was set to 45 μm giving a spectral bandwidth of 0.25 Å using the 2400 lines/mm diffraction grating in the Spex1700 spectrometer. At room temperature a slit-width of 250 μm was used which gave a bandwidth of 1.4 Å.

Table B.1: Growth Conditions of the MBE grown ZnO thin films.

Sample	Ag concentration (%)	Substrate Temperature (°C)	Environment
631	0.001	600	Stoichiometric
638	0.001	600	O-rich
641	Undoped	600	O-rich
643	0.001	800	Stoichiometric
646	0.001	400	Stoichiometric
648	Undoped	800*	Stoichiometric
659	0.05	600	O-rich

* An In-free growth block was used for this growth and preliminary BandiT measurements suggest an actual temperature of 150 °C.

B.3 Results and Discussion

The full spectrum PL signal of the samples at 3.5 K is shown in figure B.1. The inset shows the integrated intensity of the UV emission for energies greater than 3.34 eV. The PL from the samples was composed of strong UV emission with weak deep level defect emission. The sample grown with the highest Ag content

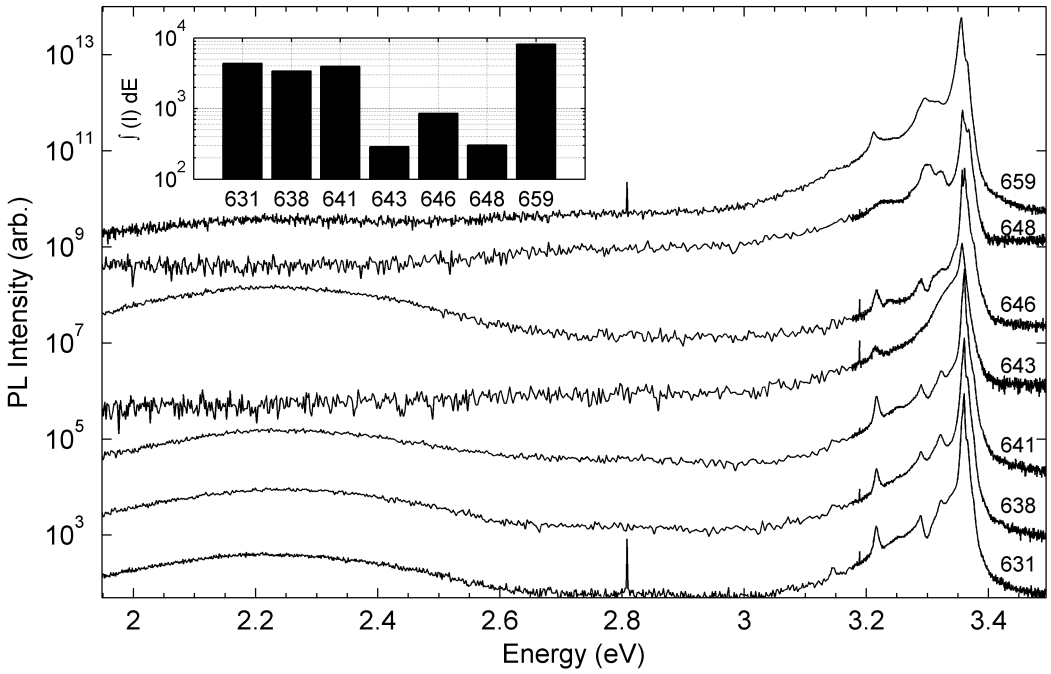

Figure B.1: PL spectra at 3.5 K (vertically offset for clarity). The inset shows the integrated intensity for energies above 3.34 eV and give a measure of relative sample quality.

of 0.05% (659) shows the highest UV emission intensity. Usually higher impurity concentrations lead to more defects which degrade PL intensity. However, it has been previously reported that Ag-doping can enhance the UV emission in ZnO.[263] Both samples grown at $T_S = 800\,^{\circ}C$ (643 and 648) have relatively poor UV emission as well as the sample grown at $T_S = 400\,^{\circ}C$. As far as UV emission is concerned, $T_S \sim 600\,^{\circ}C$ seems to be the optimum growth temperature. The three samples grown at a substrate temperature of $T_S = 600\,^{\circ}C$ undoped or with 0.001% Ag content (631, 638, and 641) all have similar UV intensities and features despite differences in the growth environment.

Near-band-edge (NBE) luminescence is shown in figure B.2. The A_T and I_x peak designations are taken from Meyer et al.[16] Table B.2 shows a summary of the peaks which are present in the samples. Their identification is based on the localization energy, i.e. the spacing of the peaks with A_T. A small shift was applied to some samples in order for the best alignment with reported peak spacings as shown in table B.2. This shift is roughly the same as the spectral uncertainty of the experiment but it was not due to machine errors as the location of the laser plasma lines are identical between scans. Comparing the samples grown at $T_S = 600\,^{\circ}C$ (631, 638, 641 and 659), it becomes clear that Ag-doping

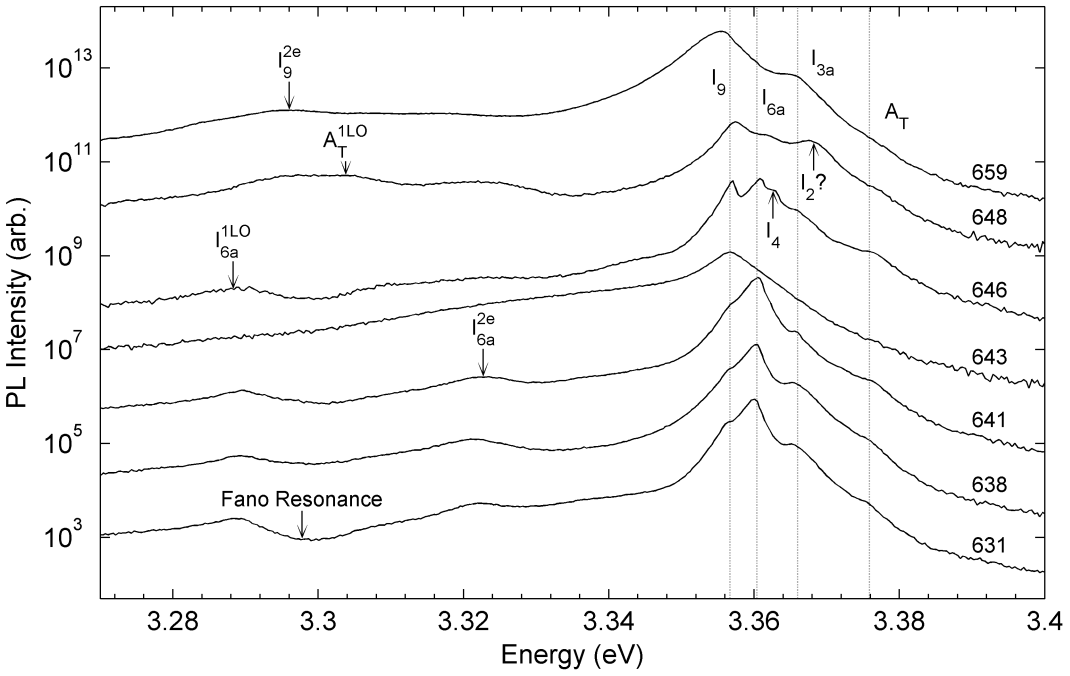

Figure B.2: Near band edge emission at 3.5 K (offset for clarity).

induced a redshift in the PL. This was likely due to an enlargement of the in-plane lattice spacing since Ag-doping increases the a lattice parameter no matter where it is incorporated in the ZnO lattice.[262]

Table B.2: Summary of PL peaks at 3.5 K

Sample	A_T	I_{6a}^+	I_{3a}	I_4	I_{6a}	I_9	Shift (meV)
631	✓	✓	✓	–	✓^{*P}	✓	-0.5
638	✓	✓	✓	–	✓^{*P}	✓	-0.5
641	✓	?	✓	–	✓^{*P}	✓	0
643	–	–	–	–	–	✓^{*P}	0
646	✓	✓	✓	✓	✓^{*P}	✓	0
648	✓	–	✓	–	✓	✓*	0.5
659	✓	–	✓	–	?	✓^{*P}	-1

* Dominant Emission
^{P} Accompanied by 2 LO-phonon replicas

Free transversal A-excitonic emission, A_T, was resolved as a shoulder in all samples except the one grown with 0.001% Ag at $T_S = 800\,^{\circ}C$ (sample 643). However, neutral donor bound exciton emission dominated the spectra. An exciton bound to an indium impurity, I_9, appeared in all the samples.[16] It dominated

the PL from the two samples grown at $T_S = 800\,°C$ (643 and 648) as well as the 0.05% Ag-doped sample (659). A two electron sattelite (TES) transition (see section 3.4, page 32) from this dominant I_9 exciton was seen at about 3.30 eV in the PL from samples 648 and 659. Indium was used to bond the substrates to the heater block and will be easily incorporated in the films due to its low vapor pressure.

In the rest of the samples (631, 638, 641, and 646) the I_{6a} exciton dominated, the origin being Al impurities.[16] I_{6a}^{+} was also observed in these samples and is an exciton bound to an ionized Al impurity.[103] The appearance of ionized donor bound excitons at low temperatures suggest the presence of some compensating acceptors. However, I_{6a}^{+} is commonly observed in unintentionally doped bulk ZnO and the origin of the compensating acceptor is unknown at this time. These I_{6a} dominant samples also show the TES transition of the I_{6a} exciton at 3.322 eV, in agreement with previously reported values.[16] Hydrogen signature was observed as the I_4 peak in the sample grown at $T_S = 400\,°C$. The lower growth temperature would help the ZnO lattice hold hydrogen, which escaped during growth of the other samples.

Two LO phonon replicas of the dominant emission were observed from all of the samples except for the undoped sample 648 grown at $T_S = 800\,°C$ (or $T_S = 150\,°C$ if the BandiT data is correct). Also, fano resonance (see reference 110 and section 3.5) was observed in the undoped and lightly doped samples grown at $T_S = 600\,°C$ and $T_S = 400\,°C$ as shown in figure B.2. The appearance of A_T, TES transitions, phonon replicas, and fano resonance are indications of good optical and structural quality of the samples. However, no evidence of acceptor-related emission was observed near the band edge in any of the samples such as acceptor bound excitons, donor acceptor pair recombination or electron-acceptor transitions.

PL signals at room temperature are shown in figure B.3. UV emission was observed from all the samples and was composed of A_T along with an LO-phonon side band. The inset of figure B.3 shows the integrated intensity of the UV emission band. Little variation was seen in the values except for the 0.001 % Ag-doped sample grown at $T_S = 400\,°C$ (646) and the undoped sample grown in the near-stoichiometric growth regime (648). The undoped sample may have been grown at a much lower substrate temperature than the 800℃ as indicated in table B.1. This could be the cause of the weak UV luminescence as the doped sample (646) was definitely grown at a low T_S and also showed weak UV emission.

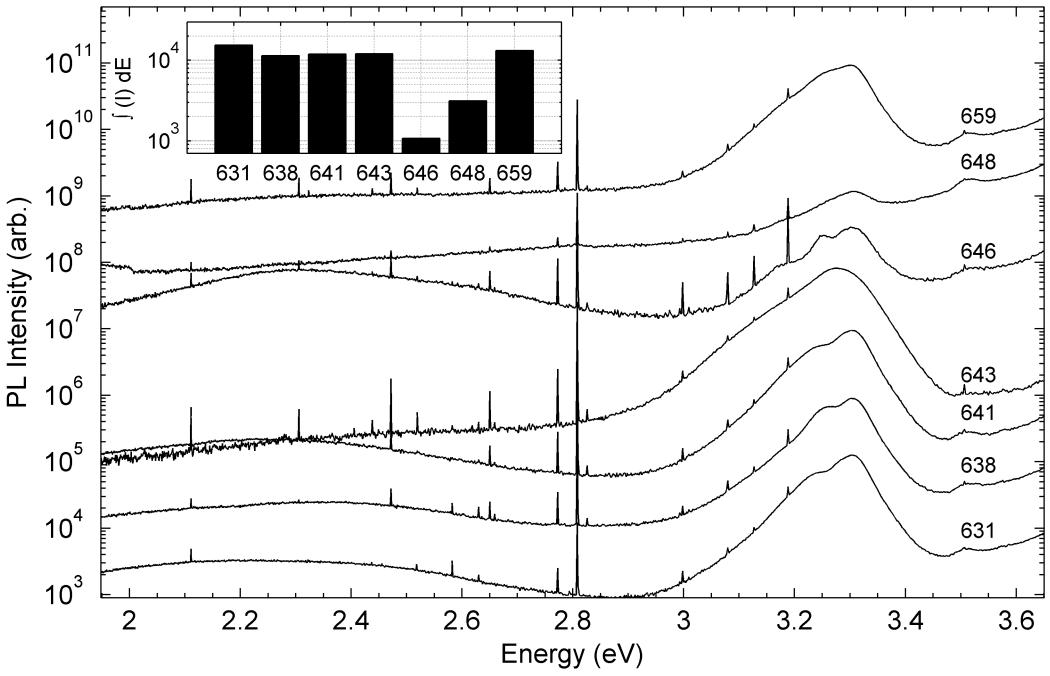

Figure B.3: Room temperature PL spectra from Ag-doped ZnO(vertically offset for clarity). The inset shows the integrated intensity of the UV band.

Deep level defect luminescence in the green part of the spectrum was weak in the samples implying good structural quality. Sample 646 which was grown at $T_S = 400\,^{\circ}\mathrm{C}$ with 0.001% Ag concentration shows the strongest green emission as well as the weakest UV emission. The ratio of the integrated intensity of the UV to green emission bands is shown in figure B.4. This ratio provides a relative measure of structural quality between samples. It is really only valid for PL spectra taken on the same equipment. Caution should be taken even when comparing the UV:green ratio for different experimental runs on the same equipment as placement of the collimating optics will effect the overal spectral response of the PL equipment.

In the undoped samples a decrease in the UV:green ratio was observed with increasing substrate temperature. However, this could be incorrect since the sample grown at $T_S = 800\,^{\circ}\mathrm{C}$ was may have been grown at a much lower temperature as noted in table B.1. For the 0.001% Ag samples the UV:green ratio increased with substrate temperature, in agreement with the 0.1% and 0.01% Ag-doped samples studied previously. The sample with the highest Ag content of 0.05% (659) showed the highest ratio out of the samples grown at $T_S = 600\,^{\circ}\mathrm{C}$. Enhancement of the UV emission with Ag-doping as mentioned earlier was the

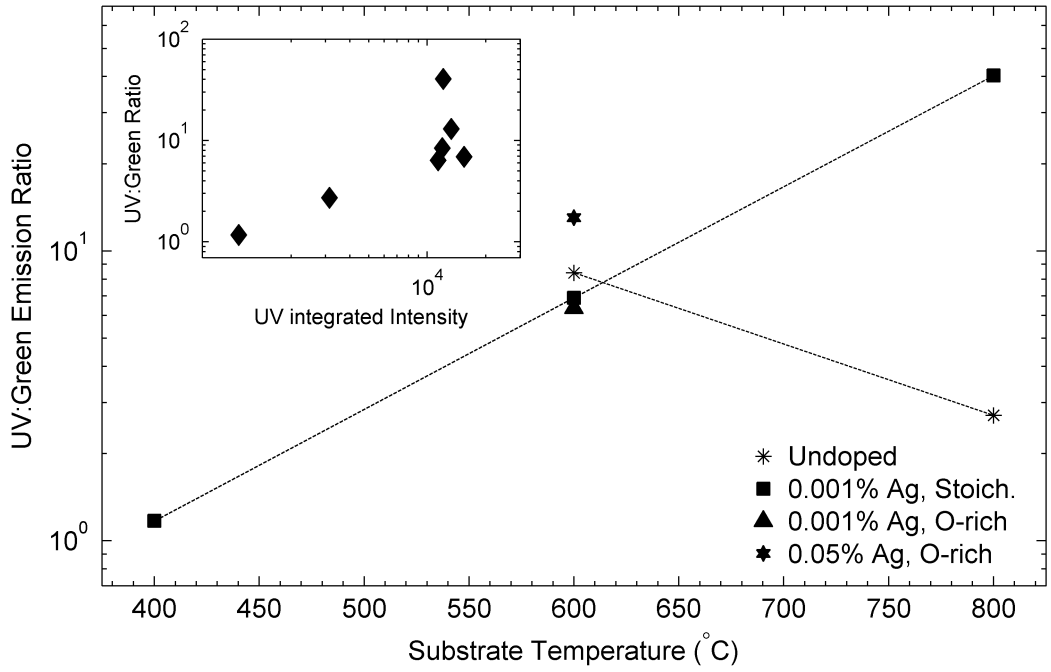

Figure B.4: UV to green integrated intensity ratio at room temperature for Ag-doped ZnO. It gives a relative measure of the structural quality between samples. The inset shows the dependence of the UV:green ratio on the integrated intensity of the UV band.

likely cause of this. The inset of figure B.4 shows the dependence of the UV:green ratio on the integrated intensity of the UV band. The samples with low UV emission intensity also have a low UV:green ratio but no clear correlation is apparent for the samples with strong UV emission. All values of the ratio are greater than 1, which is an improvement compared to the other MBE grown ZnO grown earlier by J. Chai.

B.4 Conclusion

PL signals characteristic of ZnO were observed from all the samples at low and room temperature. Low temperature spectra were dominated by neutral donor bound excitons, either I_9 or I_{6a} which are attributed to In and Al impurities respectively. The dominant emission was generally accompanied by 2 LO-phonon replicas and TES transitions. Free excitonic emission was observed in most samples as a shoulder on the high energy side of the spectra. This along with the appearance of Fano resonance, phonon replicas, and TES transitions attest to the high optical and structural quality of the samples. A small relative redshift was

seen in the spectra as Ag content increased implying expansion of the lattice by Ag inclusions.

Evidence for some compensating acceptors were observed since ionized donor bound excitons were observed at low temperature. I_{6a}^{+} and other ionized donor bound excitons are commonly observed in unintentionally doped bulk ZnO so a link between compensating acceptors and Ag-doping is unlikely. Growth in oxygen rich environments was thought to lead to Ag incorporation as an acceptor but no acceptor-related luminescence peaks were observed near the band edge in any of the samples. In fact, PL spectra of samples grown in near-stoichiometric and oxygen rich environments were essentially identical at low and room temperature.

At room temperature the PL was dominated by UV emission with relatively weak green defect emission. UV emission was from the free A exciton along with an intense LO-phonon side band. Green defect emission in ZnO has many possible origins and no suggestion as to its origin in these samples was made. The ratio of UV to green emission was seen to increase with increasing substrate temperature for the 0.001% Ag samples which is in agreement with the trends seen for 0.1% and 0.01% Ag-doped samples studied previously. The UV:green ratio was always greater than 1. This was an improvement over undoped and Ag-doped ZnO samples grown in the same system which were studied earlier. Visible emission in ZnO has many origins and may have a deep Ag acceptor-related origin. Doping at higher concentrations may reveal more about Ag inclusions in ZnO.

Appendix C

Photoluminescence of Gd-implanted ZnO

C.1 Gd Implanted ZnO

Dilute magnetic semiconductors (DMS) will enable spintronic technology to outperform conventional electronics by leaps and bounds. Provided the right dopants are used, ZnO is a good candidate for DMS material with ferromagnetic ordering at room temperature.[39,43,264] Rare earth ions have large magnetic moments and can be successfully incorporated into the ZnO lattice.[34,39,187,265] Gadolinium is a good example and there are several reports of Gd doped ZnO bulk and thin films.[265–269]

In this study, hydrothermally grown ZnO from Tokyo Denpa was implanted with Gd ions by Dr. John. Kennedy using the system described in reference 202. Unfortunately, no ferromagnetic ordering was observed in any of the implanted samples. Detailed PL experiments were carried out on several doped and undoped samples and are presented below. No clear evidence of Gd-related emission was observed but the Gd-implantation had a profound effect on the light emission from bulk ZnO.

C.2 Experimental

PL at low and room temperature was performed on 5 Gd-implanted bulk ZnO substrates supplied from Tokyo Denpa. Three of the samples which had 0.5%, 1.0%, and 2.5% Gd concentrations were furnace annealed at 750 °C for 30 min and one sample contaning 1.0% Gd was not annealed. A sample implanted with 9.0% Gd was furnace annealed for 30 min at 650 °C. All annealing was done in

vacuum. For comparison the PL emission from an unimplanted sample was taken before and after furnace annealing at 750 °C for 30 minutes.

The ZnO samples were placed in the liquid He cooled Oxford cryostat in three experimental runs. A 20 mW He-Cd continuous laser emitting at 325 nm (3.815 eV) was used for excitation. For intensity comparison the 2.5% Gd sample which was annealed (JG-16b) was placed in the cryostat in all three runs. For the unimplanted samples at low temperature the spectrometer slit widths were set to 25 μm giving a sampled bandwidth of .14 Å for the 2400 lines/mm diffraction grating. They were then opened to 35 μm (bandwidth of .19 Å) to collect PL from the implanted samples which showed weaker emission with broader line widths. The 2.5% sample was also scanned with 25 μm slits to compare the intensity to the unimplanted samples. It was found that the unimplanted unannealed sample, here after referred to as the virgin sample, was about 20 times as intense as the 2.5% Gd-implanted sample (16b). Temperature dependent scans were taken from the 2.5% annealed sample using 40 μm slits (bandwith of .22 Å). For the optimized room temperature scans, the slit widths were set to 250 μm for all samples giving a bandwith of 1.4 Å.

C.3 Results and Discussion

C.3.1 Effects of crystal polarity before and after vacuum annealing of unimplanted bulk ZnO

The 5 K PL emission across the UV and visible spectrum from the oxygen and zinc faces of the virgin sample was quite similar and is shown in figure C.1. Peak assignments in the inset were taken from Meyer et al.[16] with the I_x assignments based off their localization energy. Emission from both faces was dominated by the I_4, I_5, and I_{6a} excitons which are bound to H, an unknown, and Al neutral donors respectively.[16]. Both faces also showed emission from the transverse and longitudinal free A excitons (A_T and A_L respectively). A peak was observed around 3.383 eV which was likely due to emission from the upper polariton branch (UPB_A) superimposed on the emission from the transverse B-exciton (B_T). Emission from LPB_A was likely present in this sample but was hidden by the ionized donor bound excitonic counterparts to I_5 and I_6, labeled as I_{6a}^+ and I_5^+ in figure C.1. Deep level emissions are present on both faces giving the samples a characteristic green color when excited by the He-Cd laser. These emissions are

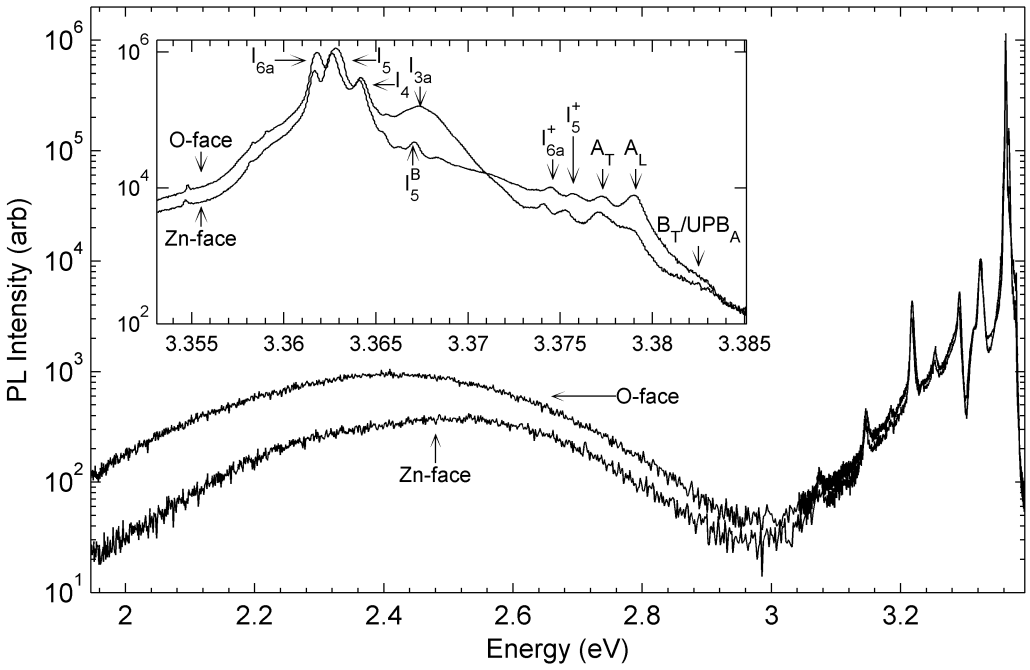

Figure C.1: PL emission at 5 K from the Zn and O face of the virgin sample. The inset shows a magnification of the NBE region.

thought to be due to oxygen vacancies and interstitials and so it is not surprising to see relatively stronger visible emission from the O-face.

The main difference in PL emission from the two faces was in the NBE region as shown in the inset of figure C.1. Compared to the dominant I_5 emission, the free excitonic peaks were less intense on the O-face then on the Zn-face. Strong emission from I_{3a} was observed on the O-face which has been tied to interstitial Zn donors.[146] Weaker emission from this region was observed on the Zn-face and the sharp peak observed around 3.367 eV was most likely the B-excitonic counterpart to I_5, labeled as I_5^B in figure C.1. These observations are consistent with previous work reported by our group.[10] Differences in the surface contaminants and the spontaneous electrical polarization of wurtzite ZnO are the most likely causes for the face-dependent PL emission. More investigation into this phenomena is needed before solid conclusions can be drawn.

After ion implantation, crystals must be annealed in order to repair damage to the structure by the ion beam. When annealing ZnO it is common to use an oxygen ambient in order to suppress oxygen desorption from the crystal.[7,19] However, for this study the implanted samples were annealed in vacuum. To separate the effects of the implantation and the annealing processes the virgin

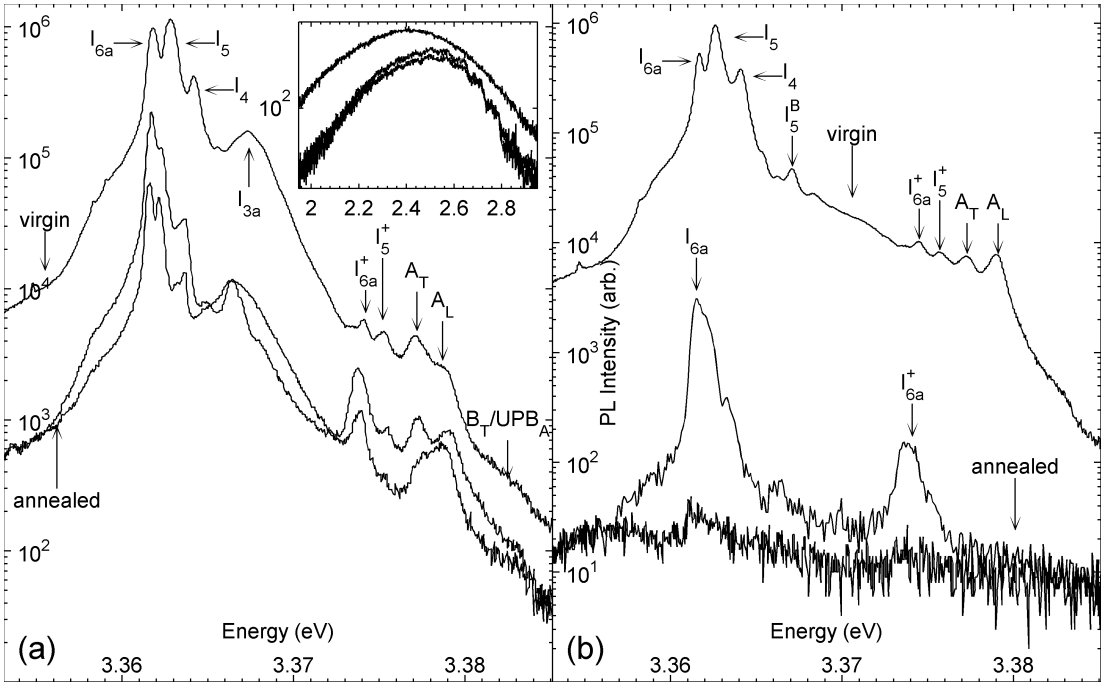

Figure C.2: PL emission from the (a)O-face and (b) Zn-face before and after vacuum annealing at 750 °C for 30 min. The two annealed samples were processed under the same conditions on different days. Visible PL emission is shown in the inset with the annealed samples below the virgin sample.

sample was cut into three pieces. One piece was kept virgin while the other two were annealed at 750 °C for 30 min under vacuum on different days. This was carried out to account for the day to day variability of the annealing procedure. The effects of annealing were apparent as soon as the annealed samples were hit with the laser. A very strong green emission was seen from both faces, noticeably stronger to the naked eye than the green emitted from the virgin sample. Also, the UV intensity was significantly reduced after annealing.

Figure C.2(a) shows the 5 K PL observed from the O-face of the virgin and the annealed samples. No vertical offset is used in this plot. After annealing, free excitons were observed with reduced intensity. Splitting between A_{T} and A_{L} was reduced in the annealed sample with weakest intensity. The A_{T}-A_{L} splitting is proportional to the oscillator strength,[81] so its not surprising to see this splitting decrease for the sample with the weakest free exciton emission. Annealing in vacuum also caused a reduction in the relative intensity of the $I_{3\mathrm{a}}$, I_4, and I_5 bound excitonic peaks. For all annealed samples the dominant emission came from the $I_{6\mathrm{a}}$ complex. Decrease in H concentration is expected for vacuum annealing, explaining the reduction of I_4 intensity. The drastic reduction in the I_5

emission after annealing suggests it may also be due to an H- or possible N-related bound exciton complex.

Annealing had a much more pronounced effect on the Zn-face as shown in figure C.2(b). UV emission was almost entirely quenched but the samples still emitted a strong green color when excited with the laser.† There was no sign of the free exciton in either annealed sample and only one of them shows D^0X emission, with I_{6a} dominant and a clear I_{6a}^+ peak. At this stage there is no explanation why the Zn-face should have such a drastic reduction in UV emission after annealing compared to the O-face. Day to day stability of the annealing process was also much better for the O-face. For implantation purposes, this result suggests implantation into the O-face would be more successful in obtaining high intensity PL emission when annealing in vacuum.

Vacuum annealing reduced the UV emission intensity by a factor of 10 to 20. At the same time the ratio of UV to visible emission decreased by only a factor of 5-10. These observations support the theory that oxygen vacancies, V_O, are the origin of the strong green luminescence in undoped ZnO.[144,270] Oxygen will desorb from the ZnO near the surface during vacuum annealing, creating more vacancies which increases the green emission. At the same time the oxygen interstitials, O_i, should decrease. Emission from O_i is thought to be around 2.1 eV giving the orange color in undoped ZnO.[271] Emission in this region is indeed reduced after annealing as seen in the inset of figure C.2(a). The visible band in the annealed samples also gains a complex LO-phonon replica structure with peaks spaced 72 meV apart. This is characteristic of Cu related emission.[272] Garces et al.[273] observed this band go from a structureless emission to the multi-phonon sideband shape after annealing in air at 900 °C for an hour. They attribute the structured emission to Cu^{2+} and the structureless emission to Cu^+. Thus, in these samples the green emission is most likely due to both V_O and Cu impurities.

C.3.2 Photoluminescence of Gd Implanted Bulk

Figure C.3 shows the full spectrum PL emission from the implanted samples measured at 5 K. Emission from the implanted and unannealed sample was nearly fully quenched, stressing the need for annealing after implantation. Gd-implanted and annealed samples gave PL signatures typical of ZnO; strong UV emission was

†The visible emission from the Zn-face was not collected as this was the last experimental run and I thought the O-face was the implanted face. To save time that I day just scanned the UV range. I probably should have done the whole spectrum!

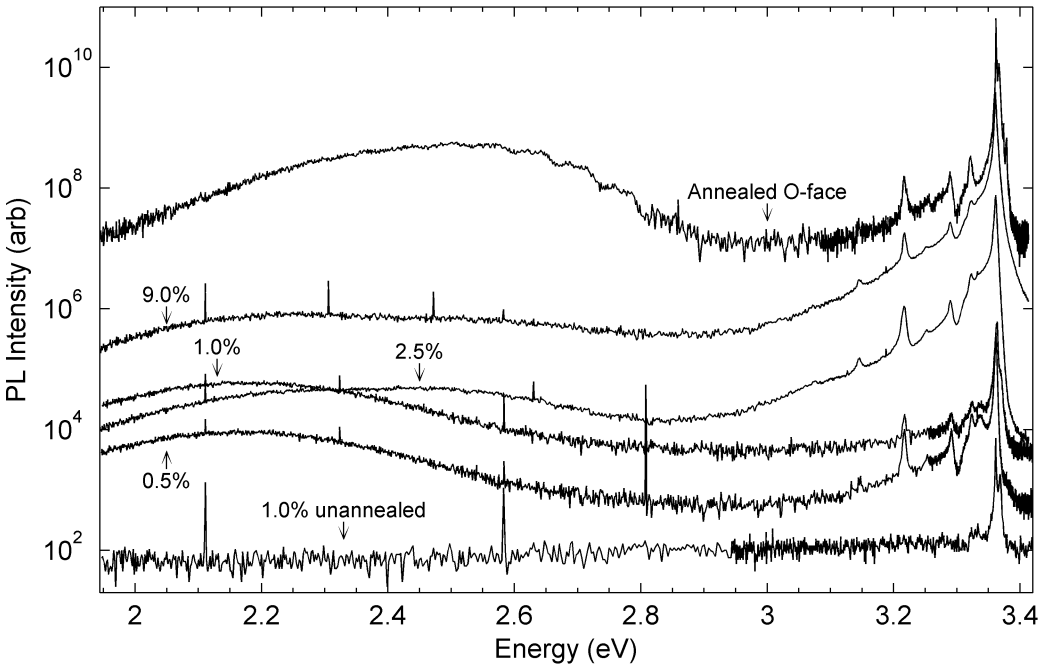

Figure C.3: PL emission of Gd Implanted ZnO at 5 K (vertically offset for clarity). The very sharp lines are plasma lines from the laser.

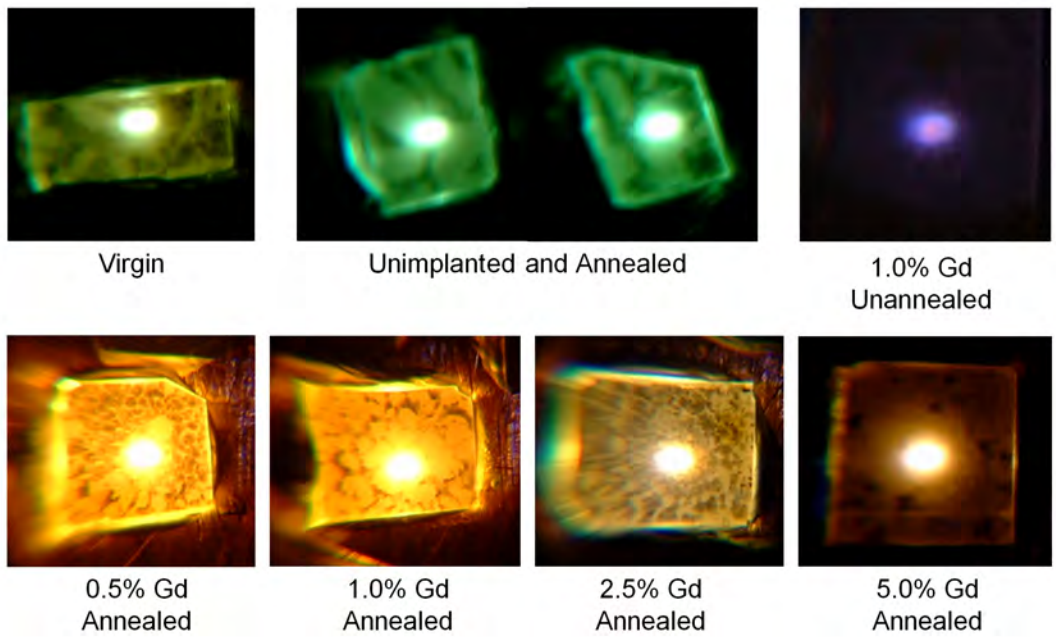

Figure C.4: Images of the PL emission at 5 K. The unimplanted sample glowed a strong green which saturated the camera. At room temperature the same colors were seen but were not quite as intense.

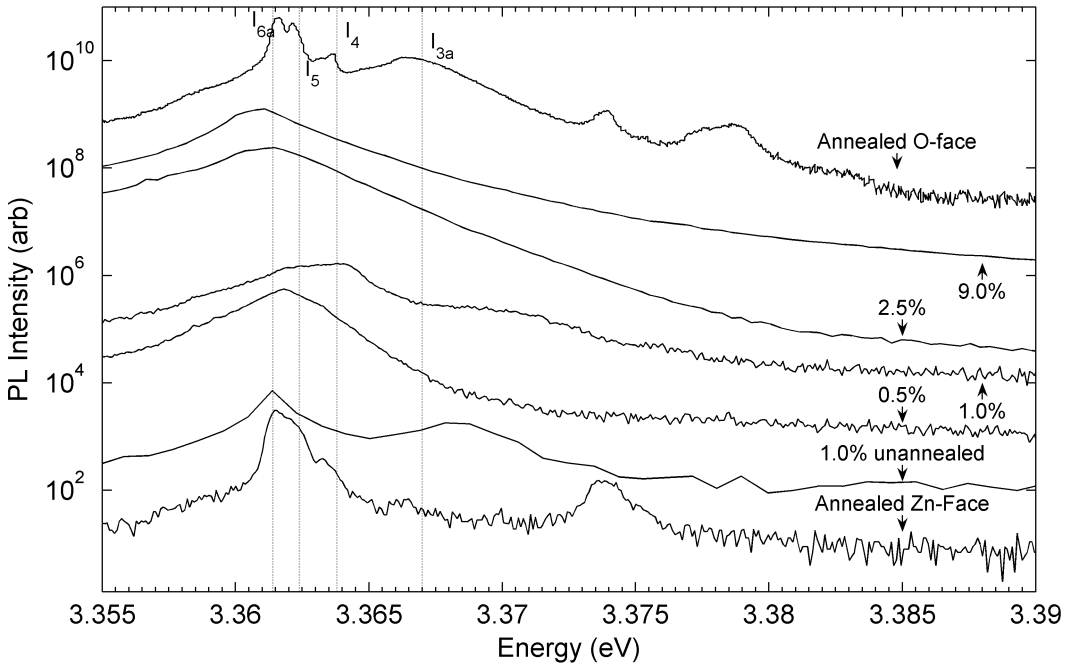

Figure C.5: Near-band-edge PL emission at 5 K of Gd-implanted ZnO (vertically offset for clarity). Also shown is the NBE emission from both faces of the undoped ZnO wafer after vacuum annealing.

observed with sharp features as well as a broad defect band at visible energies. The most notable difference between the unimplanted ZnO and the Gd-implanted ZnO was the shift in visible emission from green to orange as seen in the images shown in figure C.4. This shift in can be explained by the presence of Gd and the vacuum annealing. When ZnO is annealed in vacuum, oxygen is desorbed creating more V_O centers. In the unimplanted sample, this increased the green emission so the Gd may have moved onto the vacant oxygen sites, quenching the green V_O-related luminescence. RBS channeling experiments support this theory and indicate the Gd was mainly incorporated into the oxygen sublattice.* The orange color left over could be O_i but annealing in vacuum should significantly reduce the O_i concentration. This orange color could in fact be due to deep levels caused by Gd but no clear correlation can be seen between the orange luminescence intensity and the Gd concentration.

The near band edge UV emission from the implanted samples is shown in figure C.5 along with both faces of the annealed undoped wafer (vertically offset for clarity).† Integrated UV intensity was significantly reduced in the implanted

*To be published.

†Exactly which face was implanted is not known at this time.

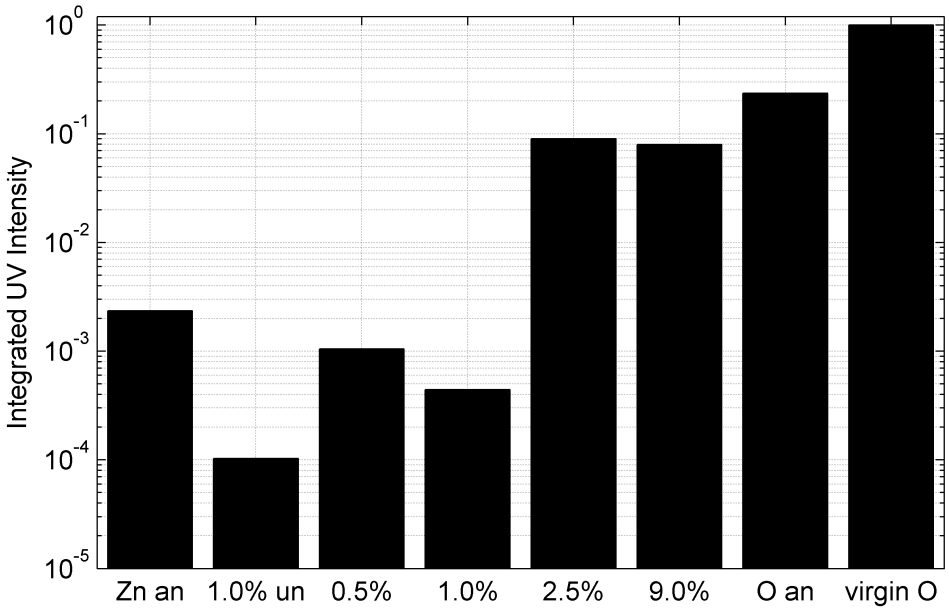

Figure C.6: Integrated UV intensity between 3.35 and 3.39 eV. Values have been normalized to the O-face of the virgin sample (Zn-face has nearly identical intensity). 'an' means annealed and 'un' means unannealed

samples compared to the unimplanted samples. Figure C.6 shows the integrated intensity between 3.35 and 3.39 eV for all the samples studied here. The intensities have been corrected for the different optical arrangements between experimental runs and normalized to the virgin sample. Annealing reduced the UV intensity of the unimplanted O-face by a factor of 4 and reduced the emission from the Zn-face by a factor of about 400. The weakest emitting sample was the 1.0% implanted but unannealed sample with an intensity just under 10,000 times less than the virgin sample, 20-200 times less than the unimplanted annealed samples, and 5-80 times less than the implanted and annealed samples. Of the implanted samples the 9.0% sample had the highest UV intensity, about 20% higher than the 2.5% annealed sample and 70-150 times higher than the rest. The 9.0% sample was annealed at a 650 °C, 100 °C less than the rest of the samples. This may explain why it has the highest UV intensity despite having the highest Gd concentration. Vacuum annealing reduced the UV emission considerably in the unimplanted bulk and the cooler annealing temperature may have helped preserve the PL intensity.

Aside from degraded UV intensity, line widths of the PL emission from the implanted samples were significantly broadened and free exciton emission was

effectively quenched. The I_4, I_5, and I_{6a} emissions appear to be present in the implanted samples in different intensity ratios. No clear correlation between the Gd concentration and relative intensities of the I_x peaks was found. The variation in relative intensities could be due to fluctuations in the annealing process although figure C.2 shows the relative intensity of the I_{4-6a} peaks stays roughly constant between annealing runs on the O-face. In the 2.5 and 9.0% samples a shoulder on the low energy side of I_{6a} was present. The exact nature of this peak is unknown at this stage and may just be a broadening of the I_{6a} feature. It could also be emission from an exciton bound to neutral Gd donors. Using lower implantation doses may prevent siginificant line broadening and may reveal Gd-related D^0X complexes.

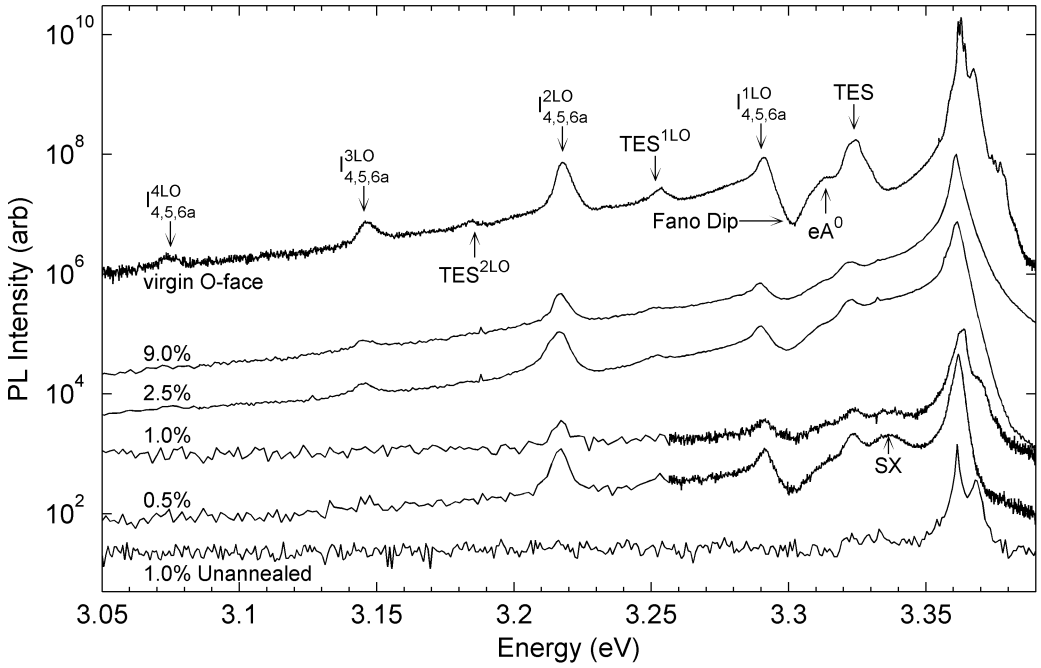

Figure C.7: Violet PL emission of Gd-implanted ZnO at 5 K. The emission from the O-face of the virgin sample is shown for comparison.

Violet emission with several features was observed from the samples and is shown in figure C.7. Four LO-phonon replicas were observed from the dominant I_x emissions in the virgin sample. The replicas from the individual I_x peaks cannot be resolved as the phonon replicas are too broad. The intensity of the 1LO replicas have been significantly reduced by Fano resonance as discussed in section 3.5. Two electron satellite (TES) emission was observed from the D^0X transitions (see section 3.4) and this two was accompanied by LO-phonon replicas.

On the low energy side of the TES emission a peak at 3.313 eV was observed which is likely due to a transition from a free-electron to neutral-acceptor (eA^0) involving basal plane stacking faults.[83]

The violet emission from the Gd-implanted and annealed samples had many common features with the unimplanted sample including TES transitions and Fano resonance. An extra peak was seen in the PL of these samples at 3.336 eV which was likely due to recombination of an exciton bound to a surface defect (SX).[11] This defect could have been introduced by the implantation or the annealing process. It has been previously observed in undoped bulk ZnO as well as nanostructures grown by PLD.[1] This peak could also be Gd-related defect-level luminescence of a free to bound or DAP nature. Power and temperature dependent PL from this emission band would help resolve its origin.

C.3.3 Temperature Dependent PL of 2.5% Gd-implanted and annealed ZnO

Temperature dependent PL was carried out on the 2.5% implanted and annealed sample (16b) to explore the PL emission further. Figure C.8 shows the observed PL spectra as a function of temperature with the NBE region magnified in the inset (vertically offset for clarity). Spectra were also taken at 250 and 300 K but are omited from the graph. At these temperatures laser scatter became an issue and only peak positions can be obtained due to the narrow slits required for low temperature emission.

I_{6a} emission dominated the PL from low temperature up until at least 200 K. Emission at room temperature was also likely dominated by I_{6a} as no sign of the free excitonic peaks were observed at any temperature. Figure C.9(a) shows the position of I_{6a} as a function of temperature. The solid line is the weighted least squares fit of the modified Manoogian equation (eq. 3.17, page 44). $E(0)$ extracted from the fit is about 1 meV higher in energy than that reported by Meyer et al.[16] but agrees well with the measured position in the undoped bulk presented in this appendix and the sample discussed in chapter 3.

Since I_{6a} survived at much higher temperatures in the Gd-implanted bulk then the undoped crystals, a reliable value for the the lattice dilation parameter U for D^0X complexes was extracted. For D^0X complexes, U was about 50% smaller than that observed for the free excitons in undoped bulk. This is in agreement with the findings in chapters 3 and 4 which suggest that lattice dilation does

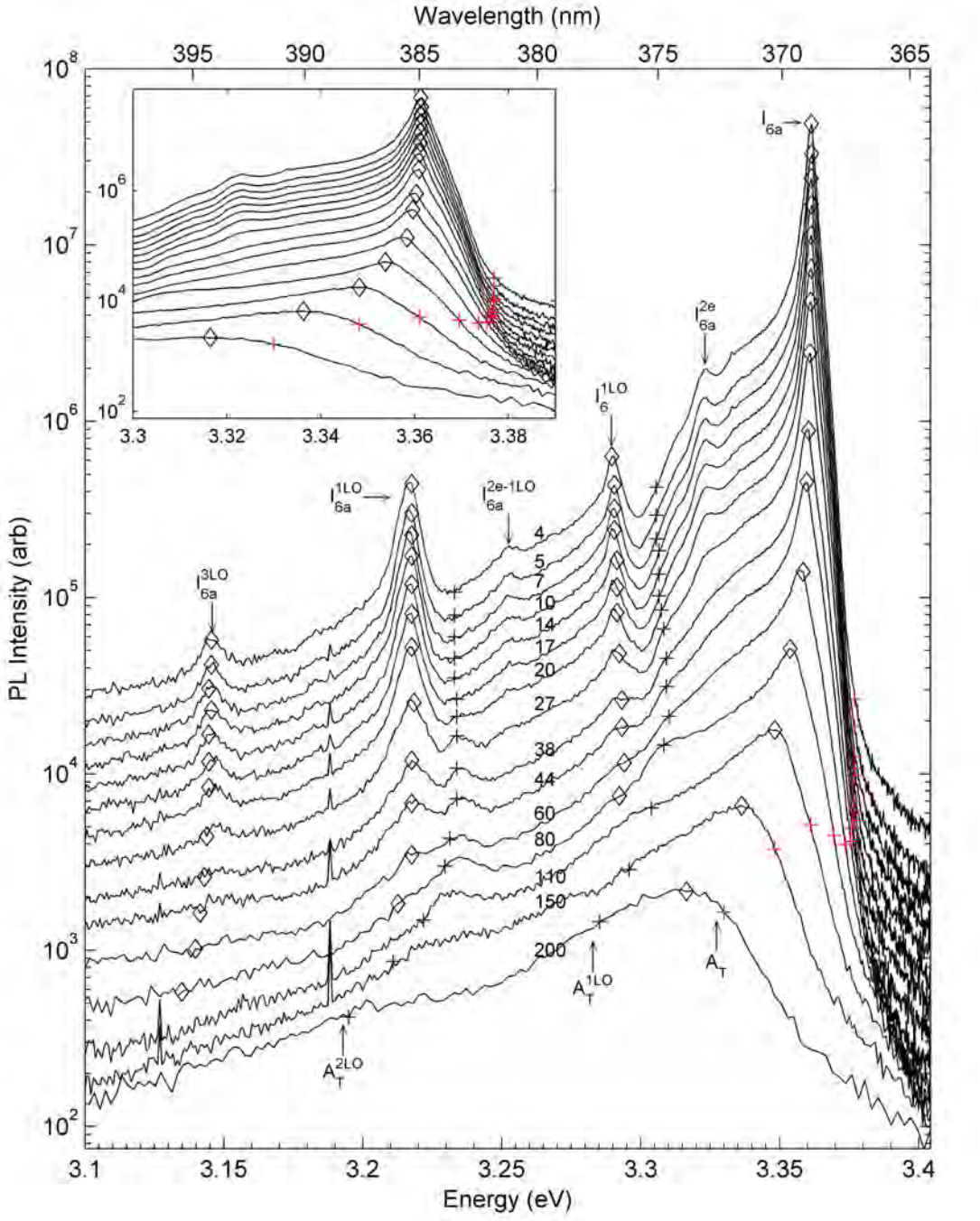

Figure C.8: Temperature dependent PL of the 2.5% Gd-implanted and annealed sample (vertically offset for clarity). The inset shows a magnification of the near-band-edge emission(also offset). Temperature in Kelvin is indicated above each spectra.

not effect bound excitons as much as free excitons. The exciton phonon coupling parameter α extracted for I_{6a} agrees with that found for the free excitons in undoped bulk as shown in table 3.3 (page 46). This may come as a surprise since α for I_{6a} in that sample was about 3 times smaller. The extracted θ value was also inconsistent with table 3.3, being about half way between the free and bound excitonic values. These inconsistencies reveal a fundamental difference in the PL emission between undoped and Gd-implanted bulk ZnO.

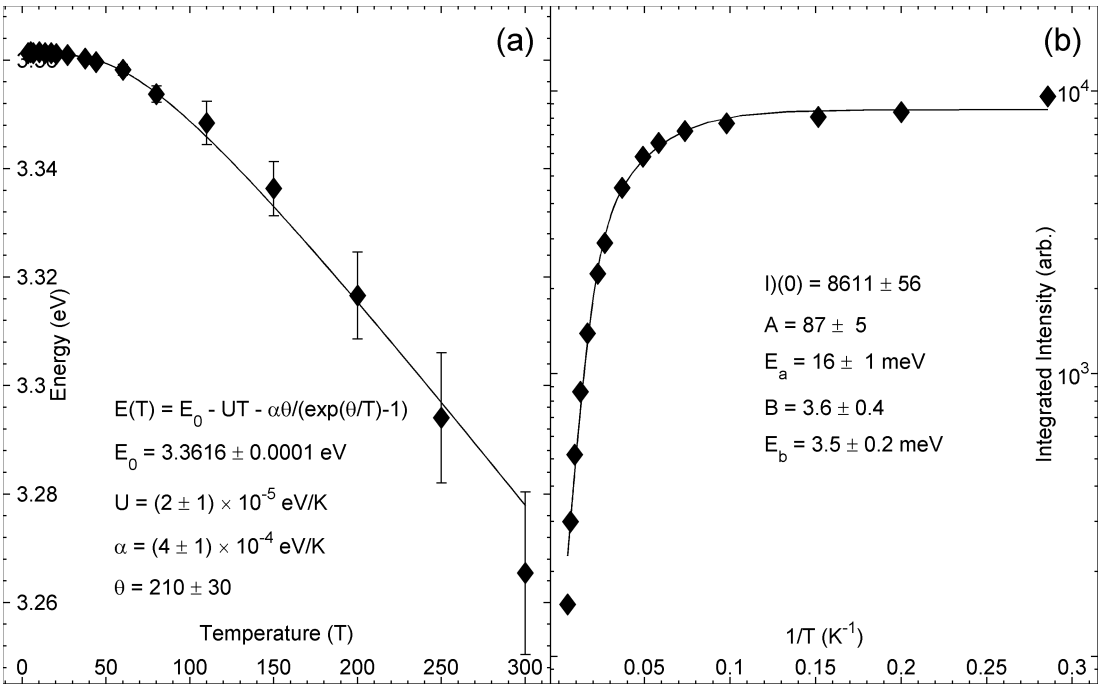

Figure C.9: Temperature dependence of the (a) emission energy and (b) integrated PL intensity of the UV emission in Gd-implanted ZnO. Solid lines are the weighted least squared fits of the (a) modified Manoogian equation (eq. 3.17, page 44) and (b) two-path Arrhenius decay (eq. 3.12, page 41).

When the temperature of ZnO gets above about 150 K, bound excitons will usually dissociate from their defects and free exciton emission will dominate the PL. Since it does not show up in this sample at low temperature, the expected position of A_T was calculated by assuming a constant localization energy of 15.5 meV for I_{6a}.[16] The results are indicated by the red +'s in figure C.8. In undoped bulk and (E)PLD grown samples an A_T shoulder clearly develops into a peak which dominates the PL as temperature is increased. In this Gd-implanted sample there is no indication of an A_T shoulder developing. However, the 1 and 2LO-phonon replicas of A_T appear at higher temperatures and are marked by the black +'s in figure C.8. Their presence is surprising considering the absence of

the zero phonon line. This may be due to relatively fast trapping of A_{T} into the $I_{6\mathrm{a}}$ state along with strong exciton-phonon coupling.

Figure C.9(b) shows an Arrhenius plot of the integrated UV intensity above 3.25 eV. The line in the figure is the best fit of a two-path Arrhenius decay given by equation 3.12 (page 41). At low temperatures the decay was dominated by the path with $B = 3.6 \pm 0.4$ and $E_(b) = 3.5 \pm 0.2$ meV. This decay path represents nonradiative recombinations of the excitons, which can be increased by lattice disorder. As temperature increases further the path with $A = 87 \pm 5$ and $E_{\mathrm{a}} = 16 \pm 1$ meV turns on and becomes the main quenching mechanism. E_{a} extracted from the Arrhenius plot agrees well with the exciton localization energy of $I_{6\mathrm{a}}$ which was measured as 15.3 ± 0.4 meV. Thus, UV emission from this sample is indeed dominated by the $I_{6\mathrm{a}}$ bound exciton up to at least 200 K. Thermal delocalization of the exciton from the neutral Al donor is the main mechanism quenching the radiative recombination in the implanted samples. However, delocalization was much less efficient in this Gd-implanted sample, allowing $I_{6\mathrm{a}}$ emission to be observed above 200 K.

C.3.4 Room Temperature PL emission

PL emission was observed from the Gd-implanted bulk at room temperature, as shown in figure C.10. UV emission characteristic of ZnO was observed from the samples as well as deep level emissions in the green and yellow part of the spectrum. Some violet emission was also observed in the annealed and the implanted samples. The ratio of UV to green emission is shown in the inset for all the samples. It can be used to gage the relative structural quality between samples measured on the same optical set up. The unimplanted annealed samples show a ratio 2 orders of magnitude smaller than that of the virgin sample, emphasizing the enhanced defect concentration due to vacuum annealing.

Blue/violet emissions at 3.06 eV are seen in all the implanted samples except the 9.0% sample. This blue/violet emission has been previously reported and there is good evidence that it is due to intersitial zinc (Zn_i).[144] The implantation of Gd could be inducing intersitial zinc to form as the Gd ions are stopped by the lattice. Another peak likely induced from the implantation and annealing process is the 2.82 eV peak seen in the 0.5% and 1.0% Gd samples. Emission at 2.81 eV has been previously reported in ZnO nanoparticles and was attributed to surface traps.[274] Green emission from V_O is seen in all the samples and is located about

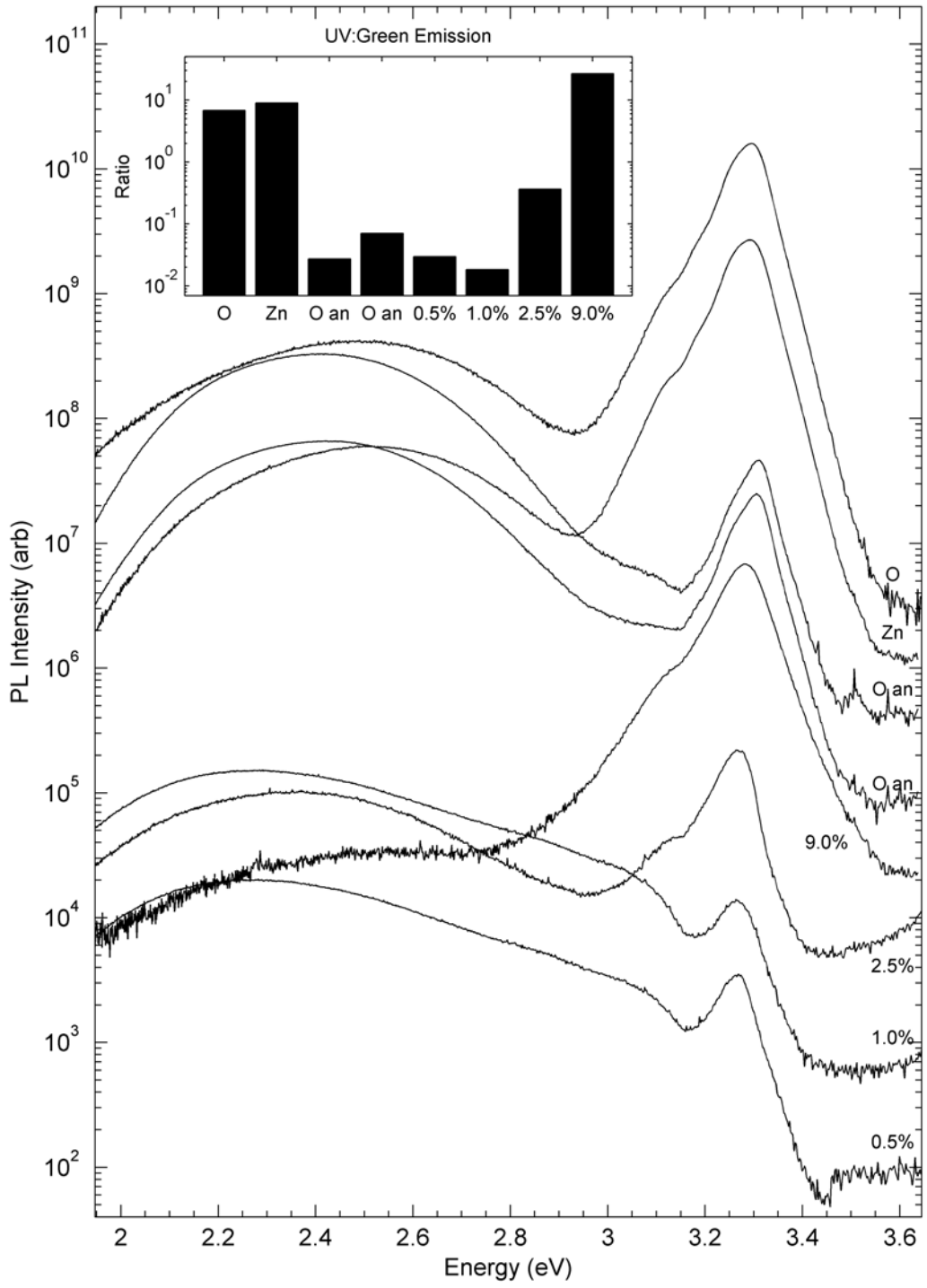

Figure C.10: Room temperature PL of Gd Implanted ZnO. Laser plasma lines were removed in software.

2.42 eV, in good agreement with reported values.[144,270] As discussed previously, the yellow emission seen at 2.16 eV appears in the Gd-implanted samples since Gd incorporation into the oxygen site after vacuum annealing quenches the green V_O-related emission. The exact nature of this orange peak is unlear at this time but it is likely either O_i or Gd related emission.

C.4 Conclusion

Photoluminescence signals characteristic of ZnO were successfully obtained at low and room temperature from the ZnO samples studied here. The only sample which showed negligible emission was the 1.0% sample that was unannealed, stressing the need for annealing after implantation. On both faces, the UV to green ratio was drastically reduced after annealing. This is evidence that the green emission in these samples is V_O-related. Annealing in vacuum effected the PL from the two faces in different ways. On the O-face, annealing significantly reduced the intensity of the UV emission. Excitonic peaks could still be resolved at low temperature with the dominant emission going from I_5 to I_{6a} after annealing. On the Zn-face the UV emission was essentially destroyed with some donor-bound-excitons surviving.

The effects of Gd-implantation were noticed as soon as the laser was hit the implanted samples. Emission from these samples was bright orange due to Gd incorporation onto the oxygen sites. This effectively quenched the green V_O-related emission and allowed the orange color to be seen. The origin of the orange emission is unknown at this stage but could be a native defect, such as O_i, or it could be Gd-related. UV emission in the implanted samples was 1 to 3 orders of magnitude less intense then the undoped bulk and was dominated by I_{6a} emission which is Al-related. Up to 3 LO-phonon replicas were observed from the dominant UV emission in the Gd-implanted bulk. Overall the emission line widths were broadened by the implantation, preventing the observation of any Gd-related excitonic features. Using lower Gd doses may prevent this line broadening and uncover a Gd-related D^0X complex in the near-band-edge region.

Temperature dependent PL measurements on the 2.5% Gd-implanted and annealed sample confirmed I_{6a} dominated the PL from the Gd-implanted samples from 5 K to at least 200 K and possibly up to room temperature. Arrhenius fitting showed the main mechanism quenching the PL had an activation energy

of $E_a = 16 \pm 1\,\text{meV}$. This corresponds to the exciton localization energy for I_{6a}, measured as $15.3 \pm 0.3\,\text{meV}$, indicating thermal dissociation of the exciton from the binding center was the main mechanism quenching the PL as temperature increased. No sign of the free exciton emission was seen at any temperature but the 1 and 2LO replicas of the free exciton appeared above about 30 K. A high defect concentration as well as a strong exciton-phonon coupling could explain this phenomenon. So far there are no reports of D^0X transisions dominating the PL at room temperature and this warrants futher investigation.

No clear evidence of Gd as an optical center was observed in the data. Intensities of the various transitions could not be clearly correlated with the Gd concentration. However, this does not rule out Gd-related emission in these samples and the orange emission is the most likely candidate for a Gd-related peak. Annealing in an oxygen atmosphere should help the ZnO retain its optical quality and may have profound effects on the visible emission. A study of the effects of Gd-implantation followed by annealing in an oxygen atmosphere would prove valuable for understanding the role of Gd in the physical and electronic structure of ZnO.

Bibliography

[1] R.J. Mendelsberg, M. Kerler, S.M. Durbin, and R.J. Reeves, Photoluminescence behavior of ZnO nanorods produced by eclipse PLD from a Zn metal target, *Superlatt. Microstruct.* 43 (2008) 594.

[2] R.J. Mendelsberg, J.V. Kennedy, S. M. Durbin, and R.J. Reeves, Unique photoluminescence from ZnO grown by eclipse pulsed laser deposition, *J. Vac. Sci. Technol. B* 27 (2009) 1698.

[3] M.W. Allen, R.J. Mendelsberg, R.J. Reeves, and S.M. Durbin, Oxidized noble metal Schottky contacts to n-type ZnO, *Appl. Phys. Lett.* 94 (2009) 103508.

[4] Ü. Özgür, Ya.I. Alivov, C. Liu, A. Teke, M.A. Reshchikov, S. Doğan, V. Avrutin, S.-J. Cho, and H. Morkoç, A comprehensive review of ZnO materials and devices, *J. Appl. Phys.* 98 (2005) 1–103.

[5] S.R. Pinnell, D. Fairhurst, R. Gillies, M.A. Mitchnick, and N. Kollias, Microfine zinc oxide is a superior sunscreen ingredient to microfine titanium dioxide, *Dermatol. Surg.* 26 (2000) 309–314.

[6] J. Nause and B. Nemeth, Pressurized melt growth of ZnO boules, *Semicond. Sci. Technol.* 20 (2005) 45–48.

[7] K. Maeda, M. Sato, I. Niikura, and T. Fukuda, Growth of 2 inch ZnO bulk single crystal by the hydrothermal method, *Semicond. Sci. Technol.* 20 (2005) S49–S43.

[8] D.C. Look, D.C. Reynolds, J.R. Sizelove, R.L. Jones, C.W. Litton, G. Cantwell, and W.C. Harsch, Electrical properties of bulk ZnO, *Solid State Commun.* 105 (1998) 399–401.

[9] D.G. Thomas, The exciton spectrum of zinc oxide, *J. Phys. Chem. Solids* 15 (1960) 86–96.

[10] M.W. Allen, P. Miller, R.J. Reeves, and S.M. Durbin, Influence of spontaneous polarization on the electrical and optical properties of bulk, single crystal ZnO, *Appl. Phys. Lett.* 90 (2007) 062104.

[11] H. Alves, D. Pfisterer, A. Zeuner, T. Riemann, J. Christen, D. M. Hofmann, and B. K. Meyer, Optical investigations on excitons bound to impurities and dislocations in ZnO, *Optical Materials* 23 (2003) 33–37.

[12] C. Boemare, T. Monteiro, M.J. Soares, J.G. Guilherme, and E. Alves, Photoluminescence studies in ZnO samples, *Phys. B: Condens. Matter* 308-310 (2001) 985–988.

[13] K.-J. Jin and S.J. Xu, Fano resonance in the luminescence spectra of donor bound excitons in polar semiconductors, *Appl. Phys. Lett.* 90 (2007) 032107.

[14] P. Klason, T. Moe Børseth, Q.X. Zhao, B.G. Svensson, A.Yu. Kuznetsov, P.J. Bergman, and M. Willander, Temperature dependence and decay times of zinc and oxygen vacancy related photoluminescence bands in zinc oxide, *Solid State Commun.* 145 (2008) 321–326.

[15] M.D. McCluskey and S.J. Jokela, Sources of n-type conductivity in ZnO, *Phys. B: Condens. Matter* 401-402 (2007) 355–357.

[16] B.K. Meyer, H. Alves, D.M. Hofmann, W. Kriegseis, D. Forster, F. Bertram, J. Christen, A. Hoffmann, M. Strassburg, M. Dworzak, U. Haboeck, and A.V. Rodina, Bound exciton and donor-acceptor pair recombinations in ZnO, *Phys. Stat. Sol. (b)* 241 (2004) 231–260.

[17] A.V. Rodina, M. Strassburg, M. Dworzak, U. Haboeck, A. Hoffmann, A. Zeuner, H.R. Alves, D.M. Hofmann, and B.K. Meyer, Magneto-optical properties of bound excitons in ZnO, *Phys. Rev. B* 69 (2004) 1252061–1252069.

[18] C. Jagadish and S. Pearton (Eds.), *Zinc Oxide Bulk, Thin Films and Nanostructures: Processing, Properties, and Applications*, Vol. Amsterdamn, Elsevier, 2006.

[19] M.J.H. Henseler, W.C.T. Lee, P. Miller, S.M. Durbin, and R.J. Reeves, Optical and photoelectrical properties of ZnO thin films and the effects of annealing, *J. Crys. Growth* 287 (2006) 48–53.

[20] W.R.L. Lambrecht, A.V. Rodina, S. Limpijumnong, B. Segall, and B.K. Meyer, Valence-band ordering and magneto-optic exciton fine structure in ZnO, *Phys. Rev. B* 65 (2002) 075207.

[21] A. Teke, Ü. Özgür, S. Doğan, X. Gu, H. Morkoç, B. Nemeth, J. Nause, and H.O. Everitt, Excitonic fine structure and recombination dynamics in single-crystalline ZnO, *Phys. Rev. B* 70 (2004) 195207.

[22] A. Kobayashi, Y. Shirakura, K. Miyamura, J. Ohta, and H. Fujioka, Structural properties of GaN grown on Zn-face ZnO at room temperature, *J. Cryst. Growth* 305 (2007) 70–73.

[23] G. Namkoong, S. Burnham, K.-K. Lee, E. Trybus, W.A. Doolittle, M. Losurdo, P. Capezzuto, G. Bruno, B. Nemeth, and J. Nause, III-nitrides on oxygen- and zinc-face ZnO substrates, *Appl. Phys. Lett.* 87 (2005) 184101.

[24] N.N. Syrbu, I.M. Tiginyanu, V.V. Zalamai, V.V. Ursaki, and E.V. Rusu, Exciton polariton spectra and carrier effective masses in ZnO single crystals, *Physica B* 353 (2004) 111–115.

[25] M.A. Reshchikov and H. Morkoç, Luminescence properties of defects in GaN, *J. Appl. Phys.* 97 (2005) 061301.

[26] A.A. High, E.E. Novitskaya, L.V. Butov, M. Hanson, and A.C. Gossard, Control of exciton fluxes in an excitonic integrated circuit, *Science* 321 (2008) 229–231.

[27] H. Gotoh, H. Sanada, H. Kamada, H. Nakano, S. Hughes, H. Ando, and J. Temmyo, Detecting coupled excitons with microphotoluminescence techniques in bilayer quantum dots, *Phys. Rev. B* 74 (2006) 115322.

[28] M.C. Horrillo, M.J. Fernández, J.L. Fontecha, I. Sayago, M. García, M. Aleixandre, J. Gutiérrez, Gràcia I., and C. Cané, Optimization of SAW sensors with a structure ZnO-SiO2-Si to detect volatile organic compounds, *Sens. Actuators B* 118 (2006) 356–361.

[29] A. Zaki, H. Elsimary, and M. Zaghloul, Miniature SAW device using MEMS technology, *Microelectron. J.* 38 (2007) 426–429.

[30] Z.L. Wang, Towards self-powered nanosystems: From nanogenerators to nanopiezotronics, *Adv. Funct. Mater.* 18 (2008) 3553–3567.

[31] D.C. Oh, T. Kato, H. Goto, S.H. Park, T. Hanada, T. Yao, and J.J. Kim, Comparative study of photoluminescences for Zn-polar and O-polar faces of single-crystalline ZnO bulks, *Appl. Phys. Lett.* 93 (2008) 241907.

[32] C. Coskun, D.C. Look, G.C. Farlow, and J.R. Sizelove, Radiation hardness of ZnO at low temperatures, *Semicond. Sci. Technol.* 19 (2004) 752–754.

[33] S.O. Kucheyev, J.S. Williams, and C. Jagadish, Ion-beam-defect processes in group-III nitrides and ZnO, *Vacuum* 73 (2004) 93–104.

[34] T. Monteiro, M. J. Soares, A. J. Neves, M. C. Carmo, M. Peres, A. Cruz, E. Alves, U. Wahl, E. Rita, V. Munoz-SanJose, and J. Zuniga-Perez, Luminescence and structural properties of defects in ion implanted ZnO, *Phys. Stat. Sol. (c)* 3 (2006) 968–971.

[35] C. Klingshirn, J. Fallert, O. Gogolin, M. Wissinger, R. Hauschild, M. Hauser, H. Kalt, and H. Zhou, Linear and nonlinear optics, dynamics, and lasing in ZnO bulk and nanostructures, *J. Lumin.* 128 (2008) 792–796.

[36] S.K. Das, M. Bock, C. O'Neill, R. Grunwald, K.M. Lee, H.W. Lee, S. Lee, and F. Rotermund, Efficient second harmonic generation in ZnO nanorod arrays with broadband ultrashort pulses, *Appl. Phys. Lett.* 93 (2008) 181112.

[37] Y.B. Zhang, S. Li, G.K.L. Goh, and S. Tripathy, Hydrothermal epitaxy of ZnO:Co diluted magnetic semiconducting single crystalline films, *Appl. Phys. Lett.* 93 (2008) 102510.

[38] P. Che, W. Liu, L. Guo, L. He, and C. Chen, High-temperature ferromagnetism in cobalt-doped ZnO single-crystalline nanorods, *J. Magn. Magn. Mater.* 320 (2008) 2563–2566.

[39] J. Qi, Y. Yang, L. Zhang, J. Chi, D. Gao, and D. Xue, Room-temperature ferromagnetism in Er-doped ZnO thin films, *Scripta Mater.* 60 (2009) 289–292.

[40] I. Žutić and J. Fabian, Spintronics: Silicon twists, *Nature* 447 (2007) 269–270.

[41] K. Ando, H. Saito, V. Zayets, and M.C. Debnath, Optical properties and functions of dilute magnetic semiconductors, *J. Phys.: Condens. Matter* 16 (2004) S5541.

[42] R. Ramesh and N.A. Spaldin, Multiferroics: Progress and prospects in thin films, *Nat. Mater.* 6 (2007) 21–29.

[43] Y.C. Yang, C.F. Zhong, X.H. Wang, B. He, S.Q. Wei, F. Zeng, and F. Pan, Room temperature multiferroic behavior of Cr-doped ZnO films, *J. Appl. Phys.* 104 (2008) 064102.

[44] Vijaya Deshpande, A note on ancient zinc smelting in India and China, *Indian Journal of History of Science* 31 (1996) 275–279.

[45] J.R. Partington, *A short history of chemistry*, 3rd Edition, Dover, 1989.

[46] H.J. Yearian, Intensity of diffraction of electrons by ZnO, *Physical Review* 48 (1935) 631–639.

[47] S.E. Harrison, Conductivity and Hall effect of ZnO at low temperatures, *Physical Review* 93 (1954) 52–62.

[48] F.A. Kroger and H.J. Vink, The origin of the fluorescence in self-activated ZnS, CdS, and ZnO, *J. Chem. Phys.* 22 (1954) 250–252.

[49] M von Ardenne, Das Elektronen-Rastermikroskop. Praktische Ausfhrung, *Z. tech. Phys.* 19 (1938) 407–416.

[50] J. Morgan, J. Notte, R. Hill, and B. Ward, An introduction to the helium ion microscope, *Microscopy Today* 14 (2006) 24–31.

[51] T.H. Maiman, Stimulated optical radiation in Ruby, *Nature* 187 (1960) 493–494.

[52] H.M. Smith and A.F. Turner, Vacuum deposited thin films using a ruby laser, *Applied Optics* 4 (1965) 147.

[53] D.B. Chrisey and G.K. Hubler (Eds.), *Pulsed Laser Deposition of Thin Films*, John Wiley & Sons, Inc., New York, NY, 1994.

[54] M.H. Emery, J.H. Gardner, and J.P. Boris, Nonlinear aspects of hydrodynamic instabilities in laser ablation, *Appl. Phys. Lett.* 41 (1982) 808–810.

[55] D. Dijkkamp, T. Venkatesan, X.D. Wu, S.A. Shaheen, N. Jisrawi, Y.H. Min-Lee, W.L. McLean, and M. Croft, Preparation of Y-Ba-Cu oxide superconductor thin films using pulsed laser evaporation from high T_c bulk material, *Appl. Phys. Lett.* 51 (1987) 619–621.

[56] P. Bilkova, J. Zemek, B. Mitu, V. Marotta, and S. Orlando, Deposition of zinc oxide thin films by reactive pulsed laser ablation, *Appl. Surf. Sci.* 252 (2006) 4604–4609.

[57] A. Fouchet, W. Prellier, B. Mercey, L. Méchin, V.N. Kulkarni, and T. Venkatesan, Investigation of laser-ablated ZnO thin films grown with Zn metal target: A structural study, *J. Appl. Phys.* 96 (2004) 3228–3233.

[58] A. Giardini, V. Marotta, S. Orlando, A. Paladini, and G.P. Parisi, RF assisted pulsed laser deposition of oxides, in: Konov V.I., Dumitras D C, and Dinescu M (Eds.), ALT '01 International Conference on 'Advanced Laser Technologies, Vol. 4762, Constanta, 2002, pp. 148–155.

[59] J.-H. Kim, S. Lee, and H.-S. Im, Effect of target density and its morphology on TiO_2 thin films grown on Si(100) by PLD, *Appl. Surf. Sci.* 151 (1999) 6–16.

[60] Kazuya Kinoshita, Hiroshige Ishibashi, and Takeshi Kobayashi, Improved surface smoothness of $YBa_2Cu_3O_y$ films and related multilayers by ArF excimer laser deposition with shadow mask 'eclipse method', *Jpn J. Appl. Phys. Part 2: Lett.* 33 (1994) 417.

[61] M. Liu, X.Q. Wei, Z.G. Zhang, G. Sun, C.S. Chen, C.S. Xue, H.Z. Zhuang, and B.Y. Man, Effect of temperature on pulsed laser deposition of ZnO films, *Appl. Surf. Sci.* 252 (2006) 4321–4326.

[62] R.J. Mendelsberg, J. Kennedy, S.M. Durbin, and R.J. Reeves, Carbon enhanced blue-violet luminescence in ZnO films grown by pulsed laser deposition, *Curr. Appl. Phys.* 8 (2008) 283–286.

[63] J.Y. Son, B.G. Kim, and J.H. Cho, Thin film growth of epitaxial, polycrystalline, and amorphous $SrRuO_3$, *Thin Solid Films* 515 (2007) 7086–7090.

[64] X.W. Sun and H.S. Kwok, Optical properties of epitaxially grown zinc oxide films on sapphire by pulsed laser deposition, *J. Appl. Phys.* 86 (1999) 408–411.

[65] Y. Sun, G.M. Fuge, and M.N.R. Ashfold, Growth mechanisms for ZnO nanorods formed by pulsed laser deposition, *Superlatt. Microstruct.* 39 (2006) 33–40.

[66] Z. Trajanovic, S. Choopun, R.P. Sharma, and T. Venkatesan, Stoichiometry and thickness variation of $YBa_2Cu_3O_{7-x}$ in pulsed laser deposition with a shadow mask, *Appl. Phys. Lett.* 70 (1997) 3461–3463.

[67] S. Acquaviva, E. D'Anna, and M.L. De Giorgi, Atomic and molecular emissions of the laser-induced plasma during zinc and zinc oxide target ablation, *J. Appl. Phys.* 102 (2007) 073109.

[68] A. Chugh, S. Ramachandran, A. Tiwari, and J. Narayan, Epitaxial ZnO/Pt layered structures and ZnO-Pt nanodot composites on sapphire (0001), *J. Electron. Mater.* 35 (2006) 840–845.

[69] P. Misra, T.K. Sharma, and L.M. Kukreja, Temperature dependent photoluminescence processes in ZnO thin films grown on sapphire by pulsed laser deposition, *Curr. Appl. Phys.* 9 (2009) 179–183.

[70] S. Yata, Y. Nakashima, and T. Kobayashi, Improved crystallinity of ZnO thin films grown by the 'Aurora PLD method', *Thin Solid Films* 445 (2003) 259–262.

[71] J. Zhao, L. Hu, Z. Wang, J. Sun, and Z. Wang, ZnO thin films on Si(1 1 1) grown by pulsed laser deposition from metallic Zn target, *Appl. Surf. Sci.* 253 (2006) 841–845.

[72] M.A. El Khakani and M. Chaker, Reactive pulsed laser deposition of iridium oxide thin films, *Thin Solid Films* 335 (1998) 6–12.

[73] T. Kobayashi, H. Akiyoshi, and M. Tachiki, Development of prominent PLD (Aurora method) suitable for high-quality and low-temperature film growth, *Appl. Surf. Sci.* 197-198 (2002) 294–303.

[74] T. Garcia, E. de Posada, M. Villagrán, J.L.S. Ll, P. Bartolo-Pérez, and J.L. Peña, Effects of an external magnetic field in pulsed laser deposition, *Appl. Surf. Sci.* 255 (2008) 2200–2204.

[75] F.W. Dabby and U.C. Paek, High- intensity laser- induced vaporization and explosion of solid material, *IEEE J. Quantum Electron.* QE-8 (1972) 106–111.

[76] F.P. Gagliano and U.C. Paek, Observation of laser-induced explosion of solid materials and correlation with theory, *Appl. Opt.* 13 (1974) 274–279.

[77] C. Chen, P.P. Ong, and H. Wang, Fabrication of TiN thin film by shadow-masked pulsed laser deposition, *Thin Solid Films* 382 (2001) 275–279.

[78] A. Marcu, C. Grigoriu, W. Jiang, and K. Yatsui, Pulsed laser deposition of YBCO thin films in a shadow mask configuration, *Thin Solid Films* 360 (2000) 166–172.

[79] J.Y. Son, C.S. Park, S.-K. Kim, and Y.-H. Shin, Writing ferroelectric domain bits on the $PbZr_0.48Ti_0.52O_3$ thin film, *J. Appl. Phys.* 104 (2008) 064101.

[80] V. Heine (Ed.), *Group Theory in Quantum Mechanics*, Dover Publications, Inc.,, 1993.

[81] C.F. Klingshirn, *Semiconductor Optics*, Springer, 1997.

[82] D.C. Reynolds, D.C. Look, B. Jogai, C.W. Litton, G. Cantwell, and W.C. Harsch, Valence-band ordering in ZnO, *Phys. Rev. B* 60 (1999) 2340–2344.

[83] M. Schirra, R. Schneider, A. Reiser, G.M. Prinz, M. Feneberg, J. Biskupek, U. Kaiser, C.E. Krill, K. Thonke, and R. Sauer, Stacking fault related 3.31-eV luminescence at 130-meV acceptors in zinc oxide, *Phys. Rev. B* 77 (2008) 125215.

[84] K. Saito, M. Hasuo, T. Hatano, and N. Nagasawa, Band gap energy and binding energies of Z_3-excitons in CuCl, *Solid State Commun.* 94 (1995) 33–35.

[85] H. Ichida, M. Nakayama, and H. Nishimura, Stimulated emission from exciton-exciton scattering in CuBr thin films, *J. Lumin.* 87 (2000) 235–237.

[86] G.H. Wannier, The structure of electronic excitation levels in insulating crystals, *Physical Review* 52 (1937) 191–197.

[87] J. Frenkel, On the transformation of light into heat in solids. II, *Physical Review* 37 (1931) 1276–1294.

[88] J. Frenkel, On the transformation of light into heat in solids. I, *Physical Review* 37 (1931) 17–44.

[89] S. Fujihara, Y. Ogawa, and A. Kasai, Tunable visible photoluminescence from ZnO thin films through Mg-doping and annealing, *Chem. Mater.* 16 (2004) 2965–2968.

[90] M.M. Denisov and V.P. Makarov, Longitudinal and transverse excitons in semiconductors, *Phys. Stat. Sol. (b)* 56 (1973) 9–59.

[91] R.L. Weiher and W.C. Tait, Mixed-mode excitons in the photoluminescence of zinc oxide-reabsorption and exciton diffusion, *Phys. Rev. B* 5 (1972) 623–627.

[92] D.C. Reynolds, D.C. Look, B. Jogai, and T.C. Collins, Polariton and free-exciton-like photoluminescence in ZnO, *Appl. Phys. Lett.* 79 (2001) 3794–3796.

[93] S. F. Chichibu, T. Sota, G. Cantwell, D. B. Eason, and C. W. Litton, Polarized photoreflectance spectra of excitonic polaritons in a ZnO single crystal, *J. Appl. Phys.* 93 (2003) 756–758.

[94] D.C. Reynolds, D.C. Look, B. Jogai, J.E. Hoelscher, R.E. Sherriff, M.T. Harris, and M.J. Callahan, Time-resolved photoluminescence lifetime measurements of the Γ_5 and Γ_6 free excitons in ZnO, *J. Appl. Phys.* 88 (2000) 2152–2153.

[95] J. Yoo, G.-C. Yi, and L.S. Dang, Probing exciton diffusion in semiconductors using semiconductor-nanorod quantum structures, *Small* 4 (2008) 467–470.

[96] D.L. Mills and A.A. Maradudin, Raman scattering from localized-mode polaritons, *Phys. Rev. B* 1 (1970) 903–909.

[97] O.L. Muskens, J. Treffers, M. Forcales, M.T. Borgström, E.P.A.M. Bakkers, and J. Gómez Rivas, Modification of the photoluminescence anisotropy of semiconductor nanowires by coupling to surface plasmon polaritons, *Opt. Lett.* 32 (2007) 2097–2099.

[98] E.H. Vivas C and J.C. Granada E, Magnon-polariton coupling in a ferromagnetic medium, *Phys. Stat. Sol. (b)* 220 (2000) 385–388.

[99] M. Zamfirescu, A. Kavokin, B. Gil, and G. Malpuech, ZnO as a material mostly adapted for realization of room-temperature polariton lasers, *Phys. Stat. Sol. (a)* 195 (2003) 563–567.

[100] C. Klingshirn, ZnO: From basics towards applications, *Phys. Stat. Sol. (b)* 244 (2007) 3027–3073.

[101] J.J. Hopfield and D.G. Thomas, On some observable properties of longitudinal excitons, *J. Phys. Chem. Solids* 12 (1960) 276–284.

[102] N. Ohashi, T. Ohgaki, S. Sugimura, K. Maeda, I. Sakaguchi, H. Ryoken, I. Niikura, M. Sato, and H. Haneda, Characterization of zinc oxide single crystals for epitaxial wafer applications, *Mater. Res. Soc. Symp. Proc.* 799 (2004) Z5.40.1.

[103] B.K. Meyer, J. Sann, S. Lautenschläger, M.R. Wagner, and A. Hoffmann, Ionized and neutral donor-bound excitons in ZnO, *Phys. Rev. B* 76 (2007) 184120.

[104] H.S. Kang, B.D. Ahn, J.H. Kim, G.H. Kim, S.H. Lim, H.W. Chang, and S.Y. Lee, Structural, electrical, and optical properties of p-type ZnO thin films with Ag dopant, *Appl. Phys. Lett.* 88 (2006) 202108.

[105] H.S. Kang, G.H. Kim, D.L. Kim, H.W. Chang, B.D. Ahn, and S.Y. Lee, Investigation on the p -type formation mechanism of arsenic doped p -type ZnO thin film, *Appl. Phys. Lett.* 89 (2006) 181103.

[106] J. R. Haynes, Experimental proof of the existence of a new electronic complex in silicon, *Phys. Rev. Lett.* 4 (1960) 361.

[107] I.C. Robin, A. Ribeaud, S. Brochen, G. Feuillet, P. Ferret, H. Marietta, D. Ehrentraut, and T. Fukuda, Low residual doping level in homoepitaxially grown ZnO layers, *Appl. Phys. Lett.* 92 (2008) 141101.

[108] X.B. Zhang, T. Taliercio, S. Kolliakos, and P. Lefebvre, Influence of electron-phonon interaction on the optical properties of III nitride semiconductors, *J. Phys.: Condens. Matter* 13 (2001) 7053–7074.

[109] Y. Toyozawa and J. Hermanson, Exciton-phonon bound state: A new quasiparticle, *Phys. Rev. Lett.* 21 (1968) 1637–1641.

[110] S.J. Xu, S.-J. Xiong, and S.L. Shi, Resonant coupling of bound excitons with LO phonons in ZnO: Excitonic polaron states and Fano interference, *J. Chem. Phys.* 123 (2005) 221105.

[111] C.G. Kuper and G.D. Whitfield (Eds.), *Polarons and Excitons*, Oliver and Boyd Ltd., London, England, 1963.

[112] C.W. Litton, D.C. Reynolds, T.C. Collins, and Y.S. Park, Exciton-LO-phonon interaction and the anti-stokes emission line in CdS, *Phys. Rev. Lett.* 25 (1970) 1619–1621.

[113] U. Fano, Effects of configuration interaction on intensities and phase shifts, *Physical Review* 124 (1961) 1866–1878.

[114] A. L. Gurskii and S. V. Voitikov, Quantum defect approach for the effect of electron-phonon coupling on impurity recombination in semiconductors, *Solid State Commun.* 112 (1999) 339–343.

[115] B. Dischler, W. Rothemund, C. Wild, R. Locher, H. Biebl, and P. Koidl, Resolved donor-acceptor pair-recombination lines in diamond luminescence, *Phys. Rev. B* 49 (1994) 1685–1689.

[116] A. Saxena, S. Yang, U. Philipose, and H.E. Ruda, Excitonic and pair-related photoluminescence in ZnSe nanowires, *J. Appl. Phys.* 103 (2008) 053109.

[117] X.-B. Chen, J. Huso, J.L. Morrison, and L. Bergman, The properties of ZnO photoluminescence at and above room temperature, *J. Appl. Phys.* 102 (2007) 116105.

[118] D. Bimberg, M. Sondergeld, and E. Grobe, Thermal dissociation of excitons bounds to neutral acceptors in high-purity GaAs, *Phys. Rev. B* 4 (1971) 3451–3455.

[119] Y.P. Varshni, Temperature dependence of the energy gap in semiconductors, *Physica* 34 (1967) 149–154.

[120] A. MANOOGIAN AND J.C. WOOLLEY, Temperature dependence of the energy gap in semiconductors, *Can. J. Phys.* 62 (1984) 285–287.

[121] A. MANOOGIAN AND A. LECLERC, Determination of the dilation and vibrational contributions to the energy band gaps in germanium and silicon, *Phys. Stat. Sol. (b)* 92 (1979) K23–K27.

[122] R. PÄSSLER, E. GRIEBL, H. RIEPL, G. LAUTNER, S. BAUER, H. PREIS, W. GEBHARDT, B. BUDA, D.J. AS, D. SCHIKORA, K. LISCHKA, K. PAPAGELIS, AND S. VES, Temperature dependence of exciton peak energies in ZnS, ZnSe, and ZnTe epitaxial films, *J. Appl. Phys.* 86 (1999) 4403–4411.

[123] L. VIÑA, S. LOGOTHETIDIS, AND M. CARDONA, Temperature dependence of the dielectric function of germanium, *Phys. Rev. B* 30 (1984) 1979–1991.

[124] R. PÄSSLER, Temperature dependence of exciton peak energies in multiple quantum wells, *J. Appl. Phys.* 83 (1998) 3356–3359.

[125] R.R. REEBER, Lattice parameters of ZnO from 4.2 to 296 K, *J. Appl. Phys.* 41 (1970) 5063–5066.

[126] J.R. TAYLOR, *Introduction to Error Analysis*, 2nd Edition, University Science Books, Sausalito,CA, 1997.

[127] D.W. HAMBY, D.A. LUCCA, M.J. KLOPFSTEIN, AND G. CANTWELL, Temperature dependent exciton photoluminescence of bulk ZnO, *J. Appl. Phys.* 93 (2003) 3214–3217.

[128] S. RUDIN, T.L. REINECKE, AND B. SEGALL, Temperature-dependent exciton linewidths in semiconductors, *Phys. Rev. B* 42 (1990) 11218–11231.

[129] S. PERMOGOROV, *Excitons*, Vol. 2, North Holland, Amsterdamn, 1982.

[130] H.-C. HSU AND W.-F. HSIEH, Excitonic polaron and phonon assisted photoluminescence of ZnO nanowires, *Solid State Commun.* 131 (2004) 371–375.

[131] T. SCHMIDT, K. LISCHKA, AND W. ZULEHNER, Excitation-power dependence of the near-band-edge photoluminescence of semiconductors, *Phys. Rev. B* 45 (1992) 8989–8994.

[132] C. KLINGSHIRN, Luminescence of ZnO under high one- and two-quantum excitation, *Phys. Stat. Sol. (b)* 71 (1975) 547–556.

[133] V.A. FONOBEROV, K.A. ALIM, A.A. BALANDIN, F. XIU, AND J. LIU, Photoluminescence investigation of the carrier recombination processes in ZnO quantum dots and nanocrystals, *Phys. Rev. B* 73 (2006) 1–9.

[134] H. YAN, Y. YANG, Z. FU, B. YANG, J. ZUO, AND S. FU, Excitation-power dependence of the near-band-edge photoluminescence of ZnO inverse opals and nanocrystal films, *J. Lumin.* 128 (2008) 245–249.

[135] Y. OHNO, H. KOIZUMI, T. TAISHI, I. YONENAGA, K. FUJII, H. GOTO, AND T. YAO, Optical properties of dislocations in wurtzite ZnO single crystals introduced at elevated temperatures, *J. Appl. Phys.* 104 (2008) 073515.

[136] E. ZACKS AND A. HALPERIN, Dependence of the peak energy of the pair-photoluminescence band on excitation intensity, *Phys. Rev. B* 6 (1972) 3072–3075.

[137] T. GOTO AND D.W. LANGER, Stimulated emission and excited states of the I_6 donor electron in ZnO, *J. Appl. Phys.* 42 (1971) 5066–5071.

[138] D. Y. SONG, M. E. HOLTZ, A. CHANDOLU, A. BERNUSSI, S. A. NIKISHIN, M. W. HOLTZ, AND I. GHERASOIU, Effect of stress and free-carrier concentration on photoluminescence in InN, *Appl. Phys. Lett.* 92 (2008) 121913.

[139] I. BALSLEV, Screening ionization of excitons in photoexcited germanium, *Phys. Rev. B* 30 (1984) 3203.

[140] D.C. REYNOLDS, D.C. LOOK, AND B. JOGAI, Combined effects of screening and band gap renormalization on the energy of optical transitions in ZnO and GaN, *J. Appl. Phys.* 88 (2000) 5760–5763.

[141] T. NAKAMURA, Y. YAMADA, T. KUSUMORI, H. MINOURA, AND H. MUTO, Improvement in the crystallinity of ZnO thin films by introduction of a buffer layer, *Thin Solid Films* 411 (2002) 60–64.

[142] S. RAMACHANDRAN, A. CHUGH, A. TIWARI, AND J. NARAYAN, Growth of highly conducting epitaxial ZnO-Pt-ZnO heterostructure on α-Al_2O_3 (0 0 0 1), *J. Cryst. Growth* 291 (2006) 212–217.

[143] R. A. Laudise and A. A. Ballman, Hydrothermal synthesis of zinc oxide and zinc sulfide, *J. Phys. Chem.* 64 (1960) 688–691.

[144] B. Cao, W. Cai, and H. Zeng, Temperature-dependent shifts of three emission bands for ZnO nanoneedle arrays, *Appl. Phys. Lett.* 88 (2006) 161101.

[145] W. Shan, T.J. Schmidt, R.J. Hauenstein, J.J. Song, and B. Goldenberg, Pressure-dependent photoluminescence study of wurtzite GaN, *Appl. Phys. Lett.* 66 (1995) 3492.

[146] B.K. Meyer, S. Lautenschläger, S. Graubner, C. Neumann, and J. Sann, Photoluminescence investigations on a native donor in ZnO, *Mater. Res. Soc. Symp. Proc.* 891 (2006) 0891–EE08–02.

[147] D. Block, A. Hervé, and R.T. Cox, Optically detected magnetic resonance and optically detected ENDOR of shallow indium donors in ZnO, *Phys. Rev. B* 25 (1982) 6049–6052.

[148] K. Johnston, M.O. Henry, D. McCabe, E. McGlynn, M. Dietrich, E. Alves, and M. Xia, Identification of donor-related impurities in ZnO using photoluminescence and radiotracer techniques, *Phys. Rev. B* 73 (2006) 165212.

[149] K. Wang, Z. Ding, T. Chen, D. Chen, S. Yao, and Z. Fu, Effects of 120 keV nitrogen and its fluence on the structural, electrical, and optical properties of ZnO film, *Nucl. Instrum. Methods Phys. Res. Sect. B* 266 (2008) 2962–2965.

[150] J. Lu, Q. Liang, Y. Zhang, Z. Ye, and S. Fujita, Improved p-type conductivity and acceptor states in N-doped ZnO thin films, *J. Phys. D: Appl. Phys.* 40 (2007) 3177–3181.

[151] C.X. Xu, G.P. Zhu, J. Kasim, S.T. Tan, Y. Yang, X. Li, Z.X. Shen, and X.W. Sun, Spatial distribution of defect in ZnO nanodisks, *Curr. Appl. Phys.* 9 (2009) 573–576.

[152] D.W. Hamby, D.A. Lucca, and M.J. Klopfstein, Photoluminescence of mechanically polished ZnO, *J. Appl. Phys.* 97 (2005) 043504.

[153] F.-Y. Jen, Y.-C. Lu, C.-Y. Chen, H.-C. Wang, C.C. Yang, B.-P. Zhang, and Y. Segawa, Temperature-dependent exciton dynamics in a ZnO thin film, *Appl. Phys. Lett.* 87 (2005) 252117.

[154] R. Cuscó, E. Alarcón-Lladó, J. Ibáñez, L. Artús, J. Jiménez, B. Wang, and M.J. Callahan, Temperature dependence of Raman scattering in ZnO, *Phys. Rev. B* 75 (2007) 165202.

[155] D.C. Reynolds, D.C. Look, B. Jogai, C.W. Litton, T.C. Collins, W. Harsch, and G. Cantwell, Neutral-donor-bound-exciton complexes in ZnO crystals, *Phys. Rev. B* 57 (1998) 12151–12155.

[156] C. Klingshirn, R. Hauschild, J. Fallert, and H. Kalt, Room-temperature stimulated emission of ZnO: Alternatives to excitonic lasing, *Phys. Rev. B* 75 (2007) 115203.

[157] X. Wang, P. Xie, F. Zhao, and Y. Wang, Time-resolved photoluminescence on the stimulated emission in polycrystalline ZnO nanoparticles, *Opt. Commun.* 282 (2009) 579–582.

[158] R.P. Wang, H. Muto, X. Gang, P. Jin, and M. Tazawa, Ultraviolet lasing with low excitation intensity in deep-level emission free ZnO films, *J. Cryst. Growth* 282 (2005) 359–364.

[159] X.Q. Zhang, Z.K. Tang, M. Kawasaki, A. Ohtomo, and H. Koinuma, Optical gain in self-assembled ZnO microcrysallite thin films, *J. Cryst. Growth* 259 (2003) 286–290.

[160] P. Zu, Z.K. Tang, G.K.L. Wong, M. Kawasaki, A. Ohtomo, H. Koinuma, and Y. Segawa, Ultraviolet spontaneous and stimulated emissions from ZnO microcrystallite thin films at room temperature, *Solid State Commun.* 103 (1997) 459–463.

[161] Z.K. Tang, G.K.L. Wong, P. Yu, M. Kawasaki, A. Ohtomo, H. Koinuma, and Y. Segawa, Room-temperature ultraviolet laser emission from self-assembled ZnO microcrystallite thin films, *Appl. Phys. Lett.* 72 (1998) 3270–3272.

[162] R. Schmidt-Grund, B. Rheinländer, C. Czekalla, G. Benndorf, H. Hochmuth, M. Lorenz, and M. Grundmann, Exciton-polariton formation at room temperature in a planar ZnO resonator structure, *Appl. Phys. B* 93 (2008) 331–337.

[163] J.H. Kim, E.-M. Kim, D. Andeen, D. Thomson, S.P. DenBaars, and F.F. Lange, Growth of heteroepitaxial ZnO thin films on GaN-

buffered Al_2O_3 (0001) substrates by low-temperature hydrothermal synthesis at 90C, *Adv. Funct. Mater.* 17 (2007) 463–471.

[164] C. Neumann, S. Lautenschläger, S. Graubner, J. Sann, N. Volbers, B.K. Meyer, J. Bläsing, A. Krost, F. Bertram, and J. Christen, Homoepitaxy of ZnO: From the substrates to doping, *Phys. Stat. Sol. (b)* 244 (2007) 1451–1457.

[165] J.-R. Duclère, C. Mc Loughlin, J. Fryar, R. O'Haire, M. Guilloux-Viry, A. Meaney, A. Perrin, E. McGlynn, M.O. Henry, and J.-P. Mosnier, ZnO thin films grown on platinum (111) buffer layers by pulsed laser deposition, *Thin Solid Films* 500 (2006) 78–83.

[166] H.-C. Hsu, Y.-K. Tseng, H.-M. Cheng, J.-H. Kuo, and W.-F. Hsieh, Selective growth of ZnO nanorods on pre-coated ZnO buffer layer, *J. Cryst. Growth* 261 (2004) 520–525.

[167] D. Zhao, C. Andreazza, P. Andreazza, J. Ma, Y. Liu, and D. Shen, Buffer layer effect on ZnO nanorods growth alignment, *Chem. Phys. Lett.* 408 (2005) 335–338.

[168] C. Andreazza-Vignolle, P. Andreazza, and D. Zhao, Catalyst effect on ZnO nanostructure shape, *Superlatt. Microstruct.* 39 (2006) 340–347.

[169] T. Yasui, M. Yasuda, D. Nezaki, M. Takata, B.P. Zhang, and Y. Segawa, Positioning growth of ZnO whiskers/dots on sapphire substrates, *Thin Solid Films* 464-465 (2004) 273–276.

[170] H. Yamada, Y. Ushimi, M. Takeuchi, Y. Yoshino, T. Makino, and S. Arai, Improvement of crystallinity of ZnO thin film and electrical characteristics of film bulk acoustic wave resonator by using Pt buffer layer, *Vacuum* 74 (2004) 689–692.

[171] H. Zhou, P. Wochner, A. Schöps, and T. Wagner, Investigation of platinum films grown on sapphire (0 0 0 1) by molecular beam epitaxy, *J. Cryst. Growth* 234 (2002) 561–568.

[172] H. Seo, T. Endoh, H. Fukuda, and S. Nomura, Highly sensitive MOSFET gas sensors with porous platinum gate electrode, *Electron. Lett.* 33 (1997) 535–536.

[173] P.D.T. Huibers and D.O. Shah, Multispectral determination of soap film thickness, *Langmuir* 13 (1997) 5995–5998.

[174] Z. Vashaei, T. Minegishi, H. Suzuki, M.W. Cho, and T. Yao, Defect and interface studies of $ZnO/Mg_xZn_{1-x}O$ heterostructures, *Journal of Physics and Chemistry of Solids* 69 (2008) 497–500.

[175] S. Permogorov, Hot excitons in semiconductors, *Phys. Stat. Sol. (b)* 68 (1975) 9–42.

[176] H. W. Kunert, D.J. Brink, F.D. Auret, J. Malherbe, J. Barnas, and V. Kononenko, Multiphonon processes in ZnO, *Phys. Stat. Sol. (c)* 2 (2005) 1131–1136.

[177] N. Pelekanos, J. Ding, Q. Fu, A. V. Nurmikko, S. M. Durbin, M. Kobayashi, and R. L. Gunshor, Hot-exciton luminescence in Zn-Te/MnTe quantum wells, *Phys. Rev. B* 43 (1991) 9354.

[178] D. Some and A.V. Nurmikko, Hot-exciton luminescence and energy transfer into *d*-electron states in $Zn_{1-x}Mn_xSe$, *Phys. Rev. B* 48 (1993) 4418–4422.

[179] R. P. Stanley, J. Hegarty, R. Fischer, J. Feldmann, E. O. Göbel, R. D. Feldman, and R. F. Austin, Hot-exciton relaxation in $Cd_xZn_{1-x}Te/ZnTe$ multiple quantum wells, *Phys. Rev. Lett.* 67 (1991) 128.

[180] E. Hendry, M. Koeberg, and M. Bonn, Exciton and electron-hole plasma formation dynamics in ZnO, *Phys. Rev. B* 76 (2007) 045214.

[181] K. Thonke, Th. Gruber, N. Teofilov, R. Schönfelder, A. Waag, and R. Sauer, Donor-acceptor pair transitions in ZnO substrate material, *Physica B* 308-310 (2001) 945–948.

[182] G. Xiong, K.B. Ucer, R.T. Williams, J. Lee, D. Bhattacharyya, J. Metson, and P. Evans, Donor-acceptor pair luminescence of nitrogen-implanted ZnO single crystal, *J. Appl. Phys.* 97 (2005) 043528.

[183] P.W. Yu, Excitation-dependent emission in Mg-, Be-, Cd-, and Zn-implanted GaAs, *J. Appl. Phys.* 48 (1977) 5043–5051.

[184] D.C. Look, D.C. Reynolds, C.W. Litton, R.L. Jones, D.B. Eason, and G. Cantwell, Characterization of homoepitaxial p-type ZnO grown by molecular beam epitaxy, *Appl. Phys. Lett.* 81 (2002) 1830.

[185] R. Hauschild, H. Priller, M. Decker, J. Brckner, H. Kalt, and C. Klingshirn, Temperature dependent band gap and homogeneous line broadening of the exciton emission in ZnO, *Phys. Stat. Sol. (c)* 3 (2006) 976.

[186] S.J. Jiao, Y.M. Lu, D.Z. Shen, Z.Z. Zhang, B.H. Li, Zh.H. Zheng, B. Yao, J.Y. Zhang, D.X. Zhao, and X.W. Fan, Donor-acceptor pair luminescence of nitrogen doping p-type ZnO by plasma-assisted molecular beam epitaxy, *J. Lumin.* 122-123 (2007) 368–370.

[187] Z. Pan, S.H. Morgan, A. Ueda, R. Aga Jr., A. Steigerwald, A.B. Hmelo, and R. Mu, Er-doped ZnO films grown by pulsed e-beam deposition, *J. Phys.: Condens. Matter* 19 (2007) 266216.

[188] H. Chen, L.W. Quo, Q. Cui, Q. Hu, Q. Huang, and J.M. Zhou, Low-temperature buffer layer for growth of a low-dislocation-density SiGe layer on Si by molecular-beam epitaxy, *J. Appl. Phys.* 79 (1996) 1167–1169.

[189] K. Miyamoto, M. Sano, H. Kato, and T. Yao, High-electron-mobility ZnO epilayers grown by plasma-assisted molecular beam epitaxy, *J. Cryst. Growth* 265 (2004) 34–40.

[190] R.K. Singh, Spatial thickness variations in laser-deposited thin films, *Mater. Sci. Eng. B* 45 (1997) 180–185.

[191] D. Zemsky, R. Shneck, P.J. Dagdigian, and I. Bar, Structure and morphology of pulsed laser depos ited boron carbide films: Influence of deposition geometry, *J. Appl. Phys.* 102 (2007) 104309.

[192] E. Burstein, Anomalous optical absorption limit in InSb, *Physical Review* 93 (1954) 632–633.

[193] M. Sahal, B. Hartiti, A. Ridah, M. Mollar, and B. Marí, Structural, electrical and optical properties of ZnO thin films deposited by sol-gel method, *Microelectron. J.* 39 (2008) 1425–1428.

[194] H.J. Ko, Y.F. Chen, S.K. Hong, H. Wenisch, T. Yao, and D.C. Look, Ga-doped ZnO films grown on GaN templates by plasma-assisted molecular-beam epitaxy, *Appl. Phys. Lett.* 77 (2000) 3761–3763.

[195] M. Schilling, R. Helbig, and G. Pensl, Bound exciton luminescence of Ar- and Al-implanted ZnO, *J. Lumin.* 33 (1985) 201–212.

[196] Michio Tajima, Quantitative impurity analysis in Si by the photoluminescence technique, *Jpn. Annu. Rev. Electron. Comput. Telecommun.* 1 (1982) 1–12.

[197] R. Laiho, L.S. Vlasenko, and M.P. Vlasenko, Optical detection of magnetic resonance and electron paramagnetic resonance study of the oxygen vacancy and lead donors in ZnO, *J. Appl. Phys.* 103 (2008) 123709.

[198] K. Vanheusden, W.L. Warren, J.A. Voigt, C.H. Seager, and D.R. Tallant, Impact of Pb doping on the optical and electronic properties of ZnO powders, *Appl. Phys. Lett.* 67 (1995) 1280.

[199] S.-M. Zhou, X.-H. Zhang, X.-M. Meng, S.-K. Wu, and S.-T. Lee, Synthesis and optical properties of Pb-doped ZnO nanowires, *Phys. Stat. Sol. (a)* 202 (2005) 405–410.

[200] J. Klikorka, P. Lošťák, Horák J., and L. Fojtík, Zinc-oxide with high luminescence in the ultraviolet region, *Crystal Res. & Technol.* 17 (1982) 1571–1577.

[201] Dewei Chu, Yu-Ping Zeng, and Dongliang Jiang, Hydrothermal synthesis and optical properties of Pb^{2+} doped ZnO nanorods, *Materials Letters* 60 (2006) 2783–2785.

[202] A. Markwitz and J. Kennedy, Group-IV and v ion implantation into nanomaterials and elemental analysis on the nanometre scale, *Int. J. Nanotechnol.* 6 (2009) 369–383.

[203] J.P. Biersack, Computer simulations of sputtering, *Nucl. Instrum. Methods Phys. Res. Sect. B* 27 (1987) 21–36.

[204] S. Amoruso, B. Toftmann, and J. Schou, Thermalization of a UV laser ablation plume in a background gas: From a directed to a diffusionlike flow, *Phys. Rev. E Stat. Nonlinear Soft Matter Phys.* 69 (2004) 056403.

[205] C.X. Shan, Z. Liu, and S.K. Hark, Temperature dependent photoluminescence study on phosphorus doped ZnO nanowires, *Appl. Phys. Lett.* 92 (2008) 073103.

[206] J.C. SLATER, Atomic radii in crystals, *J. Chem. Phys.* 41 (1964) 3199–3204.

[207] R. D. SHANNON, Revised Effective Ionic-Radii And Systematic Studies Of Interatomic Distances In Halides And Chalcogenides, *Acta Crystallogr. A* 32 (1976) 751–767.

[208] E. RITA, E. ALVES, U. WAHL, J.G. CORREIA, T. MONTEIRO, M.J. SOARES, A. NEVES, AND M. PERES, Stability and luminescence studies of Tm and Er implanted ZnO single crystals, *Nucl. Instrum. Methods Phys. Res. Sect. B* 242 (2006) 580–584.

[209] S.B. ORLINSKII, J. SCHMIDT, P.G. BARANOV, D.M. HOFMANN, C. DE MELLO DONEGÁ, AND A. MEIJERINK, Probing the wave function of shallow Li and Na donors in ZnO nanoparticles, *Phys. Rev. Lett.* 92 (2004) 476031–476034.

[210] H. RENNER, G. SCHLAMP, I. KLEINWÄCHTER, E. DROST, H.M. LÜSCHOW, P. TEWS, P. PANSTER, M. DIEHL, J. LANG, T. KREUZER, A. KNÖDLER, K. A. STARZ, K. DERMANN, J. ROTHAUT, R. DRIESELMANN, C. PETER, AND R. SCHIELE, Platiunum Group Metals and Compounds, *Ulmann's Encyclopedia of Industrial Chemistry* 1 (2005) 1.

[211] L. W. ALVAREZ, W. ALVARES, F. ASARO, AND H. V. MICHEL, Extraterrestrial Cause For The Cretaceous-Tertiary Extinction - Experimental Results And Theoretical Interpretation, *Science* 208 (1980) 1095–1108.

[212] J. EMSLEY, *Nature's Building Blocks: An A-Z Guide to the Elements.*, Oxford University Press, 2003.

[213] M. CLEMENT, J. OLIVARES, E. IBORRA, S. GONZÃLEZ CASTILLA, N. RIMMER, AND A. RASTOGI, AlN films sputtered on iridium electrodes for bulk acoustic wave resonators, *Thin Solid Films* 517 (2009) 4673–4678.

[214] Z. LIU, Z. BIAN, F. HAO, D. NIE, F. DING, Z. CHEN, AND C. HUANG, Highly efficient, orange-red organic light-emitting diodes using a series of green-emission iridium complexes as hosts, *Org. Electron.: phys. mater. appl.* 10 (2009) 247–255.

[215] J.J. LIN, S.M. HUANG, Y.H. LIN, T.C. LEE, H. LIU, X.X. ZHANG, R.S. CHEN, AND Y.S. HUANG, Low temperature electrical transport prop-

erties of RuO_2 and IrO_2 single crystals, *J. Phys.: Condens. Matter* 16 (2004) 8035–8041.

[216] J.-T. Yu and Y.-S. Huang, Electron paramagnetic resonance of a molecular defect in -irradiated IrO_2 single crystals, *Phys. Rev. B* 40 (1989) 4281–4288.

[217] S.H. Brewer, D. Wicaksana, J.-P. Maria, A.I. Kingon, and S. Franzen, Investigation of the electrical and optical properties of iridium oxide by reflectance FTIR spectroscopy and density functional theory calculations, *Chem. Phys.* 313 (2005) 25–31.

[218] R.K. Kawar, P.S. Chigare, and P.S. Patil, Substrate temperature dependent structural, optical and electrical properties of spray deposited iridium oxide thin films, *Appl. Surf. Sci.* 206 (2003) 90–101.

[219] R. S. Chen, Y. S. Chen, Y. S. Huang, Y. L. Chen, Y. Chi, C. S. Liu, K. K. Tiong, and A. J. Carty, Growth of IrO_2 films and nanorods by means of CVD: An example of compositional and morphological control of nanostructures, *Chem. Vap. Deposition* 9 (2003) 301–305.

[220] L.M. Zhang, Y.S. Gong, C.B. Wang, Q. Shen, and M.X. Xia, Substrate temperature dependent morphology and resistivity of pulsed laser deposited iridium oxide thin films, *Thin Solid Films* 496 (2006) 371–375.

[221] W.C. Dautremont-Smith, G. Beni, L.M. Schiavone, and J.L. Shay, Solid-state electrochromic cell with anodic iridium oxide film electrodes, *Appl. Phys. Lett.* 35 (1979) 565–567.

[222] D.O. Wipf, F. Ge, T.W. Spaine, and J.E. Baur, Microscopic measurement of pH with iridium oxide microelectrodes, *Anal. Chem.* 72 (2000) 4921–4927.

[223] R.W. Schutz, Ruthenium enhanced titanium alloys: Minor ruthenium additions produce cost effective corrosion resistant commercial titanium alloys, *Platinum Metals Rev.* 40 (1996) 54–61.

[224] T. Funaki, M. Yanagida, N. Onozawa-Komatsuzaki, K. Kasuga, Y. Kawanishi, and H. Sugihara, A 2-quinolinecarboxylate-substituted ruthenium(II) complex as a new type of sensitizer for dye-sensitized solar cells, *Inorg. Chim. Acta* 362 (2009) 2519–2522.

[225] A. Paskaleva, M. Tapajna, E. Atanassova, K. Fröhlich, A. Vincze, and E. Dobročka, Effect of Ti doping on Ta_2O_5 stacks with Ru and Al gates, *Appl. Surf. Sci.* 254 (2008) 5879–5885.

[226] D. Ferizović, L.K. Hussey, Y.-S. Huang, and M. Muñoz, Determination of the room temperature thermal conductivity of RuO_2 by the photothermal deflection technique, *Appl. Phys. Lett.* 94 (2009) 131913.

[227] Se-Hee Lee, Ping Liu, Hyeonsik M. Cheong, C. Edwin Tracy, and Satyen K. Deb, Electrochromism of amorphous ruthenium oxide thin films, *Solid State Ionics* 165 (2003) 217–221.

[228] H. Neil McMurray, Peter Douglas, and Duncan Abbot, Novel thick-film pH sensors based on ruthenium dioxide-glass composites, *Sens. Actuators B* 28 (1995) 9–15.

[229] K. Fröhlich, D. Machadík, V. Cambel, I. Kostič, and S. Pignard, Epitaxial growth of low-resistivity RuO_2 films on (1 $\bar{1}$ 0 2)-oriented Al_2O_3 substrate, *J. Cryst. Growth* 235 (2002) 377–383.

[230] K. Leinartas, P. Miecinskas, and E. Juzeliūnas, Ruthenium dioxide quartz crystal nano-balance, *Sens. Actuators B* 137 (2009) 762–767.

[231] Q. X. Jia, X. D. Wu, S. R. Foltyn, A. T. Findikoglu, P. Tiwari, J. P. Zheng, and T. R. Jow, Heteroepitaxial growth of highly conductive metal-oxide RuO_2 thin-films by pulsed-laser deposition, *Appl. Phys. Lett.* 67 (1995) 1677–1679.

[232] X. Fang, M. Tachiki, and T. Kobayashi, Deposition and properties of PLD grown RuO_2 thin film, in: 3rd International Conference on Thin Film Physics and Applications, Vol. 3175, Shanghai, 1998, pp. 331–335.

[233] Mihály Óvári, Gábor Muránszky, Michaela Zeiner, István Virág, Ilse Steffan, Victor G. Mihucz, Eniko Tatár, Sergio Caroli, and Gyula Záray, Determination of Pt in urine of tram drivers by sector field inductively coupled plasma mass spectrometry, *Microchemical Journal* 87 (2007) 159–162.

[234] L. Maya, L. Riester, T. Thundat, and C.S. Yust, Characterization of sputtered amorphous platinum dioxide films, *J. Appl. Phys.* 84 (1998) 6382–6386.

[235] Carolyn Rubin Aita, Optical behavior of sputter-deposited platinum-oxide films, *J. Appl. Phys.* 58 (1985) 3169–3173.

[236] R. Ahuja, S. Auluck, B. Johansson, and M.A. Khan, Optical properties of PdO and PtO, *Phys. Rev. B* 50 (1994) 2128–2132.

[237] M. Fleischmann, S. Pons, M. Hawkins, and R.J. Hoffman, Measurement of gamma rays from cold fusion, *Nature* 339 (1989) 667.

[238] Yansheng Gong, Chuanbin Wang, Qiang Shen, and Lianmeng Zhang, Effect of annealing on thermal stability and morphology of pulsed laser deposited Ir thin films, *Appl. Surf. Sci.* 254 (2008) 3921–3924.

[239] R.E. Leuchtner, D.B. Chrisey, J.S. Horwitz, and K.S. Grabowski, The preparation of epitaxial platinum films by pulsed laser deposition, *Surf. Coat. Technol.* 51 (1992) 476–482.

[240] S. Bouhtiyya and L. Roué, On the characteristics of Pd thin films prepared by pulsed laser deposition under different helium pressures, *Int. J. Hydrogen Energy* 33 (2008) 2912–2920.

[241] N. Patel, R. Fernandes, G. Guella, A. Kale, A. Miotello, B. Patton, C. Zanchetta, P.M. Ossi, and V. Russo, Pulsed-laser deposition of nanostructured Pd/C thin films: A new entry into metal-supported catalysts for hydrogen producing reactions, *Appl. Surf. Sci.* 254 (2007) 1307–1311.

[242] J. Paillier, S. Bouhtiyya, G.G. Ross, and L. Roué, Influence of the deposition atmosphere on the characteristics of Pd-Mg thin films prepared by pulsed laser deposition, *Thin Solid Films* 500 (2006) 117–123.

[243] V.Val. Sobolev, Optical properties and electronic structure of PdO, *Inorg. Mater.* 40 (2004) 166–170.

[244] K.C. Hass and A.E. Carlsson, Band structures of nonmagnetic transition-metal oxides: PdO and PtO, *Phys. Rev. B* 46 (1992) 4246–4249.

[245] J. Uddin, J.E. Peralta, and G.E. Scuseria, Density functional theory study of bulk platinum monoxide, *Phys. Rev. B* 71 (2005) 155112.

[246] N. Seriani, Z. Jin, W. Pompe, and L.C. Ciacchi, Density functional theory study of platinum oxides: From infinite crystals to nanoscopic particles, *Phys. Rev. B* 76 (2007) 155421.

[247] H.A.E. Hagelin, J.F. Weaver, G.B. Hoflund, and G.N. Salaita, Electron energy loss spectroscopic investigation of palladium metal and palladium(II) oxide, *J. Electron Spectrosc. Relat. Phenom.* 124 (2002) 1–14.

[248] J. Tauc, *Amorphous and liquid semiconductor*, Plenum, New York, 1974.

[249] N. Barreau, A. Mokrani, F. Couzinié-Devy, and J. Kessler, Bandgap properties of the indium sulfide thin-films grown by co-evaporation, *Thin Solid Films* 517 (2009) 2316–2319.

[250] S. Sirohi and T. P. Sharma, Bandgaps of cadmium telluride sintered film, *Optical Materials* 13 (1999) 267–269.

[251] Jin Zhensheng, Xi Chanjuan, Zeng Qingmei, Yin Feng, Zhao Jiazheng, and Xue Jinzhen, Catalytic behavior of nanoparticle α-PtO_2 for ethanol oxidation, *J. Mol. Catal. A: Chem.* 191 (2003) 61–66.

[252] M.A. El Khakani and M. Chaker, Highly conductive and optically transparent polycrystalline iridium oxide thin films grown by reactive pulsed laser deposition, *Mater. Res. Soc. Symp. Proc.* 472 (1997) 373.

[253] P.O. Nilsson and M.S. Shivaraman, Optical properties of PdO in the range of 0.5-5.4 eV, *J. Phys. C: Solid State Phys.* 12 (1979) 1423–1427.

[254] Ashok K. Goel, G. Skorinko, and Fred H. Pollak, Optical properties of single-crystal rutile RuO_2 and IrO_2 in the range 0.5 to 9.5 eV, *Phys. Rev. B* 24 (1981) 7342.

[255] D. Dellasega, A. Facibeni, F. Di Fonzo, V. Russo, C. Conti, C. Ducati, C.S. Casari, A. Li Bassi, and C.E. Bottani, Nanostructured high valence silver oxide produced by pulsed laser deposition, *Appl. Surf. Sci.* 255 (2009) 5248–5251.

[256] M. Bielmann, P. Schwaller, P. Ruffieux, O. Gröning, L. Schlapbach, and P. Gröning, AgO investigated by photoelectron spectroscopy: Evidence for mixed valence, *Phys. Rev. B* 65 (2002) 235431.

[257] H. Tsai, E. Hu, K. Perng, M. Chen, J.-C. Wu, and Y.-S. Chang, Instability of gold oxide Au_2O_3, *Surf. Sci.* 537 (2003) L447.

[258] E. Irissou, M.-C. Denis, M. Chaker, and D. Guay, Gold oxide thin film grown by pulsed laser deposition in an O_2 atmosphere, *Thin Solid Films* 472 (2005) 49–57.

[259] M.W. Allen, S.M. Durbin, and J.B. Metson, Silver oxide Schottky contacts on n-type ZnO, *Appl. Phys. Lett.* 91 (2007) 053512.

[260] S.M. Sze, *Physics of Semiconductor Devices*, Wiley, New York, 1981.

[261] W. Mönch, Barrier heights of real Schottky contacts explained by metal-induced gap states and lateral inhomogeneities, *J. Vac. Sci. Technol. B* 17 (1999) 1867–1876.

[262] Q. Wan, Z. Xiong, J. Dai, J. Rao, and F. Jiang, First-principles study of Ag-based p-type doping difficulty in ZnO, *Optical Materials* 30 (2008) 817–821.

[263] L. Duan, B. Lin, W. Zhang, S. Zhong, and Z. Fu, Enhancement of ultraviolet emissions from ZnO films by Ag doping, *Appl. Phys. Lett.* 88 (2006) 232110.

[264] S. Zhou, Q. Xu, K. Potzger, G. Talut, R. Grötzschel, J. Fassbender, M. Vinnichenko, J. Grenzer, M. Helm, H. Hochmuth, M. Lorenz, M. Grundmann, and H. Schmidt, Room temperature ferromagnetism in carbon-implanted ZnO, *Appl. Phys. Lett.* 93 (2008) 232507.

[265] M. Ungureanu, H. Schmidt, Q. Xu, H. von Wenckstern, D. Spemann, H. Hochmuth, M. Lorenz, and M. Grundmann, Electrical and magnetic properties of RE-doped ZnO thin films (RE = Gd, Nd), *Superlatt. Microstruct.* 42 (2007) 231–235.

[266] W. Lin, R. Ma, W Shao, and B. Liu, Structural, electrical and optical properties of Gd doped and undoped ZnO:Al (ZAO) thin films prepared by RF magnetron sputtering, *Appl. Surf. Sci.* 253 (2007) 5179 – 5183.

[267] V. Ney, S. Ye, T. Kammermeier, A. Ney, H. Zhou, J. Fallert, H. Kalt, F.-Y. Lo, A. Melnikov, and A. D. Wieck, Structural, magnetic, and optical properties of Co- and Gd-implanted ZnO(0001) substrates, *J. Appl. Phys.* 104 (2008) 083904.

[268] K. Potzger, Shengqiang Zhou, F. Eichhorn, M. Helm, W. Skorupa, A. Mücklich, J. Fassbender, T. Herrmannsdörfer, and

A. BIANCHI, Ferromagnetic Gd-implanted ZnO single crystals, *Journal of Applied Physics* 99 (2006) 063906.

[269] M. UNGUREANU, H. SCHMIDT, H. VON WENCKSTERN, H. HOCHMUTH, M. LORENZ, M. GRUNDMANN, M. FECIORU-MORARIU, AND G. GÜNTHERODT, A comparison between ZnO films doped with $3d$ and $4f$ magnetic ions, *Thin Solid Films* 515 (2007) 8761–8763.

[270] K. VANHEUSDEN, C.H. SEAGER, W.L. WARREN, D.R. TALLANT, AND J.A. VOIGT, Correlation between photoluminescence and oxygen vacancies in ZnO phosphors, *Appl. Phys. Lett.* 68 (1996) 403–405.

[271] X.L. WU, G.G. SIU, C.L. FU, AND H.C. ONG, Photouminescence and cathodoluminescence studies of stoichiometric and oxygen-deficient ZnO films, *Appl. Phys. Lett.* 78 (2001) 2285–2287.

[272] R. DINGLE, Luminescent transitions associated with divalent copper impurities and the green emission from semiconducting zinc oxide, *Phys. Rev. Lett.* 23 (1969) 579–581.

[273] N.Y. GARCES, L. WANG, L. BAI, N.C. GILES, L.E. HALLIBURTON, AND G. CANTWELL, Role of copper in the green luminescence from ZnO crystals, *Appl. Phys. Lett.* 81 (2002) 622.

[274] M.L. KAHN, T. CARDINAL, B. BOUSQUET, M. MONGE, V. JUBERA, AND B. CHAUDRET, Optical properties of zinc oxide nanoparticles and nanorods synthesized using an organometallic method, *ChemPhysChem* 7 (2006) 2392–2397.